NATIONAL TECHNICAL UNIVERSITY OF ATHENS
SCHOOL OF APPLIED SCIENCES
DEPARTMENT OF PHYSICS
HIGH ENERGY PHYSICS LABORATORY

First observation of the associated production of Z bosons with prompt and non-prompt J/ψ mesons in pp collisions at $\sqrt{s} = 8\,\mathrm{TeV}$ and contribution to the Micromegas detectors for the New Small Wheel upgrade of the ATLAS experiment

A dissertation presented by

Stefanos G. Leontsinis

to

The Department of Physics
for the degree of
Doctor of Philosophy
in the subject of

Physics

National Technical University of Athens
June 2015

First observation of the associated production of Z bosons with prompt and non-prompt J/ψ mesons in pp collisions at $\sqrt{s} = 8\,\mathrm{TeV}$ and contribution to the Micromegas detectors for the New Small Wheel upgrade of the ATLAS experiment

PhD THESIS

Stefanos G. Leontsinis

Advisors: Theodoros Alexopoulos
Professor, NTU-Athens

Exam committee:

....

T. Alexopoulos   E. Gazis   G. Tsipolitis

Professor NTUA   Professor NTUA   Professor NTUA

....

E. Katsoufis   C. Kourkoumelis   V. Polychronakos   D. Fassouliotis

Emeritus professor NTUA   Professor NKUA   Senior Researcher BNL   Associate professor NKUA

Athens, (June 2015)

....
Stefanos G. Leontsinis

ΕΘΝΙΚΟ ΜΕΤΣΟΒΙΟ ΠΟΛΥΤΕΧΝΕΙΟ
ΣΧΟΛΗ ΕΦΑΡΜΟΣΜΕΝΩΝ ΜΑΘΗΜΑΤΙΚΩΝ
ΚΑΙ ΦΥΣΙΚΩΝ ΕΠΙΣΤΗΜΩΝ

Πρώτη παρατήρηση της ταυτόχρονης παραγωγής Z μποζονίου με J/ψ μεσόνια σε συγκρούσεις πρωτονίων σε ενέργεια κέντρου μάζας 8 TeV και συνεισφορά στη μελέτη των ανιχνευτών Micromegas για την αναβάθμιση του New Small Wheel του πειράματος ATLAS

ΔΙΔΑΚΤΟΡΙΚΗ ΔΙΑΤΡΙΒΗ

Στέφανου Γ. Λεοντσίνη

Διπλωματούχου Φυσικού Εφαρμογών Ε.Μ.Π.

ΕΠΙΒΛΕΠΩΝ :
Θ. ΑΛΕΞΟΠΟΥΛΟΣ
Καθηγητής Ε.Μ.Π.

ΑΘΗΝΑ, Ιούνιος 2015

ΕΘΝΙΚΟ ΜΕΤΣΟΒΙΟ ΠΟΛΥΤΕΧΝΕΙΟ
ΣΧΟΛΗ ΕΦΑΡΜΟΣΜΕΝΩΝ ΜΑΘΗΜΑΤΙΚΩΝ
ΚΑΙ ΦΥΣΙΚΩΝ ΕΠΙΣΤΗΜΩΝ

Πρώτη παρατήρηση της ταυτόχρονης παραγωγής Z μποζονίου με J/ψ μεσόνια σε συγκρούσεις πρωτονίων σε ενέργεια κέντρου μάζας 8 TeV και συνεισφορά στη μελέτη των ανιχνευτών Micromegas για την αναβάθμιση του New Small Wheel του πειράματος ATLAS

ΔΙΔΑΚΤΟΡΙΚΗ ΔΙΑΤΡΙΒΗ

Στέφανου Γ. Λεοντσίνη

Διπλωματούχου Φυσικού Εφαρμογών Ε.Μ.Π.

ΤΡΙΜΕΛΗΣ ΣΥΜΒΟΥΛΕΥΤΙΚΗ ΕΠΙΤΡΟΠΗ:
1. Θ. Αλεξόπουλος, Καθ. Ε.Μ.Π.
2. Ε. Γαζής, Καθ. Ε.Μ.Π.
3. Γ. Τσιπολίτης, Καθ. Ε.Μ.Π.

ΕΠΤΑΜΕΛΗΣ ΕΞΕΤΑΣΤΙΚΗ ΕΠΙΤΡΟΠΗ:
1. Θ. Αλεξόπουλος, Καθ. Ε.Μ.Π.
2. Ε. Γαζής, Καθ. Ε.Μ.Π.
3. Γ. Τσιπολίτης, Καθ. Ε.Μ.Π.
4. Η. Κατσούφης, Ομ. Καθ. Ε.Μ.Π.
5. Χ. Κουρκουμέλη, Καθ. Ε.Κ.Π.Α.
6. Β. Πολυχρονάκος, Ερευνητής Α, BNL
7. Δ. Φασουλιώτης, Αν. Καθ. Ε.Κ.Π.Α.

ΑΘΗΝΑ, Ιούνιος 2015

....
Στέφανος Γ. Λεοντσίνης

Δεν υπάρχουν λόγια για να περιγράψω την ευγνωμοσύνη μου προς αυτούς που με στηρίζουν και με βοήθησαν να φτάσω ως εδώ.

Πρώτα προς την οικογένεια μου. Δε θα μπορούσα να ζητήσω καλύτερη οικογένεια από αυτή που έτυχα να ανήκω. Θα ήθελα να αφιερώσω τη διατριβή αυτή προς αυτούς, και να τους ζητήσω παράλληλα συγγνώμη για τις στιγμές που δεν ήμουν αυτός που έπρεπε. Ελπίζω μια μέρα να ανταποδώσω το καλό που μου έχετε προσφέρει. Στον πατέρα μου Γρηγόρη, στη μητέρα μου Χριστίνα και στον αδερφό μου Σταμάτη.

Θα ήθελα επίσης να αφιερώσω τη δουλειά αυτή στο πατατάκι μου που είναι συνέχεια στο πλάι μου ακούραστη. Είναι ό,τι καλύτερο μου έχει συμβεί. Ελπίζω να το της το δείχνω όπως πρέπει. ☺

Περίληψη

Η ταυτόχρονη παραγωγή μποζονίων με βαρέα quarkonia αποτελεί έναν πολύ σημαντικό τρόπο για την κατανόηση της παραγωγής των quarkonia. Η διατριβή αυτή μελετάει την παραγωγή J/ψ με-σονίων σε συσχέτιση με μποζόνια Z χρησιμοποιώντας δεδομένα σύγκρουσης πρωτονίων σε ενέργειες $\sqrt{s} = 8\,\mathrm{TeV}$ που έχουν συλλεχθεί από το πείραμα ATLAS. Επειδή τα μεσόνια J/ψ παράγονται στο πείραμα είτε από άμεσες διαδικασίες κβαντοχρωμοδυναμικής είτε από τη διάσπαση αδρονίων που περιέχουν ένα b-quark (τα οποία παρουσιάζουν μεγαλύτερους χρόνους ημιζωής), μελετούνται και οι δύο τρόποι.

Ο ρυθμός ταυτόχρονης παραγωγής Z μποζονίων με άμεσα (ή έμμεσα) J/ψ μεσόνια μετράται ως προς την αποκλειστική παραγωγή Z μποζονίων. Ο τρόπος διάσπασης των σωματιδίων αυτών που επιλέχτηκε ήταν $Z \to \ell^+\ell^-$, όπου $\ell = \mu, e$ και $J/\psi \to \mu^+\mu^-$. Για να διορθώσουμε τη μέτρηση λόγω της αναποτελεσματικής ανακατασκευής των τροχιών των μιονίων από το J/ψ (η αποδοτικότητα των σωματιδίων που διασπάται το Z απλοποιείται στο λόγο των ενεργών διατομών), η αποδοτικότητα ανακατασκευής μιονικών τροχιών στο πείραμα ATLAS μετράται χρησιμοποιώντας τη μέθοδο βρες-και-έλεγξε με διασπάσεις $J/\psi \to \mu^+\mu^-$.

Τα σωμάτια που μελετούνται μπορούν να παραχθούν ταυτόχρονα είτε μέσω αλληλεπίδρασης ενός ζευγαριού παρτονίων (μονή σκέδαση παρτονίων) είτε από δύο ζευγάρια (διπλή σκέδαση παρ-τονίων). Η συνεισφορά της διπλής σκέδασης παρτονίων στη τελική κατάσταση μελετάται και αφαιρείται από τη μέτρηση ώστε να μπορεί να συγκριθεί με θεωρητικούς υπολογισμούς. Θεω-ρητικά μοντέλα colour singlet προέβλεψαν πως η ταυτόχρονη παραγωγή Z μποζονίων και J/ψ με-σονίων δε θα ήταν δυνατό να παρατηρηθεί με τα δεδομένα που συλλέγησαν από το πείραμα κατά το 2012. Αντίθετα, θεωρητικά μοντέλα colour octet υπολογίζουν την παρατήρηση λίγοστών γεγονότων. Συγκεκριμένα, τα CO και CS μοντέλα προβλέπουν 5 φορές χαμηλότερο ρυθμό παραγωγής για $p_\mathrm{T} > 18\,\mathrm{GeV}$.

Η ενεργός διατομή της διπλής σκέδασης παρτονίων (σ_eff) θεωρείται πως είναι ανεξάρτητη από τη διαδικασία που χρησιμοποιείται για τη μέτρησή της και παρουσιάζει μια μικρή συσχέτιση με την ενέργεια σύγκρουσης στο κέντρο μάζας. Η μεταβλητή της αζιμουθαικής γωνίας μεταξύ του Z μποζονίου και του J/ψ μεσονίου, επειδή επηρεάζεται από τη διπλή σκέδαση παρτονίων, χρησιμοποιείται για τον υπολογισμό κατώτερου ορίου της (σ_eff). Η πληροφορία αυτή είναι η πρώτη που παρουσιάζεται στην ενέργεια $\sqrt{s} = 8\,\mathrm{TeV}$.

Παράλληλα, μελετάται η σπάνια διάσπαση του B_s μεσονίου σε δύο μιόνια. Παρουσιάζονται οι μέθοδοι που χρησιμοποιήθηκαν για το διαχωρισμό του σήματος και του υποβάθρου και ο υπολογισμός του αριθμού γεγονότων του καναλιού $B^\pm \to J/\psi K^\pm$, το οποίο χρησιμοποιείται ως κανάλι κανονικοποίησης για τη μέτρηση.

Σε ότι αφορά στο μέλλον του πειράματος ATLAS, η διατριβή αυτή περιέχει τη μελέτη διαφόρων προτύπων του ανιχνευτή micromegas ως μέρους της αναβάθμισης του μικρού τροχού. Παρουσιάζει

τα χαρακτηριστικά του ανιχνευτή αυτού (απόδοση και διακριτική ικανότητα), χρησιμοποιώντας δεδομένα που συλλέχθηκαν από τον ανιχνευτή αυτό σε δοκιμαστικές δέσμες και από το πείραμα ATLAS.

Abstract

The associated production of vector boson with heavy quarkonia is a key observable for understanding the quarkonium production mechanism. This thesis studies the production of J/ψ mesons in association with Z bosons, using pp collision data at $\sqrt{s} = 8\,\text{TeV}$ collected with the ATLAS experiment at the LHC. Since the J/ψ meson can be produced in the experiment either by prompt QCD processes or by a subsequent decay of a b-hadron (having longer lifetimes than prompt), both $Z+$ prompt J/ψ and $Z+$ non-prompt J/ψ productions are examined.

The associated production rate of $Z+$ prompt (or non-prompt) J/ψ is measured as a function of the inclusive Z production. The decay modes chosen for this study were the $Z \rightarrow \ell^+\ell^-$, where $\ell = \mu, e$ and $J/\psi \rightarrow \mu^+\mu^-$. In order to correct for the muon reconstruction inefficiency of the J/ψ muons (the Z decay products reconstruction efficiency cancels in the ratio), the muon reconstruction efficiency of the ATLAS experiment is measured using the tag-and-probe method with $J/\psi \rightarrow \mu^+\mu^-$ decays.

The two final state particles, Z and J/ψ, may occur from either a single pair of interacting partons (single parton scattering) or two pairs of partons (double parton scattering). The contribution from double parton scattering is examined and subtracted in order to compare the measurement with theory calculations. Colour singlet theoretical models predicted that this process could not be observed with the data collected from the LHC during 2012, while colour octet models calculated a handful of events. From the result of the measurement, CO models underestimate the data by a factor 5 in the high-p_T region.

The double parton scattering effective cross-section (σ_{eff}) is considered to be process independent and slightly correlated with $\sqrt{s}$. The azimuthal angle observable between the Z and the J/ψ being sensitive to double parton scattering is used to derive a lower limit on σ_{eff}. This was the first information on σ_{eff} for $\sqrt{s} = 8\,\text{TeV}$.

Furthermore, the search for the $B_s \rightarrow \mu^+\mu^-$ is presented. For this rare process, the separation of the signal to background is described as well as the extraction of the $B^\pm \rightarrow J/\psi K^\pm$ reference channel, used in the cross-section measurement.

Looking towards the future and the upgrades of the ATLAS experiment, this thesis studies the micromegas detector as part of the new small wheel. It presents its main characteristics in terms of efficiency and performance, derived from test-beam studies and from data collected from micromegas placed in the ATLAS cavern.

Acknowledgements

I find it very difficult to list all the people for their help and constant support during this PhD. A couple of lines in paper would be inadequate to encapsulate the gratefulness I feel to the people that truly stood by me and supported me. I would like to acknowledge the help from:

* Jona Bortfeldt

* James Catmore

* Evangelos Gazis

* Giorgos Iakovidis

* Paolo Iengo

* George Karananas

* Kostas Karakostas

* Vato Kartvelishvili

* Kostas Ntekas

* Sandro Palestini

* Darren Price

* Yorgos Tsipolitis

* Miriam Watson

* Joerg Wotschack

At this point I would like to thank people that are not directly related with this PhD, but inevitably helped me finish it.

* Panos Gkountoumis

* Loukas Gouskos

* Themos Karananas

* Paris Moschovakos

* Nikos Tsitsilonis

I feel that I need to specifically show my respect and gratitude to:

- Theo Alexopoulos for the confidence he showed me upon entrusting me with this PhD, with his guidance throughout it, his unreserved attention, his advice and, most importantly, with the opportunity he gave me to research upon an extremely interesting subject and to carry out this PhD thesis.

- Alex Cerri, with whom I had the pleasure of working with. I should thank him for many things, but what I would like to point is that from a stressful collaboration I gained a good friend.

- Vinnie Polychronakos, for the invaluable and constant support and our discussions, in matters related to analyses and not.

As J.F. Kennedy said, "As we express our gratitude, we must never forget that the highest appreciation is not to utter words, but to live by them". From the above list, some had major contribution and some smaller. I do hope that my behaviour and actions reflect my gratitude towards their major or smaller contribution for the realisation of this PhD.

Πέρα κι Αϊβαλί έγινε καταστροφή μα μια Ιδέα,
από τον ξεριζωμό, γεννήθηκε από Πρόσφυγες εδώ

Μια Ιστορία από την Πόλη μας μεγαλώνει από παιδιά.
Το μεγαλείο σου δεν τελειώνει, Εσύ Ιδέα μοναδικά

Εικόνες αλησμόνητες ισόβια μεσ'το μυαλό μου
μεσ'του Βοσπόρου τα στενά ξεκίνησε το όνειρο μου
το'φεραν οι παππούδες μας στης Φιλαδέλφειας τα μέρη
εκεί σε πρωτογνώρισα, ολόκληρη η γη το ξέρει

Ανώνυμος, 2013

x

Contents

Chapter 1

Theory

1.1 Standard model

The Standard Model (SM) of particle physics is an extremely successful framework that has made possible to describe in a consistent way and on equal footing three out of the four fundamental forces; the electromagnetic, the weak and the strong. It offers a solid ground for calculations and predictions [1, 2] and has proven to hold, although recent experiments have put it under serious scrutiny [3].

The SM is based on the gauge principle, a concept elegant in its simplicity; an interaction follows immediately from the localisation of a symmetry that was initially global. The symmetry group of this theory is described by $SU(3)_C \times SU(2)_L \times U(1)_Y$, where the $SU(2)_L \times U(1)_Y$ reflects the unification of the electromagnetic and weak interactions and $SU(3)_C$ the strong interactions. These three are the symmetry groups that dictate the presence of the $3^2 - 1 = 8$ gluons, the 3 weak force carriers ($W^\pm$, Z) and the photon[1].

Particle physics aims at including all the observed phenomena to a (as small as possible) set of basic laws and theories that will be able to predict and verify experimental observations. Four classes of fundamental interactions are realised in Nature: strong, electromagnetic, weak and gravitational. These are summarised in table 1.1.

Table 1.1: *The four fundamental interactions and their carriers.*

Force	boson	charge	spin
Strong	g-gluon	0	1
Electromagnetic	γ-photon	0	1
Weak	$W^\pm - Z^0$	$\pm - 0$	1
Gravitational	G-graviton	0	2

The aforementioned forces are transmitted by gauge bosons, which mediate interactions between the fermions and each other. For example, photons mediate electromagnetic interaction, whereas the weak force is transmitted by the massive $W^\pm$ and Z bosons.

---

[1]A special unitary group with N dimensions has $N^2 - 1$ generators.

1.1.1 Quarks and leptons

When these forces are probed in high energy collisions, many new particles appear. These particles, due to their unstable nature, decay to more stable particles.

Apart from the gauge bosons g, γ, W and Z, there are two other types of particles that are produced: hadrons and leptons. The leptons comprise a family of six particles and are grouped in three generations (see table 1.2).

Quarks are grouped to form hadrons and are held together by the strong force. There are various flavours of quarks (see table 1.2) and are governed, together with the gluon, by the rules of Quantum Chromo-Dynamics (QCD). Quarks can carry one of three possible colours (red, blue or green) whereas gluons carry two.

Only coloured particles can emit or absorb a gluon, making the gluon self-interaction possible. This leads to colour confinement (quarks cannot be observed isolated in Nature) and asymptotic freedom (the force between the quarks is weaker at short distances and becomes stronger as the distance increases). Colour confinement is the reason that quarks form hadrons (combinations of two or three quarks).

The leptons, together with the quarks, the gauge bosons and the Higgs particle are the basis for our present understanding of the physical world.

Table 1.2: *The periodic table of the standard model.*

	Name - Symbol		Generation	Spin
	up - u	down - d	I	
Quarks	charm - c	strange - s	II	$\frac{1}{2}$
	top - t	bottom - b	III	
Charge	$+2/3$	$-1/3$		
	electron - e	electron neutrino - ν_e	I	
Leptons	muon - μ	muon neutrino - ν_μ	II	$\frac{1}{2}$
	tau - τ	tau neutrino - ν_τ	III	
Charge	1	0		

1.2 Quarkonium

Hadrons include a combination of two (called mesons) or three (called baryons) quarks. The combination of two heavy quarks, in a $q\bar{q}$ state, with $q = b, c$ is named as quarkonium. Notice that $q\bar{q}$ states, when $q = u, d$ or s, are not considered quarkonia. This is because these particles are lighter and are superpositions of states. Meanwhile, the t quark has too small lifetime to form a toponium state, although some models allow it [4].

The J/ψ meson was the first $c\bar{c}$ bound state (charmonium) that was discovered in 1974, simultaneously at Brookhaven National Laboratory [5] and Stanford Linear Accelerator Centre (SLAC) [6]. The first observation of a bottomonium ($b\bar{b}$ state) followed a few years later [7].

The quarkonium is either produced by QCD sources, or from a subsequent decay of a *b*-hadron in proton–proton collisions.

1.3 Prompt J/ψ production

Prompt quarkonia can be produced in two ways. Either directly from parton–parton interactions, or from feed-down from higher mass charmonium states (like the $\chi_c, \psi(2\text{S})$) by emitting photons or pions. The most popular models describing the formation of the charmonium system are listed below.

1.3.1 Colour singlet model

The Colour Singlet Model (CSM) was the first to be proposed for the production of quarkonia [8, 9, 10]. CSM assumes that the quarkonium states are produced from a pair of heavy quarks (quark - antiquark) having the same quantum numbers (spin and colour) with the formed particle. Subsequently, the formed quarkonium is dominated by the state of the original quarks (see figure 1.1(a)). The probability that the $q\bar{q}$ pair will evolve into a quarkonium state is calculated from the values of the colour singlet $q\bar{q}$ wavefunction. These stem from potential models of the $q\bar{q}$ system and are constrained with experimental data on quarkonium decay widths.

1.3.2 Colour evaporation model

Another mechanism for describing the quarkonium production is offered by the Colour Evaporation Model (CEM). In the CEM, the probability of forming a specific quarkonium state is assumed to be independent of the colour and spin of the $q\bar{q}$ pair [11, 12, 13, 14]. The $q\bar{q}$ pair will acquire the correct spin and colour numbers by soft gluon interactions and evolve in the quarkonium state. The cross-section for the production of a quarkonium state H is some fraction F_H of the cross-section for production of $q\bar{q}$ pairs. F_H is universal and determined from data. Furthermore, it can be used to predict cross-sections in other processes and in other kinematic regions.

1.3.3 k_T factorisation model

In the previous models it is assumed that the partons have the same direction with the incoming particle (collinear approximation). However, in large energies the transverse momenta k_T of the partons become important [15, 16]. In this theory, the cross-sections are factorised into a k_T dependent partonic cross-section that takes into account the non-vanishing transverse momenta of the gluons.

1.3.4 Non-relativistic QCD

Finally, the Colour Octet Mechanism (COM) proposes that the $q\bar{q}$ pair can be produced with any combination of quantum numbers and evolve in the particular quarkonium, through the emission of soft gluons (see figure 1.1(b)). This model is similar to CEM,

but describes the J/ψ quarkonium production using the framework of Non-Relativistic Quantum Chromodynamics (NRQCD). The production consists of two parts. A short distance cross-section that is fully calculable, and the long distance matrix elements (LDME). The LDMEs reflect the probability that a $q\bar{q}$ pair in a given spin and colour state can evolve into a quarkonium state, and are derived from experimental results.
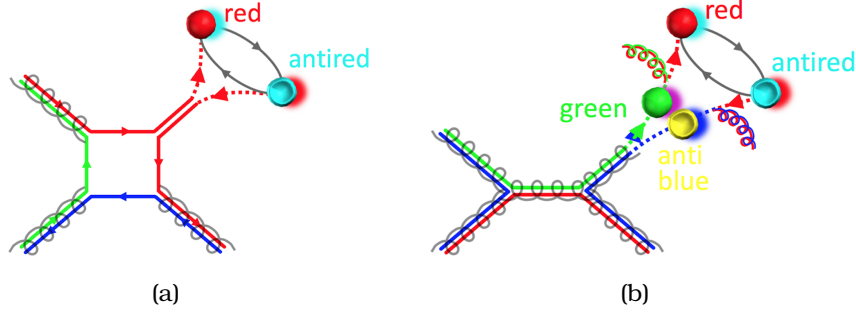

Figure 1.1: *Schematic of (a) CSM and (b) COM models.*

1.4   Non-prompt J/ψ production

Non-prompt charmonium originates from decays of b-hadrons. They can be separated from promptly produced J/ψ, due to their long lifetime. Two tools are available for the description of non-prompt J/ψ production. First is, the Next to Leading Order (NLO) approach and second, the Fixed Order Next to Leading-Log model [17, 18].

1.5 J/ψ spin-alignment

An important observable in the production of the J/ψ meson is, its polarisation, which is sensitive to its production mechanism.

The polarisation of the quarkonium is measured experimentally from the angular distributions of the decay products of the quarkonium (see figure 1.2). The di-lepton decays of the J/ψ are used for such measurements. Sensitive angular variables for such measurements include: θ^*, which is the angle between the direction of the positive muon in that frame and the direction of J/ψ in the laboratory frame, which is directed along the z^* axis and the ϕ^*, which is the angle between the J/ψ production $(x^* - z^*)$ plane and its decay plane formed by the direction of the J/ψ and the lepton ℓ^+.

Apart from the rest frame of the quarkonia, two other frames are also used for such measurements. These are the Collins-Soper (CS) frame [19] and the Gottfried-Jackson frame [20].

The angular distribution of the lepton pair in its rest frame is described by

$$\frac{\mathrm{d}N}{\mathrm{d}\Omega} = \frac{1}{3 + \lambda_\theta} \left[1 + \lambda_\theta \cos^2 \theta + \lambda_\phi \sin^2 \theta \cos 2\phi + \lambda_{\theta\phi} \sin 2\theta \cos \phi \right] \tag{1.1}$$
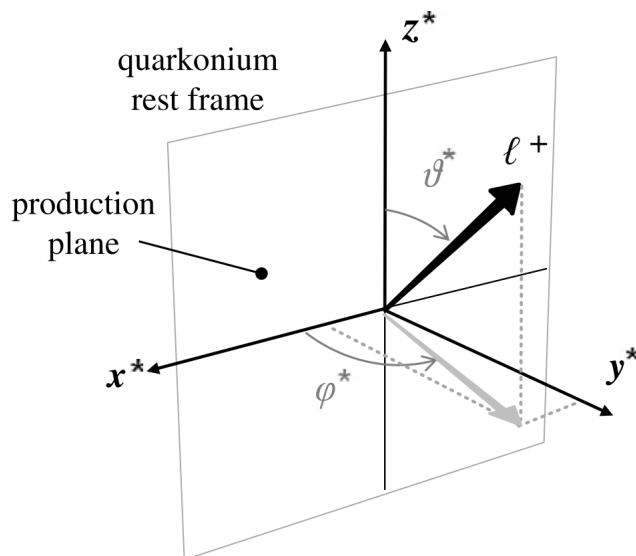
Figure 1.2: *Definitions of the J/ψ spin-alignment angles in the J/ψ decay frame.*

where λ variables are related to the angular momentum composition of the produced quarkonia. For purely transverse polarised J/ψ mesons, $\lambda_\theta = 1$ and $\lambda_\phi = \lambda_{\theta\phi} = 0$, while for longitudinal polarisation $\lambda_\theta = -1$ and $\lambda_\phi = \lambda_{\theta\phi} = 0$.

1.6 Charmonium production in association with a Z boson

Both CS and CO models support the production of a Z boson in association with prompt J/ψ mesons [21, 22, 23, 24]. Tree level diagrams describing this process are illustrated in figure 1.3.

1.6.1 Estimates of Z Boson and J/ψ production cross-sections at the LHC

There are many studies in the literature involving the associated production of electroweak bosons (W or Z) and heavy quarkonia (Υ or J/ψ) [25, 26, 27, 28]. Recent interest was expressed for the $Z+$ prompt J/ψ production, from various theoretical groups [22, 23, 24]. In this section, the estimation of the production rates of the $Z+$ prompt J/ψ final state is described.

Two processes contributing to the $p + p \rightarrow J/\psi + Z$ are considered at leading order. First, the $g + g \rightarrow c\bar{c}[n] + Z$ and second, the $q + \bar{q} \rightarrow c\bar{c}[n] + Z$, where q can be either u, d, s, c and $n = {}^3S_1^{(8)}$, ${}^1S_0^{(8)}$ or ${}^3S_1^{(1)}$ (following the ${}^{2S+1}L_J^{(n)}$ notation).

The cross-section of the associated production of prompt J/ψ mesons with Z boson
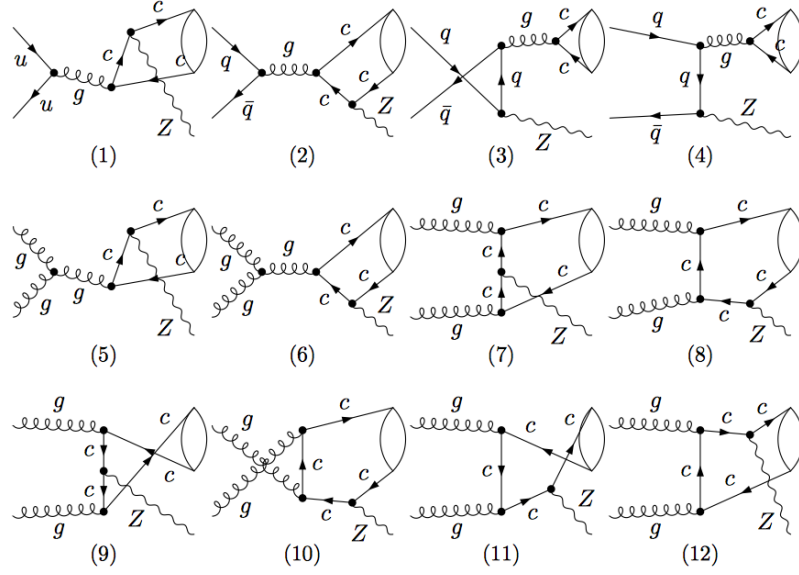
Figure 1.3: *Tree-level Feynman diagrams for the production of prompt $J/\psi + Z$. Diagrams $1-4$ show the diagrams with $q\bar{q}$ initial state and $5-12$ with gg.*

in the framework of NRQCD is given by

$$\sigma(pp \to Q + Z + X) = \sum_{n} \hat{\sigma}(pp \to c\bar{c}(n) + Z + X)\langle O^{Q}(n)\rangle , \qquad (1.2)$$

where $\hat{\sigma}(pp \to c\bar{c}(n) + Z + X)$ is the short distance cross-section and $\langle O^{Q}(n)\rangle$ is the long distance matrix elements (LDME). Effects of the order of $Q^2/m_Q^2 \geq 1$ (m_Q being the quark mass and Q the momentum transfer in a production process), are encoded in short distance coefficients, can be estimated by using perturbation theory. On the other hand, effects of the order of $Q^2/m_Q^2 < 1$ hadronisation, are factorised into long distance matrix elements, expressed in powers of v (the intrinsic heavy-quark velocity) and measured from lattice simulations or from experimental data. LDME are expected to be process-independent, not to depend on the production mechanism of the perturbative heavy quarks and at present they can't be computed from first principles.

The LDME are related to the non-perturbative transition probabilities from a $Q\bar{Q}$ system in a quarkonia state and they scale with a definite power of v. Thus, studies including Υ mesons may be more suitable for the understanding of the NRQCD factorisation formalism, since the mass of the bottomonium is heavier than the charmonium of the order of about 3, implying smaller v^2, thus faster convergence[2]. In addition, the asymptotic behaviour for the Υ is reached at much higher values of transverse momentum (p_T), due to the fact that $m_b > m_c$.

Charmonium on the other hand has the advantage that its mass is closer to Λ_{QCD} than the bottomonium. This enables us to perform a non-relativistic treatment of a quarkonia state for the understanding of the production and decay of bound states of heavy quarks. This strategy makes it possible to embed the present approach in the framework of NRQCD.

---

[2]Charmonium ground state: $v^2 \sim 0.3$, bottomonium ground state: $v^2 \sim 0.1$.

The parameter values used as an input for the calculations are [29]:

- CTEQ6L1 PDF set

- $m_Z = 91.18\,\text{GeV}$

- $\alpha_S(m_Z) = 0.1184$

- $m_c = 1.275\,\text{GeV}$, $m_u = 2.3\,\text{MeV}$, $m_d = 4.8\,\text{MeV}$, $m_s = 95.5\,\text{MeV}$

- $\alpha = 7.297 \times 10^{-3}$

- $\mu_R = \mu_F = m_Z$

- NRQCD matrix elements for the charmonium production [30]

  - $\langle O(J/\psi)[^3S_1^{(1)}]\rangle = 1.64\,\text{GeV}^3$
  - $\langle O(J/\psi)[^3S_1^{(8)}]\rangle = 0.3 \times 10^{-3}\,\text{GeV}^3$
  - $\langle O(J/\psi)[^1S_0^{(8)}]\rangle = 8.9 \times 10^{-2}\,\text{GeV}^3$

Additional kinematic cuts were applied to the J/ψ meson, following the acceptance of the experiments in the LHC. These, include a requirement on the transverse momentum of the J/ψ to be $p_T^{J/\psi} > 8\,\text{GeV}$ and in its rapidity, $|y^{J/\psi}| < 2.4$.

The results of every process are summarised in table 1.3, where only statistical errors are shown. $q + \bar{q} \to c\bar{c}[^3S_1^{(1)}] + Z$ processes are expected to have very low cross-sections. This is because the c-quark line of the charmonium is connected with the q-quark line by the gluon that transmits colour to the $c\bar{c}$. This was checked with simulation and can be seen from the absence of these processes from table 1.3 and the very low cross-section of the process where $q = c$.

Table 1.3: *Cross-sections tree level at* $\sqrt{s} = X\,\text{TeV}$

Process	cross-section [fb]		
	$\sqrt{s} = 7\,\text{TeV}$	$\sqrt{s} = 8\,\text{TeV}$	$\sqrt{s} = 14\,\text{TeV}$
$g + g \to Z + c\bar{c}[^3S_1^{(8)}]$	11.3 ± 3.6	14.1 ± 5.0	32.8 ± 12.1
$c + \bar{c} \to Z + c\bar{c}[^3S_1^{(8)}]$	15.7 ± 5.2	19.7 ± 6.0	47.4 ± 26.1
$u + \bar{u} \to Z + c\bar{c}[^3S_1^{(8)}]$	195.5 ± 20.4	204.4 ± 29.7	408.3 ± 50.7
$d + \bar{d} \to Z + c\bar{c}[^3S_1^{(8)}]$	148.0 ± 21.3	157.4 ± 19.8	342.5 ± 40.4
$s + \bar{s} \to Z + c\bar{c}[^3S_1^{(8)}]$	56.0 ± 10.7	70.3 ± 13.3	181.1 ± 54.4
$g + g \to Z + c\bar{c}[^1S_0^{(8)}]$	281.0 ± 36.0	300.5 ± 42.5	823.1 ± 101.3
$c + \bar{c} \to Z + c\bar{c}[^1S_0^{(8)}]$	0.4 ± 2.9	1.1 ± 1.7	8.2 ± 8.4
$g + g \to Z + c\bar{c}[^3S_1^{(1)}]$	7.0 ± 0.9	9.1 ± 1.0	20.5 ± 2.7
$c + \bar{c} \to Z + c\bar{c}[^3S_1^{(1)}]$	1.8 ± 0.4	2.1 ± 0.8	5.4 ± 1.9

Cross-sections were calculated for the associated production of a Z boson with a prompt J/ψ meson in proton-proton collisions to leading order. All the partonic

contributions to the total cross-section are listed, considering the $c\bar{c}[^{2S+1}L_J^{(c)}]$, with the total spin $S = 1, 2$, orbital angular momentum $L = S$, total angular momentum $J = 0, 1$ and $c = 1, 8$. The results obtained are visualised in figure 1.4 and summarised in table 1.4.
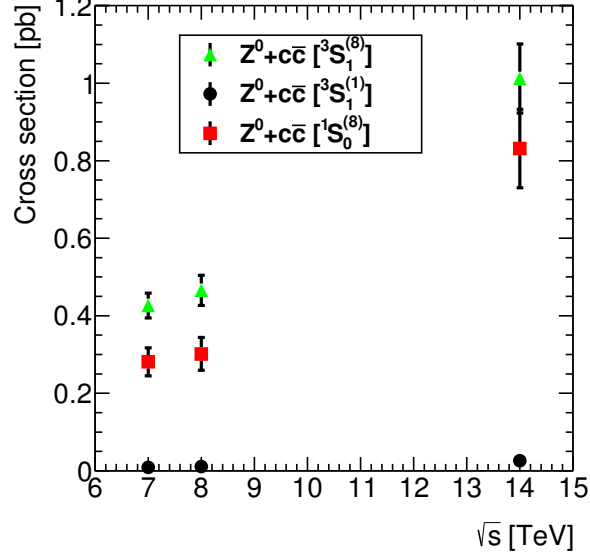

Figure 1.4: *Cross-sections as a function of $\sqrt{s}$.*

The production of Z in association with a J/ψ was studied before in NLO accuracy [23, 24]. Based on the selection criteria of this study and the choice of renormalisation and factorisation scales, small enhancements are expected from next to leading order contributions.

Table 1.4: *cross-sections tree level at $\sqrt{s} = X$ TeV*

	cross-section [fb]		
Process	$\sqrt{s} = 7$ TeV	$\sqrt{s} = 8$ TeV	$\sqrt{s} = 14$ TeV
$Z + c\bar{c}[^3S_1^{(8)}]$	426.6 ± 32.0	465.8 ± 38.9	1012.1 ± 89.4
$Z + c\bar{c}[^1S_0^{(8)}]$	281.4 ± 36.2	301.6 ± 42.5	831.3 ± 101.3
$Z + c\bar{c}[^3S_1^{(1)}]$	8.8 ± 1.0	11.1 ± 1.3	25.9 ± 3.3

It is clear that these processes are reachable within the statistics at the LHC, with the colour-octet process being dominant. The observation of the associated production will provide a better determination of the $\langle O^{J/\psi}[^{2S+1}L_J^{(c)}]\rangle$ elements and a good test of the NRQCD factorisation formalism.

From the results, tabulated in table 1.4, the colour-octet process is dominantly contributing at the tree level. With the collected luminosity at the LHC, it is estimated that there will be enough events to perform a cross-section measurement. The predictions are compared with the ATLAS measurement [31] in chapter 4.

1.7   New physics in the $Z + J/\psi$ associated production

The Higgs boson was observed recently both from ATLAS [32] and CMS [33] collaborations. After the observation of the new particle, studies concentrated on measuring the couplings of the new boson to the particle content of SM. Couplings to fermions, like c quark, are more difficult to be studied due to low branching fractions and higher backgrounds [34]. First results include measurements of couplings to τ [35] and μ [36] leptons.
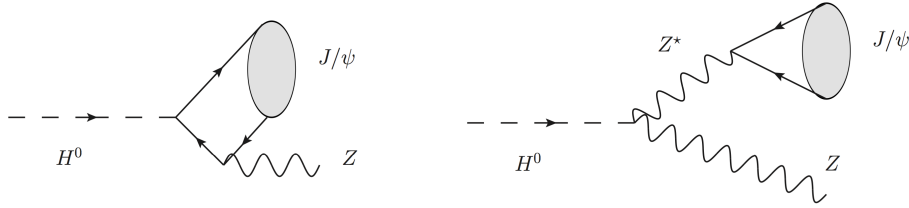

Figure 1.5: *Feynman diagrams for $H^0 \to ZJ/\psi$ at leading order.*

Direct charm/beauty coupling to Higgs at tree level, and vector final state allows for discrimination of P-even / P-odd Higgs couplings to quarks through angular analysis [37, 38, 39]. $H \to ZJ/\psi$ decay (see figure 1.5) can be used for the measurement of Higgs coupling to the charm quark.

The $Z + J/\psi$ analysis can be also used as a probe for the dark sector (Z_d boson). It features the same final state, as the $H \to ZZ_d$ decay [40, 41]. Such searches suggest that Z_d have an invariant mass in the range of $0 - 34\,\text{GeV}$.

The associated production of $Z + J/\psi$ analysis, together with the $W + J/\psi$, is already used to constrain BSM models that suppose the existence of a light scalar particle [42], other from the Higgs.

1.8   Rare decay of $Z \to \ell\ell J/\psi$

The rare decay of $Z \to \ell\ell J/\psi$ was proposed for the first time in 1993 [43, 44, 45]. The motivation was that the big sample of Z bosons gathered in the LEP experiment [46], could be used for searching rare Z decays involving quarkonia. Some of these decays are $Z \to ggJ/\psi$, $Z \to c\bar{c}J/\psi$ and $Z \to \gamma J/\psi$ [47, 48, 43]. The decay though, of $Z \to \ell\ell J/\psi$ is particularly interesting experimentally, due to its clean final state of four leptons. The branching ratio of this decay in leading order is calculated to be 2.3×10^{-6} [44], close to the already observed decay of $Z \to \ell\ell\ell\ell$ [49, 50] which is 4.2×10^{-6} [29].
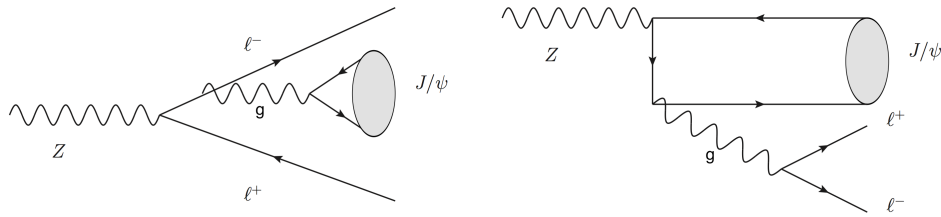
Figure 1.6: *Feynman diagrams for $Z \to \ell^+\ell^- J/\psi$ at leading order.*

1.9 Previous studies of vector boson and heavy (hidden or open) flavour associated production

Previous searches for the related processes $W + \Upsilon(1S)$ and $Z + \Upsilon(1S)$ were performed by CDF. After analysing $9.4\,\text{fb}^{-1}$ of $p\bar{p}$ collisions, CDF experiment reported no evidence for the associated-production of vector-bosons and quarkonia and set limits on their production rate [51, 52].

The first observation of such process was done by the ATLAS experiment [53]. This analysis, searched for W bosons, produced in association with prompt J/ψ mesons, using $4.9\,\text{fb}^{-1}$ of pp collisions. Enough events passed the selection requirements (see figure 1.7 for the J/ψ invariant and W transverse mass respectively) allowing the calculation of the $W + J/\psi$ to inclusive W cross-section ratio.
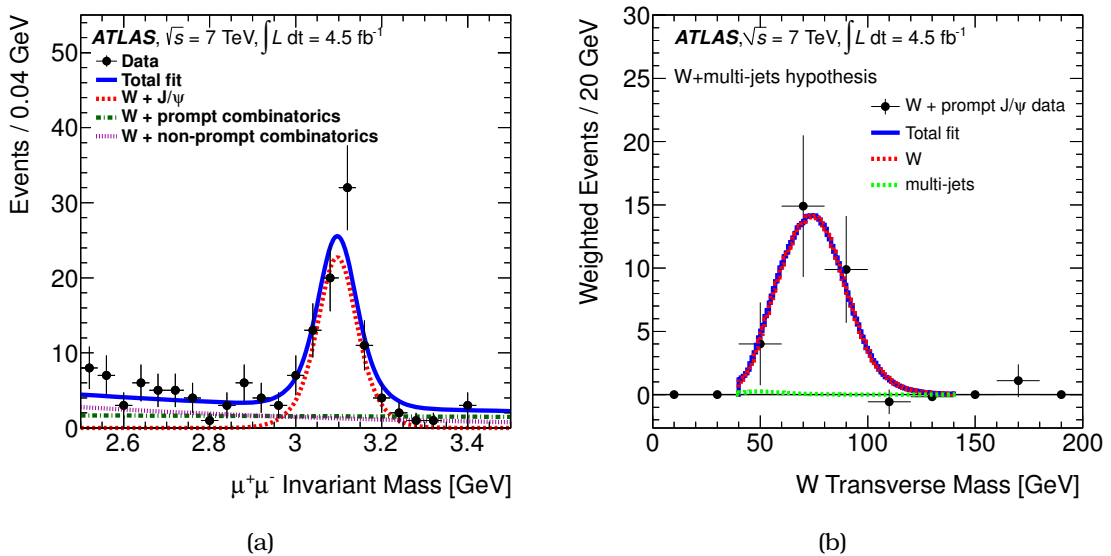

Figure 1.7: *(a) Invariant mass of the J/ψ candidates produced in association with a W boson. (b) Weighted W boson transverse mass distribution for the W bosons associated with the J/ψ candidates in (a).*

An interesting study of associated production of Z bosons with open charm hadrons was performed by the LHCb experiment [54]. After analysing $1\,\text{fb}^{-1}$ of pp collisions at

$\sqrt{s} = 7\,\text{TeV}$, LHCb observed the associated production of Z with D^+ and D^0 mesons with a combined significance of 5.1σ. Despite the small statistics, as shown in figure 1.8, a cross-section was calculated.
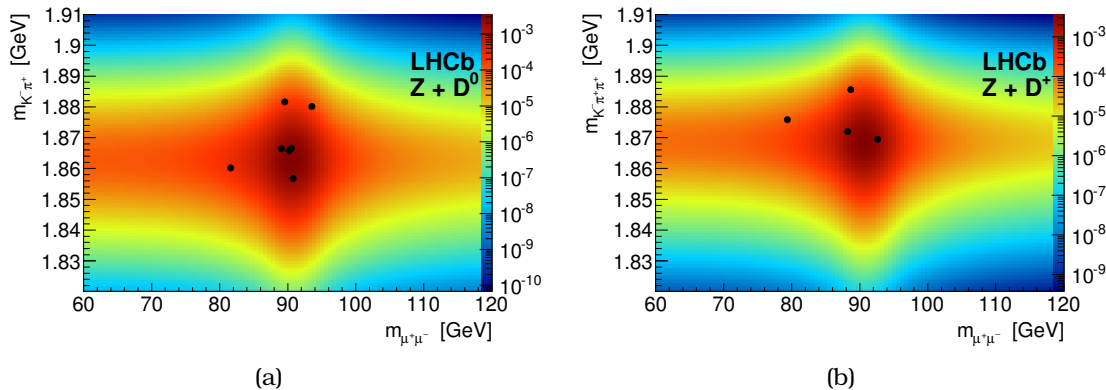

Figure 1.8: *Scatter plots of the associated production of Z bosons with (a) D^0 and (b) D^+ mesons as observed from LHCb Collaboration [54].*

ATLAS experiment using pp collision data, collected during 2012 at $\sqrt{s} = 8\,\text{TeV}$ made the first observation of the associated production of Z bosons with both prompt and non-prompt J/ψ mesons [31]. Looking for $Z \to \ell\ell$ decays, with $\ell = \mu, e$ and $J/\psi \to \mu\mu$, the observation of this process was done with a significance of above 5σ. As also described in later chapter (chapter 4) a lower limit on the double parton scattering effective cross-section was derived.

1.10 Multi parton interactions

The evolution of the hadron colliders is followed by an increase of the centre of mass energy of the colliding hadrons. During the first run, LHC managed to collide protons in an $\sqrt{s} = 8\,\text{TeV}$ energy. The motivation for higher energies is new particle production, A heavy particle with mass m can only be created if there is enough energy ($E = mc^2$) in the centre of mass frame.

In such high energies, hadrons behave like a very dense object that could be considered as a cloud of partons. As $\sqrt{s}$ increases, so does the probability that more than one parton–parton interaction will occur, among the same hadron–hadron collision. These are named Multi Parton Interactions (MPI). When two parton–parton interactions of the MPI are hard enough to be identified in the detector, this process is classified as Double Parton Scattering (DPS). A graphic representation of DPS is illustrated in figure 1.9(a). There, two different pairs of partons from the two incoming protons interact to produce A and B, in comparison to Single Parton Scattering (SPS) where the A and B are produced by a single pair of interacting partons (see figure 1.9(b)). The very first measurement of a DPS process was performed at CERN's Intersecting Storage Rings (ISR), using a $4j$ final state [55].
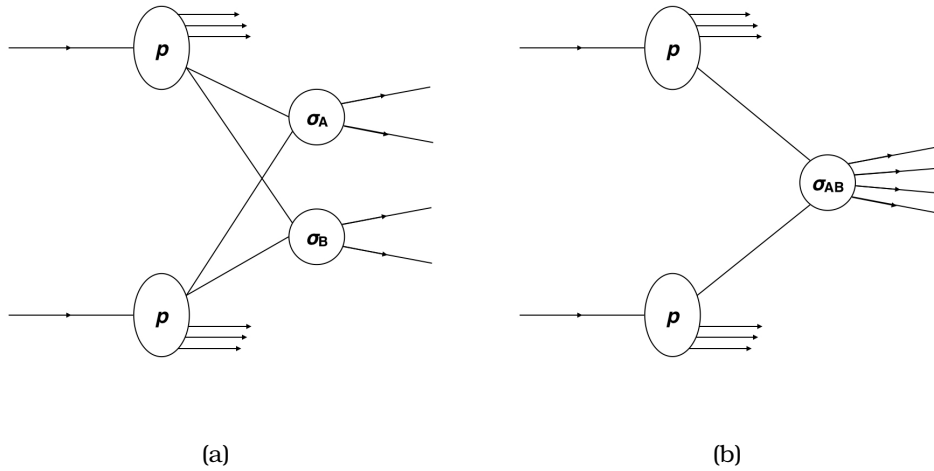
Figure 1.9: *Schematic picture of the single parton and double scattering.*

In a model independent way, the DPS cross-section can be written as a function of the elementary proton–proton single parton cross-sections as

$$\sigma_{\text{DPS}} = \frac{m}{2} \frac{\sigma_{\text{A}} \sigma_{\text{B}}}{\sigma_{\text{eff}}} \,, \tag{1.3}$$

where σ_{A} and σ_{B} are the cross-sections of two independent partonic scatterings A and B. The factor m is equal to unity when processes A and B are indistinguishable, while $m = 2$ otherwise [38, 41]. The process-independent scaling parameter σ_{eff}, has units of cross-section.

It is natural to assume a dependence between the $\sqrt{s}$ and the σ_{eff}. Unfortunately, from the experimental side, only a handful of measurements is available (see figure 1.10). Therefore, it is not yet possible to reach a solid conclusion and quantify this effect. Most recent results include measurements from LHC [56] and Tevatron [57, 58, 59, 60]. Up to this day, the only information provided about DPS in $\sqrt{s} = 8\,\text{TeV}$, comes from the associated production of $Z + J/\psi$ analysis [31].
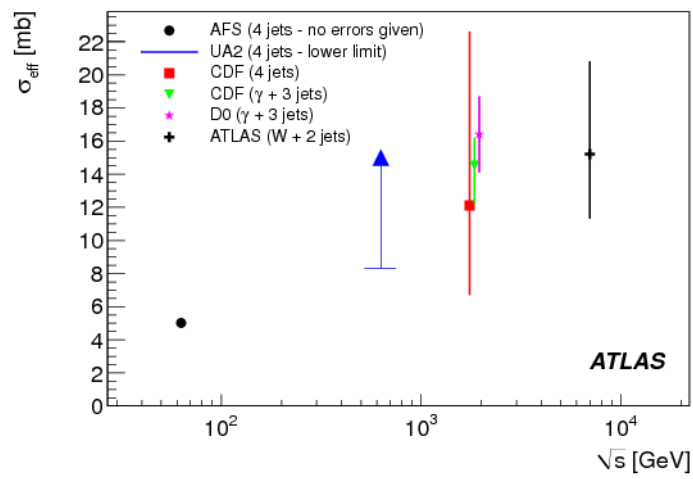
Figure 1.10: *DPS effective cross-section measurements (figure taken from [61]).*

Chapter 2

The Large Hadron Collider and the ATLAS detector

2.1 Large Hadron Collider

The Large Hadron Collider (LHC) [62] is a two-ring superconducting hadron accelerator and collider, located in the borders between France and Switzerland, in the Geneva area. It uses the same tunnel with CERN's previous accelerator, the Large Electron-Positron collider (LEP) [46].

Protons, before being injected into the LHC, are passing through stages of focusing and acceleration, in smaller accelerators in the LHC complex (see figure 2.1). The protons are extracted from a bottle of hydrogen gas, with the use of an electric field. The first acceleration phase is performed by LINAC 2, which accelerates the protons to the energy of 50 MeV. After LINAC 2, the energy of the beam is increased to 1.4 GeV and 25 GeV, using the Proton Synchotron Booster (PSB) and the Proton Synchotron (PS) respectively. The last pre-accelerator, before the LHC, is the Super Proton Synchotron (SPS), where the protons are accelerated to an energy of 450 GeV.
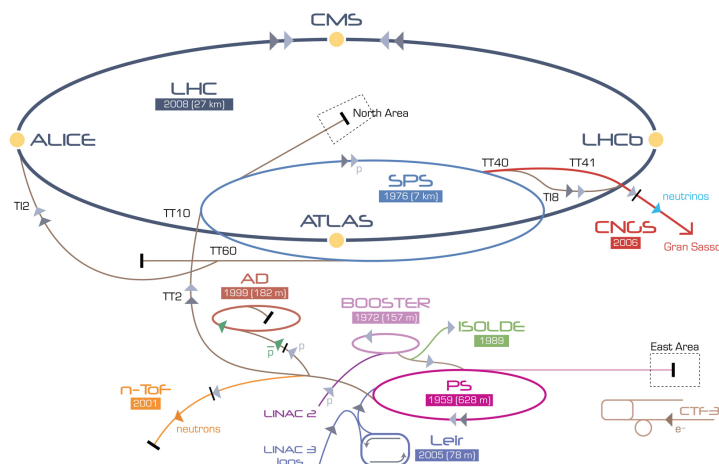

Figure 2.1: *Overview of the LHC complex*

LHC delivered the first high energy colliding beams of protons ($\sqrt{s} = 7\,\text{TeV}$), on July 2010, where the $48.1\,\text{pb}^{-1}$ were delivered, of which $45.0\,\text{pb}^{-1}$ were recorded, at the ATLAS experiment by the end of 2010). The next years the excellent performance of the LHC led to the delivery of $5.46\,\text{fb}^{-1}$ of data in 2011 and $22.8\,\text{fb}^{-1}$ in 2012 [63].

The rate of a process in the LHC is defined from $N_{\text{events}} = \mathcal{L}\sigma_{\text{process}}$, where σ_{process} is the cross-section of the process under study and $\mathcal{L}$ the machine luminosity. The luminosity is given by the formula

$$\mathcal{L} = n_b N_p^2 f_r / A,$$

where n_b is the number of bunches, N_p the number of protons per bunch, f_r is the LHC revolution frequency ($f_r \sim 10^4\,\text{Hz}$) and A is the collision effective area ($A = 4\pi\sigma_b^2$, with the transverse area of the beam being equal to $\sigma_b = 16\,\mu\text{m}$). The conditions of the running parameters during RUN-1 are summarised in table 2.1.

Table 2.1: *LHC parameters for RUN-1 compared to the nominal conditions.*

Parameter	2010	2011	2012	Nominal
beam energy	3.5	3.5	4.0	7.0
bunch spacing [ns]	150	75/50	50	25
n_b	368	1380	1380	2808
N_p ($10^{11}\,p$/bunch)	1.2	1.45	1.6	1.15
$\mathcal{L}\,[\text{cm}^{-2}\text{s}^{-1}]$	2×10^{32}	3.5×10^{33}	7.6×10^{33}	10^{34}
average pile-up	8	17	38	26

For the beginning of RUN-2 (2015), the foreseen centre of mass energy is $\sqrt{s} = 13\,\text{TeV}$. The LHC is aiming in a peak luminosity of $0.8 - 1.2 \times 10^{34}\,\text{cm}^{-2}\text{s}^{-1}$, with each bunch containing 1.2×10^{11} protons. The average pile-up in these conditions is calculated to be between 22 to 36.

The LHC complex features 8 entry points, where in two of which host the two general purpose experiments (ATLAS [64] and CMS [65]). There are several other smaller experiments located in the LHC ring, two of which are the ALICE [66] experiment, designed for heavy ion operation and the LHCb [67], dedicated for studying $b-$physics.

2.2   Coordinate system of the ATLAS experiment

The ATLAS experiment uses the right handed coordinate system. The $z-$axis follows the beam pipe, and the plane perpendicular to the beam pipe is defined as the $x - y-$plane. The positive $x-$axis is pointing from the interaction point towards the centre of the LHC while the positive $y-$axis is going upwards. The positive side of the $z-$axis is pointing towards the side A (direction Geneva) of the ATLAS detector, while negative $z-$values are assigned to the side C (direction Jura). Due to the cylindrical symmetry of the ATLAS detector, the use of cylindric coordinates (ϕ, θ and R) is useful. In this coordinate system the transverse distance to the $z-$axis is defined as the radius R. The azimuthal angle ϕ is measured around the beam axis, starting with $\phi = 0$ on the $x-$axis

and $\phi = \pi/2$ on the y−axis. The azimuthal angle is defined within $\phi \in [-\pi, \pi]$. The polar angle θ is defined within $\theta \in [0, \pi]$, where $\theta = 0$ is on the positive z−axis. In terms of the particle's momentum components p_x, p_y and p_z, the two angles ϕ and θ can be written as $\tan \phi = p_x/p_y$ and $\tan \theta = \sqrt{p_x^2 + p_y^2}/p_z$

A more convenient way to express the polar angle θ is to use the pseudorapidity variable, which can be either expressed in terms of the polar angle or in terms of the particles momentum

$$\eta = -\ln\left(\tan\frac{\theta}{2}\right) = -\frac{1}{2}\ln\left(\frac{|\boldsymbol{p}| + p_z}{|\boldsymbol{p}| - p_z}\right)$$

where $|\boldsymbol{p}| = \sqrt{p_x^2 + p_y^2 + p_z^2}$.

Rapidity is a second variable that is often used instead of pseudorapidity and is given by the following formula:

$$y = \frac{1}{2}\ln\left(\frac{E + p_z}{E - p_z}\right) = \ln\left(\frac{\sqrt{m^2 + p_T^2 \cosh^2\eta} + p_T \sinh\eta}{\sqrt{m^2 + p_T^2}}\right). \tag{2.1}$$

as a function of the energy E and momentum p_z or as a function of transverse momenta $\left(p_T = \sqrt{p_x^2 + p_y^2}\right)$ and pseudorapidity.

For the $x - y$−plane, η is equal to zero. In the beam direction $\eta \to \pm\infty$ which corresponds to $\theta = 0$ and $\theta = \pi$. The polar angle θ is not preferable compared to rapidity and pseudorapidity, because the latter variables have the advantage of being invariant, under Lorentz transformations. Measurements in η or y are not dependent on a reference frame (rest frame of the particle or the laboratory frame), unlike the variable θ.

Starting from equation 2.1 and supposing a Lorentz boost on z with a velocity β

$$y' = \frac{1}{2}\ln\left(\frac{E + p_z}{E - p_z}\frac{1 - \beta}{1 + \beta}\right) = \frac{1}{2}\ln\left(\frac{E + p_z}{E - p_z}\right) + \ln\sqrt{\frac{1 - \beta}{1 + \beta}}$$

where the last part of the equation can be written as

$$\ln\sqrt{\frac{1 - \beta}{1 + \beta}} = \tanh^{-1}\left(\tanh\ln\sqrt{\frac{1 - \beta}{1 + \beta}}\right) = \tanh^{-1}\left(\frac{\sqrt{\frac{1-\beta}{1+\beta}} - \sqrt{\frac{1+\beta}{1-\beta}}}{\sqrt{\frac{1-\beta}{1+\beta}} + \sqrt{\frac{1+\beta}{1-\beta}}}\right) = \tanh^{-1}\left(\frac{(1 - \beta) - (1 + \beta)}{(1 - \beta) + (1 + \beta)}\right) = -\tanh^{-1}\beta$$

thus ending that the equation of transformation of rapidity due to a Lorentz boost parallel to beam axis is $y' = y - \tanh^{-1}\beta$.

Using this formulation, it is easy to show that the difference in rapidities, is also invariant in the primed or in the unprimed frame

$$y_1' - y_2' = (y_1 - \tanh^{-1}\beta - (y_2 - \tanh^{-1}\beta)) = y_1 - y_2.$$

2.3   The ATLAS experiment

The ATLAS (A Toroidal LHC Apparatus) experiment is described in detail here [64]. It consists of three main components: the Inner Detector (ID), the electromagnetic and hadronic calorimeters, and the Muon Spectrometer (MS). The detector systems are enclosed by a magnetic field created by two different types of magnets. A solenoid, aligned on the beam axis, provides a $2\,\mathrm{T}$ axial magnetic field for the inner detector and a toroid produces a toroidal magnetic field enclosing the muon detectors in the central and endcap regions.

    A sketch of the ATLAS experiment is shown in figure 2.2.
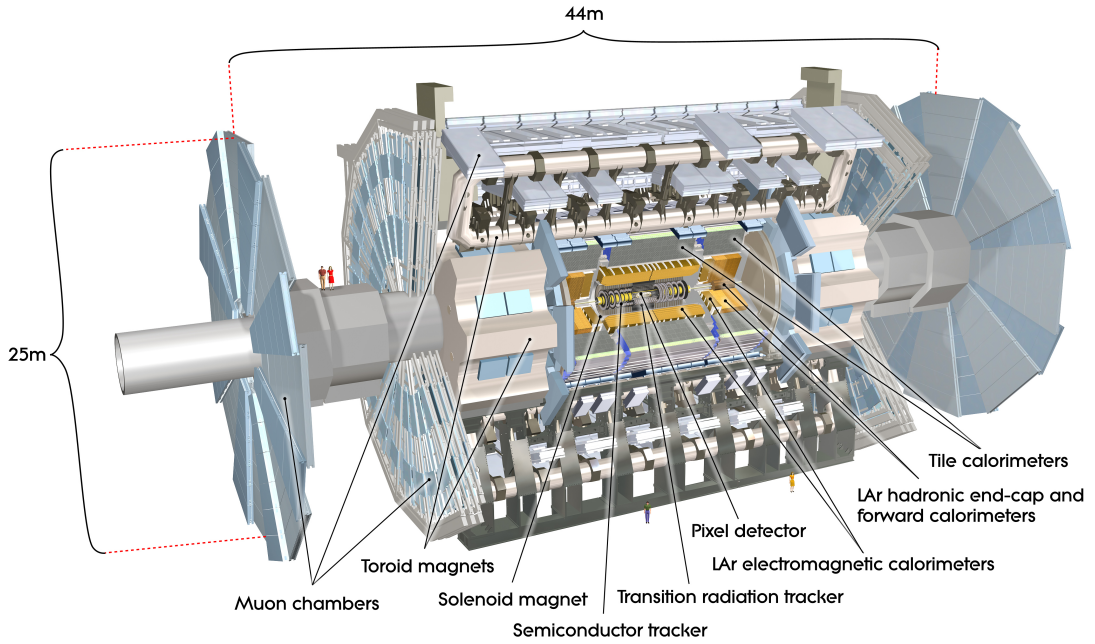
Figure 2.2: *Overview of the ATLAS experiment*

2.3.1   Inner detector

The ATLAS ID provides identification, using pattern recognition techniques, for all charged particle tracks within $|\eta| < 2.5$ and full coverage in ϕ. The ID has a cylindrical shape and is enclosed in a solenoidal magnetic field of $2\,\mathrm{T}$. It consists of three complementary and autonomous sub-detectors. These three systems are, starting from the interaction point and moving outwards, the silicon pixel, the Semi Conductor Tracker (SCT) and the Transition Radiation Tracker (TRT). A typical track that transverses the barrel region of the ID leaves 3 Pixel hits, 8 SCT hits and 30 TRT hits.

Pixel detector

Pixel detector is the closest detector to the beam pipe and features ~ 80 million channels. Pixel layers are segmented in $R - \phi$ and z with three cylindrical layers (with the

closest being 50.5 mm away from the beam pipe, the second 88.5 mm and the third 122.5 mm) in the barrel and three discs in each side of the endcaps. This configuration results in an accuracy of 10 μm ($R - \phi$) and 115 μm in z.

SemiConductor Tracker (SCT)

The pixel sub-system is complemented by the four layers of SCT detectors in the barrel and nine disks in each side of the endcaps. SCT in the barrel region use small angle stereo strips to measure two coordinates, with the one placed in parallel to the beam axis. SCT has ~ 6 million channels and has an intrinsic accuracy of 17 μm ($R - \phi$) and 580 μm in z.

Transition Radiation Tracker (TRT)

The outermost layer of the ID hosts the TRT sub-detector system. TRT consists of 4 mm strawtubes and provides coverage up to $|\eta| = 2.0$. It has 350 000 readout channels and an intrinsic accuracy of 130 μm per straw. The large number of hits expected in TRT compensates for the small number of hits in the other subsystems and ensures a robust track momentum measurement.

2.3.2 Calorimetry

The calorimeter system in ATLAS covers a range of $|\eta| < 4.9$ and measures the energies of charged and neutral particles. For the pseudorapidity range where the ID also provides coverage, the ElectroMagnetic calorimeter (EM), is ideally suited for precision measurements of electrons and photons. The calorimeter system has a twofold purpose. First, to provide good containment for electromagnetic and hadronic showers and at the same time limit high energetic particles from reaching the muon spectrometer (punch-throughs).

Electromagnetic calorimetry

The EM calorimeter is split into two parts; the barrel ($|\eta| < 1.475$) and the endcap ($1.375 < |\eta| < 3.2$). The EM is a lead-Liquid Argon (LAr) detector with accordion-shaped formation. It has three longitudinal layers, named as strip, middle and back layers. The first layer features high-grained strips in the η direction providing discrimination against multiple photon showers (as well as $\gamma - \pi^0$ separation), the second collects most of the energy deposited in the calorimeter by photon and electron showers and the third provides measurements of energy deposited in the tails of these showers. Two complimentary pre-sampler detectors complete the EM, correcting for energy lost in the material before the calorimeter. This fine segmentation provides electron identification in conjunction with the inner detector in the $|\eta| < 2.5$ region.

Hadronic calorimetry

The hadronic calorimeter is composed of the tile calorimeter, the LAr Hadronic Endcap Calorimeter (HEC) and the LAr Forward Calorimeter (FCal). The tile calorimeter is the

one that follows the EM. In the barrel it provides coverage in the $|\eta| < 1.0$ region and its two extended barrels cover the $0.8 < |\eta| < 1.7$ range. The HEC is located in the endcaps (two independent wheels per endcap) and extends the coverage up to $|\eta| = 3.2$. The FCal is also located in the endcaps, improving the uniformity of the calorimetric coverage and extending the coverage to $|\eta| = 4.9$. FCal also features shower identification capability due to its fine lateral granularity and longitudinal segmentation into three layers.

2.3.3   Muon spectrometer

The Muon Spectrometer (MS) is based on the bent of the muon tracks caused by the ATLAS magnet system, in the barrel region ($|\eta| < 1.4$) due to the large barrel toroid and in the endcaps ($1.6 < |\eta| < 2.7$) due to the smaller endcap magnets in the end of the barrel toroid. The $1.4 < |\eta| < 1.6$ area, is called transition region, as the magnetic field is a combination of the barrel and endcap fields.

The MS features both trigger and high-precision tracking chambers. These are arranged in three cylindrical layers around the beam axis and in three planes perpendicular to it. The tracking chambers consist of two technologies, Monitored Drift Tubes (MDT) in the barrel and endcap region and Cathode Strip Chambers (CSC) in the forward region. Resistive Plate Chambers (RPC) in the barrel and Thin Gap Chambers (TGC) in the endcaps consist the trigger system, providing trigger information up to $|\eta| < 2.4$.

Monitored Drift Tubes

MDT chambers, are pressurised drift tubes operating with a gas mixture of $Ar : CO_2$ $93 : 7$. These chambers consist of three to eight layers of drift tubes. A single tube has a resolution of about $80\,\mu m$ and the resolution of the full chamber reaches $35\,\mu m$. They cover an area with $|\eta| < 2.7$ and are used for precision momentum measurement.

Cathode Strip Chambers

CSC are multi-wire proportional chambers and they are located in the forward region ($2.0 < |\eta| < 2.7$). They have an intrinsic resolution that varies from $40\,\mu m$ in the bending plane to $5\,mm$ in the transverse plane. A big advantage of the CSC, is their ability to provide efficient two-track detection with good resolution.

Resistive Plate Chambers

RPC are gaseous parallel electrode-plate detectors and compliment the precision chambers, to cover the need of the MS for triggering on muon tracks. The RPC sub-system covers the barrel region ($|\eta| < 1.05$) and provides measurements in both η and ϕ coordinates. It is made of three concentric cylindrical layers around the beam axis. The one located further from the beam axis allows to trigger in high momentum tracks, while the two inner chambers provide trigger to lower momentum muons.

Thin Gap Chambers

TGC are multi-wire proportional chambers, covering a region of ($1.05 < |\eta| < 2.4$) and apart from the trigger information, determine the second, azimuthal coordinate to complement the measurement of the MDT detectors in the radial direction. Seven layers of TGC chambers complement the MDT in the middle layer of the endcap region and two layers in the inner part. The coordinate in the outer MDT wheel is obtained by extrapolating the track from the information collected in the middle layer.

2.4   ATHENA - ATLAS analysis framework

The vast amount of data recorded with the ATLAS experiment, as well as the MC sample produced (simulation and reconstruction) were processed using the ATLAS software framework, ATHENA [68]. ATHENA uses Python in order to configure and load C++ objects. It is based on LHCb's Gaudi framework [69] and relies on the CLHEP libraries [70], which hold routines designed for high-energy physics.

All ATHENA algorithms can be divided in three parts: the initialisation, the loop on the events and the finalisation. During the first step, the services and libraries are loaded so that they can be called by the event loop. During the loop on the events the libraries and algorithms are called sequentially on each event and the calculations on the candidate hits/tracks are performed. Finally, after the loop has finished, the algorithms are terminated and the objects are deleted. The outcome of a successful ATHENA run is, the processed data file and the report on the CPU and memory usage.

There are four types of data formats that are analysed with the ATHENA framework. Ordering them with the per-event size in bytes, first is the RAW data format. The RAW data hold all the information coming from the detector, in a byte-stream format, and a typical event occupies approximately $1.5\,\mathrm{MB}$ of hard-disk space. The second type of data are the Event Summary Data (ESD). ESD files are essentially the output of the reconstruction algorithms, containing objects like lepton and jet information and a single event is about $1\,\mathrm{MB}$ in size. A subset of the ESD are the Analysis Object Data (AOD), which contain physical objects for analyses and their usual size is of the order of $100\,\mathrm{KB}$.

In the quarkonia analyses the Derived from Analysis Object Data (DAOD) files are used. These files contain information from the AODs with additional variables that are created using the B-physics analysis framework. The most common tool used in almost every B-physics subgroup, is the two particle vertexing (usually $J/\psi \to \mu\mu$ decays), the two muons plus single track vertexing (like the $B^{\pm} \to J/\psi K^{\pm}$ decays) and the two muons plus two tracks vertexing (for the $B_s \to J/\psi \phi$ decays, where ϕ decays to a pair of K). Usually, information on jets and photons are not present in order to slim down their size (exceptions include $\chi_c \to J/\psi \gamma$ studies). From these files, flat n-tuples are generated, to be analysed later using the ROOT framework [71].

2.4.1   Monte Carlo generation

The simulation of physics processes within the ATLAS experiment is a multi-stage procedure. The standard HepMC format [72] is used for the generation of the events. The generator creates the information for all the physics processes, which are then read into the simulation. In the generation stage, the detector geometry is not taken into account, but fiducial cuts can be applied in order to reduce the size of the files and significantly reduce time. The configuration of the detector, written in Geant4 [73], is then activated when the particles are propagated through the ATLAS detector and energies deposited in the active areas are recorded as hits. Hits are then passed on to the digitisation, which is the last stage before the actual reconstruction of the events.

MC samples are available in all data formats described above. Apart from information for the reconstructed objects of the event, the information of the particle is also available, prior to detector simulation. This is called "truth" information and is frequently used for efficiency and acceptance calculations.

2.4.2   Validation of MC samples and ATHENA framework

The ATLAS detector, together with the beam conditions and the ATHENA framework, are constantly changing adopting and incorporating changes in the beam and/or the ATLAS detector. Examples include the addition the Insertable B-Layer [74] and the beam structure change from 50 ns bunch spacing to 25 ns. The ATHENA framework itself, also improves, aiming to faster and more efficient algorithms. Due to these changes, before a sample is created with big statistics, it is necessary to be validated, to ensure that the changes didn't alter the characteristics of the detector.

For the B-Physics group, the validation process was done using $J/\psi \to \mu\mu$ and $B_s \to J/\psi\phi$ ($\phi \to K^+\phi^-$) decays. The variables tested are J/ψ mass, L_{xy}, p_T and rapidity. Examples of these validation studies, where 4 different samples are compared, are shown in figures 2.3. These variables are particularly sensitive to detector effects, as a possible change in detector resolution would be evident in in the J/ψ invariant mass distribution.

Figure 2.3(a) shows an example of problematic generation of J/ψ rapidity (comparison of bottom two samples) and figure 2.3(b) shows the agreement of the J/ψ reconstructed mass between these samples. On the top of these figures, the normalised distributions are plotted for the test and reference samples and on the 3 lower plots, the residuals between the reference and the 3 test samples are shown.

2.5   Detector Control System of the ATLAS experiment

All the conditions of the ATLAS experiment, either the functional parameters of the experiment or the environmental parameters of the cavern hosting the detector, are monitored and controlled with a Detector Control System (DCS) [75]. The main purpose of this system is the safe operation of all the systems in the ATLAS experiment.

The DCS was developed within the frame of the Joint Controls Project (JCOP) [76], a collaboration of the controls group and the DCS groups of the LHC experiments.
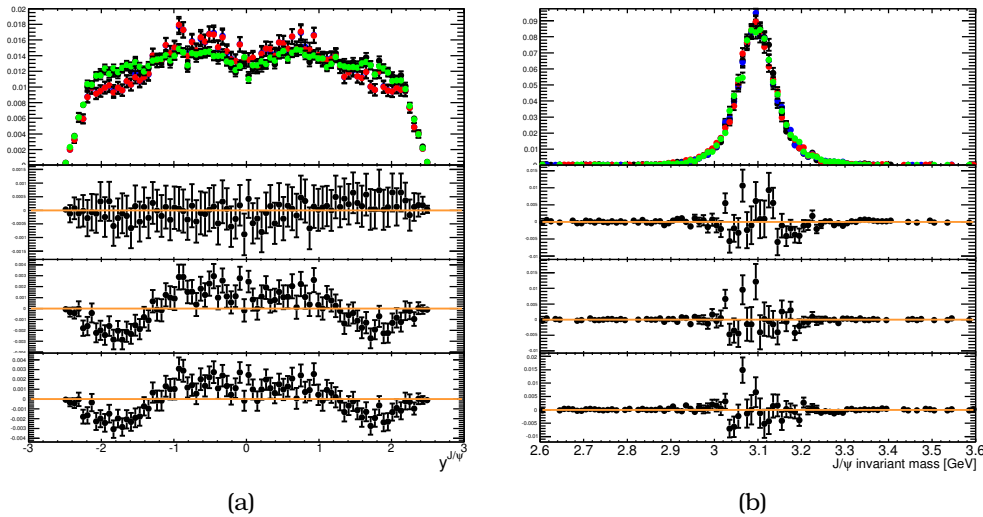
Figure 2.3: *Comparison of J/ψ (a) rapidity and (b) reconstructed mass between 4 different samples. The three test samples are generated with newer ATHENA release and reflect future upgrades of the detector (IBL and FTK).*

Among the common software and hardware systems established were: the field buses, protocols and a Supervisory Control and Data Acquisition (SCADA) system, the WinCC (formerly known as PVSS).

As shown in figure 2.4, the DCS system is divided in front-end and back-end. Systems that monitor environmental variables, the cooling systems and information about the racks are included in the front-end. WinCC is the SCADA system that is used in order to monitor and control them.

The back-end is further divided in local, sub-detector and global control stations. The local control station is used for the connection of the front-end hardware and its readout. The Sub-detector Control Station (SCS) is used for the stand-alone operation of the systems and the Global Control Stations (GCS) integrate all the sub detectors into the common ATLAS DCS.

2.5.1 A DCS system for the high and low voltage control of the MDTs

As described in section 2.3.3 MDT tubes are part of the MS of the ATLAS experiment. A total of 1150 MDT chambers are included in the MS, out of which 494 are on the endcaps and the rest in the barrel. Both partitions (barrel and endcap) are divided in two regions: side A and side C by a vertical cross section containing the interaction point. Another grouping of the chambers is Inner, Middle and Outer, according to their distance from the interaction point, if they are located in the barrel, or if they are placed in the Small Wheel, the Big Wheel or the Outer Wheel, for the endcaps.

The subsequent division of the layers is the number of stations. Stations show the position of the chambers with respect to the interaction point in the direction parallel to the beam axis, while for the endcaps, the stations show the position of the
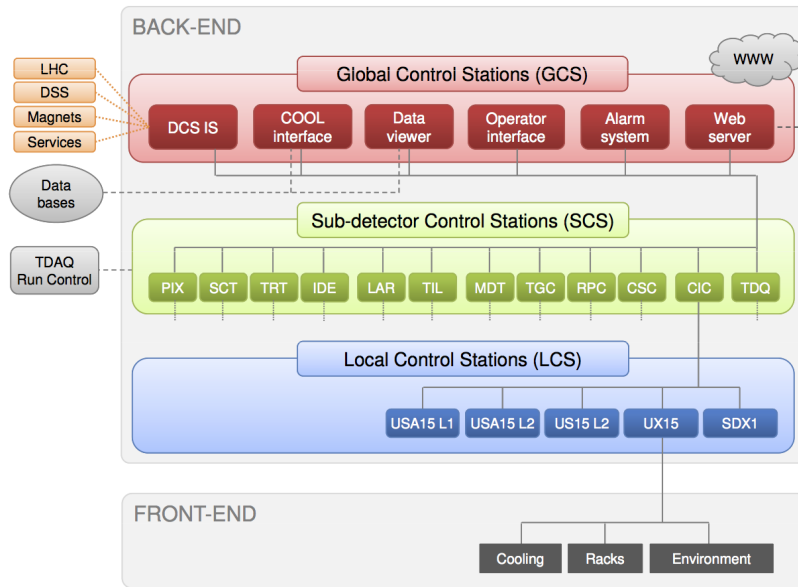
Figure 2.4: *ATLAS DCS architecture*

chamber with respect to the axis in the radial coordinate $(1 - 6)$. Finally, based on the azimuthal coordinate of the chambers they form 16 sectors which contain different types of chambers with respect to their size. The odd sectors are named as Large and the even as Small.

The tubes require high voltage (HV) in order to function properly and the front-end electronics need a low voltage (LV) supply. The HV channel require $3080\,\text{V}$ provided to each multilayer and the LV is $5\,\text{V}$ for the read-out electronics. The power for these purposes is provided by CAEN power supply modules and hardware dedicated to their control. The A3540P module is used for the HV supply and the A3025B or the A3016B are used for the LV (as shown in figure 2.5), with the difference between these cards being the maximum current allowed ($25\,\text{A}$ and $16\,\text{A}$ respectively).
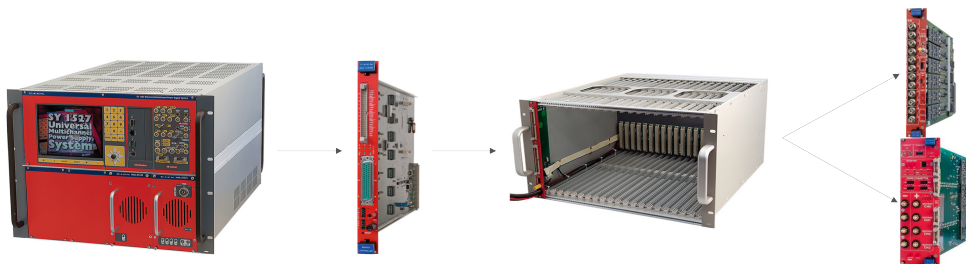
Figure 2.5: *CAEN hardware chain.*

These boards are mounted in crates (EASY 3000) and are located, as the boards, in the ATLAS cavern. The EASY 3000 crate can host both LV and HV modules, occupying 2 and 4 slots respectively, in a total of 21 slots. The crates are further connected in a chain and controlled by the A1676 branch controller. The branch controller can manage up to 6 crates, and can be further connected and placed in two SY4527 mainframes located in the Underground Service Area (USA15). Channel ID numbers reveal this

structure. For example, $01 - 3 - 05 - 002$ indicates a channel with number 2 of a board located in slot 5, housed in crate 3 controlled by the branch controller 1.

Finite State Machine model

The hardware is controlled with a Finite State Machine [77]. The FSM tree includes three different types of nodes; Control Unit (CU), Logical Unit (LU) and Device Unit (DU) nodes.

The top of the structure includes two CU nodes, one for each side (A or C), pattern that is repeated for both barrel and endcap. Each of these nodes includes its status and all the layer-children, which are CU nodes.

2.5.2   Endcap Extension chambers

A good fraction (approximately 52 out of 62) of the Endcap Extension (EE) chambers were not installed in the muon spectrometer, due to time limitations, accounting for losses in efficiency where the barrel and endcap meet ($1.0 < |\eta| < 1.3$). This pseudorapidity region is shown in figure 2.7(a). The missing chambers were reflected in muon reconstruction efficiency studies, when the efficiency is plotted as a function of the pseudorapidity of the muons. This is shown in figure 2.7(b), where the two inefficient regions are clearly visible in the range of $1.0 < |\eta| < 1.3$.

Part of the EE chambers were installed during the Xmas shutdown of 2011. A series of panels (an example is shown in figure 2.6) and tools was developed (or modified) in order to properly include the new EE chambers in the FSM tree. Apart from the software side, the necessary HV and LV modules were installed in the experimental cavern.

The addition of the chambers provided an extra measurement, for the reconstruction of muons trajectories. By looking on data collected during 2012, it is clear that one of the inefficient regions, around $-1.3 < \eta < -1.0$, is recovered (see figure 2.7(c)).

The rest of the chambers were installed during the first Long Shutdown (LS1).

2.5.3   MDT DCS conditions data and DCS COOL folder configuration

Information coming from the DCS related to the state and status of the chambers in the ATLAS experiment, is used for many purposes. These include the run flagging and the data quality monitoring (DQ). The information needed for offline reconstruction is stored in the Conditions Database. The muon community decided to restrict variables that are accessible from the ATHENA framework (see section 2.4) to be taken from the COnditions Objects for LCG (COOL) database. In the COOL database, objects are stored and referenced with an associated start and end time, inside which they are valid [79].

COOL is a software package that provides support for several similar database technologies, like Oracle and MySQL. Its purpose is to provide common components and tools for the handling of the conditions data of the LHC experiments. The main developers of this are the CERN IT group and the ATLAS and LHCb experiments.
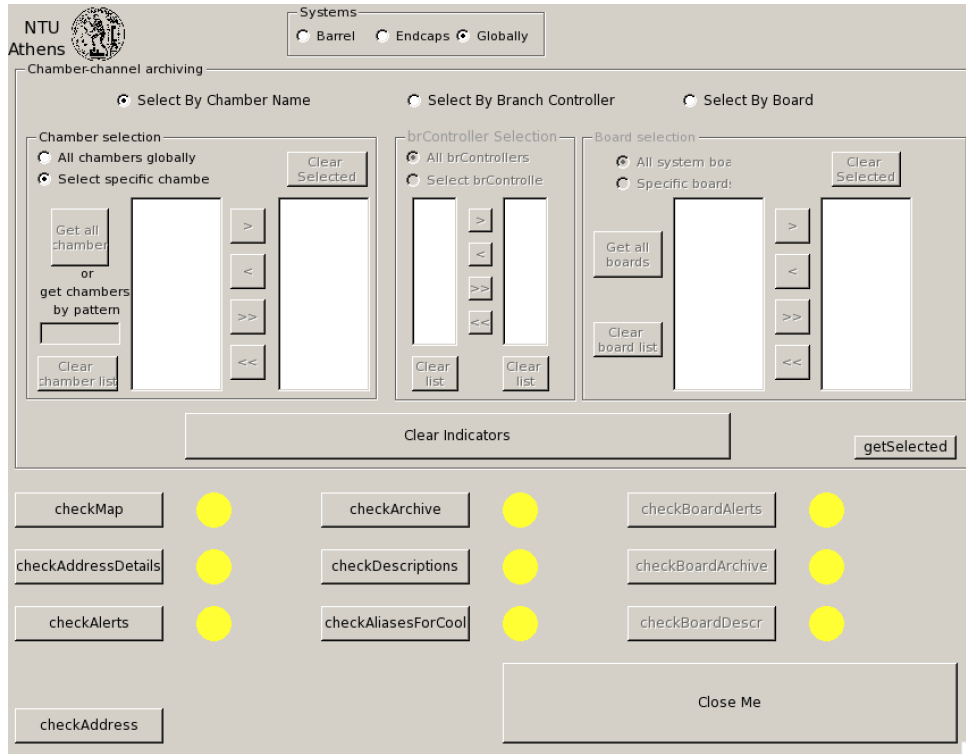
Figure 2.6: *An example of a panel used for the validation of all the parameters of the HV/LV DCS system.*

In the ATLAS experiment, the information from the ATLAS DCS are stored in folders in the COOL database which are created by a dedicated panel created by the central DCS. This panel uses Collection Def Files (.CDF) that must contain the necessary information and in the appropriate structure. The CDF files need to include fieldTypes, channels and fields with the following format:

- *fieldNames:* $\text{name}_{i=1}$! $\cdots$! $\text{name}_{i=N}$

- *fieldTypes:* $\text{type}_{i=1}$! $\cdots$! $\text{type}_{i=N}$

   - *channel:* $\text{ID}^{j=1}$
   - *fields* $\text{DPE}_{i=1}^{j=1}$! $\cdots$! $\text{DPE}_{i=N}^{j=1}$
   - *channel:* $\text{ID}^{j=2}$
   - *fields* $\text{DPE}_{i=1}^{j=2}$! $\cdots$! $\text{DPE}_{i=N}^{j=2}$
   - $\vdots$
   - *channel:* $\text{ID}^{j=K}$
   - *fields* $\text{DPE}_{i=1}^{j=K}$! $\cdots$! $\text{DPE}_{i=N}^{j=K}$

The needs of the MDT chambers are the storing of information about the High Voltage (HV), Low Voltage (LV) and Joint Test Action Group (JTAG) of the MDT chambers. The complete list of the individual variables within these three folders are listed in
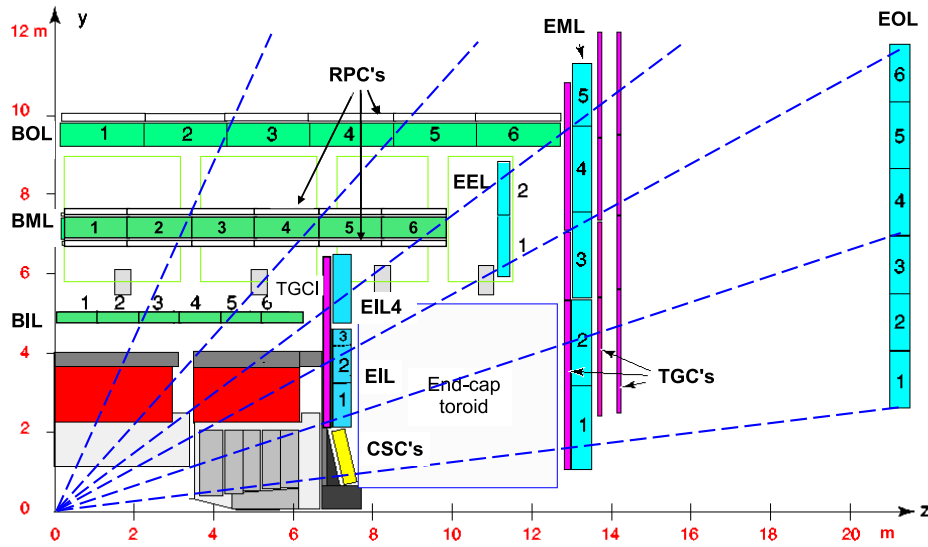
(a)
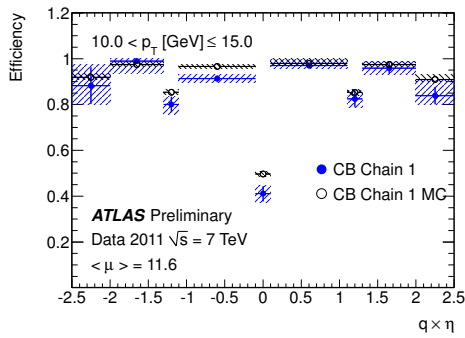
(b)
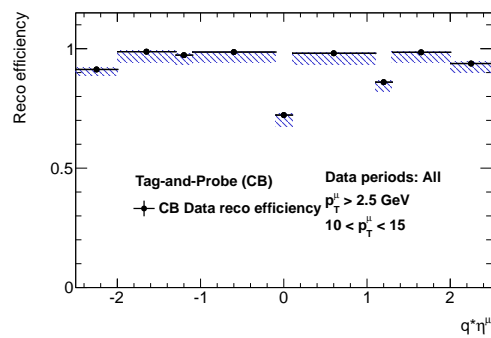
(c)

Figure 2.7: *(a) A $z - y$ view of the ATLAS detector. MDT chambers are shown with green for barrel and cyan for the endcaps and CSC with yellow. RPC are sketched as white boxes and TGC with magenta. (b) Efficiency for combined muons as a function of $q \times \eta$ [78] using 2011 data. (c) Same plot as (b) but using data recorded on 2012 data. The innefficient area in the EE chambers region is now corrected, where the rest of the bins are left the same.*

ref [80]. These three folders are created by CDF files, which are generated by a dedicated panel.

The creation of the COOL folders were validated with the first cosmic data collected on 2014.

2.6   Overall performance of the ATLAS experiment

ATLAS detector operated with high efficiency and collected $5.08\,\mathrm{fb}^{-1}$ of $\sqrt{s} = 7\,\mathrm{TeV}$ pp collision data during 2011 and $21.3\,\mathrm{fb}^{-1}$ of $\sqrt{s} = 8\,\mathrm{TeV}$ pp collision data during 2012 (shown in figure 2.8(a)). During the whole RUN-1, ATLAS recorded collision data with

an efficiency greater than 99% (see table 2.2).

Table 2.2: *Overall performance for the ATLAS detector.*

ATLAS performance for pp collisions at $\sqrt{s} = 8\,\mathrm{TeV}$										
Inner Detector			Calorimeters		Muon Spectrometer				Magnets	
Pixel	SCT	TRT	LAr	Tile	MDT	RPC	CSC	TGC	Solenoid	Toroid
99.9%	99.1%	99.8%	99.1%	99.6%	99.6%	99.8%	100%	99.6%	99.8%	99.5%

The quality of the data recorded by the ATLAS experiment were checked by a specific Data Quality (DQ) group. This group's responsibility was to flag the runs as useful for physics analysis. This evaluation is performed by Luminosity Blocks (LB), which are periods of time in a run. The LBs where all the components of the ATLAS detector were functioning properly and data were collected in the optimum conditions and the beams were considered as "stable" from the LHC, are marked as "good-run" lists. After applying this requirement, the luminosity that was available for physics analysis for the data collected during 2012 is $20.3\,\mathrm{fb}^{-1}$ (see figure 2.8(a)).

The delivered luminosity accounts for the luminosity delivered from the start of stable beams until the LHC requests ATLAS to put the detector in a safe standby mode, to allow a beam dump or perform beam studies. The recorded luminosity reflects the DAQ inefficiency, as well as the inefficiency of the "warm start" (when the stable beam flag is raised, the tracking detectors undergo a ramp of the high-voltage and, for the pixel system, the preamplifiers are turned on).

An interesting observable is the number of interactions per bunch-crossing (μ). The μ parameter is calculated as $\mu = \mathcal{L}_{\mathrm{bunch}}\sigma_{\mathrm{inel}}/f_r$, where $\mathcal{L}_{\mathrm{bunch}}$ is the instantaneous luminosity per bunch, σ_{inel} is the inelastic cross section (taken to be $73\,\mathrm{mb}$) and f_r is the LHC revolution frequency [81].

Pileup is one of the biggest challenges for the experiment, as it is causing problems in event reconstruction. The mean number of interactions per bunch-crossing for the 2012 data is shown in figure 2.8(b). The $\langle\mu\rangle = 21$ interactions per bunch crossing required many changes in the offline analysis algorithms, since that high levels were not expected for the early operation of the LHC.

(a)

(b)
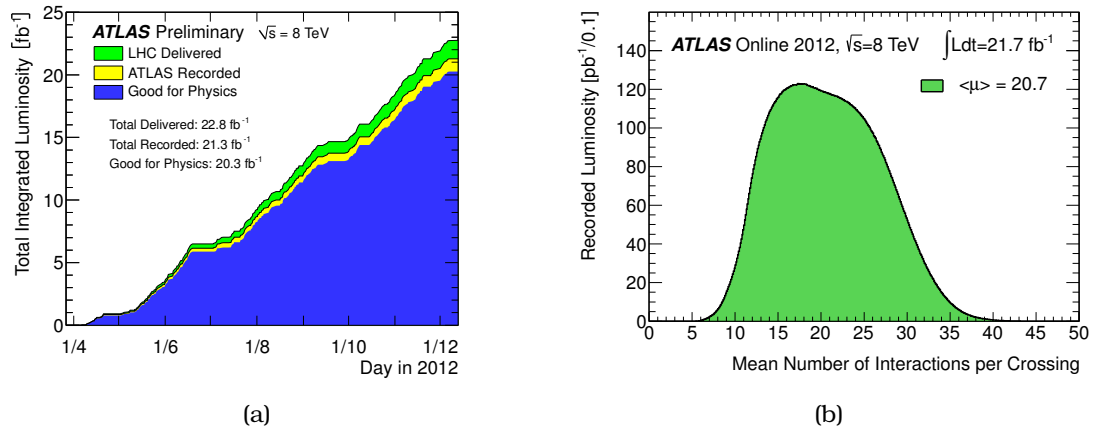
Figure 2.8: *(a) Cumulative luminosity delivered (green), recorded (yellow), and certified to be good quality data (blue) during stable beams by the ATLAS experiment for pp collisions at 8 TeV centre-of-mass energy in 2012 versus time. (b) Luminosity-weighted distribution of the mean number of interactions per crossing for 2012.*

Muon reconstruction performance

After giving an overview of the ATLAS experiment in section 2, the performance of the muon spectrometer is discussed. The muon reconstruction performance is examined using proton–proton collision data at $\sqrt{s} = 8\,\text{TeV}$ collected during 2012.

3.1 Introduction

In this chapter the procedure, cross-checks and results of measuring the muon reconstruction efficiency is described. Studies used $J/\psi \rightarrow \mu^+\mu^-$ decays for the low (2.5 – 20 GeV) transverse momenta region and $Z \rightarrow \mu^+\mu^-$ decays for the higher momenta. ATLAS has used 3 different muon reconstruction algorithms (STACO, MUID and MUONS[1]). The measurement is based on the tag-and-probe technique, which has been used previously for efficiency measurements in ATLAS [83].

Muon pair candidates are first selected by requiring a well-reconstructed muon candidate that is named the *tag* muon, and an ID track, named as the *probe*, for which the tag-probe system invariant mass can be calculated. The invariant mass distribution of all tag-probe pairs is further divided in intervals of probe transverse momentum and pseudorapidity.

Focusing on the J/ψ resonance region, $2.7 \leq m_{\text{tag−probe}} < 4.2$ GeV, the reconstruction efficiency of the probes, which are selected independently using MS information, can be determined by comparing the yields of resonant J/ψ observed in the tag-probe invariant mass distribution, to the observed yield when the probe is required to have been reconstructed as a muon. The resultant muon reconstruction efficiencies are derived relative to the efficiency to reconstruct the ID probe track and are presented as a function of muon pseudorapidity and transverse momentum.

---

[1] in this thesis only the results concerning the STACO chain are presented, since this was the type of muons that were used for both $B_s \rightarrow \mu\mu$ and $Z + J/\psi$ analyses. All figures and results for all three reconstruction chains are included in reference [82].

3.2 Muon and track reconstruction

Four types of muon reconstruction criteria are used, based on the available information from the ATLAS sub-detectors (illustrated on figure 3.1). The type of muons that their trajectory is reconstructed using information coming only from MS is called "stand-alone" (SA - see figure 3.1(a)). The muon track parameters are defined by extrapolating the track to the interaction point, taking into account the energy loss from the calorimeters. This type of muons is used mainly to extend the coverage of the ID ($2.5 < |\eta| < 2.7$) and to search for long lived objects that decay after the pixel layers.

The main type of reconstructed muons used by ATLAS is the "combined" muons (CB - see figure 3.1(b)). The CB muon tracks are formed from a successful combination of a MS with an ID track. The tracks in ATLAS are formed by information collected from the pixel, SCT and TRT sub-detector systems of the ID. The "inside-out" strategy is followed, where the trajectories of track candidates in the pixel and SCT detectors are fitted to the TRT in order to reconstruct a full ID track. These tracks are further matched with the tracks (or segments) reconstructed in the MS in order to form muon tracks. The momentum information is calculated by a statistical combination of the ID and MS detectors, after applying a correction for parameterised energy loss in the calorimeter. These muons are named as combined, having a low contamination from hadrons (fakes).

ID tracks that are associated with at least one segment in the MDT or CSC chambers are classified as segment-tagged muons (ST). ST muons (see figure 3.1(c)) are used in regions with reduced MS acceptance and when, mainly low p_T, muons cross only one layer of the MS.

The last type of muons are the "calorimeter-tagged" (CaloTag) muons (see Fig. 3.1(d)). These are formed by ID tracks that are associated to an energy deposit in the calorimeter compatible with a minimum ionising particle. Although this type has the lowest purity, compared to the other three mentioned above, it recovers acceptance in the un-instrumented regions of the MS.

In *B*-physics analyses the muon types that are used are the CB and ST. Including ST muons in physics analyses improves the efficiency of muon reconstruction at low p_T, at the expense of increased fake rates, as low p_T muon may not cross a sufficient number of MS precision chambers to allow an independent momentum measurement in the MS, and thus would otherwise be rejected from the CB algorithm definition. Due to this, the muon reconstruction efficiency in the low p_T region was measured only for these two types of muons.

3.3 Data and MC samples

For this study data from pp collisions at $\sqrt{s} = 8\,\text{TeV}$ were used. The integrated luminosity of the data sample is 20.3fb^{-1} and was collected during 2012. For the comparison with the MC, a variety of J/ψ MC samples is used, with different selections in the J/ψ muon's p_T and different production ways of the J/ψ. The combinations used were ($p_T^{\mu_1} > 2.5\,\text{GeV}$, $p_T^{\mu_2} > 2.5\,\text{GeV}$), ($p_T^{\mu_1} > 4\,\text{GeV}$, $p_T^{\mu_2} > 4\,\text{GeV}$), ($p_T^{\mu_1} > 4\,\text{GeV}$, $p_T^{\mu_2} > 6\,\text{GeV}$) and ($p_T^{\mu_1} > 6\,\text{GeV}$, $p_T^{\mu_2} > 6\,\text{GeV}$) and the J/ψ was produced either promptly or from a
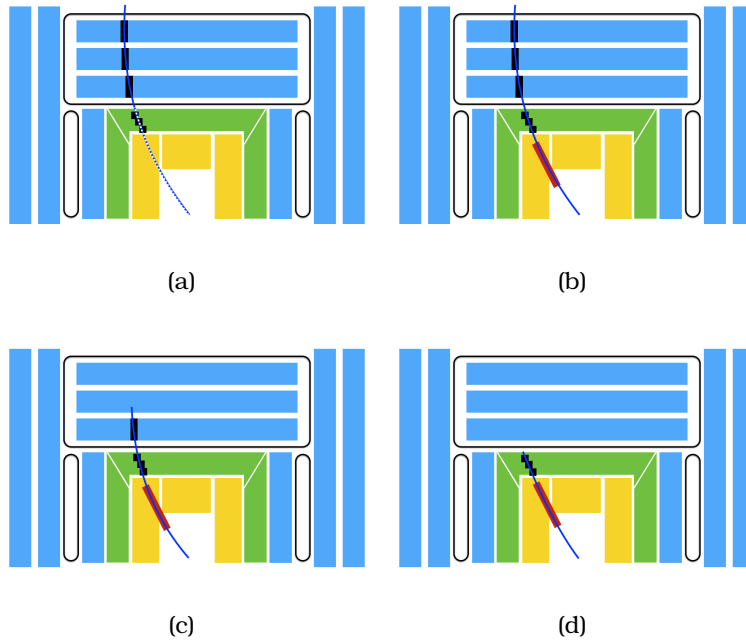
Figure 3.1: *Schematic of the different types of muons. (a) Stand-Alone (b) Combined (c) Segment-tagged and (d) Calorimeter-tagged. In this sketch, the inner detector is presented with yellow, the calorimeters with green and the muon chambers with blue colour.*

decay of a *b*-hadron.

3.4 Tag-and-probe selection

The basic data selection requires good detector conditions for the tracking and muon reconstruction systems, and makes use of the good run list: data12_8TeV.periodAllYear_DetStatus-v58-pro14-01_DQDefects-00-00-33_PHYS_StandardGRL_All_Good.xml. Collision data is selected by requiring at least one reconstructed primary vertex built from three or more ID tracks. The primary vertex (PV) is selected as the vertex whose constituent tracks have the highest $\sum p_{\mathrm{T}}^2$.

3.4.1 Trigger selection

Events are selected online with a suite of triggers that selects a single muon candidate (this triggered muon becomes the tag). Although a suite of dedicated $J/\psi \rightarrow \mu^+\mu^-$ triggers exist, these di-muon trigger signatures cannot be used for this measurement as these impose muon reconstruction requirements on the tag muon that would bias the tag-and-probe method results. Triggers used include single muon, muon+track, isolated muon and muon+non-muon object (MET, photon) triggers. The exact composition of triggers used are detailed below. The selected triggers were chosen based on the presence of a significant $J/\psi \rightarrow \mu^+\mu^-$ signal in offline data.

List of triggers EF_mu24_j65_a4tchad_EFxe40_tclcw, EF_mu4T_j65_a4tchad_xe60_tclcw_loose, EF_mu24_j65_a4tchad, EF_mu18_tight_e7_medium1, EF_mu4T_j65_a4tchad_xe70_tclcw_veryloose, EF_mu24_j65_a4tchad_EFxe60_tclcw, EF_mu24_tight_b35_medium_EF_j35_a4tchad, EF_mu20i_tight_g5_loose_TauMass, EF_mu6_Trk_Jpsi_loose, EF_mu24i_tight, EF_mu24i_tight_MuonEF, EF_mu24i_tight_MG, EF_mu24i_tight_l2muonSA, EF_mu24_tight_3j35_a4tchad, EF_mu24_g20vh_loose, EF_mu40_MSonly_barrel_tight, EF_mu50_MSonly_barrel_tight, EF_mu24_tight_EFxe40, EF_mu24_tight_L2StarB, EF_mu18_medium, EF_mu24_medium, EF_mu24_tight, EF_mu24_tight_MuonEF, EF_mu24_tight_MG, EF_mu24_tight_L2StarC, EF_mu36_tight, EF_mu40_tight, EF_mu20it_tight, EF_mu24_g20vh_medium, EF_mu18_2g10_medium, EF_mu24_muCombTag_NoEF_tight, EF_mu10i_loose_g12Tvh_medium, EF_mu10i_loose_g12Tvh_medium_TauMass, EF_mu18_2g10_loose, EF_mu10i_g10_medium_TauMass, EF_mu20i_tight_g5_medium_TauMass, EF_mu24_tight_3j45_a4tchad, EF_mu24_tight_4j45_a4tchad, EF_mu24_tight_4j35_a4tchad, EF_mu4T, EF_mu6, EF_mu15, EF_mu40_slow_tight, EF_mu60_slow_tight1, EF_mu22_IDTrkNoCut_tight, EF_mu8_4j45_a4tchad_L2FS, EF_mu6_Trk_Jpsi_loose_L2StarB, EF_mu6_Trk_Jpsi_loose_L2StarA, EF_mu24_j65_a4tchad_EFxe40wMu_tclcw, EF_mu24_j65_a4tchad_EFxe60wMu_tclcw, EF_mu6T_2b55_medium_2j55_a4tchad_L1J20_match, EF_mu24i_tight_muFast, EF_mu4T_L2StarB, EF_mu6_L2StarB, EF_mu15_vbf_L1TAU8_MU10

3.4.2 ID track selection

ID tracks associated to tag and probe candidates must satisfy the following good quality requirements:

- at least one hit in the innermost layer of the pixel detector, if the track was expected to intersect this detector layer;

- the sum of the number of pixel hits and dead pixel sensors crossed by the track is required to be greater than one;

- the sum of the number of semiconductor tracker (SCT) hits and dead SCT sensors crossed by the track is required to be greater than six;

- the number of missing pixel layers (layers crossed by the track but not registering hits) plus the number of missing SCT layers must not exceed one;

- for absolute pseudorapidities less than 1.9 the total number of Transition Radiation Tracker (TRT) hits was required to be greater than five;

- in the case where the total number of TRT hits is greater than five, the fraction of TRT outlier hits to the total is required to be less than 90%.

3.4.3 Tag selection

The tag muons selected must satisfy the following requirements:

- must be a combined STACO muon;

- must be associated to an ID track satisfying good quality requirements (above);

- the ID track transverse momentum must be greater than 4 GeV and the absolute pseudorapidity less than 2.5;

- must be consistent with being the muon candidate that was involved in the trigger decision. This requirement is imposed by checking that the reconstructed muon candidate in the MS is within a radius of 0.05 in $\eta - \phi$ space of the corresponding region of interest (RoI) where the muon trigger signature was reconstructed.

3.4.4 Probe selection

The probe track selected must satisfy the following requirements:

- the ID track must satisfy the good quality requirements;

- the ID track measurements must satisfy $p_T > 2.5$ GeV and $|\eta| < 2.5$;

- must satisfy a separation requirement between the tag and probe requiring $|\Delta\phi(\text{tag}, \text{probe})| > 0.4$ or $|\Delta\eta(\text{tag}, \text{probe})| > 0.4$;

- a common vertex fit of probe and tag ID tracks must converge;

- have opposite electric-charge to the tag;

- the invariant mass of the tag-probe system must be within $2.7 \leq m_{\text{tag}-\text{probe}} < 4.2$ GeV.

The lower range of transverse momentum is limited by the average energy loss (~ 3 GeV) of a muon traversing the calorimeter, which limits the chance of low momentum muons reaching the MS system, in particular for high rapidity muon candidates, and the increasing likelihood of fake candidates. In each event, all valid tag-probe combinations are considered. The above selection results in 74×10^6 tag-probe candidates with probe tracks covering transverse momenta of $2.5 - 30$ GeV and $|\eta| < 2.5$.

3.5 Efficiency measurement methodology

The selected tag-probe pairs are categorised into intervals of probe transverse momentum and charge-signed pseudorapidity (that will correspond to the binning of the two-dimensional muon reconstruction efficiency maps).
p_T (GeV): 2.5, 3.25, 4.0, 4.25, 4.5, 4.75, 5.0, 5.25, 5.5, 5.75, 6.0, 6.25, 6.5, 6.75, 7.0, 7.5, 8.0, 8.5, 9.0, 10.0, 11.0, 12.0, 13.0, 15.0, 17.0, 20.0

η: -2.5, -2.3, -1.9, -1.7, -1.52, -1.37, -1.3, -1.2, -1.1, -0.8, -0.6, -0.4, -0.2, -0.05, 0.05, 0.2, 0.4, 0.6, 0.8, 1.1, 1.2, 1.3, 1.37, 1.52, 1.7, 1.9, 2.3, 2.5

By studying the invariant mass distribution of tag-probe pairs in the mass region of the J/ψ resonance the muon reconstruction efficiency can be extracted. The J/ψ offers a distinctive signature, a resonant structure centred around a mass of 3.096 GeV with width dominated by the detector resolution (the natural width being in the keV range), that can be identified above the continuum background sources.

In the case where the probe is identified as a muon candidate, the invariant mass distribution is largely background-free, with backgrounds dominantly arising at lower transverse momentum from combinatorial pairings of real muons from prompt or heavy flavour decay sources, or from decays in flight of kaons or pions, or occasionally from fake contributions due to hadronic punch-through. When the probe is selected independently of MS information, the background rates are substantially higher due to non-muonic contributions and increased combinatorics, but an identifiable $J/\psi \to \mu^+\mu^-$ peak can still be observed (see figure 3.2).

The invariant mass distribution where the probe MS information is required, and where it is not, can be fitted with resonant signal and continuum background shapes to extract the resonant $J/\psi \to \mu^+\mu^-$ yields in both cases. In the case of perfect muon reconstruction efficiency, the $J/\psi \to \mu^+\mu^-$ signal yields in both cases would be equal. Any reduction in the signal yield in the case where probes must be identified as muons relative to the total tag-probe sample represents an inefficiency in the muon reconstruction algorithm. By building the invariant mass distributions within a given range of probe kinematics, the reconstruction efficiency of muon candidates in this particular kinematic interval is determined.

Examples of such distributions are shown in figure 3.2. In these figures, the J/ψ invariant mass distributions are shown for the $10 < p_T^\mu < 12.5$ GeV bin and a pseudorapidity region in the barrel (figure 3.2(a)) and in the centre of the detector (see figure 3.2(a)). It is evident that in the latter case, where the MS provides smaller coverage, the efficiency is 23% lower, compared to the barrel region.

3.5.1 Efficiency definition 2012

A binned maximum likelihood fit is performed in the full mass range defined in the analysis - 2.7 GeV to 3.5 GeV. The fit model is a Gaussian for the signal plus a second order polynomial for the background description. The two samples (Muon + Track and Muon + !Muon) are fitted simultaneously using the same mean and width to describe the signal. The efficiency is calculated using the extracted yields from the two fits from the formula:

$$\epsilon_{\text{reco}}^i = 1 - \frac{N(J/\psi \text{ with probe NOT identified as a muon})}{N(J/\psi \text{ all probes})} \tag{3.1}$$
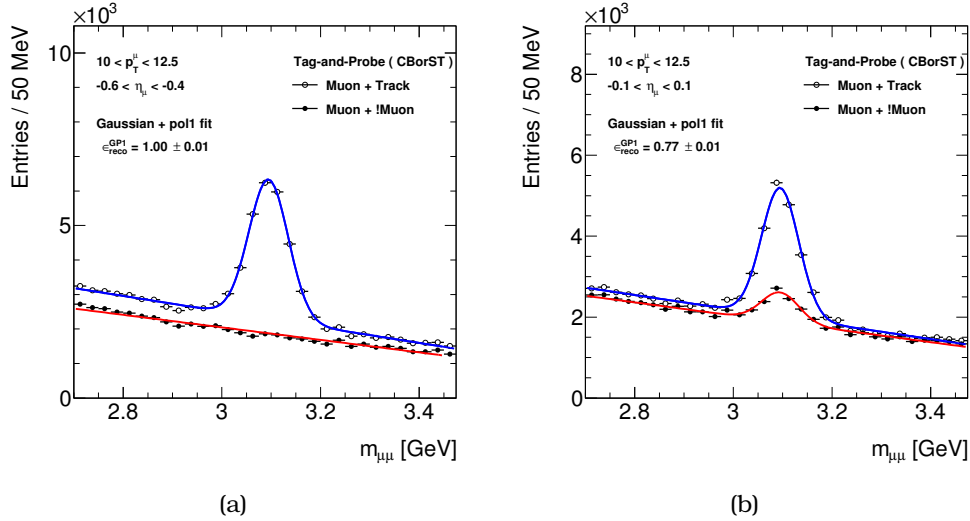
Figure 3.2: *Example of fits in the (a) barrel and (b) central region.*

3.6 Systematic uncertainties and cross-checks

3.6.1 Systematic uncertainties

Systematic uncertainties on the efficiency measurement originate from the fitting procedure. The systematic uncertainties were calculated by varying the background modelling and using first and third order polynomial.

J/ψ **pseudo-proper time dependence** A series of cross-checks were performed to ensure that the calculation of the reconstruction efficiencies is unbiased. First check was the dependence of the reconstruction efficiencies of the production mode of the J/ψ (see figure 3.3).

In order to check possible biases due to the pseudo-proper time of the J/ψ, the full sample was split in two. J/ψ mesons, produced by subsequent b-decays have longer pseudo-proper times. Based on this, four different requirements are used: (i) $|\tau| > 0.2 \, \text{ps}$ and (ii) $|\tau| > 0.3 \, \text{ps}$ (and the complimentary "<" comparison for both cases). Reconstruction efficiencies are extracted for each of the four configurations and the two-dimensional efficiency maps are derived. The division of each possible scenario considered with the reconstruction efficiency map calculated using the full statistics would indicate potential biases.

Figure 3.3 shows the result of this exercise. A full closure is observed, where in all four cases all bins are equal to 1, with exceptions in the central pseudorapidity and low momentum, where statistics are low.

Pileup dependence Events with high pileup are expected to degrade the performance of the MS and subsequently lower the muon reconstruction efficiency. This was examined by splitting the full J/ψ sample in two, after applying a cut on the number of reconstructed primary vertices of the event ($N_{\text{PV}} > (<)12$). The muon reconstruction
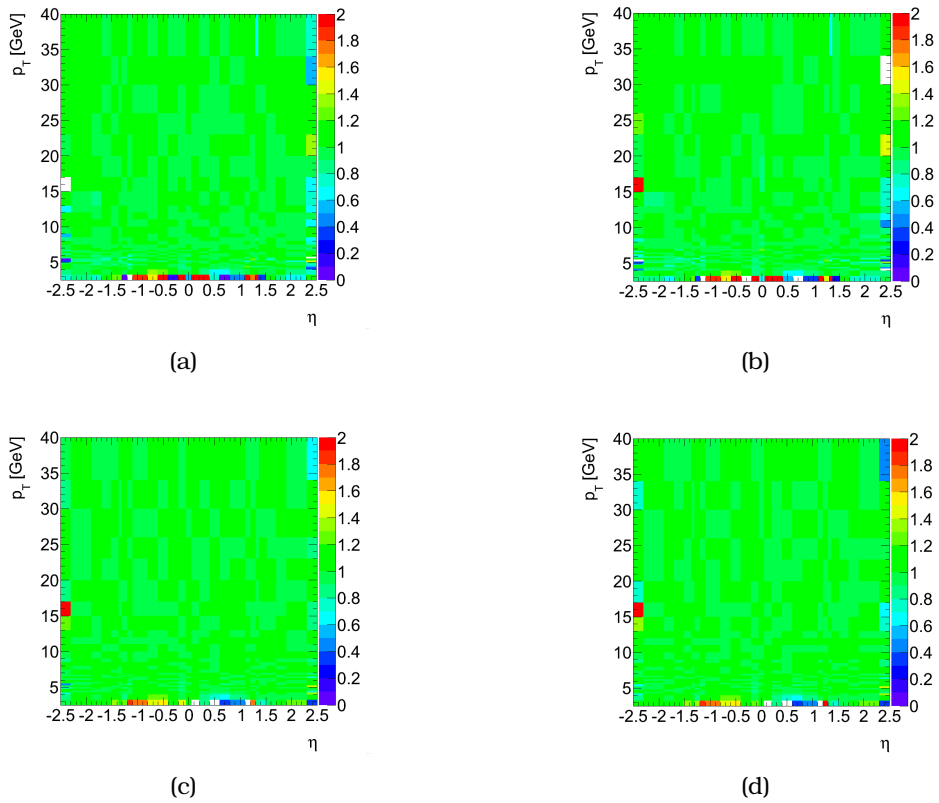
Figure 3.3: *Comparison of efficiency maps as a function of J/ψ lifetime. (a) $|\tau_{J/\psi}| > 0.2$, (b) $|\tau_{J/\psi}| < 0.2$, (c) $|\tau_{J/\psi}| > 0.3$ and (d) $|\tau_{J/\psi}| < 0.3$*

efficiency maps, evaluated from these two samples is further compared to the efficiency map derived from the full statistics sample.

The result is shown in figure 3.4(a) for $N_{PV} > 12$ and in figure 3.4(b) for $N_{PV} < 12$. Again, all bins have values close to unity.

Trigger dependence   Possible variation of the muon reconstruction efficiencies due to the choice of the trigger was also examined. A test sample was created by applying only J/ψ triggers. Efficiencies are derived from this sample and compared with the nominal efficiency map. No bias is observed, since all bins in the comparison of the two efficiency maps (see figure 3.5(a)) are close to 1. Except from the J/ψ trigger, two other samples were also created, by applying all single muon triggers and triggers including isolated muons. This test also showed no variation in the efficiency calculation.

Efficiencies as a function time that the data is collected   A final check was performed, based on the time that the data were recorded. The full dataset is split in four subsamples by grouping periods AB, CD, EG and HIJL. Biases are examined by comparing the efficiencies derived from these samples to the efficiencies calculated using the full data sample. Figure 3.5(b) shows the result of the EG period comparison, where, as expected, all bins are close to 1.

(a)   (b)
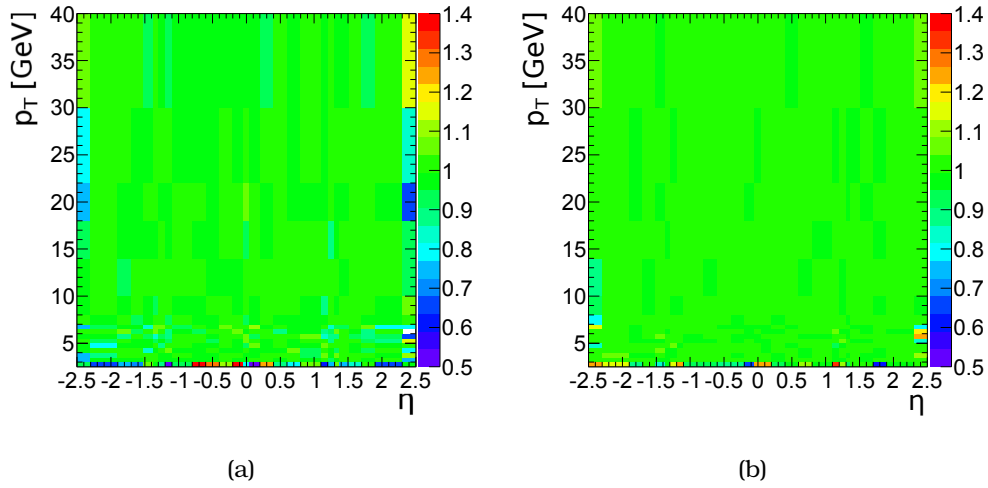
Figure 3.4: *Comparison of efficiency maps as a function of the primary vertices of the event. (a) $N_{PV} > 12$, (b) $N_{PV} < 12$*

(a)   (b)
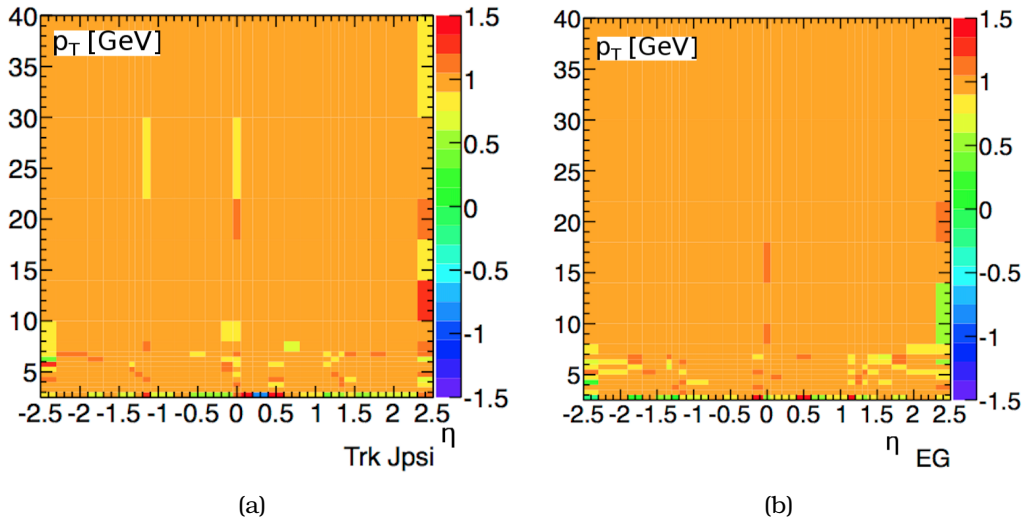
Figure 3.5: *Comparison of efficiency maps as a function of (a) the trigger that is used and (b) the sub-period that the data are collected.*

Comparison with 2011 muon reconstruction efficiencies   Studies were performed using the first data collected during 2011 for the performance of the muon reconstruction. $J/\psi \rightarrow \mu^+\mu^-$ decays were used in order to reach the low-p_T region. The results were calculated in broad bins of transverse momentum and pseudo-rapidity.

Data collected during 2012 are binned in the same bins as the 2011 analysis and then compared. The comparison of the efficiencies as a function of the pseudo-rapidity of the J/ψ was shown in figures 2.7(b) and 2.7(c), where it is clear that the installation of the EE chambers improved the overall efficiency.

Comparison of the muon reconstruction efficiencies, as a function of the muon's transverse momentum, between the two datasets is shown in figure 3.6. The agreement

is good across all p_T bins.
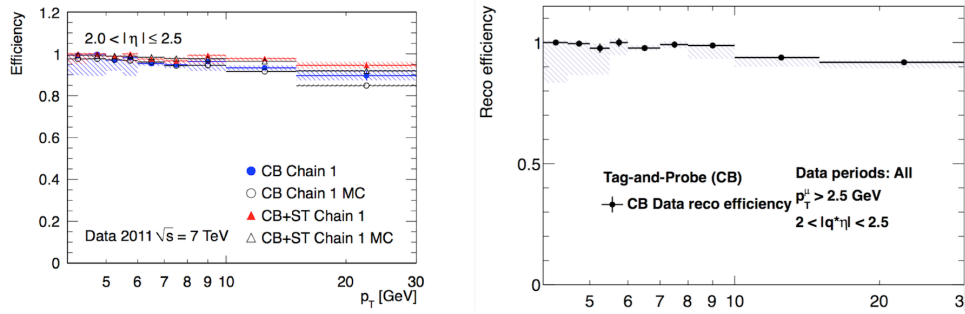
Figure 3.6: *Comparison of muon reconstruction efficiencies as a function of p_T, using data collected during 2011 (left) and 2012 (right).*

3.7 Measured reconstruction efficiencies

Projections of the two-dimensional maps are shown in figure 3.7. Figures 3.7(a) and 3.7(c) present the measurement of the muon reconstruction efficiencies as a function of the charged pseudo-rapidity and figures 3.7(b) and 3.7(d) as a function of the transverse momentum of the J/ψ meson. It is clear that going from the CB to the ST efficiencies (upper plots of figure 3.7 to lower ones) a significant fraction of efficiency is gained, due to the inclusion of, usually, lower momentum ST muons. The gain is pronounced in the low-p_T region in figures 3.7(b) and 3.7(d).

3.8 Data-MC scale factors 2012

ATLAS physics analyses typically use (*"Scale Factors"* - SF) to correct the detector simulation efficiency response to that measured in data, rather than using the measured efficiencies directly. The same tag-and-probe measurement procedure is thus applied to simulated $J/\psi \to \mu^+\mu^-$ decays and the MC efficiencies derived in the same kinematic intervals as in the data, and the two-dimensional efficiency maps (in transverse momentum and charge-signed pseudorapidity) from data and MC are compared to derive correction factors $C = \epsilon_{\text{Data}}/\epsilon_{\text{MC}}$ that can be applied to MC samples to improve the simulation description.

Available MC generators fail to describe the kinematics of the J/ψ production. In particular, the transverse momentum and rapidity distributions of J/ψ and the distributions of the muons from the subsequent $J/\psi \to \mu^+\mu^-$ decay are known to be mismodelled. As we measure muon reconstruction efficiencies over some finite kinematic interval, the efficiency determined in simulation is dependent upon the kinematic spectra of muons populating that interval. In order to make a fair comparison between the efficiencies measured in data and those measured in MC simulation, the available MC samples are combined using a re-weighting of the probe kinematics in MC to match that in data.

(a)

(b)

(c)

(d)
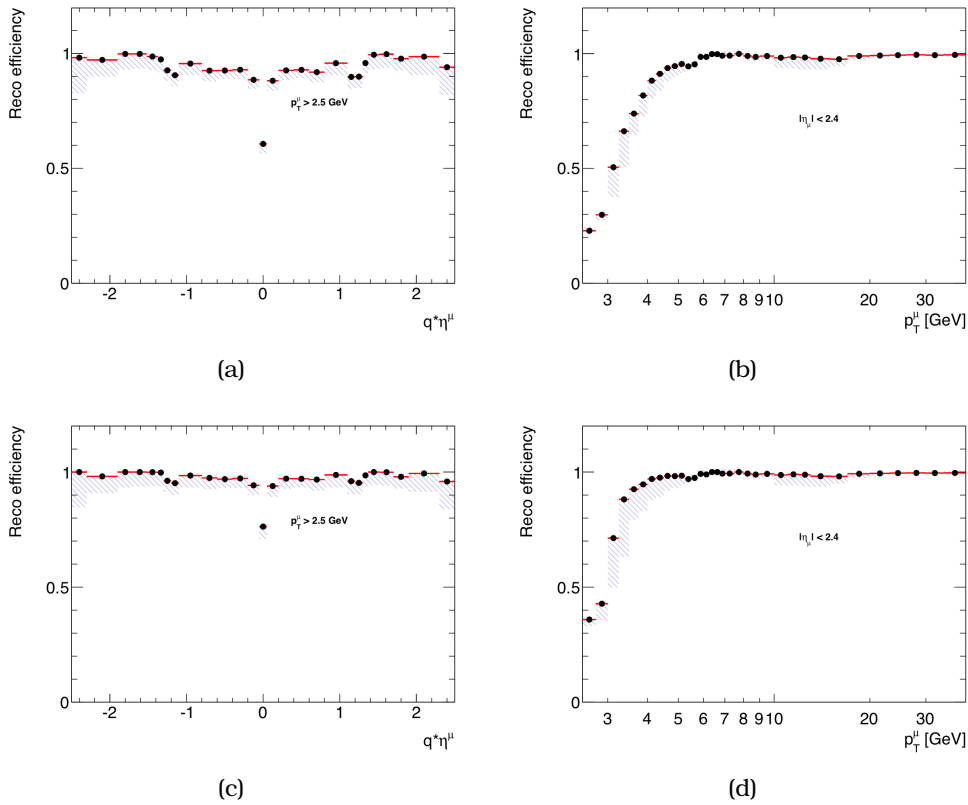
Figure 3.7: *Muon reconstruction efficiencies as a function of (a),(c) η and (b),(d) p_T. Results in top row correspond to CB muons and bottom to ST. Systematic uncertainties are presented with the shaded area.*

With the re-weighting applied to MC, the efficiencies are determined as for data. The MC scale factors $C = \epsilon_{\text{Data}}/\epsilon_{\text{MC}}$ are shown in figure 3.8(a) and in figure 3.8(b) for CB and ST muons respectively.

3.9 Probing the high-p_T region with $Z \rightarrow \mu^+\mu^-$ decays

Using the $Z \rightarrow \mu^+\mu^-$ decays, the higher-p_T range can be probed. The tag-and-probe method is applied in a wide range of $Z \rightarrow \mu^+\mu^-$ decays. Figure 3.9 shows the muon reconstruction efficiency for CB and ST muons. A steep rise is observed in the low-p_T region, especially for the CB muons, since a muon must have a transverse momentum greater than 3 GeV in order to transverse the calorimeter and cross at least two layers of MS stations. In the high-p_T region, no dependence of the transverse momentum is observed.

The drop in efficiency, measured by the $J/\psi \rightarrow \mu^+\mu^-$ decays, is caused from the inefficiency of the MS to reconstruct muons with small angular separation (expected from highly boosted J/ψ). This drop is reproduced in the MC and the SF derived from both $J/\psi \rightarrow \mu^+\mu^-$ and $Z \rightarrow \mu^+\mu^-$ decays are in good agreement in the overlapping region.

(a)   (b)
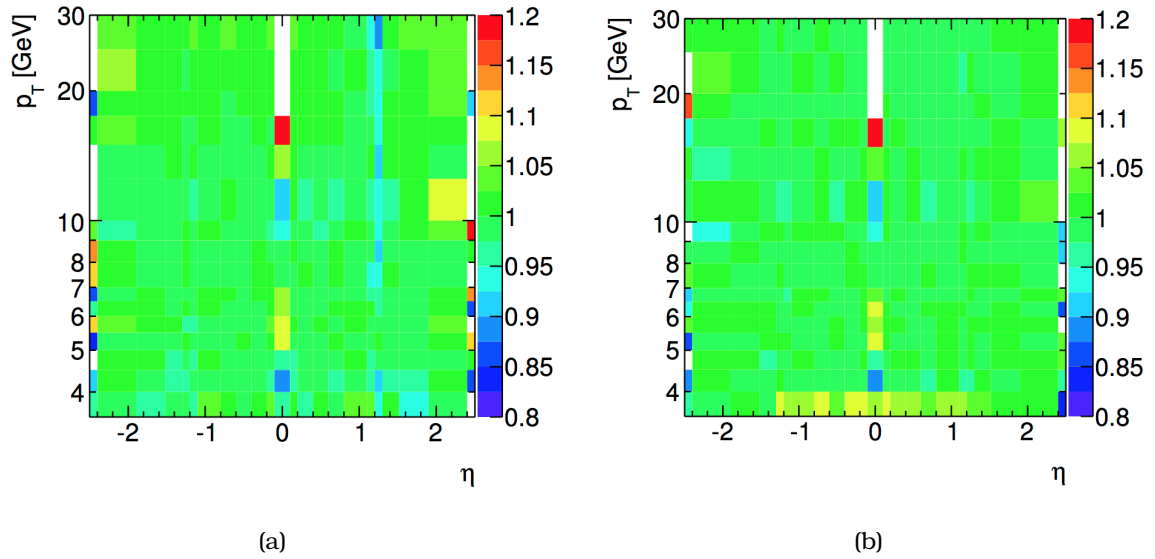
Figure 3.8: *Scale factors for (a) CB and (b) ST muons.*

(a)   (b)
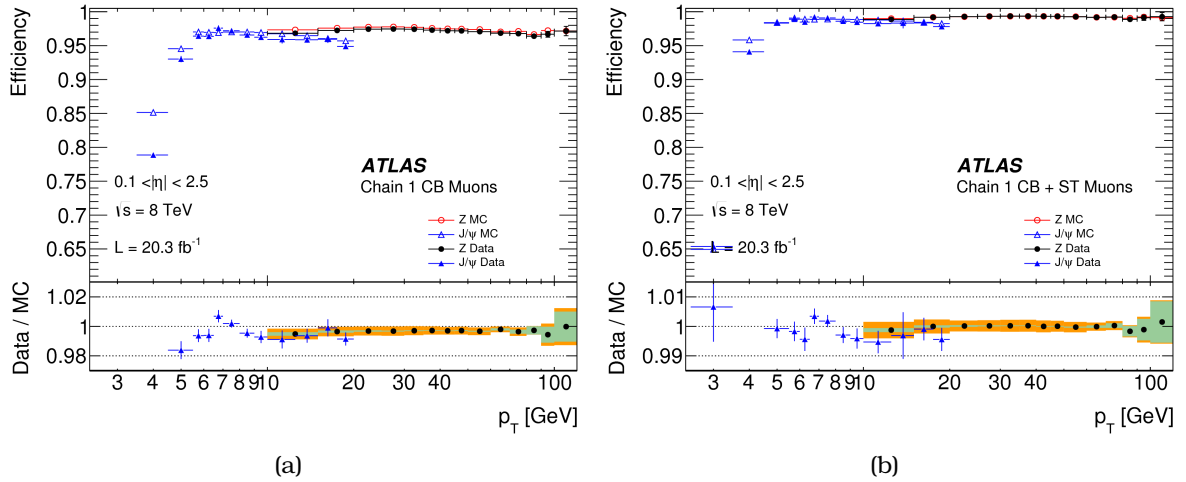
Figure 3.9: *Muon reconstruction efficiency results using J/ψ (blue points) and Z (black and red points) di-muon decays as a function of η and p_T.*

Chapter 4

Production of prompt and non-prompt J/ψ mesons in association with a Z boson

4.1 Introduction

There are two ways that a J/ψ meson can be produced in association with a Z boson in the Standard Model. First, it can be produced with a prompt QCD process and second, through a subsequent decay of a b-hadron into a J/ψ (non-prompt). The associated production of Z bosons with J/ψ mesons can further be divided into two ways, where the two particles occur from the interaction of a single pair of partons in the colliding protons and from the interaction of two separate pairs of partons, referred as DPS (see section 1.10). The study of additional observables in the production of prompt J/ψ mesons can give valuable information in the formation mechanisms of the $c\bar{c}$ state (see section 1.3). Theory predictions vary, suggesting a higher contribution from CO processes compared to CS, as described in section 1.6.

The analysis described in the sections below, presents the first observation for the associated production of Z bosons with prompt and non-prompt J/ψ mesons. Both Z and J/ψ are experimentally favoured, due to their leptonic decay which are essentially background free and their masses can be fully reconstructed. For the decay of the Z, the di-electron and di-muon decay modes are considered and for the J/ψ only the di-muon. Di-electron decays of the J/ψ meson were not considered since the $J/\psi \rightarrow e^+e^-$ mode features larger backgrounds and more strict kinematic cuts that would cause an order of magnitude smaller J/ψ yield. The analysis uses pp collision data at $\sqrt{s} = 8\,\text{TeV}$.

4.2 Data and MC samples

Data used in this analysis are collected during 2012 and included in the Egamma and Muon stream of DAOD datasets. An algorithm based in the ATHENA framework was developed, which matches two pairs of muons or a pair of muons and a pair of electrons (leptons in pair required to have opposite charges) into two separate vertices. The $\chi^2/\text{n.d.f}$ requirement is very loose. Although, looking at the selected events, all signal candidates are included in the $\chi^2/\text{n.d.f} < 10$ region. Events that a lepton is

shared between the two reconstructed vertices are rejected. Events where two such vertices are successfully reconstructed, their invariant mass is between $2.0 - 4.0\,\mathrm{GeV}$ and $66 - 116\,\mathrm{GeV}$ and at least one of the four leptons is matched with the lepton that fired the trigger in the event, are saved and marked as signal candidate events.

A second algorithm was developed for selecting the inclusive Z events. It follows closely the associated production code, but without requiring the second vertex to be reconstructed. This algorithm was run over the Muon and Egamma AOD files, since the DAOD datasets include a-priori the requirement that a di-muon vertex must be reconstructed and its invariant mass to be within $1.5 - 15\,\mathrm{GeV}$.

At the time that this study started, there was no option available within the ATLAS software infrastructure of simulating the associated production of Z bosons with either prompt or non-prompt J/ψ mesons. To overcome this, a feature of Pythia8 was used [84] that enables the production of the Z boson as a second hard process, along with the J/ψ production. Since there are two independent hard scatters that produce the two final state particles, the Z and the J/ψ have no correlation between them, resulting in a purely DPS sample. This is confirmed by the difference of the azimuthal angle between the Z and the J/ψ ($\Delta\phi$), where a no dependence indicates uncorrelated production of the two particles (see figure 4.1).
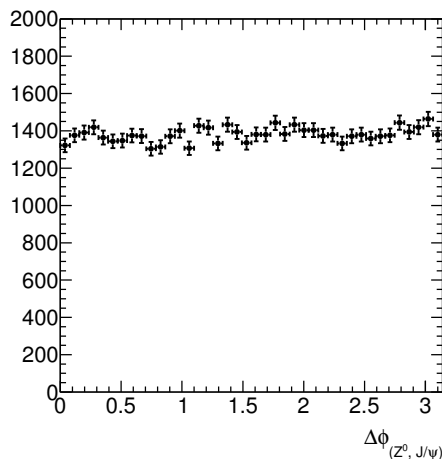
Figure 4.1: *Azimuthal openening angle between the Z boson and the J/ψ meson ($\Delta\phi(Z, J/\psi)$), produced from two independent hard scatters. Since the two particles are produced from two pairs of interacting partons, they show no dependence over $\Delta\phi(Z, J/\psi)$.*

This option was used in order to create MC datasets for the $Z \to \ell^+\ell^-$ ($\ell = \mu, e$) and $J/\psi \to \mu^+\mu^-$ associated production. Samples where the J/ψ is a subsequent decay of a b-hadron were also generated, for the $Z+$ non-prompt J/ψ production studies.

4.3 Selections

The muon and track reconstruction is described in section 3.2. In this analysis, since the trigger requirement is satisfied from Z decay products, the J/ψ muons requirements

can be rather loose. Due to this ability, the type of muons used for the J/ψ reconstruction are either combined or segment-tagged. Muons originating from Z decays are required to be combined.

The electrons originating from the Z boson are reconstructed from energy depositions in the electromagnetic calorimeter after they are matched to a track in the inner detector. The pattern recognition algorithm and global χ^2 fit takes into account energy losses and candidate electrons are further fitted with a Gaussian-sum filter to further account for bremsstrahlung energy losses [85]. In this analysis, electrons matching the Loose++ and Medium++ electrons are used [86]. The quality requirements for these types of electrons are summarised in table 4.1.

Table 4.1: *Selections used in the Loose++ and Medium++ electron identification criteria in the central region of the detector* ($|\eta| < 2.47$).

Category	Description
Loose++	
Acceptance	$|\eta| < 2.47$
Hadronic leakage	Ratio of E_T in the first layer of the hadronic calorimeter ($|\eta| < 0.8$ and $|\eta| > 1.37$) or E_T in whole hadronic calorimeter ($|\eta| < 0.8$ and $|\eta| > 1.37$) to E_T of the EM cluster
Middle layer of the EM	Ratio of energies in $e \times 7$ cells over 7×7 cells
	Lateral width of the shower
Front layer of the EM	Total shower width
	Ratio of the energy difference associated with the largest and second largest energy deposits in the cluster over their sum
Track quality and track-cluster matching	Number of hits in the pixel detector (≥ 1)
	Number of hits in the pixel and SCT detectors (≥ 7)
	$\Delta\eta$ between the cluster position in the first layer and the extrapolated track (< 0.015))
Medium++ (includes Loose++)	
Track quality and track-cluster matching	Number of hits in the b-layer > 0 for $|\eta| < 2.01$
	Number of pixel hits > 1 for $|\eta| < 2.01$
	Transverse impact parameter $5\,\text{mm}$
	Tighter $|\Delta\eta|$ cut (< 0.005)
TRT	Loose cut on TRT high-threshold fraction

The "All_Good" GRL, after the recommendation of the data quality group is applied to all data. The trigger used requires at least one lepton with $p_T > 24\,\text{GeV}$. These are high efficiency triggers in collecting $Z \to \ell^+\ell^-$ and also not pre-scaled during 2012 data taking. The total integrated luminosity after the trigger requirement and quality selections is $20.3\,\text{fb}^{-1}$. At least one leg of the Z must match to a trigger object that fired the trigger and the matched leg must have $p_T > 25\,\text{GeV}$, must be Medium++ in case of

electrons and for muons, the η is required to be $|\eta| < 2.4$.

Incompletely built events, events with LAr errors and events where the electrons fail to pass the good Object Quality (OQ) criteria are rejected.

Non-prompt leptons from the decay of heavy quarks and fake electrons form mis-identified jets (charged hadrons or photon conversions) are excluded using isolation requirements based on calorimetric and tracking information. The scalar sum of the transverse momenta, $\sum p_\mathrm{T}$, of inner detector tracks inside a cone of size $\Delta R = 0.2$ around the lepton is required to be no more than 15% of the lepton's p_T.

For the cross-section ratio calculation a cut on the Z mass of $\pm 10\,\mathrm{GeV}$ around the PDG mass of the Z ($81.1876 - 101.1876\,\mathrm{GeV}$) is applied. The selections for leptons decaying from the Z and the J/ψ are listed in tables 4.2, 4.3 and 4.4

Table 4.2: $Z \rightarrow \mu^+\mu^-$ *selections*

Triggers	EF_mu24i_tight or EF_mu36_tight
Transverse momentum	$p_\mathrm{T}^\mu > 15$ GeV
Isolation	$\sum p_\mathrm{T}^{\mathrm{cone}}(0.2)/p_\mathrm{T}^l < 0.15$
Pseudorapidity	$|\eta| < 2.5$
$m_{\mu^+\mu^-}$	$66 - 116$ GeV
Fit to vertex	use combined measurement

Table 4.3: $Z \rightarrow e^+e^-$ *selections*

Electron type	Loose++
Triggers	EF_e24vhi_medium1 or EF_e60_medium1
Transverse momentum	$p_\mathrm{T}^e > 15$ GeV
Isolation	$\sum p_\mathrm{T}^{\mathrm{cone}}(0.2)/p_\mathrm{T}^l < 0.15$
Pseudorapidity	$|\eta| < 2.47$
m_{ee}	$66 - 116$ GeV (using cluster energy)
Fit to vertex	using GSF track + correction from cluster energy

Table 4.4: $J/\psi \rightarrow \mu^+\mu^-$ *selections*

At least one muon	combined
Transverse momentum	$p_\mathrm{T} > 2.5(3.5)\,\mathrm{GeV}$
	$|\eta| > 1.3\,(|\eta| < 1.3)$
	at least one muon with $p_\mathrm{T} > 4\,\mathrm{GeV}$
Pseudorapidity	$|\eta| < 2.5$
$m_{\mu^+\mu^-}$	$2.6 - 3.6$ GeV
Fit to vertex	using ID measurement

The two final state particles are reconstructed from di-lepton vertices, where for the J/ψ candidate, the ID information is used, for the $Z \rightarrow \mu^+\mu^-$, combined tracks, and for the $Z \rightarrow e^+e^-$, ID tracks, corrected by the Gaussian Sum Filter is used. In order to

reduce contamination from pileup (two separate proton-proton collisions forming a Z and a J/ψ) studies were performed for the separation of the two vertices.

Several possible methods to reduce the contamination from pileup events have been considered. These studies were based on the two-process $Z + J/\psi$ MC samples. Possible selection requirements include:

- both J/ψ and Z have the shortest flight distance from the same primary vertex (a_0);

- both J/ψ and Z have the shortest flight distance in z from the same primary vertex (a_0^z);

- both J/ψ and Z vertices are separated by a minimum distance;

- both J/ψ and Z vertices are separated by a minimum distance in z;

- tracks for the candidates have a minimum d_0, z_0 with respect to the status=0 primary vertex.

These selection variables are applied to $Z \rightarrow \mu^+\mu^- + J/\psi \rightarrow \mu^+\mu^-$ (shown in figure 4.2(a)) and $Z \rightarrow e^+e^- + J/\psi \rightarrow \mu^+\mu^-$ MC (shown in figure 4.2(b)). The x-axis of these figures follow the format: "A, B", where "A" can be pass or fail and "B" is the requirement on the sample. The requirement can be either: "both signal", "Z signal and J/ψ background (fake)", "Z background and J/ψ signal" and "both background".

(a)   (b)
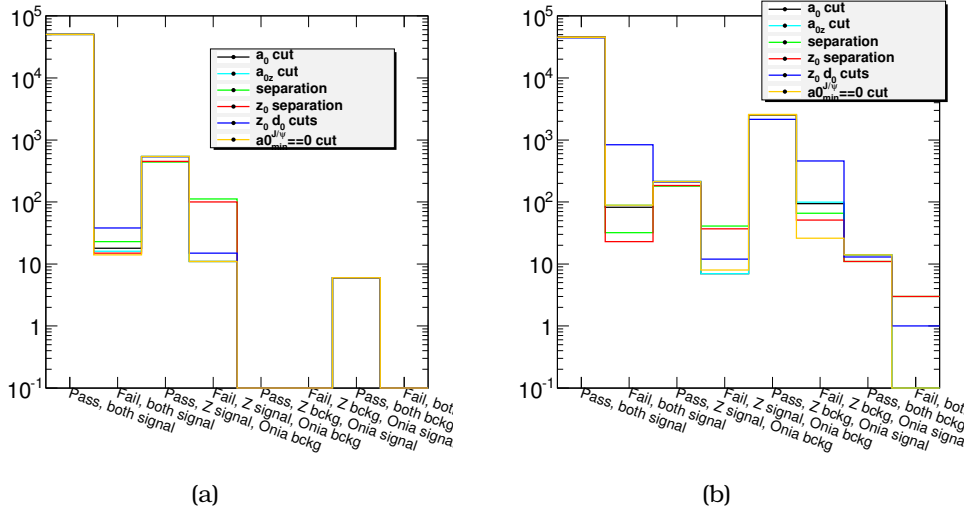
Figure 4.2: *Events satisfying a variety of requirements for the separation of the Z and J/ψ reconstructed vertices. For each requirement, the combinations of "true" or "fake" particles are compared for (a) $Z(\rightarrow \mu^+\mu^-) + J/\psi(\rightarrow \mu^+\mu^-)$ and (b) $Z(\rightarrow e^+e^-) + J/\psi(\rightarrow \mu^+\mu^-)$.*

The aim is to optimise mainly the ratio of the first two bins. The first bin shows the number of true signal events that pass the cuts and the second shows the events that do not. The performance of the requirement against fake candidates was also checked.

Based on this study, the z_0 separation of the J/ψ and Z vertices was chosen as the discriminant variable. Its value was chosen by repeating the same exercise, as described above, but by varying the values of Δz_0.

(a)

(b)
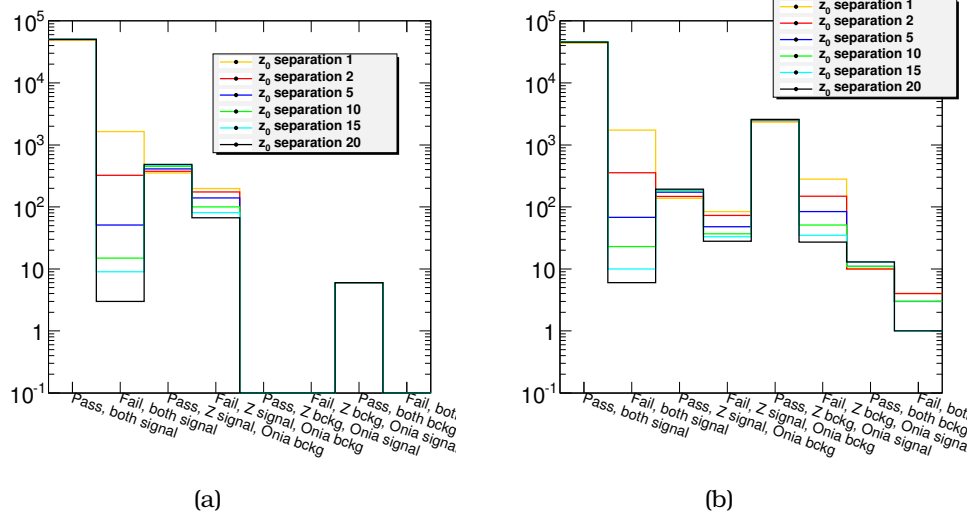
Figure 4.3: *Various z_0 cuts applied on $Z + J/\psi$ MC. For each requirement, the combinations of "true" or "fake" particles are compared for (a) $Z(\to \mu^+\mu^-) + J/\psi(\to \mu^+\mu^-)$ and (b) $Z(\to e^+e^-) + J/\psi(\to \mu^+\mu^-)$.*

The chosen value of Δz_0 was $10\,\text{mm}$. This choice was chosen based on the tests for the contamination of fakes (see figure 4.3) and bearing in mind that a larger value will result in more background events from pileup and DPS. Finally, a strict Δz_0 cut will create biases in the non-prompt J/ψ yield, as it is described in section 4.11.4.

The total number of events, after the application of the selection described above, is summarised in table 4.5 and visualised in figure 4.4(a).

Table 4.5: *Number of events for $Z \to \ell^+\ell^-$ and $J/\psi \to \mu^+\mu^-$ reported seperately for $\ell = \mu$ and $\ell = e$ and the two rapidity bins of the analysis.*

Mode	All	$|y_{J/\psi}| < 1.0$	$1.0 < |y_{J/\psi}| < 2.1$
$Z \to \mu^+\mu^- + J/\psi \to \mu^+\mu^-$	178	84	94
$Z \to e^+e^- + J/\psi \to \mu^+\mu^-$	186	88	98
$Z \to \ell^+\ell^- + J/\psi \to \mu^+\mu^-$	364	172	192

In figure 4.4(a) the correlation plot of the reconstructed mass of the two formed vertices is displayed. The bulk of the data is gathered in the Z and J/ψ mass region, indicating the associated production of these two particles.

The J/ψ candidates are further plotted in figure 4.4(b) in mass and pseudo-proper time projections. The pseudo-proper time of the J/ψ candidates is the variable used to distinguish prompt and non-prompt contributions, and is defined as

$$\tau = \frac{L_{xy} m_{\mathrm{PDG}}^{J/\psi}}{p_{\mathrm{T}}^{J/\psi}}$$

with $L_{xy} = \boldsymbol{L} \cdot \boldsymbol{p}_{\mathrm{T}}^{J/\psi} p_{\mathrm{T}}^{J/\psi}$, $\boldsymbol{L}$ is the vector from the primary vertex to the J/ψ decay vertex, $m_{\mathrm{PDG}}^{J/\psi}$ is the world-average mass of the J/ψ meson, $\boldsymbol{p}_{\mathrm{T}}^{J/\psi}$ the transverse momentum of the J/ψ and $p_{\mathrm{T}}^{J/\psi} = |\boldsymbol{p}_{\mathrm{T}}^{J/\psi}|$ its magnitude. The mass variable $m_{\mathrm{PDG}}^{J/\psi}$ was preferred compared to the reconstructed value, $m_{\mathrm{VTX}}^{J/\psi}$, in order to have uncorrelated mass and lifetime information.
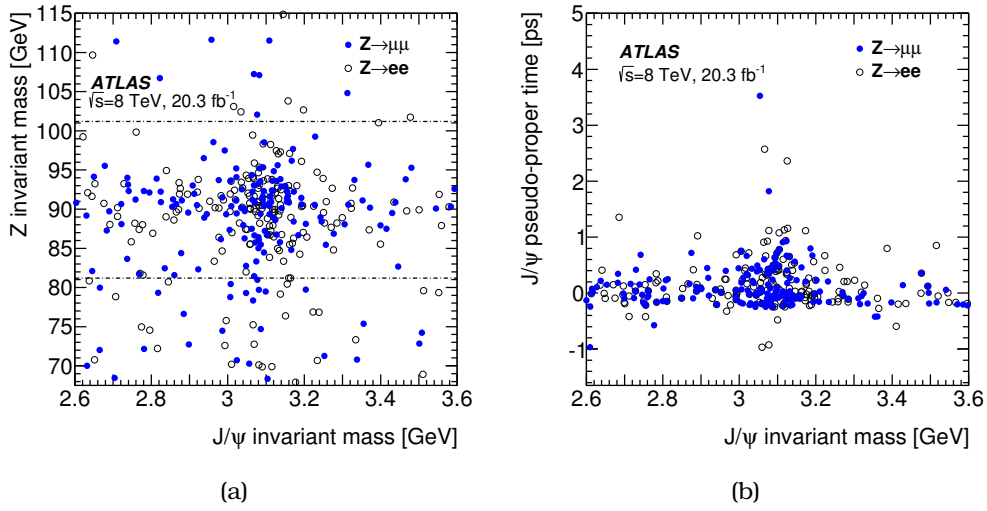
Figure 4.4: *Selected Z + J/ψ candidates in (a) Z boson mass versus J/ψ boson mass, with ℓ = e, μ and (b) J/ψ pseudo-proper time versus J/ψ invariant mass, discussed in Section 4.3. Z boson candidates decaying to muons are shown with full circles and to electrons with empty circles. The horizontal dotted lines indicate the signal region considered in the analysis.*

4.4   Event displays

Using ATLANTIS [87] software, two events, a $Z \to e^+ e^-$ and $J/\psi \to \mu^+ \mu^-$ and $Z \to \mu^+ \mu^-$ and $J/\psi \to \mu^+ \mu^-$ are shown in figures 4.5 and 4.6 respectively.
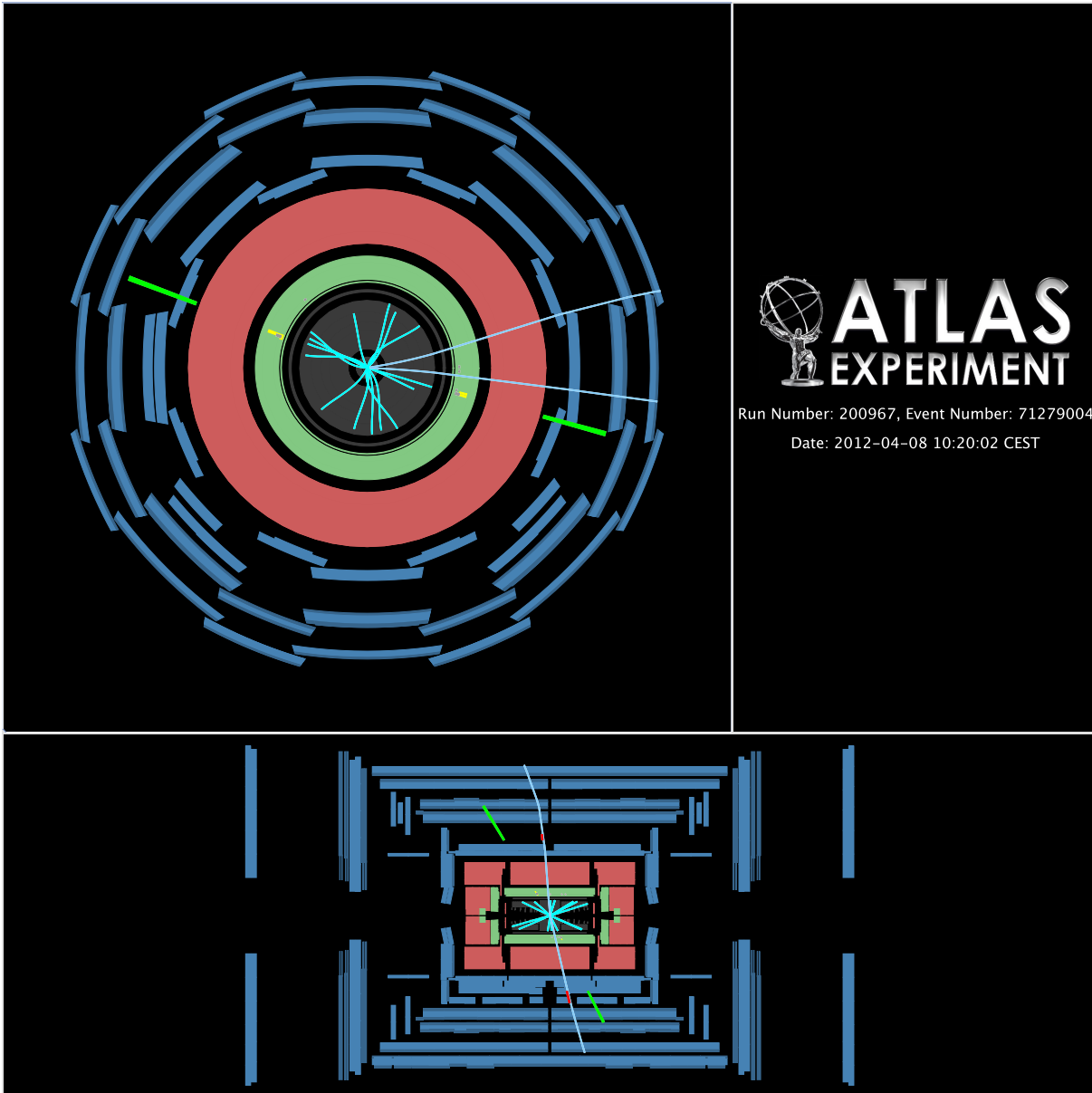
Figure 4.5: *The main event display for event 71279004 in run 200967. Z electrons have $p_T^{e_1} = 41\,\text{GeV}$, $p_T^{e_2} = 36\,\text{GeV}$ and $\eta^{e_1} = -0.6$, $\eta^{e_2} = 0.5$ (e_1 pointing at 10 o'clock and e_2 at 4 o'clock). J/ψ muons have $p_T^{\mu_1} = 9\,\text{GeV}$, $p_T^{\mu_2} = 16\,\text{GeV}$ and $\eta^{\mu_1} = -0.1$, $\eta^{\mu_2} = 0.2$ (μ_1 pointing at 2 o'clock and μ_2 at 3 o'clock). The invariant mass of the Z boson candidate is found to be $87.2\,\text{GeV}$ and J/ψ $3.1\,\text{GeV}$.*
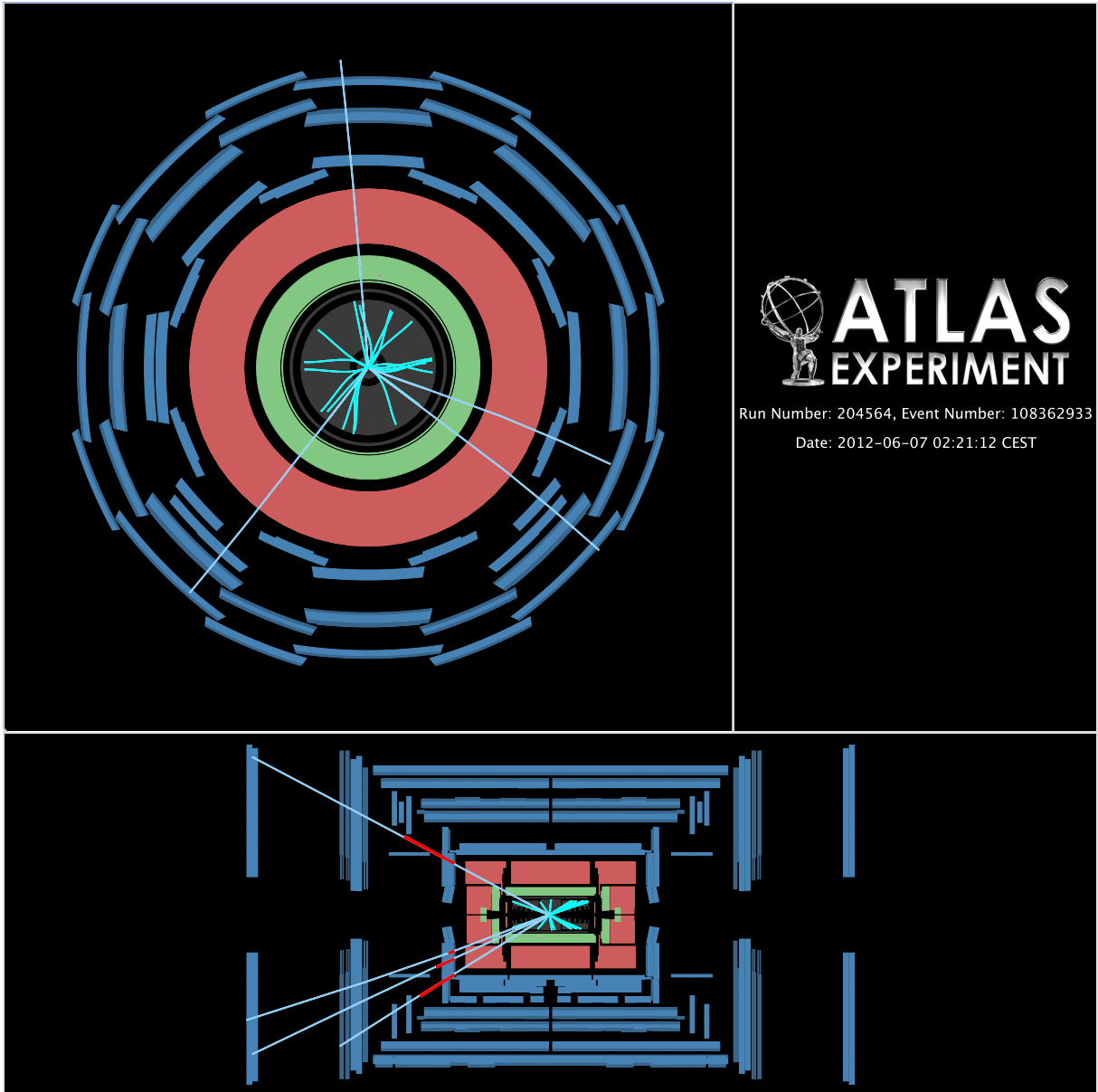
Figure 4.6: *The main event display for event 108362933 in run 204564. Z muons have $p_T^{\mu_1} = 60\,\text{GeV}$, $p_T^{\mu_2} = 17\,\text{GeV}$ and $\eta^{\mu_1} = -0.4$, $\eta^{\mu_2} = -2.2$ (μ_1 pointing at 1 o'clock and μ_2 at 8 o'clock). J/ψ muons have $p_T^{\mu_3} = 7\,\text{GeV}$, $p_T^{\mu_4} = 7\,\text{GeV}$ and $\eta^{\mu_3} = 1.8$, $\eta^{\mu_4} = 1.4$ (μ_3 pointing at 6 o'clock and μ_4 at 6 o'clock). The invariant mass of the Z boson candidate is found to be $85.0\,\text{GeV}$ and J/ψ $3.1\,\text{GeV}$.*

4.5   *J/ψ* **yield extraction**

The invariant mass spectrum of the $J/\psi \to \mu^+\mu^-$ candidates consist of four components. First component is made from the *J/ψ* candidates that are formed from the *pp* interaction. These candidates create a peaking structure in the di-muon invariant mass (see figure 4.7(a) left) and have very small pseudo-proper times (figure 4.7(a) right). The second component is made from $b\bar{b}$ production, where one of the *b*-quarks forms a *b*-hadron, which subsequently decays into a *J/ψ* meson. This still contributes to the *J/ψ* peak, since they are real *J/ψ*, but has longer pseudo-proper times. The other two components, are the prompt and non-prompt backgrounds, shown as a continuum in the di-muon invariant mass spectrum.

The four components are distinguished by a two-dimensional unbinned maximum likelihood fit performed on both invariant mass and pseudo-proper time. The di-muon invariant mass is modelled with a double Gaussian function, both for prompt and non-prompt signal components and an exponential function for the backgrounds.

The pseudo-proper time of the signal component is modelled using a double Gaussian distribution. A double-sided exponential convolved with the prompt signal function (in order to account for resolution effects) is used for the prompt background. A single-sided exponential convolved with the prompt signal function is used for the non-prompt signal and for the non-prompt background the sum of a single-sided and a double-sided exponential convolved with the signal function is used.

Due to the limited statistics, an inclusive *J/ψ*, made from 100 000 events, selected with the same criteria applied in the main analysis, is used simultaneously in the fit. The shape-related parameters in the fit are linked between the two samples, so the rich statistics inclusive sample will drive the associated production sample to form an accurate description.

The fit is performed in two subsamples, based on the rapidity of the *J/ψ*. This is done, so the two mass resolutions in the $|y_{J/\psi}| < 1.0$ and $1.0 < |y_{J/\psi}| < 2.1$ bins can be better modelled. This difference is created from increased multiple scattering and the decrease of the magnetic field integral at high rapidity. The projections of the di-muon invariant mass and pseudo-proper time of the fits performed in the two rapidity bins, in both samples are shown in figure 4.7 for $|y_{J/\psi}| < 1.0$ and in figure 4.8 for $1.0 < |y_{J/\psi}| < 2.1$.

4.5.1   **Fit model cross-checks**

Since the fit model used for the prompt and non-prompt *J/ψ* meson separation is very complicated, and drives the final result of the analysis, a series of checks were performed to validate it.

Validation of the fit procedure

The validation of the fit model was done using inclusive *J/ψ* MC samples. The same fit model used in the analysis was applied in the following four MC samples:

- prompt *J/ψ* MC sample - rich statistics;

- non-prompt *J/ψ* MC sample - rich statistics;
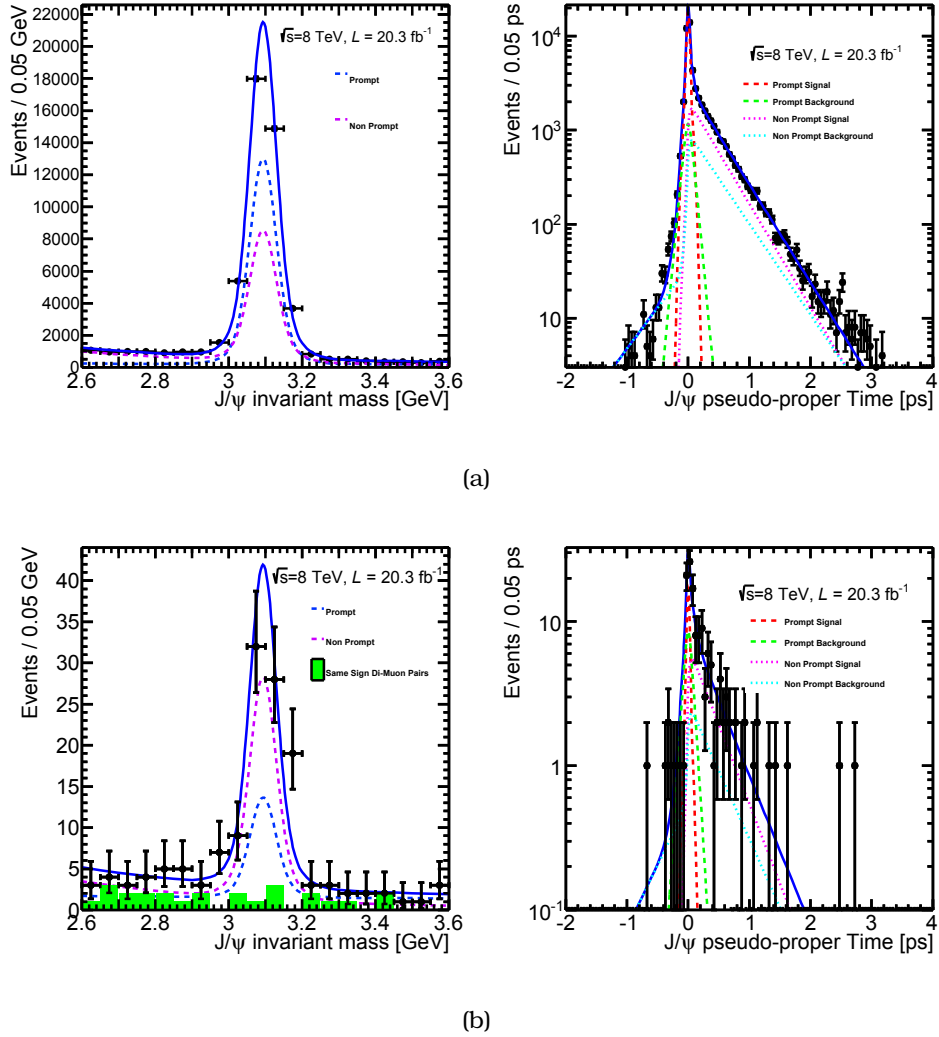
Figure 4.7: *(a) Fit results on the inclusive J/ψ sample. (b) Fit results on the associated production J/ψ sample. Both results shown are for $|y_{J/\psi}| < 1.0$.*

- mixture of the two samples above;

- mixture of the two samples above with reduced "data-like" statistics;

These samples cover a variety of possible prompt - non-prompt combinations, from prompt-only to non-prompt only datasets. The last sample mentioned in the list above was created in order to be closer to the number of events observed in the analysis.

From these fits the prompt - non-prompt ratio is extracted and compared with the truth ratio. Although all four MC samples are signal only (either prompt or non-prompt), the components of the fit model that describe the background were not excluded from the fit. In all cases, as shown in figure 4.9, the true ratio (solid lines) was reproduced within uncertainties (data points). More details including all fit projections are available here [88].

(a)

(b)
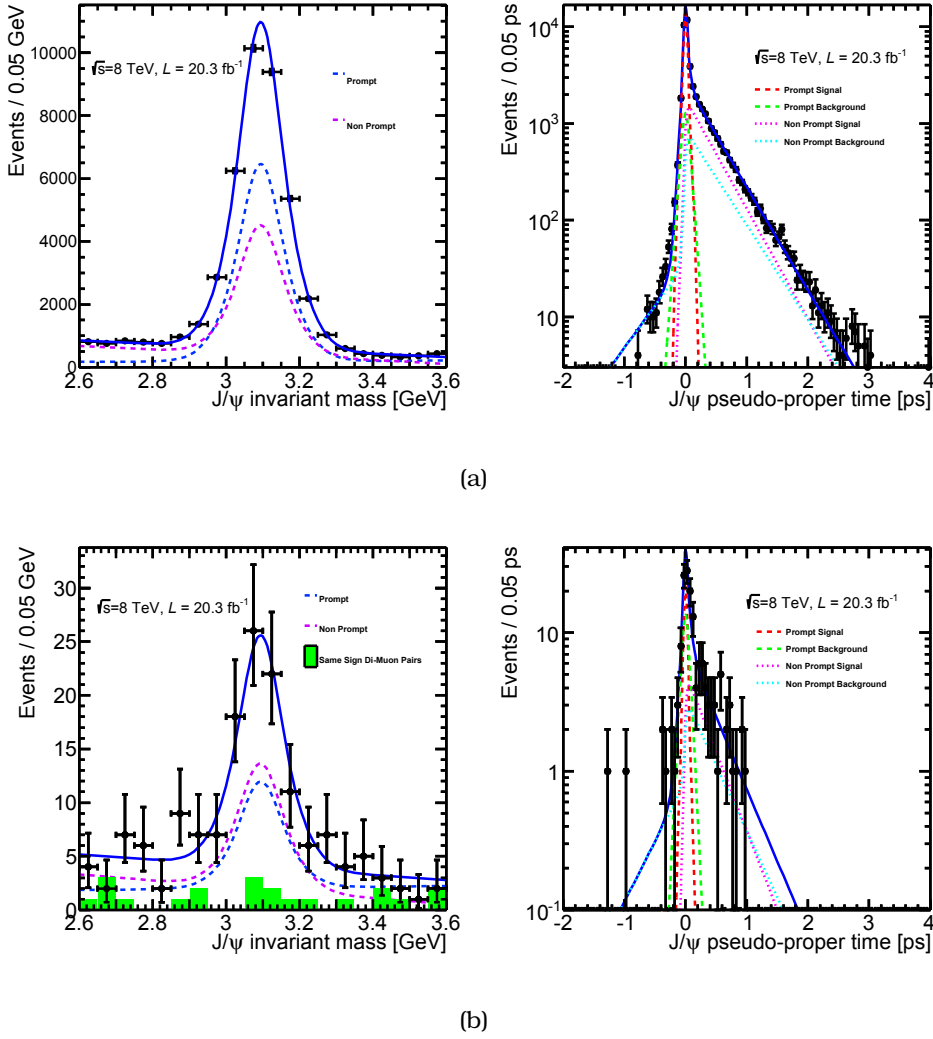
Figure 4.8: *(a) Fit results on the inclusive J/ψ sample. (b) Fit results on the associated production J/ψ sample. Both results shown are for $1.0 < |y_{J/\psi}| < 2.1$.*

Bias check

A second check performed was to verify that the yields returned from the fit were unbiased and their statistical uncertainty properly calculated. For this check, "toy" MC events were generated using the fit model. Each set is then fitted with the fit model and the variable

$$\text{pulls} = \frac{x_{\text{obs}} - x_{\text{input}}}{\sigma(x)}$$

is extracted, where x_{obs} is the fitted value of the parameter, x_{input} is the parameter value used in the generation and $\sigma(x)$ the error on x extracted from the fit.

Pulls distribution must be gaussian-like. In order for the uncertainty returned from the fit to be reliable, 67% of the fitted values should lie within one standard deviation
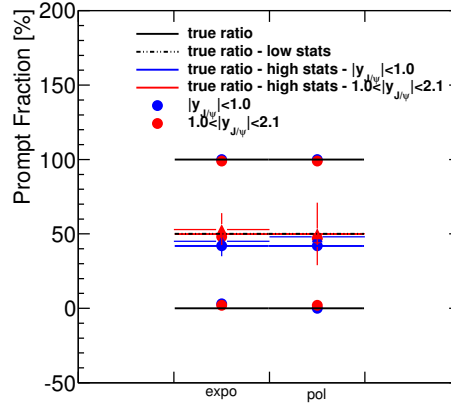
Figure 4.9: *Input and fitted prompt fractions for prompt only, non-prompt only and mixed sample MC.*

of the generated value. If the gaussian is not centred at 0, the yield extraction is biased and if the width is less than unity then the error is underestimated, and if it is greater than 1 then the error is overestimated.

Results for both prompt and non-prompt yield extraction for the first rapidity bin are illustrated in figure 4.10. The pulls are fitted with a gaussian, where for each case the fitted gaussian's mean and width is shown within. The mean of the gaussians vary between $0.00 - 0.02$ and the width between $0.99 - 1.02$ which indicates an unbiased yield extraction.

Fit parameter correlation

A further check for biases is to examine potential correlations of the fit parameters. An $n_{\mathrm{par}} \times n_{\mathrm{par}}$ matrix reflecting the correlations between the fit model parameters is shown in figure 4.11.

There is a correlation between the parameters of the fit function that describes the mass, mostly due to the fact that a single gaussian would be enough to describe the data, since resolution differences in the invariant mass changes radically in the forward rapidity. Indeed, as figure 4.11(b) show, the correlation is absent in the second rapidity bin, as there the double gaussian is necessary in modelling the data in this bin.

4.5.2   Significance calculation

The p-value and significance are calculated using pseudo-experiments. The background-only and background-plus-signal hypotheses are fitted to Poisson-fluctuated yields generated from the prompt and non-prompt J/ψ and combinatoric yields. The number of occurrences that the background will fluctuate upwards, to reach the yield measured from data (see figure 4.12) after correcting for the pileup contamination, are counted.

From the two rapidity bins we extract two individual significance levels $p_1^{\mathrm{value}} = \alpha_1$ and $p_2^{\mathrm{value}} = \alpha_2$. Since, the two significances originate from two independent tests, then
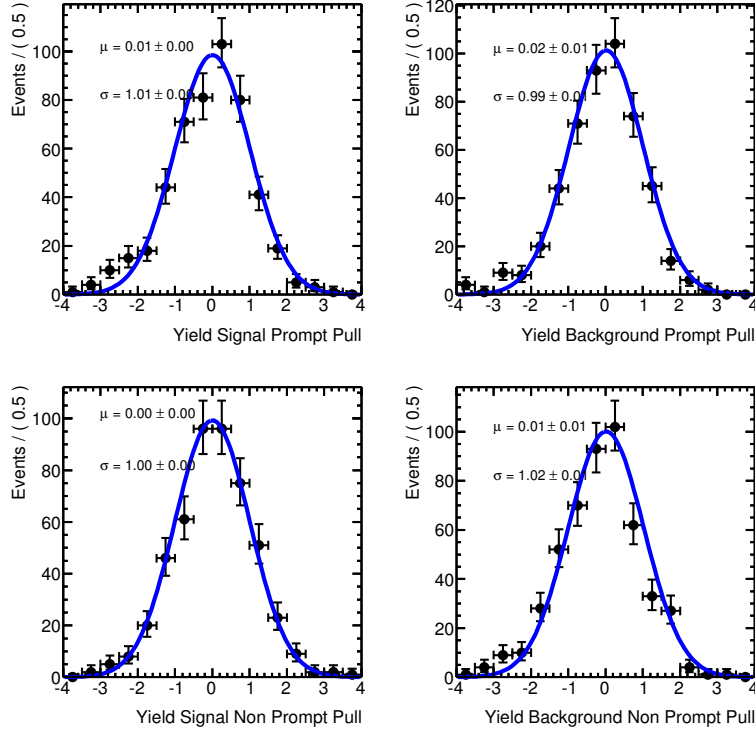
Figure 4.10: *Pull distributions for the 4 components of the fit: prompt and non-prompt J/ψ signal, prompt and non-prompt J/ψ background.*

(a) (b)
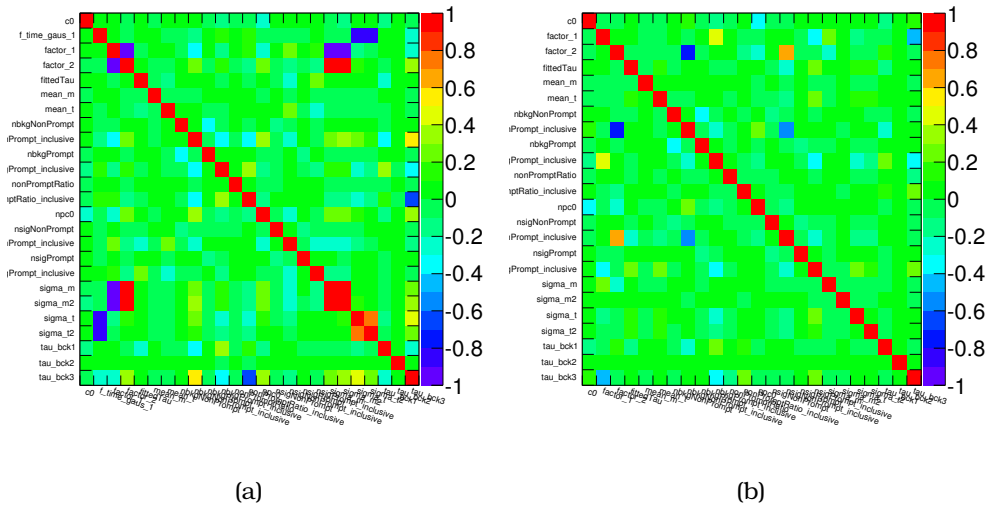
Figure 4.11: *Correlation matrix of the parameters from the fit for the (a) first and (b) second rapidity bin.*

the overall significance level p^{value} could be given by the product $\alpha = \alpha_1 \alpha_2$, since the probability of finding simultaneously $p_1^{\text{value}} \leq \alpha_1$ and $p_2^{\text{value}} \leq \alpha_2$ is $\alpha_1 \alpha_2$. But, although
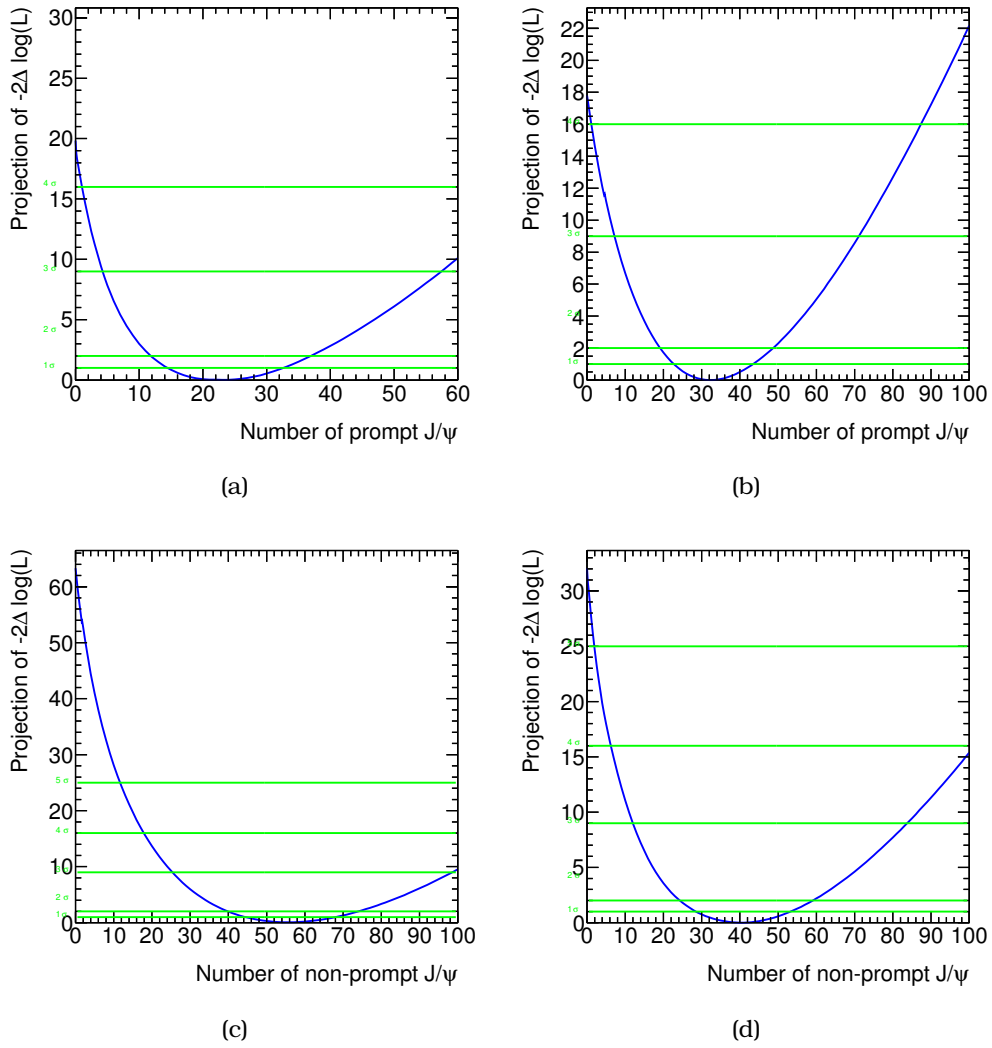
Figure 4.12: *The profile likelihood ratio for the Z + (a), (b) prompt and (c), (d) non prompt J/ψ.*

$p_1^{\text{value}} \leq \alpha_1$ and $p_2^{\text{value}} \leq \alpha_2$ is a sufficient condition for $p_1^{\text{value}} p_2^{\text{value}} \leq \alpha_1 \alpha_2$, it is not a necessary one. The probability is given by integrating the curve of p_1^{value} and p_2^{value}, given that they are uniform between 0 and 1 under the null hypothesis. This is called the Fisher formalism [89] and the formula is:

$$p^{\text{value}} = p_1^{\text{value}} p_2^{\text{value}} \left(1 - \log(p_1^{\text{value}} p_2^{\text{value}}) \right)$$

where p_1^{value} corresponds to the first rapidity bin and p_2^{value} to the second. The significance is calculated using the formula

$$\text{significance} = \sqrt{2} \, \text{erf}^{-1} \left\{ 1 - 2 p_1^{\text{value}} p_2^{\text{value}} \left(1 - \log(p_1^{\text{value}} p_2^{\text{value}}) \right) \right\}$$

The results of the fit procedure, together with the significances are summarised in table 4.6.

Table 4.6: *Significances on each rapidity bin.*

Process	$\|y_{J/\psi}\| < 1.0$ ($\pm$ stat. $\pm$ syst.)	$1.0 < \|y_{J/\psi}\| < 2.1$ ($\pm$ stat. $\pm$ syst.)	Total
Prompt signal	$24 \pm 6 \pm 2$	$32 \pm 8 \pm 5$	56 ± 10
Non Prompt signal	$54 \pm 9 \pm 3$	$41 \pm 8 \pm 7$	95 ± 12
Background	$61 \pm 11 \pm 6$	$77 \pm 13 \pm 7$	138 ± 17
prompt p-value - significance	1×10^{-4} - 3.7	7.5×10^{-5} - 3.8	1.5×10^{-7} - 5.1
non prompt p-value - significance	4.2×10^{-14} - 7.5	1.5×10^{-7} - 5.1	3×10^{-19} - 8.9

4.5.3 Weights for prompt and non-prompt J/ψ production

After the fit is performed, the sPlot tool is used [90] for the derivation of weights, based on the yield parameters of the fit model. sPlot tool is used, in order to determine the distribution of observables, associated with a specific contribution of the fit model, like the prompt and non-prompt J/ψ signal.

Before using sPlot, possible correlations between the discriminating variable used to separate signal from background and the distributions examined, are checked. sPlot requires these to be uncorrelated. A negligible correlation is observed between the mass, pseudo-proper time and J/ψ kinematic spectra, as shown in figure 4.13.
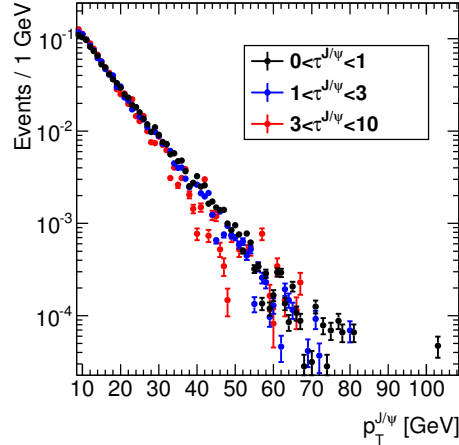
Figure 4.13: *MC study of pT spectra for non-prompt $J\psi$ in three slices of the lifetime $(0 - 1, 1 - 3, 3 - 10\,\mathrm{ps})$, which are in good agreement, as expected.*

An example of the application of weights extracted from the prompt and non-prompt J/ψ signal components of the fit model to the p_{T} spectrum of the prompt and non-prompt yields is shown in figures 4.14. Figure 4.14(a) shows the transverse momentum distribution of the prompt J/ψ mesons that are associated with a Z boson and figure 4.14(b) the non-prompt J/ψ.
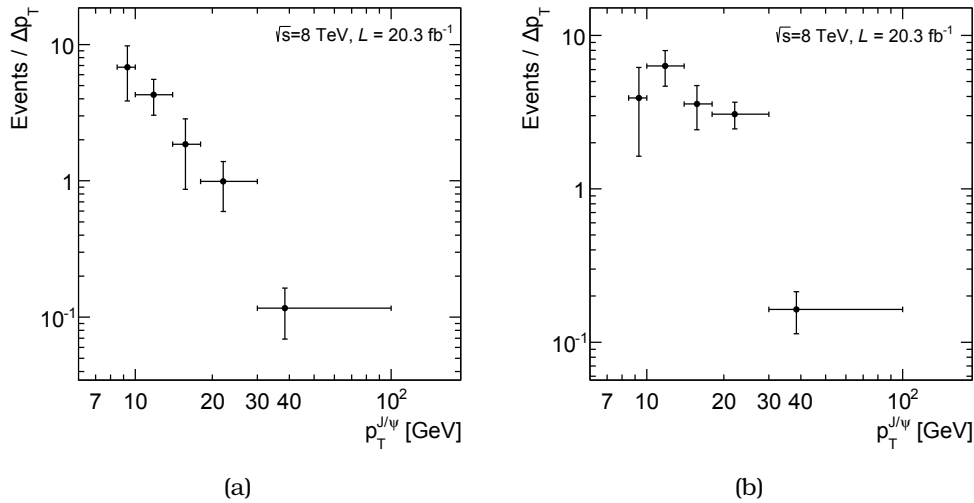
Figure 4.14: *Event yield distribution for prompt and non-prompt production of J/ψ in association with a Z boson as a function of the p_T of the J/ψ.*

4.6 Backgrounds

Apart from backgrounds for the J/ψ, that are effectively treated by the two-dimensional fit, two other backgrounds sources are examined. First the pileup, where two independent proton interactions create the Z and the J/ψ and the electroweak and QCD background, under the Z peak.

4.6.1 Pileup background

During the 2012 data taking, a large number of proton–proton collisions were occurring in a single bunch crossing. The distribution of the average number of interactions per bunch crossing is shown in figure 2.8(b). Although it is most probable that these are low momentum events with no interest, there is still a probability that these interactions can create a hard scatter.

The requirement that the Z and J/ψ reconstructed vertices are not separated by more than 10 mm in the z direction, certainly reduces that probability, but any contamination must be calculated. This requires four ingredients:

1. the mean number of pileup collisions occurring within 10 mm of a given Z vertex;

2. the spread of the beam spot in z (see figure 4.15(a));

3. the number of inclusive Z bosons;

4. J/ψ production cross-sections from pp collisions at $\sqrt{s} = 8$ TeV.

From all the above, the only component that is not available, is the J/ψ cross-sections at $\sqrt{s} = 8$ TeV. Since there is no measurement of J/ψ cross-section at this

energy, we used the FONLL package [17, 91]. Assuming that the ratio of prompt to non-prompt cross-sections is stable between 7 and 8 TeV, we use the $\sqrt{s} = 7\,\text{TeV}$ results from ATLAS [92] and non-prompt predictions from FONLL to derive the prompt cross-sections at 8 TeV (more details are included in appendix A).

To estimate the mean number of pileup collisions occurring within 10 mm of a given Z vertex, a toy MC procedure is used. First, the luminosity-weighted distribution of $\langle \mu \rangle$ (mean number of collisions per bunch crossing - figure 4.15(b)) is sampled. Each value is taken to be the mean of a Poisson distribution, from which a number of pileup vertices is sampled. To simulate the distribution in z of pile-up vertices across the beam spot, these vertices are distributed according to a Gaussian with width $48 \pm 3\,\text{mm}$ (as defined from the beam spread measurement during 2012 $\sqrt{s} = 8\,\text{TeV}$ - figure 4.15(a)). A random vertex is then named as the Z vertex. Finally, the number of additional vertices within 10 mm of the selected vertex is extracted. This procedure is repeated approximately 10 million times, and the number of additional pileup vertices is taken as the average of these events (see figure 4.15(c)).

The result of this procedure is found to be 2.3 ± 0.2 additional vertices within 10 mm of the Z vertex. The number of extra vertices is then translated to number of events for every analysis bin (see table 4.7) with the expression:

$$P_{J/\psi}^{ij} = \sigma_{J/\psi}^{ij}/\sigma_{\text{inel}},$$

where $\sigma_{J/\psi}^{ij}$ is the cross-section for J/ψ production in the respective p_{T}^{i} and rapidity y^{j} bin.

(a)

(b)

(c)
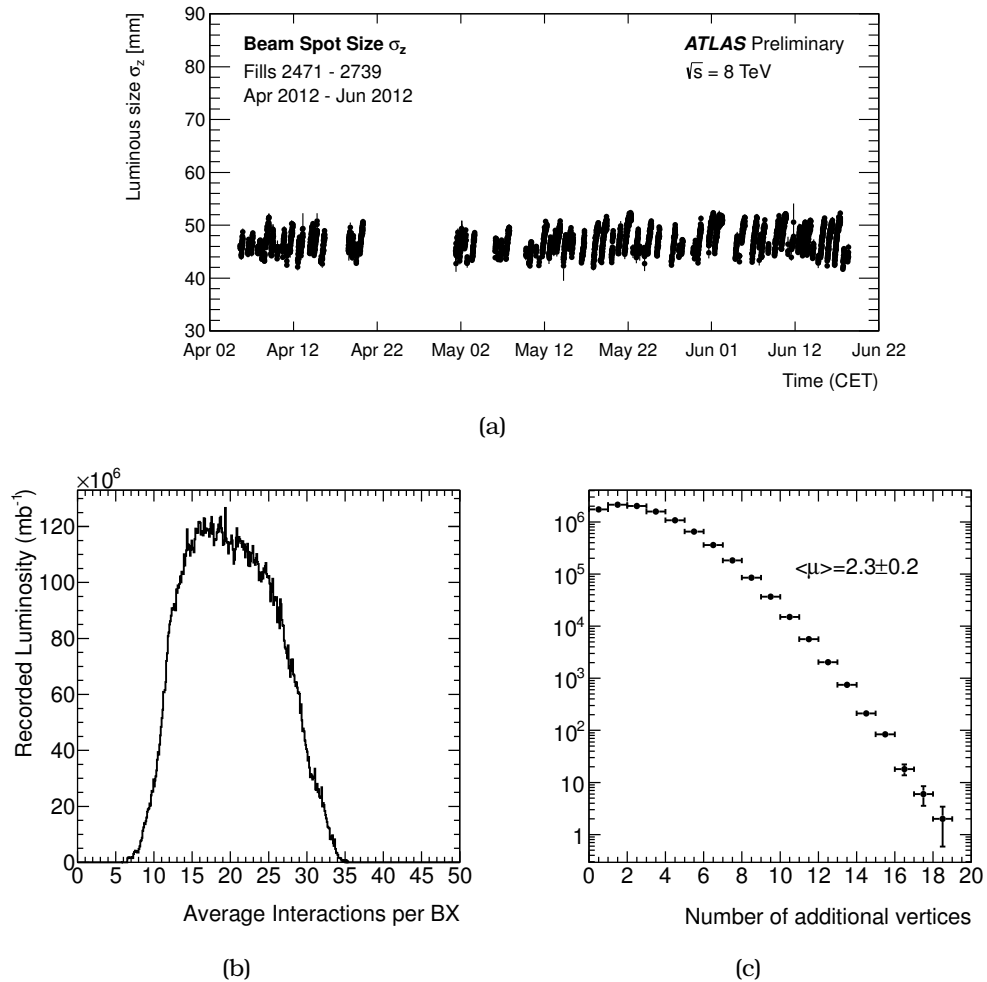
Figure 4.15: *(a) Size in z of the luminous region in ATLAS over the course of pp running in 2012 at $\sqrt{s} = 8\,\mathrm{TeV}$. The data points are the result of a maximum likelihood fit to the spatial distribution of primary vertices collected over ten minutes. Errors are statistical only. (b) The distribution of the average interactions per bunch crossing.(c) Distibution of additional vertices within $10\,\mathrm{mm}$ of the Z boson vertex.*

Table 4.7: *Pileup estimation. The first column shows the bin in $|y| \times p_T$ space of the J/ψ. The second column is (top) the computed prompt inclusive J/ψ cross-section in this kinematic bin, evaluated from the published 7 TeV ATLAS data [92], (bottom) FONLL predictions. The third column shows for a $\left(|y_{J/\psi}|, p_T^{J/\psi}\right)$-bin, the probability for a J/ψ to be produced in a pp collision in the same kinematic bin. $n_{\text{vertex}}^{\text{extra}}$ is calculated with a MC (described above), $\sigma_{\text{inel}} = 73$ mb. We take σ_{inel} to be 73 mb in order to be consistent with $\langle\mu\rangle$ distribution used to calculate N_{extra}. In principle the number of pileup events should be independent of σ_{inel}. The fourth column shows the values of the third column normalised by the size of the bin in the $|y| \times p_T$ space. The fifth column shows the average acceptance $\times$ efficiency from inclusive J/ψ in each bin, which is used to estimate the number of pileup events in our sample. The sixth column shows the expected yield of pileup events. It is calculated from the product of the Z candidates from our inclusive Z sample, times the $< \epsilon \times \mathcal{A} >$, times the $n_{\text{vertex}}^{\text{extra}}\sigma_{\text{bin}}/\sigma_{\text{inel}}$.*

	Pileup background estimation - Prompt				
Bin $|y| \times p_T$ GeV	$\sigma(\text{Prompt } J/\psi \to \mu^+\mu^-)$ (nb)	$n_{\text{vertex}}^{\text{extra}}\sigma_{\text{bin}}/\sigma_{\text{inel}}$ (10^{-8})	$\frac{1}{\sigma_{\text{bin}}}\frac{d^2\sigma}{dyp_T}$ (10^{-8})	$\langle \epsilon \times \mathcal{A} \rangle$	Expected yield
$(0,1) \times (8.5,10)$	$6.16^{+2.28}_{-1.61}$	$19.41^{+7.36}_{-5.35}$	$6.47^{+2.46}_{-1.78}$	0.23	$0.73^{+0.28}_{-0.20}$
$(0,1) \times (10,14)$	$5.37^{+1.76}_{-1.27}$	$16.93^{+5.74}_{-4.26}$	$2.12^{+0.72}_{-0.53}$	0.39	$1.06^{+0.36}_{-0.27}$
$(0,1) \times (14,18)$	$1.17^{+0.33}_{-0.26}$	$3.67^{+1.10}_{-0.88}$	$0.46^{+0.14}_{-0.11}$	0.53	$0.32^{+0.09}_{-0.08}$
$(0,1) \times (18,30)$	$0.53^{+0.13}_{-0.11}$	$1.66^{+0.44}_{-0.38}$	$0.07^{+0.02}_{-0.02}$	0.65	$0.17^{+0.05}_{-0.04}$
$(0,1) \times (30,100)$	$0.027^{+0.009}_{-0.008}$	$0.178^{+0.028}_{-0.028}$	$0.007^{+0.000}_{-0.000}$	0.76	$0.01^{+0.00}_{-0.00}$
$(1,2.1) \times (8.5,10)$	$6.27^{+2.28}_{-1.58}$	$19.76^{+7.38}_{-5.27}$	$6.00^{+2.24}_{-1.60}$	0.39	$1.26^{+0.47}_{-0.34}$
$(1,2.1) \times (10,14)$	$4.85^{+1.58}_{-1.12}$	$15.27^{+5.14}_{-3.78}$	$1.74^{+0.58}_{-0.43}$	0.49	$1.21^{+0.41}_{-0.30}$
$(1,2.1) \times (14,18)$	$0.98^{+0.28}_{-0.21}$	$3.09^{+0.92}_{-0.73}$	$0.35^{+0.10}_{-0.08}$	0.63	$0.31^{+0.09}_{-0.07}$
$(1,2.1) \times (18,30)$	$0.44^{+0.11}_{-0.09}$	$1.39^{+0.36}_{-0.30}$	$0.05^{+0.01}_{-0.01}$	0.73	$0.16^{+0.04}_{-0.04}$
$(1,2.1) \times (30,100)$	$0.019^{+0.005}_{-0.005}$	$0.058^{+0.017}_{-0.016}$	$0.002^{+0.000}_{-0.000}$	0.84	$0.01^{+0.00}_{-0.00}$
Number of Z candidates in inclusive Z sample $= (16148 \pm 66) \times 10^3$					$5.24^{+1.79}_{-1.33}$

	Pileup background estimation - Non-prompt				
Bin $|y| \times p_T$ GeV	$\sigma(\text{Non} - \text{prompt } J/\psi \to \mu^+\mu^-)$ (nb)	$n_{\text{vertex}}^{\text{extra}}\sigma_{\text{bin}}/\sigma_{\text{inel}}$ (10^{-8})	$\frac{1}{\sigma_{\text{bin}}}\frac{d^2\sigma}{dyp_T}$ (10^{-8})	$\langle \epsilon \times \mathcal{A} \rangle$	Expected yield
$(0,1) \times (8.5,10)$	$2.42^{+0.86}_{-0.58}$	$7.64^{+2.79}_{-1.95}$	$2.55^{+0.93}_{-0.65}$	0.23	$0.29^{+0.10}_{-0.07}$
$(0,1) \times (10,14)$	$2.69^{+0.86}_{-0.60}$	$8.47^{+2.79}_{-2.02}$	$1.06^{+0.35}_{-0.25}$	0.39	$0.53^{+0.17}_{-0.13}$
$(0,1) \times (14,18)$	$0.84^{+0.22}_{-0.17}$	$2.63^{+0.74}_{-0.57}$	$0.33^{+0.09}_{-0.07}$	0.53	$0.23^{+0.06}_{-0.05}$
$(0,1) \times (18,30)$	$0.52^{+0.11}_{-0.09}$	$1.64^{+0.39}_{-0.32}$	$0.07^{+0.02}_{-0.013}$	0.65	$0.17^{+0.04}_{-0.03}$
$(0,1) \times (30,100)$	$0.087^{+0.014}_{-0.012}$	$0.276^{+0.049}_{-0.045}$	$0.002^{+0.000}_{-0.000}$	0.76	$0.03^{+0.01}_{-0.01}$
$(1,2.1) \times (8.5,10)$	$2.24^{+0.80}_{-0.54}$	$7.06^{+2.58}_{-1.80}$	$2.14^{+0.78}_{-0.55}$	0.39	$0.45^{+0.16}_{-0.11}$
$(1,2.1) \times (10,14)$	$2.43^{+0.77}_{-0.54}$	$7.67^{+2.53}_{-1.82}$	$0.87^{+0.29}_{-0.21}$	0.49	$0.61^{+0.20}_{-0.14}$
$(1,2.1) \times (14,18)$	$0.73^{+0.20}_{-0.14}$	$2.31^{+0.65}_{-0.50}$	$0.26^{+0.07}_{-0.06}$	0.63	$0.23^{+0.07}_{-0.05}$
$(1,2.1) \times (18,30)$	$0.44^{+0.10}_{-0.08}$	$1.38^{+0.33}_{-0.26}$	$0.05^{+0.01}_{-0.01}$	0.73	$0.16^{+0.04}_{-0.03}$
$(1,2.1) \times (30,100)$	$0.067^{+0.010}_{-0.009}$	$0.210^{+0.037}_{-0.034}$	$0.001^{+0.000}_{-0.000}$	0.84	$0.03^{+0.01}_{-0.00}$
Number of Z candidates in inclusive Z sample $= (16148 \pm 66) \times 10^3$					$2.72^{+0.86}_{-0.63}$

The total number of pileup events in the prompt component was found to be $5.2^{+1.8}_{-1.3}$ and for the non-prompt $2.7^{+0.9}_{-0.6}$ events.

4.6.2 QCD and electroweak

The estimation of the Z background is obtained using both MC models and data-driven techniques. The signal is modelled using the NLO generator POWHEG (R1556) [93, 94, 95], interfaced to PYTHIA (8.160) [96]. The same generator was used to study Drell–Yan contributions away from the Z peak and $Z \to \tau\tau$ or $W \to \ell\nu_\ell$ backgrounds. The parton density function used, is the CT10 PDF set [97], with the ATLAS AU2 tune [98]. NLO generator MC@NLO (4.03) [99, 100], interfaced to HERWIG (6.52) [101] for parton showering and JIMMY (4.31) [102] for the underlying-event modelling with the ATLAS AUET2 tune [103] and the CT10 PDFs is used for top quark processes (like $t\bar{t}$ or single top production). ACERMC (3.8) [104] generator, using the CTEQ6L1 PDF set [105] and interfaced to PYTHIA (6.42) [106] is used to model for single-top Wt processes. Finally, HERWIG (6.52) and Jimmy generators with the ATLAS AUET2 tune and the CTEQ6L1 PDF set are used for modelling the di-boson production (WZ, WW and ZZ). For all the above, the ATLAS simulation infrastructure [68] based on the GEANT4 toolkit [73] was used to model the detector response.

The trigger and selection criteria of the main analysis is applied to the MC samples mentioned above, with the only difference being a wider Z invariant mass range ($20 < m_z < 120\,\text{GeV}$). The number of Z bosons that pass the cuts are scaled to the same luminosity as the data and then summed to provide the total background estimate from electroweak sources (see figure 4.16).

(a)   (b)
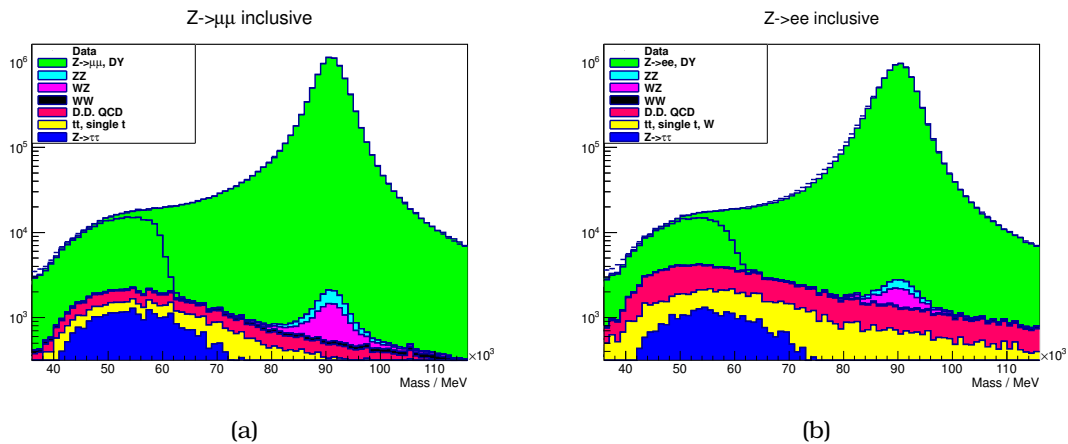
Figure 4.16: *4.16(a) Signal and background plot for $Z \to \mu^+\mu^-$ (EW bkds from MC, QCD background from data). 4.16(b) Signal and background plot for $Z \to e^+e^-$.*

A data-driven approach ("ABCD" method) is used for the multi-jet and fake lepton background estimation. Four categories are defined, based on the isolation requirement, defined in section 4.3 and the di-lepton mass. The four categories are the following:

1. $40 < m_{\ell^+\ell^-} < 60\,\text{GeV}$ and isolated leptons;

2. $40 < m_{\ell^+\ell^-} < 60\,$GeV and anti-isolated leptons;

3. $81 < m_{\ell^+\ell^-} < 101\,$GeV and isolated leptons (signal region);

4. $81 < m_{\ell^+\ell^-} < 101\,$GeV and anti-isolated leptons.

Relying in the statement that the ratio of isolated and non-isolated events is independent of $m_{\ell^+\ell^-}$ for QCD background events, the four regions are related by A/B ∼ C/D and subsequently the QCD contribution can be estimated by (A/B) × D. Before using this technique, electroweak backgrounds are estimated and subtracted from the sample. All background estimates are summarised in table 4.8.

Table 4.8: *QCD and electroweak backgrounds in the inclusive Z sample.*

	Electroweak [%]	QCD [%]	Total [%]
$Z \to \mu^+\mu^-$	0.24 ± 0.03	0.04 ± 0.17	0.28 ± 0.17
$Z \to e^+e^-$	0.34 ± 0.08	0.16 ± 0.80	0.49 ± 0.80

4.7 Double parton scattering

The DPS contribution to the $J/\psi + Z$ sample is treated as part of the signal. The number of DPS events is measured using the J/ψ cross-sections at $\sqrt{s} = 8\,$TeV (derived as discussed in appendix A) and the effective cross-section for double parton interactions (σ_{eff}) as measured by ATLAS using $W + 2j$ events [61]. The ATLAS $W + 2j$ analysis was performed in pp collisions in a lower $\sqrt{s}$ energy, but we make the assumption that the σ_{eff} is independent from the $\sqrt{s}$ or that the change between $\sqrt{s} = 7\,$TeV and $8\,$TeV is negligible.

Based on the assumptions that σ_{eff} is process-independent [60], and that the two hard scatters are uncorrelated, for a collision where a Z boson is produced, the probability that a J/ψ is produced in addition due to a second hard process is

$$P_{J/\psi|Z}^{ij} = \sigma_{J/\psi}^{ij}/\sigma_{\text{eff}},$$

where σ_{eff} is taken to be $\sigma_{\text{eff}} = 15 \pm 3\,\text{(stat.)}_{-3}^{+5}\,\text{(sys.)}\,$mb according to the ATLAS measurement [61]. The background contributions are estimated for each rapidity bin separately and can be seen analytically in table 4.9.

Table 4.9: *Double parton scattering estimation. The first column shows the bin in $|y| \times p_T$ space of the J/ψ. The second column is the computed prompt (top half) and non-prompt (bottom half) inclusive J/ψ cross-section in this kinematic bin, evaluated from the published 7 TeV ATLAS data [92] and non-prompt FONLL predictions. The third column shows the probability that a J/ψ is produced in a particular $|y|$ and p_T bin, in association with a hard scattering that produces a Z boson. The cross-section σ_{eff} used in column 3 is taken from the ATLAS measurement of $W + 2$ jets, and is approximately equal to 15 mb. The fourth column shows the values of the third column normalised by the size of the bin in the $|y| \times p_T$ space. The fifth column shows the average acceptance $\times$ efficiency from inclusive J/ψ in each bin, which is used to estimate the number of DPS events in our sample. The sixth column shows the expected yield of DPS events. It is calculated from the product of the Z candidates from our inclusive Z sample, times the $< \epsilon \times \mathcal{A} >$, times the $\sigma_{\mathrm{bin}}/\sigma_{\mathrm{eff}}$.*

Double parton scattering background estimation - Prompt					
Bin $\|y\| \times p_T$ GeV	$\sigma(\text{Prompt } J/\psi \to \mu^+\mu^-)$ (nb)	$\sigma_{\mathrm{bin}}/\sigma_{\mathrm{eff}}$ (10^{-8})	$\frac{1}{\sigma_{\mathrm{eff}}}\frac{\mathrm{d}^2\sigma}{\mathrm{d}y p_T}$ (10^{-8})	$\langle \epsilon \times \mathcal{A} \rangle$	Expected yield
$(0,1) \times (8.5,10)$	$6.16^{+2.28}_{-1.61}$	$41.07^{+21.96}_{-19.18}$	$13.69^{+7.32}_{-6.39}$	0.23	$1.54^{+0.83}_{-0.72}$
$(0,1) \times (10,14)$	$5.37^{+1.76}_{-1.27}$	$35.83^{+18.16}_{-16.23}$	$4.48^{+2.27}_{-2.03}$	0.39	$2.24^{+1.14}_{-1.02}$
$(0,1) \times (14,18)$	$1.17^{+0.33}_{-0.26}$	$7.77^{+3.74}_{-3.47}$	$0.97^{+0.47}_{-0.43}$	0.53	$0.67^{+0.32}_{-0.30}$
$(0,1) \times (18,30)$	$0.53^{+0.13}_{-0.11}$	$3.50^{+1.61}_{-1.54}$	$0.15^{+0.07}_{-0.06}$	0.65	$0.37^{+0.17}_{-0.16}$
$(0,1) \times (30,100)$	$0.027^{+0.009}_{-0.008}$	$0.178^{+0.090}_{-0.089}$	$0.001^{+0.001}_{-0.001}$	0.76	$0.02^{+0.01}_{-0.01}$
$(1,2.1) \times (8.5,10)$	$6.27^{+2.28}_{-1.58}$	$41.82^{+22.19}_{-19.31}$	$12.67^{+6.72}_{-5.85}$	0.39	$2.66^{+1.41}_{-1.23}$
$(1,2.1) \times (10,14)$	$4.85^{+1.58}_{-1.12}$	$32.32^{+16.33}_{-14.57}$	$3.67^{+1.86}_{-1.66}$	0.49	$2.56^{+1.29}_{-1.16}$
$(1,2.1) \times (14,18)$	$0.98^{+0.28}_{-0.21}$	$6.54^{+3.14}_{-2.90}$	$0.74^{+0.36}_{-0.33}$	0.63	$0.66^{+0.32}_{-0.29}$
$(1,2.1) \times (18,30)$	$0.44^{+0.11}_{-0.09}$	$2.93^{+1.34}_{-1.27}$	$0.11^{+0.05}_{-0.05}$	0.73	$0.34^{+0.16}_{-0.15}$
$(1,2.1) \times (30,100)$	$0.019^{+0.005}_{-0.005}$	$0.124^{+0.059}_{-0.058}$	$0.001^{+0.000}_{-0.000}$	0.84	$0.02^{+0.01}_{-0.01}$
Number of Z candidates in inclusive Z sample $= (16148 \pm 66) \times 10^3$					$11.08^{5.65}_{5.04}$

Double parton scattering background estimation - Non-prompt					
Bin $\|y\| \times p_T$ GeV	$\sigma(\text{Non}-\text{prompt } J/\psi \to \mu^+\mu^-)$ (nb)	$\sigma_{\mathrm{bin}}/\sigma_{\mathrm{eff}}$ (10^{-8})	$\frac{1}{\sigma_{\mathrm{eff}}}\frac{\mathrm{d}^2\sigma}{\mathrm{d}y p_T}$ (10^{-8})	$\langle \epsilon \times \mathcal{A} \rangle$	Expected yield
$(0,1) \times (8.5,10)$	$2.42^{+0.859}_{-0.58}$	$16.16^{+8.48}_{-7.36}$	$5.39^{+2.83}_{-2.45}$	0.23	$0.61^{+0.32}_{-0.28}$
$(0,1) \times (10,14)$	$2.69^{+0.855}_{-0.60}$	$17.92^{+8.97}_{-7.99}$	$2.24^{+1.12}_{-1.00}$	0.39	$1.12^{+0.56}_{-0.50}$
$(0,1) \times (14,18)$	$0.84^{+0.223}_{-0.17}$	$5.56^{+2.62}_{-2.42}$	$0.70^{+0.327}_{-0.30}$	0.53	$0.48^{+0.22}_{-0.21}$
$(0,1) \times (18,30)$	$0.52^{+0.114}_{-0.09}$	$3.47^{+1.54}_{-1.47}$	$0.15^{+0.06}_{-0.06}$	0.65	$0.36^{+0.16}_{-0.15}$
$(0,1) \times (30,100)$	$0.087^{+0.014}_{-0.012}$	$0.583^{+0.243}_{-0.239}$	$0.004^{+0.002}_{-0.002}$	0.76	$0.06^{+0.03}_{-0.03}$
$(1,2.1) \times (8.5,10)$	$2.24^{+0.80}_{-0.54}$	$14.94^{+7.84}_{-6.80}$	$4.53^{+2.38}_{-2.06}$	0.39	$0.95^{+0.50}_{-0.43}$
$(1,2.1) \times (10,14)$	$2.43^{+0.77}_{-0.54}$	$16.22^{+8.12}_{-7.23}$	$1.84^{+0.92}_{-0.82}$	0.49	$1.29^{+0.64}_{-0.57}$
$(1,2.1) \times (14,18)$	$0.73^{+0.20}_{-0.14}$	$4.88^{+2.29}_{-2.12}$	$0.55^{+0.26}_{-0.24}$	0.63	$0.49^{+0.23}_{-0.21}$
$(1,2.1) \times (18,30)$	$0.44^{+0.10}_{-0.08}$	$2.92^{+1.30}_{-1.23}$	$0.11^{+0.05}_{-0.05}$	0.73	$0.34^{+0.15}_{-0.14}$
$(1,2.1) \times (30,100)$	$0.067^{+0.010}_{-0.009}$	$0.444^{+0.185}_{-0.182}$	$0.003^{+0.001}_{-0.001}$	0.84	$0.06^{+0.03}_{-0.02}$
Number of Z candidates in inclusive Z sample $= (16148 \pm 66) \times 10^3$					$5.76^{+2.84}_{-2.55}$

The total number of estimated events are $11.1^{+5.7}_{-5.0}$ for the prompt component and $5.8^{+2.8}_{-2.6}$ for the non prompt.

The DPS contributions are indistinguishable in an event-by-event basis. One discriminant variable that can be used for checking the contamination of a sample from DPS, is the azimuthal opening angle of the two particles ($\Delta\phi(Z, J/\psi)$). Assuming that the two particles come from an interaction of different pairs of partons, then their opening angle would be randomly distributed along $\Delta\phi$ (see figure 4.1). SPS events on the contrary, will populate the $\Delta\phi = \pi$ region, with an additional smearing, due to detector effects, as the Z boson and the J/ψ meson are expected to be produced in a back-to-back configuration, due to a single parton interaction.

Figure 4.17 illustrates the $\Delta\phi$ variable, after applying the sPlot weights, derived from the prompt and non-prompt J/ψ components of the fit model. A mixture of two contributions (SPS and DPS) described above is visible, with a more evident contamination of DPS in the prompt component (figure 4.17(a)). Assuming no dependence of pileup and DPS events over the $\Delta\phi$ variable, the number of events originating from these two effects, as calculated from the methods described above, is overlaid to the data measurements.

(a)   (b)
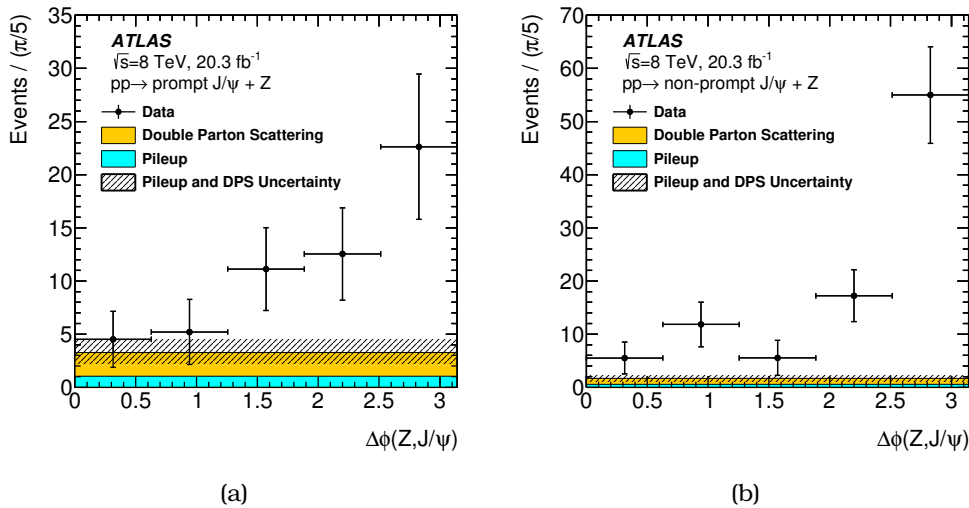
Figure 4.17: *Azimuthal angle between the Z boson and the J/ψ meson after the application of the sPlot weights to separate the prompt (left) and non-prompt (right) yield from background contributions. The estimated DPS (yellow band) and pileup (cyan band) contributions to the observed data are overlaid. The hashed region show the DPS and pileup uncertanties added in quadrature.*

4.8   Inclusive Z production

The strategy of the measurement is to derive the cross-section ratio of the associated production of Z bosons with prompt and non-prompt J/ψ mesons to inclusive Z production. In this section, the derivation of the inclusive Z sample is described.

The *Z* boson signal yield is extracted using the same cuts applied to the *Z* bosons in the associated production sample. This yield, except from the production cross-section ratio is used also for the calculation of the DPS and pileup contamination.

Figure 4.18 shows the invariant mass distributions for the inclusive $Z \to \mu^+\mu^-$ and $Z \to e^+e^-$ samples. All the events within $10\,\text{GeV}$ from the nominal *Z* mass, after the subtraction of the QCD and electroweak backgrounds are considered as signal events. The number of candidates are summarised in table 4.10, including separately the estimated numbers of background events, as evaluated in section 4.6.

| | (a) | | (b) |
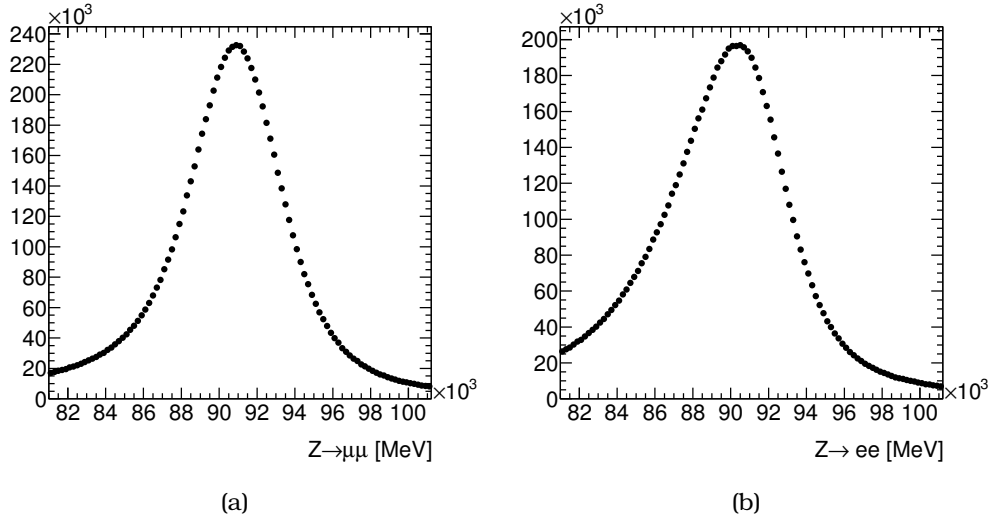
Figure 4.18: $Z \to \ell^+\ell^-$ invariant mass distributions. (a) $Z \to \mu^+\mu^-$ (b) $Z \to e^+e^-$.

Table 4.10: Total yields of $Z \to \mu^+\mu^-$ and $Z \to e^+e^-$.

Mode	Number of Events $\times 10^3$	Estimated Background $\times 10^3$	Signal Events $\times 10^3$
$\mu^+\mu^-$	8222 ± 3	23 ± 14	8197 ± 14
ee	7990 ± 3	39 ± 64	7951 ± 64
Total	16210 ± 4	62 ± 65	16148 ± 66

The estimated total background in the $m_Z \pm 10\,\text{GeV}$ window is found to be $0.4 \pm 0.4\%$. After the background subtraction we have 16.15 million *Z* bosons, out of which 8.20 million are observed with the $Z \to \mu^+\mu^-$ decay and 7.95 million with $Z \to e^+e^-$ decay mode.

As a cross-check, the ratio of the associated production $Z + J/\psi$ sample to the inclusive *Z* sample, both $Z \to \mu^+\mu^-$ and $Z \to e^+e^-$, are compared. The ratios are found to be consistent, within statistical uncertainties (0.92 ± 0.11 and 1.03 ± 0.01 for the di-muon and di-electron respectively).

4.9   Closure Test

An important cross-check of the analysis was the closure test performed on J/ψ MC. The idea behind it is that, by applying all the corrections in the reconstructed MC, the truth information of the MC can be reproduced. This is important, since these corrections are applied to the measurements in order to correct for the detector effects.

The closure test is performed doing the following:

- require that the J/ψ muons fall within the ATLAS acceptance range;

- build a 2D map $(p_T^{J/\psi}, y^{J/\psi})$ using the MC truth information;

- with the same acceptance requirement, build the same map using the MC reconstructed information, applying a weight that is based in the formula

$$w^{-1} = \epsilon_{CB}^{+}\epsilon_{CB\|ST}^{-} + \epsilon_{CB}^{-}\epsilon_{CB\|ST}^{+} - \epsilon_{CB}^{+}\epsilon_{CB}^{-}$$

where the ϵ is the efficiency of the combined (CB) or segment-tagged (ST) muon.

These two maps are divided, and if the efficiencies are calculated (described in chapter 3) and applied correctly, the result would be unity in all bins. The result of this exercise can be seen in figure 4.19. Figure 4.19(a) shows the full y and p_T range, while figure 4.19(b) focus on the $8.5 < p_T < 15\,\mathrm{GeV}$ region. All bins are within unity, taking into account the uncertainties calculated. We further project this map in the two axes as shown in figures 4.19(c) for the x-axis and figure 4.19(d) for the y-axis. All bins close and no dependence with either p_T or y is observed.

4.10 Z bosons produced in association with prompt and non-prompt J/ψ mesons

As discussed in previous sections, after the fit is performed, the sPlot technique is used in order to observe the distributions correlated with the prompt and non-prompt produced J/ψ mesons. Figure 4.20 shows the fit projection on the two rapidity.

In order to verify that the Z bosons that accompany the prompt and non-prompt J/ψ mesons are true Z bosons, and estimate the contamination from QCD and electroweak background, the sPlot weights are applied to the $Z \to e^+e^-$ and $Z \to \mu^+\mu^-$ distributions. Figure 4.21(a) shows the $Z \to \ell^+\ell^-$ bosons associated with prompt J/ψ mesons and figure 4.21(b) with non-prompt.

The sPlot weighted distributions are fitted with signal and multijet background templates. The templates were derived separately for $Z \to e^+e^-$ and $Z \to \mu^+\mu^-$ decays from MC and data respectively. The fit model used for the signal component, was chosen to be a Gaussian distribution convolved with a Breit-Wigner function, with an additional Gaussian, with smaller mean value compared to the core Gaussian, to model the radiative tails. The multijet background is parameterised an exponential function. The unbinned maximum likelihood fits are performed to the sPlot-weighted Z invariant mass distributions and the results are summarised in table 4.11.

(a)

(b)

(c)

(d)
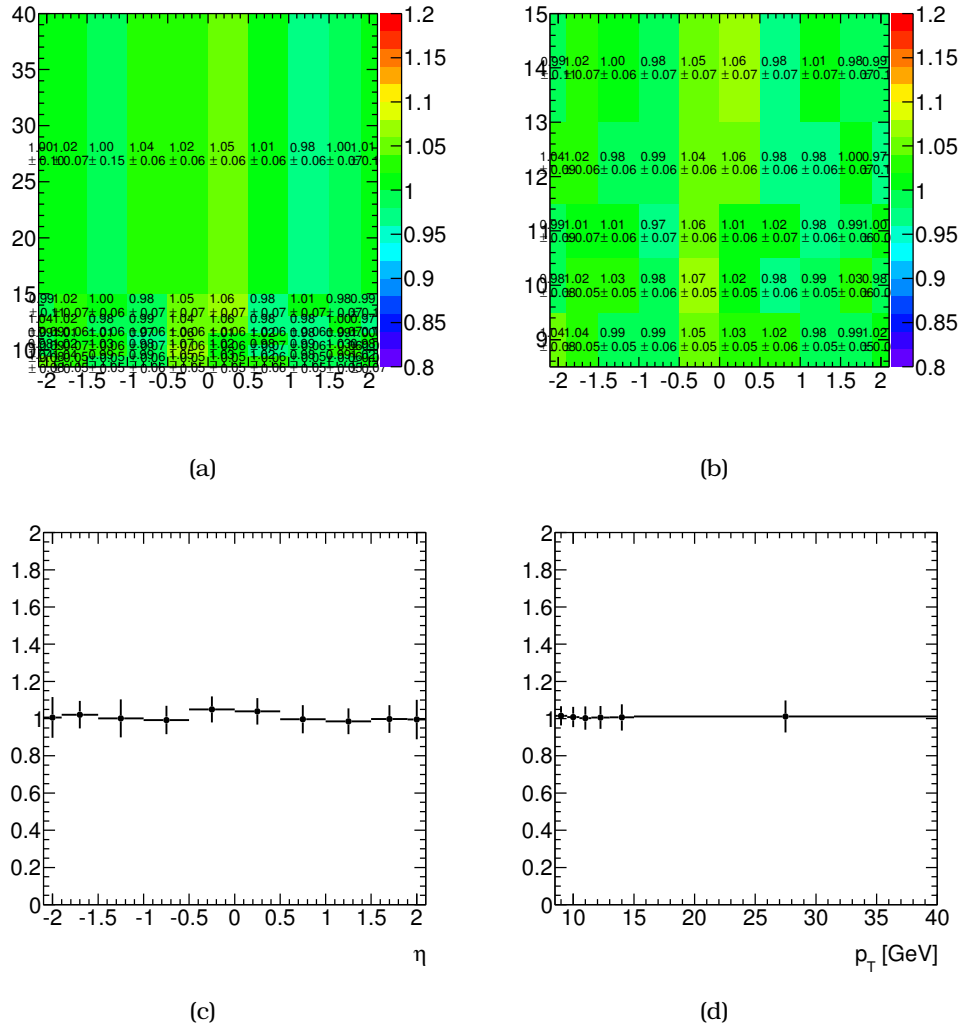
Figure 4.19: *Division of MC truth with reconstructed MC after the application of the weights. (a)(b) 2D map. (c)(d) η and p_T projections.*

Table 4.11: *Multijet background under the Z invariant mass within a $m_\mathrm{PDG}^Z \pm 10\,\mathrm{GeV}$ window.*

	$Z \to e^+e^-$	$Z \to \mu^+\mu^-$
prompt	0 ± 4	1 ± 4
non-prompt	1 ± 5	0 ± 5

The multijet yields indicate a negligible background contamination under the weighed Z distributions. Due to the application of the sPlot weights, the uncertainties on the events in the Z distributions look unnatural. This is a probable bias, in the fit result, and was checked with toy experiments. These toys use the signal and background fitted templates, in order to generate n number of background events, where $n = 1, \ldots, 16$. For each n, 10 000 distributions were generated and fitted, with the difference between
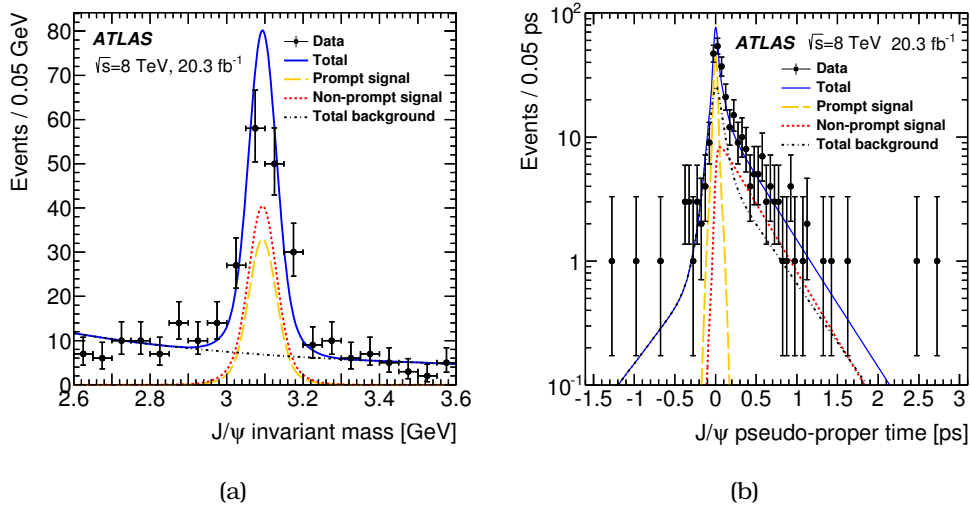
Figure 4.20: *Projections of the unbinned mass and pseudo-proper time maximum-likelihood fit in (a) invariant mass and (b) pseudo-proper time of the associated-production sample. The fit is used to extract the prompt and non-prompt signal fractions and is performed in two rapidity regions: $|y_{J/\psi}| < 1.0$ and $1.0 < |y_{J/\psi}| < 2.1$. The results are combined, presenting the mass and pseudo-proper time of all candidates inside the analysis phase-space.*

the fitted yield and the generated number of events calculated. The result of this test is illustrated in figure 4.22, where it is shown that for every configuration the difference between the true and extracted yield is 0, within uncertainties.

4.11 Systematic Uncertainties

Four sources of systematic uncertainty are considered for this analysis. First is the uncertainty that originates from the choice of fitting model. Second, possible differences in Z efficiencies when the Z is produced in association with a J/ψ meson or inclusively. Finally, uncertainties from using reconstruction efficiencies for correcting the muons based on their kinematic properties and biases that come from the choice of z_0 separation are examined. All the systematic uncertainties are summarised in the following sections and in table 4.12.

4.11.1 Fit model uncertainties

Systematic uncertainties that come from the fit model chosen in the analysis are calculated by varying the probability density functions used for the J/ψ mass and pseudo-proper time. An alternative model with different parameterisation in mass and pseudo-proper time was considered.

This alternative model features a Gaussian function for the J/ψ signal and exponential for function for the combinatorial background. The pseudo-proper time was modelled with the sum of a Gaussian and a double-sided exponential function con-
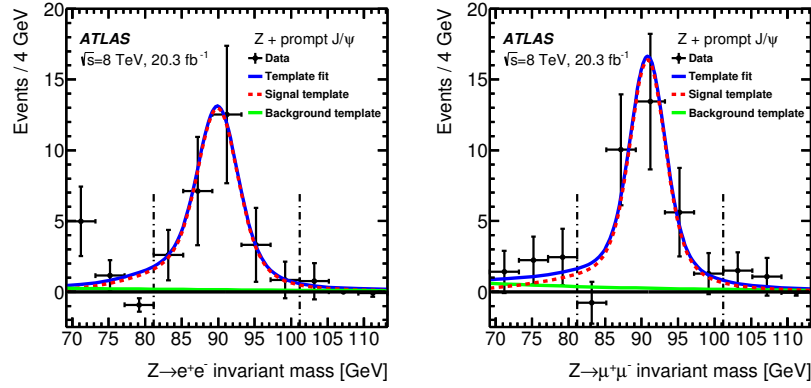
(a) $Z \to e^+e^-$ (left) and $Z \to \mu^+\mu^-$ (right) associated with prompt J/ψ.
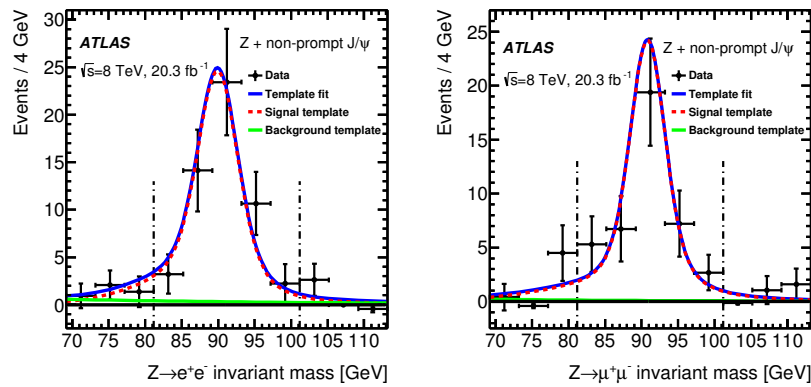
(b) $Z \to e^+e^-$ (left) and $Z \to \mu^+\mu^-$ (right) associated with non-prompt J/ψ.

Figure 4.21: $Z \to e^+e^-$ (left) and $Z \to \mu^+\mu^-$ (right) candidate invariant mass distributions after the application of the sPlot weights coming from the (a) prompt and (b) non-prompt J/ψ component of the fit. A template fit for the signal and background component, derived from MC simulation and data respectively, is overlaid on the distributions. The vertical dot-dashed lines indicate the signal region considered in the analysis.

volved with a Gaussian resolution function for the prompt J/ψ and prompt combinatorial background component, and an exponential function convolved with a Gaussian resolution function for the non-prompt J/ψ and non-prompt combinatorial background.

Pseudo-proper time of the J/ψ mesons is affected by the kinematic properties of the J/ψ. Since in the main model a high statistics inclusive J/ψ sample is used to drive the shaper related parameters of the fit, the possible differences between the kinematic properties of J/ψ mesons produced inclusively and in association with a Z boson must be taken into account. This is checked by removing the link between the two samples, and the associated production data are fitted alone.

Possible mis-modelling of the continuum background was tested, by changing the exponential function to polynomial. This was applied in all possible variations, the main model of the analysis, the alternative described above, with or without linking the parameters to the inclusive J/ψ sample.
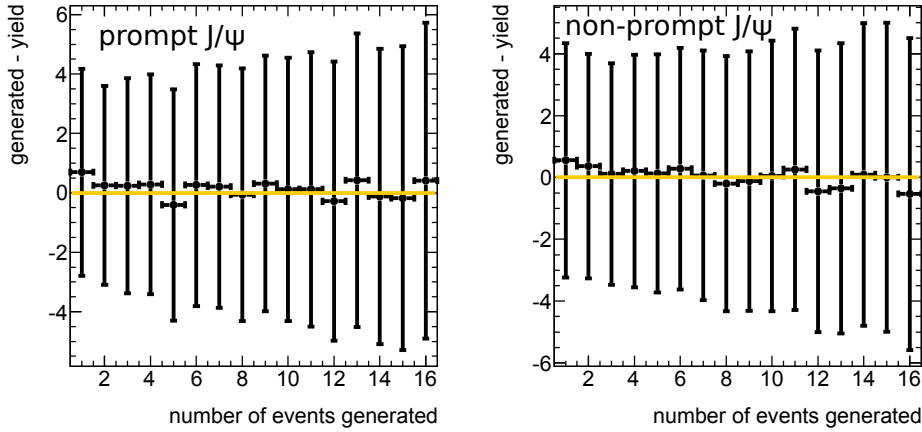
Figure 4.22: *Result of the toy MC for possible biases in the extraction of the background events. For various numbers of background events, the difference between extracted yield and true number of events is shown. The templates are for the $Z \rightarrow e^+e^-$ distributions associated with prompt (left) and non-prompt (right) J/ψ mesons.*

The systematic uncertainty is calculated using a toy MC technique. All possible fit models are fitted to a large number of simulated data samples generated for the two rapidity bins. The uncertainties were extracted by taking the maximal variation in the mean yield calculated from each of the fit models, compared to the nominal one. This results to a 3% uncertainty for prompt production and $4\% - 8\%$ for non-prompt, depending on the rapidity of the J/ψ candidate.

4.11.2 Z boson efficiencies

The analysis measures the cross-section ratio of the associated production of $Z + J/\psi$ to inclusive Z, which gives the advantage that the efficiencies and the luminosity uncertainties cancel in the ratio.

$$R = \mathcal{B}(J/\psi \rightarrow \mu^+\mu^-) \frac{N(Z + J/\psi)}{N(Z)} \frac{\epsilon_Z^{\text{associated}} \mathcal{A}_Z^{\text{associated}} \epsilon_{J/\psi} \mathcal{A}_{J/\psi}}{\epsilon_Z^{\text{inclusive}} \mathcal{A}_Z^{\text{inclusive}}}$$

This uses the assumption that the efficiency of the Z boson, either produced inclusively or in association with a J/ψ meson, is the same.

Possible differences were studied using the $Z + J/\psi$ MC and comparing it to inclusive Z MC as shown in figure 4.23. Although the efficiencies between the two production modes are in good agreement, the fact that the MC is not describing the SPS $Z + J/\psi$ process, a data driven method was employed. The reconstruction and trigger efficiencies calculated using the associated production data sample and the inclusive Z MC sample, re-weighted to match the observed $Z+J/\psi$ p_{T} spectrum were compared. The differences in the efficiencies between these two samples, were considered as systematic uncertainties, and are found to be $(1 \pm 1)\%$.
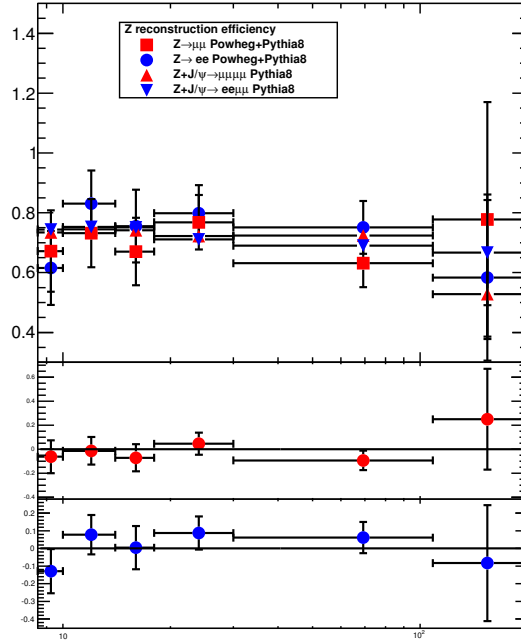
Figure 4.23: *Efficiency of reconstructing a Z boson in derived from the Z + J/ψ and inclusive Z MC sample. Both di-electron and di-muon decays are compared in the lower plots (red being the $Z \to \mu^+\mu^-$ and blue the $Z \to e^+e^-$).*

4.11.3 Muon reconstruction efficiency uncertainties

Muon reconstruction efficiencies were derived using the tag-and-probe method in $Z \to \mu^+\mu^-$ decays for high-p_T muons (see figures 4.24(c) and 4.24(d)) and $J/\psi \to \mu^+\mu^-$ decays for low-p_T muons (see figures 4.24(a) and 4.24(b)). The calculation of the efficiencies is described extensively in chapter 3. These two-dimensional data-derived maps, are used for correcting and calculating the inclusive cross-section and depend on the muon pseudorapidity and transverse momentum. For the calculation of the uncertainties induced by the use of these maps, each bin of these maps is varied within its uncertainty and the effect on the extracted yield when applied to the data is examined. They were calculated to be of the order of 1%.

4.11.4 Systematic uncertainty from vertex separation

In order to reduce the pileup and DPS contamination and ensure that the Z boson and J/ψ meson originate from the same interaction, a cut is applied in the separation between the two vertices along the z-axis. This cut was chosen to be 10 mm.

A tight cut on Δz_0 though, between the non-prompt J/ψ and Z vertices, would be very inefficient, biasing the non-prompt J/ψ signal. The non-prompt J/ψ mesons, produced by a decay of a b-hadron, travel a longer distance before decaying, hence the distance between the Z and J/ψ vertices are longer (see figure 4.26) and experience longer pseudo-proper times (see figure 4.25).
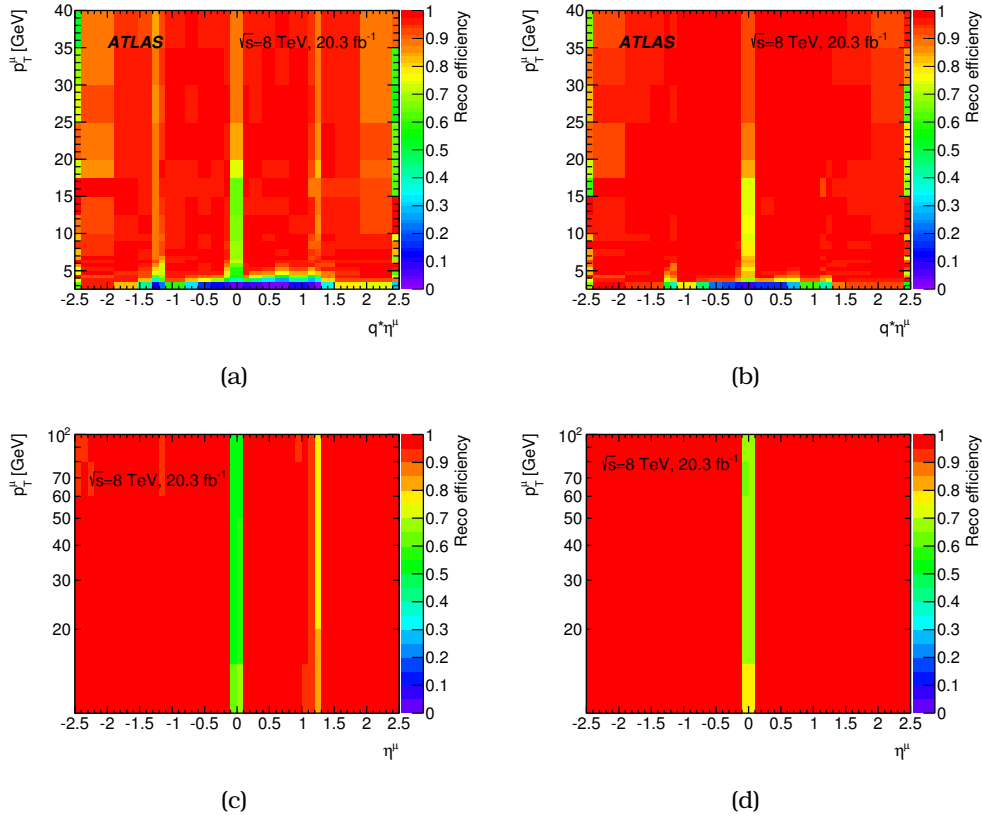
Figure 4.24: *(a), (b) low and (c), (d) high p_T muon reconstruction efficiencies for combined (left) and combined or segment-tagged muons.*
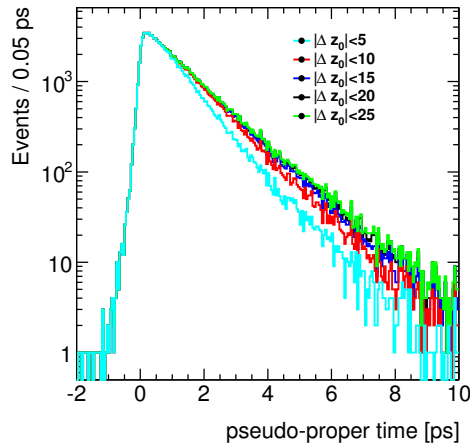
Figure 4.25: *Pesudo-proper time distributions for non-prompt J/ψ mesons applying various Δz_0 cuts. The stricter the Δz_0 cut becomes, the more signfianct the distortion becomes in the tails of the distributions, especially at high τ values.*

The distributions of Δz are shown for the two rapidity bins of the analysis and for prompt and non-prompt J/ψ mesons in figure 4.26. It is evident that a stringer selection

cut is introducing a bias in the measurement, as it rejects part of the signal, especially in the $Z+$ non-prompt J/ψ associated production.
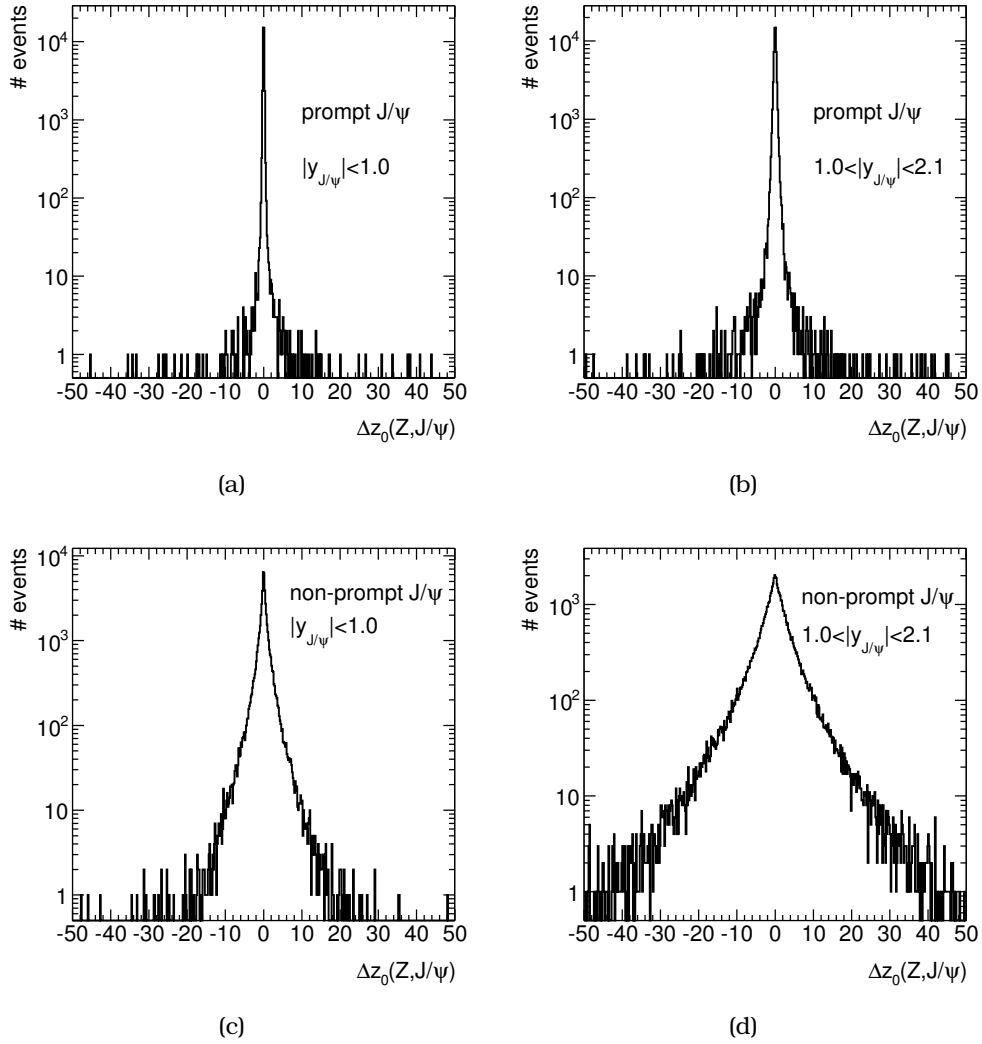
Figure 4.26: Δz_0 *distributions for prompt and non-prompt J/ψ mesons for the two rapidity bins of the analysis. The distributions are from MC.*

The systematic uncertainty is calculated by loosening the Δz to $20\,\text{mm}$ and repeating the measurement. The fit is performed to the new dataset with the relaxed cut and the difference in the extracted yield, after correcting for the enhanced pileup contaminations, is taken as a systematic uncertainty. The variation of the event yields is found to be between 2% and 16%, depending on the rapidity of the J/ψ.

4.11.5   Summary of systematic uncertainties

Among the uncertainties described above, a possible contribution from the decay of $Z \rightarrow \ell^+\ell^- J/\psi$ was also examined and found to be negligible (see section 4.14). Additionally, the polarisation of the Z boson in associated production relative to inclusive production,

due to high detector acceptance for Z boson decays, was considered negligible to the measurement. The rest of the sources of systematic uncertainties are summarised in table 4.12.

Table 4.12: *Summary of experimental systematic uncertainties.*

Source	Prompt		Non-prompt	
	$|y_{J/\psi}| < 1.0$	$1.0 < |y_{J/\psi}| < 2.1$	$|y_{J/\psi}| < 1.0$	$1.0 < |y_{J/\psi}| < 2.1$
Fit procedure	3 %	3 %	4%	8%
Z boson kinematics	1%	1%	1%	1%
$\mu_{J/\psi}$ efficiency	1%	1%	1%	1%
Vertex separation	7%	16%	2%	15%

4.12 Measurement of the cross-section ratio $Z + J/\psi : Z$

The results of the two-dimensional maximum likelihood fit are shown in table 4.13 for the two rapidity regions along with the DPS and pileup estimations. The background-only hypothesis is excluded for both prompt and non-prompt $Z + J/\psi$ production at 5σ and 9σ respectively (see section 4.5.2).

Table 4.13: *Results of the fit with statistical (first) and systematic (second) uncertainties. The total number of background events is measured in the $2.6 < m_{\mu^+\mu^-} < 3.6$ GeV window. The last column presents the expected number of pileup events for the prompt and non-prompt component, and their statistical uncertainty.*

Process	$|y_{J/\psi}| < 1.0$	$1.0 < |y_{J/\psi}| < 2.1$	Total	
			Events found	From pileup
Prompt signal	$24 \pm 6 \pm 2$	$32 \pm 8 \pm 5$	$56 \pm 10 \pm 5$	$5.2^{+1.8}_{-1.3}$
Non-prompt signal	$54 \pm 9 \pm 3$	$41 \pm 8 \pm 7$	$95 \pm 12 \pm 8$	$2.7^{+0.9}_{-0.6}$
Background	$61 \pm 11 \pm 6$	$77 \pm 13 \pm 7$	$138 \pm 17 \pm 9$	

All the cross-section ratio measurements (fiducial, inclusive and DPS-subtracted) are reported for J/ψ mesons produced in a phase-space of 8.5 GeV $< p_T^{J/\psi} < 100$ GeV and $|y_{J/\psi}| < 2.1$.

4.12.1 Fiducial cross-section measurements

After the background is subtracted, the yields for $Z+$ prompt J/ψ and $Z+$ non $-$ prompt J/ψ are corrected for detector efficiency effects. After this correction, the production cross-section ratios are determined in a restricted fiducial volume, as defined in section 4.3. The $Z + J/\psi$ cross-section measurements are normalised by the inclusive Z production cross-section, $R_{Z+J/\psi}^{\text{fid}}$. The production cross-section ratio is defined as:

$$R_{Z+J/\psi}^{\text{fid}} = \mathcal{B}(J/\psi \to \mu^+\mu^-) \frac{\sigma_{\text{fid}}(pp \to Z + J/\psi)}{\sigma_{\text{fid}}(pp \to Z)} = \frac{1}{N(Z)} \sum_{p_T \text{ bins}} \left[N^{\text{ec}}(Z + J/\psi) - N_{\text{pileup}}^{\text{ec}} \right],$$

where, $\mathcal{B}(J/\psi \to \mu^+\mu^-)$ is the branching fraction for the $J/\psi \to \mu^+\mu^-$ decay [29], $N(Z)$ is the background-subtracted yield of the inclusive Z events and $N^{\text{ec}}(Z + J/\psi)$ is the yield of $Z+$ prompt or non-prompt J/ψ yields, after applying corrections due to muon reconstruction inefficiency. From the yield of $N^{\text{ec}}(Z + J/\psi)$, the efficiency-corrected pileup yield ($N_{\text{pileup}}^{\text{ec}}$) is subtracted. The cross-section ratios for prompt and non-prompt J/ψ mesons are measured to be:

$$\text{prompt: } ^{\text{p}}R_{Z+J/\psi}^{\text{fid}} = (36.8 \pm 6.7 \pm 2.5) \times 10^{-7}$$

$$\text{non-prompt: } ^{\text{np}}R_{Z+J/\psi}^{\text{fid}} = (65.8 \pm 9.2 \pm 4.2) \times 10^{-7}$$

where the first uncertainty is statistical and the second is systematic. The results are represented in the first bin of figure 4.27(a) for $Z+$ prompt J/ψ and figure 4.27(b) for $Z+$ non $-$ prompt J/ψ.

From the results, it is shown, that this process is one of the rarest processes observed, with the associated production of a Z boson with a J/ψ meson occurring approximately ten times per million Z bosons production.

(a)   (b)
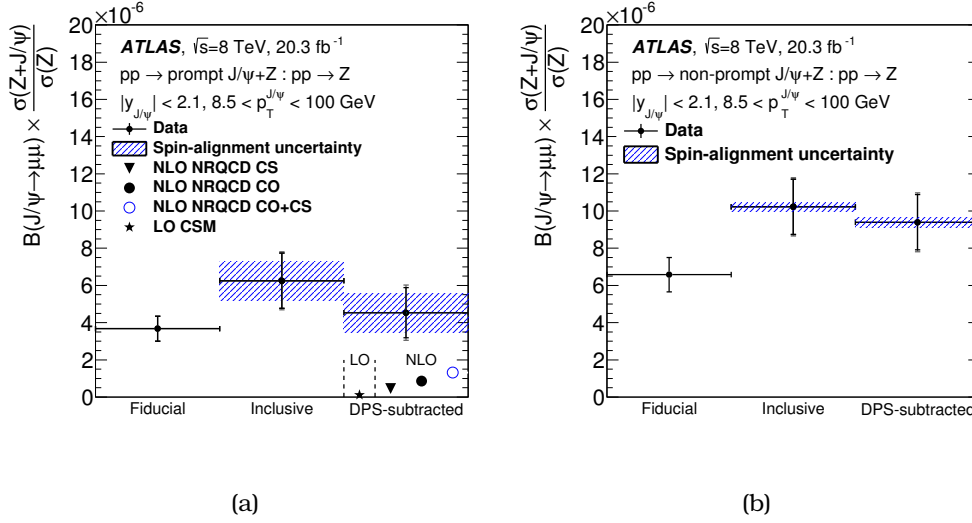
Figure 4.27: *Production cross-sections ratios of J/ψ in association with a Z boson, relative to inclusive Z production, for prompt and non-prompt J/ψ production. The first point indicates the total integrated cross-section ratio measured in the defined fiducial volume, the second point shows the same quantity corrected for detector acceptance effects on the J/ψ reconstruction, and the third point illustrates the corrected cross-section ratio after subtraction of the double parton scattering contribution as discussed in the text. The inner error bars represent statistical uncertainties and the outer error bars represent statistical and systematic uncertainties added in quadrature. Also shown are LO [23] and NLO [24] predictions for the inclusive SPS production rates in the colour-singlet (CS) and colour-octet (CO) formalisms.*

4.12.2   Inclusive cross-section measurements

Measurements of production rates of J/ψ mesons from the experiments are compared to theoretical predictions, that are often presented within a limited J/ψ phase-space, without applying kinematic requirements on the decay products. In order to allow such a comparison, corrections are applied to the measured fiducial cross-section ratios to account for the geometrical acceptance loss from the kinematic requirements (muons' transverse momentum and pseudorapidity) as described in section 4.3.

The corrections are applied on the p_T and rapidity of the J/ψ and the angular distribution of the di-muon system of the J/ψ decay, which depends on the spin-alignment state of the produced J/ψ mesons. For the measurements, the unpolarised production of the J/ψ was considered. Due to possible differences of the polarisation state of the J/ψ meson (see section 1.5), caused by the presence of the Z boson, other polarisation scenarios are examined.

The J/ψ spin-alignment scenarios considered in the analysis are the following:

1. Isotropic distribution, independent of θ^* and ϕ^*, with $\lambda_\theta = \lambda_\phi = \lambda_{\theta\phi} = 0$. Used for

the nominal measurement (see figure 4.28(a));

2. Full longitudinal alignment with $\lambda_\theta = -1$, $\lambda_\phi = \lambda_{\theta\phi} = 0$ (see figure 4.28(b));

3. Transverse-0 alignment with $\lambda_\theta = +1$, $\lambda_\phi = \lambda_{\theta\phi} = 0$ (see figure 4.28(c));

4. Transverse-M alignment with $\lambda_\theta = +1$, $\lambda_\phi = -1$, $\lambda_{\theta\phi} = 0$ (see figure 4.28(d));

5. Transverse-P alignment with $\lambda_\theta = \lambda_\phi = +1$, $\lambda_{\theta\phi} = 0$ (see figure 4.28(e)).

The largest difference in the resulting cross-section ratios is considered as a spin-alignment uncertainty. This was estimated as 24% for $|y_{J/\psi}| < 1.0$ and 23% for $1.0 < |y_{J/\psi}| < 2.1$. Non-prompt J/ψ mesons produced from b-decays, show lower spin-alignment effects, compared to promptly produced J/ψ, by a factor of $\sim 10\%$ [107]. The spin-alignment uncertainty for the non-prompt J/ψ was found to be 3% for $|y_{J/\psi}| < 1.0$ and 2% for $1.0 < |y_{J/\psi}| < 2.1$.

After the corrections for the acceptance of the J/ψ mesons, the inclusive production cross-section ratios, $R_{Z+J/\psi}^{\text{incl}}$, are calculated by:

$$R_{Z+J/\psi}^{\text{incl}} = \mathcal{B}(J/\psi \to \mu^+\mu^-)\,\frac{\sigma_{\text{incl}}(pp \to Z + J/\psi)}{\sigma_{\text{incl}}(pp \to Z)} = \frac{1}{N(Z)}\sum_{p_{\mathrm{T}}\text{ bins}}\left[N^{\text{ec+ac}}(Z + J/\psi) - N_{\text{pileup}}^{\text{ec+ac}}\right],$$

where $N^{\text{ec+ac}}(Z + J/\psi)$ is the yield of the $Z+$ prompt/non$-$prompt J/ψ after the acceptance corrections and efficiency corrections of the J/ψ and $N_{\text{pileup}}^{\text{ec+ac}}$ is the pileup contribution in the full J/ψ phase-space. The inclusive production cross-section ratios are measured to be:

$$\text{prompt: } {}^{\text{p}}R_{Z+J/\psi}^{\text{incl}} = (\ 63 \pm 13 \pm 5 \pm 10) \times 10^{-7}$$
$$\text{non-prompt: } {}^{\text{np}}R_{Z+J/\psi}^{\text{incl}} = (102 \pm 15 \pm 5 \pm\ 3) \times 10^{-7}$$

where the first uncertainty is statistical, the second uncertainty is systematic, and the third uncertainty is due to the unknown J/ψ spin-alignment in the $Z + J/\psi$ production. The results are shown in the second bin of figure 4.27.

4.12.3 Comparison with theoretical calculations and double parton scattering contributions

In section 4.7, the estimation of the contribution from DPS is described, for $Z+$ prompt and non-prompt J/ψ mesons. The DPS estimations are subtracted from the inclusive measurement and the $R_{Z+J/\psi}^{\text{DPS sub}}$ is calculated. The subtracted ratios essentially reflect the SPS $Z + J/\psi$ production and thus can be compared with the theoretical predictions (see figure 1.3). The resulting DPS subtracted cross-section ratios are measured to be:

$$\text{prompt: } {}^{\text{p}}R_{Z+J/\psi}^{\text{DPS sub}} = (45 \pm 13 \pm 6 \pm 10) \times 10^{-7}$$
$$\text{non-prompt: } {}^{\text{np}}R_{Z+J/\psi}^{\text{DPS sub}} = (94 \pm 15 \pm 5 \pm\ 3) \times 10^{-7}$$

(a)

(b)

(c)

(d)

(e)
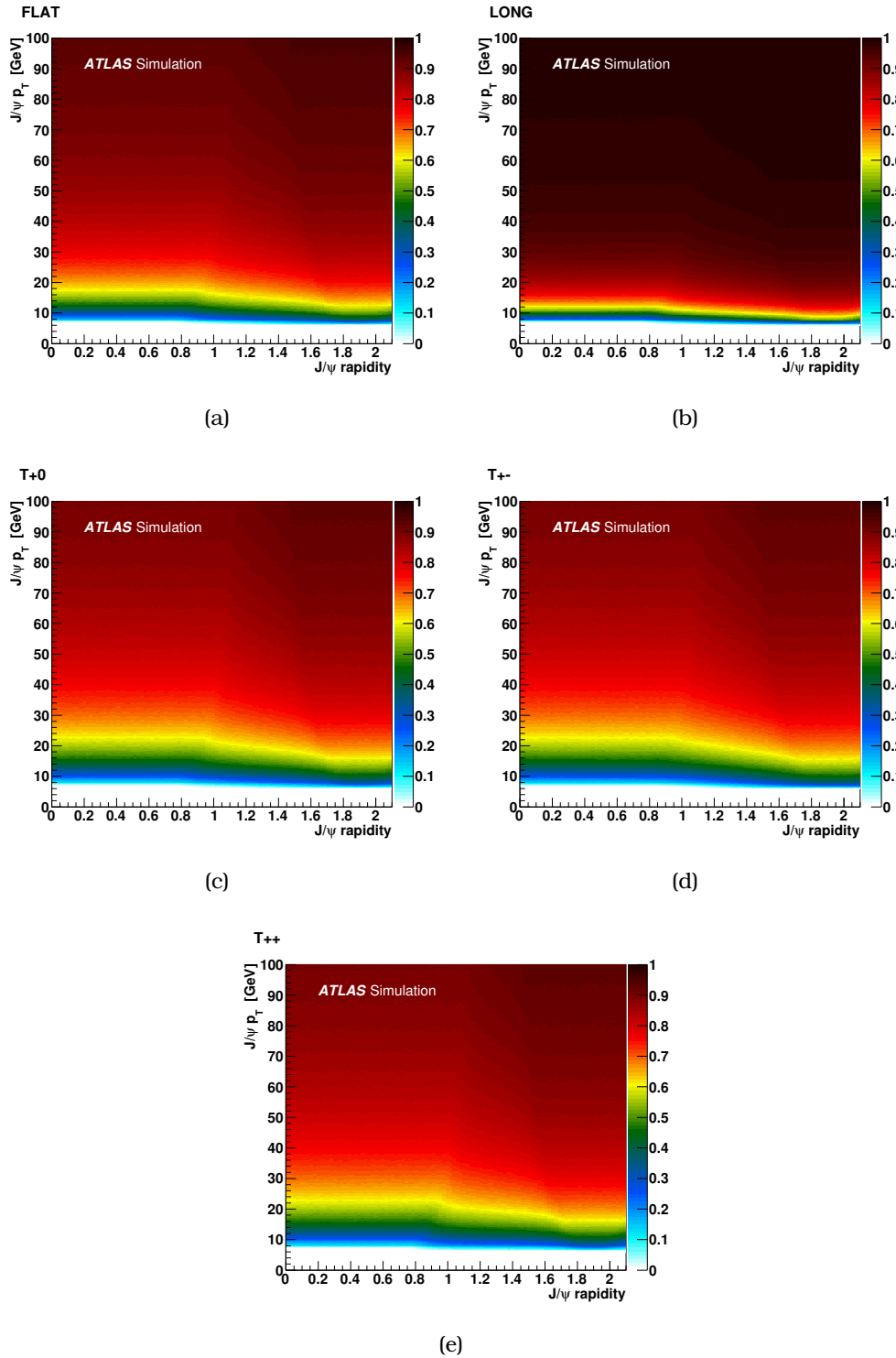
Figure 4.28: *The J/ψ acceptance for the isotropic (FLAT) spin-alignment scenario.*

where the first uncertainty is statistical, the second is systematic and the third is the uncertainty arising from the choice of spin-alignment scenario. The results are represented in the third bin of figure 4.27.

From the inclusive and DPS-subtracted cross-section ratios, the DPS fractions can be extracted for $Z+$ prompt and non-prompt J/ψ meson production. The DPS fraction is measured to be $(29 \pm 9)\%$ for the $Z+$ prompt J/ψ signal and $(8 \pm 2)\%$ for the non-prompt signal (shown in figure 4.29).
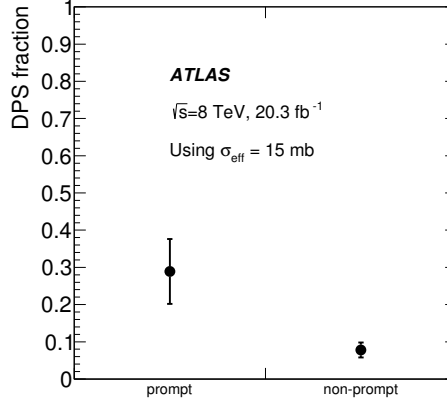
Figure 4.29: *Prompt and non-prompt fractions in $Z+$ prompt and non-prompt J/ψ prodcution.*

The DPS-subtracted measurements are compared with LO CS predictions and NLO CS and CO models [23, 24]. Both theory groups offered LO CS calculations, which differ from $(11.6 \pm 3.2) \times 10^{-8}$ and $(46.2^{+6.0}_{6.5}) \times 10^{-8}$. The difference originates from the different choice of scale for the central predictions (either the Z mass, or the J/ψ transverse mass $m_T = \sqrt{m_{J/\psi}^2 + p_T(J/\psi)}$). CO calculations use the NRQCD LDME values from reference [108] and predict $(25.1^{+3.3}_{-3.5}) \times 10^{-8}$ at LO and $(86^{+20}_{-18}) \times 10^{-8}$ at NLO. The comparison between data and theory calculations can be seen in figure 4.27.

Further comparison, between the measurement and other CO and CS predictions, as described in reference [21] are shown in figure 4.30. These calculations agree with other predictions, that the contributions from the CS model are too small to make this process visible in the LHC data, but foresee higher rates from CO models, in agreement with the cross-section ratio measured.

4.12.4   Differential production cross-section measurements

The cross-section ratio measurement is also performed differentially, as a function of the transverse momenta and absolute rapidity of the J/ψ meson, as described below.

Differential cross-section ratio as a function of $p_T^{J/\psi}$

After measuring the inclusive cross-section ratio, the differential cross-section ratio $dR_{Z+J/\psi}^{inc}/dp_T^{J/\psi}$ is calculated for both prompt and non-prompt J/ψ. The results are shown in five bins in figure 4.31 and summarised in table 4.14. The DPS estimation is overlaid and the differential cross-section from theory are added on them.

It is evident that the p_T spectrum of the J/ψ mesons produced in association with a Z boson is harder compared to inclusive J/ψ production. Also, theory predictions
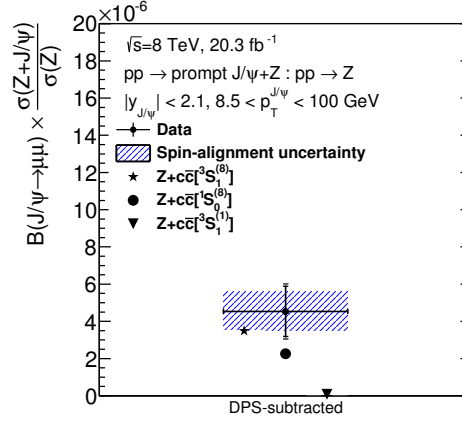
Figure 4.30: *Comparison of DPS-subtracted cross-section ratios with CS and CO model predictions from reference [21].*

Table 4.14: *The inclusive (SPS+DPS) cross-section ratio $\mathrm{d}R^{\mathrm{incl}}_{Z+J/\psi}/\mathrm{d}p_{\mathrm{T}}$ for prompt and non-prompt J/ψ. Estimated DPS contributions for each bin, based on the assumptions made in this study, are presented.*

$p_{\mathrm{T}}^{J/\psi}$ [GeV]	Inclusive prompt ratio [$\times 10^{-7}/\,\mathrm{GeV}$] value $\pm$ (stat) $\pm$ (syst) $\pm$ (spin)			Estimated DPS [$\times 10^{-7}/\,\mathrm{GeV}$] assuming $\sigma_{\mathrm{eff}} = 15\,\mathrm{mb}$
$(8.5, 10)$	10.8 ± 5.9	± 1.9	± 3.1	5.5 ± 2.1
$(10, 14)$	5.6 ± 1.9	± 0.8	± 1.2	1.7 ± 0.6
$(14, 18)$	1.9 ± 1.1	± 0.1	± 0.3	0.4 ± 0.1
$(18, 30)$	0.87 ± 0.37	± 0.12	± 0.09	0.05 ± 0.02
$(30, 100)$	0.090 ± 0.037	± 0.012	± 0.006	0.00042 ± 0.00020
$p_{\mathrm{T}}^{J/\psi}$ [GeV]	Inclusive non-prompt ratio [$\times 10^{-7}/\,\mathrm{GeV}$] value $\pm$ (stat) $\pm$ (syst) $\pm$ (spin)			Estimated DPS [$\times 10^{-7}/\,\mathrm{GeV}$] assuming $\sigma_{\mathrm{eff}} = 15\,\mathrm{mb}$
$(8.5, 10)$	5.1 ± 4.2	± 0.9	± 0.3	2.07 ± 0.77
$(10, 14)$	9.2 ± 2.5	± 1.2	± 0.3	0.85 ± 0.30
$(14, 18)$	3.3 ± 1.2	± 0.4	± 0.1	0.26 ± 0.09
$(18, 30)$	3.04 ± 0.59	± 0.04	± 0.04	0.05 ± 0.02
$(30, 100)$	0.115 ± 0.039	± 0.002	± 0.001	0.00146 ± 0.00046

show a factor of two bigger contribution from CO processes compared to CS, with the CO being increasingly dominant for higher transverse momenta. CO and CS models cannot predict the data measurement, with the difference reaching a factor of 5 for J/ψ mesons with $p_{\mathrm{T}} > 18\,\mathrm{GeV}$.
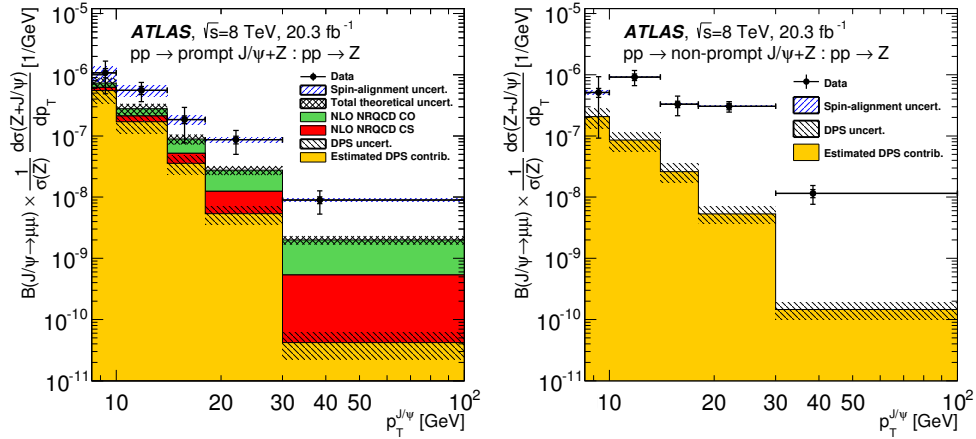
Figure 4.31: *Normalised production cross-section of J/ψ in association with a Z boson as a function of the p_T of prompt J/ψ, and non-prompt J/ψ. Overlaid on the measurement is the contribution to the total signal originating from double parton scattering (DPS) interactions. Theoretical predictions at NLO accuracy for the SPS contributions from colour-singlet (CS) and colour-octet (CO) processes are added to the DPS estimate and presented in comparison to the data as solid bands.*

Differential cross-section ratio as a function of $|y_{J/\psi}|$

The differential fiducial, inclusive and DPS-subtracted measurements of the cross-section ratio was also calculated as a function of the absolute rapidity of the J/ψ. Due to limited statistics this measurement was performed only in two rapidity bins. This is shown in figure 4.32 with the results summarised in table 4.15.

Within uncertainties, there is no difference in the cross-section ratios between the two rapidity bins ($|y_{J/\psi}| < 1.0$ and $1.0 < |y_{J/\psi}| < 2.1$) for the promptly produced J/ψ mesons, as expected. For non-prompt J/ψ mesons, a lower cross-section ratio is observed for the higher rapidity bin, compatible with previous ATLAS measurements [109].

Table 4.15: *The fiducial, inclusive (SPS+DPS) and DPS-subtracted differential cross-section ratio $dR_{Z+J/\psi}/dy$ as a function of $y_{J/\psi}$ for prompt and non-prompt J/ψ.*

$y_{J/\psi}$	Prompt cross-section ratio							
	Fiducial [$\times 10^{-7}$]		Inclusive [$\times 10^{-7}$]			DPS-subtracted [$\times 10^{-7}$]		
	value $\pm$ (stat) $\pm$	(syst)	value $\pm$ (stat) $\pm$	(syst) $\pm$	(spin)	value $\pm$ (stat) $\pm$	(syst) $\pm$	(spin)
$|y_{J/\psi}| < 1.0$	7.6 $\pm$ 2.1	$\pm$ 0.5	13.9 $\pm$ 4.6	$\pm$ 0.8	$\pm$ 3.4	9.4 $\pm$ 4.6	$\pm$ 1.1	$\pm$ 3.4
$1.0 < |y_{J/\psi}| < 2.1$	9.8 $\pm$ 2.2	$\pm$ 1.3	15.8 $\pm$ 4.5	$\pm$ 2.1	$\pm$ 3.5	12.0 $\pm$ 4.5	$\pm$ 2.7	$\pm$ 3.5
$y_{J/\psi}$	Non-prompt cross-section ratio							
	Fiducial [$\times 10^{-7}$]		Inclusive [$\times 10^{-7}$]			DPS-subtracted [$\times 10^{-7}$]		
	value $\pm$ (stat) $\pm$	(syst)	value $\pm$ (stat) $\pm$	(syst) $\pm$	(spin)	value $\pm$ (stat) $\pm$	(syst) $\pm$	(spin)
$|y_{J/\psi}| < 1.0$	18.0 $\pm$ 3.3	$\pm$ 0.6	29.9 $\pm$ 5.0	$\pm$ 0.9	$\pm$ 1.1	27.8 $\pm$ 5.0	$\pm$ 1.0	$\pm$ 1.1
$1.0 < |y_{J/\psi}| < 2.1$	13.5 $\pm$ 2.9	$\pm$ 1.9	19.3 $\pm$ 5.0	$\pm$ 2.1	$\pm$ 0.8	17.5 $\pm$ 5.0	$\pm$ 2.1	$\pm$ 0.8
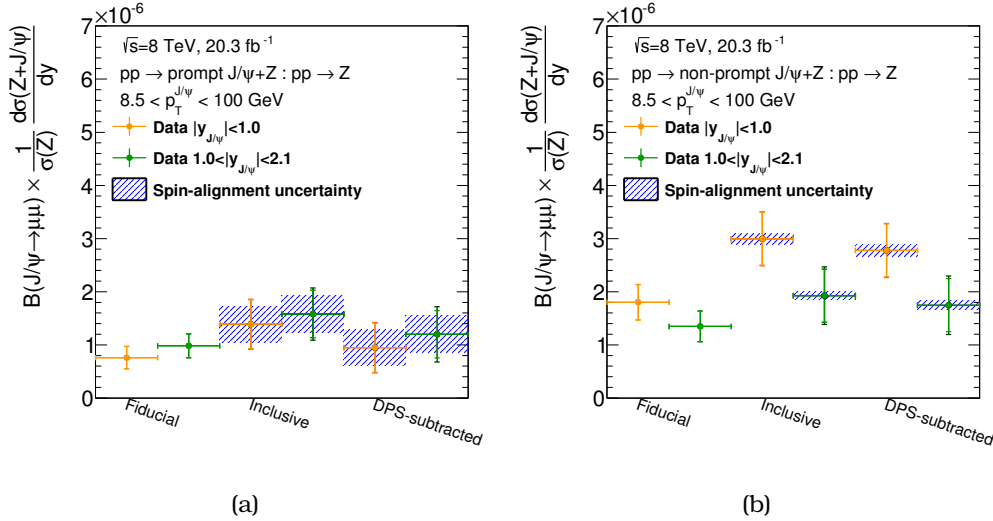
Figure 4.32: *(a) Prompt and (b) non-prompt differential cross-section ratios as a function of the absolute rapidity of the J/ψ. Measurements are presented in a fiducial space, corrected for the acceptance of the J/ψ and after the subtraction of the DPS contributions.*

4.13 Double parton scattering studies

The effective cross-section, σ_{eff}, for the estimation of the DPS events in the analysis was taken to be $\sigma_{\text{eff}} = 15 \pm 3(\text{stat.}) \pm^{+5}_{-3} (\text{stat.})\,\text{mb}$, as measured from the ATLAS experiment using $W + 2j$ events [61]. The $\Delta\phi(Z, J/\psi)$ observable, being sensitive to DPS, can be used for the calculation of σ_{eff}.

The lower region of $\Delta\phi$ variable, as observed from MC simulations [53], is dominated from SPS (see figure 4.33(a)). With this assumption, the $\Delta\phi(Z, J/\psi) < \pi/5$ region (first bin) of the prompt $\Delta\phi(Z, J/\psi)$ distribution, is considered to be populated from DPS. By fluctuating the effective cross-section, the estimation of the DPS increases up to where the observed data and uncertainties can support. This is shown in figure 4.33(b).

The lower limit of σ_{eff} extracted by the data measurement and its uncertainties is $\sigma_{\text{eff}} > 5.3\,\text{mb}\,(3.7\,\text{mb})$ at 68%(95%) confidence level. A comparison between a variety of measurements from and the LHC [56] and Tevatron [57, 58, 59, 60] is illustrated in figure 4.34. The limit extracted is in agreement with the other measurements performed in different centre-of-mass energy and use a different final state.

Setting an upper limit would require an SPS model description of the $\Delta\phi$ observable from theory, not available at that time.

4.13.1 Using a $\sigma_{\text{eff}} = 5.3$mb

The extracted lower limit of $\sigma_{\text{eff}} = 5.3\,\text{mb}$ is further used for the estimation of the DPS events. The new DPS contamination is used for comparison with the differential cross section measurement as a function the J/ψ transverse momentum.

The comparison shows, that with a $\sigma_{\text{eff}} = 5.3\,\text{mb}$, the low p_T bins originate purely from DPS process, with the higher-p_T bins dominated by SPS. This is more prominent in the $Z+$ prompt J/ψ production (see figure 4.35(a)), where a bigger contamination

(a)   (b)
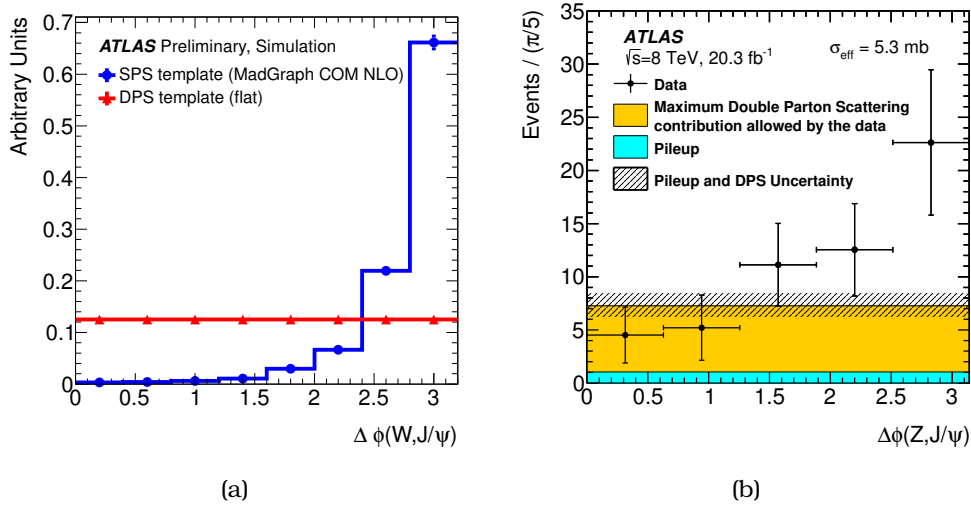
Figure 4.33: *(a) $\Delta\phi(W, J/\psi)$ for the DPS contribution using a flat DPS template validated using PYTHIA8 MC simulation. The SPS contribution is simulated with the NLO COM by MadGraph. (b) $\Delta\phi(Z, J/\psi)$ plot for prompt production with DPS σ_{eff} set to its minimum limit, $\sigma_{\text{eff}} = 5.3$ mb at 68% confidence level (maximum double parton scattering contribution).*
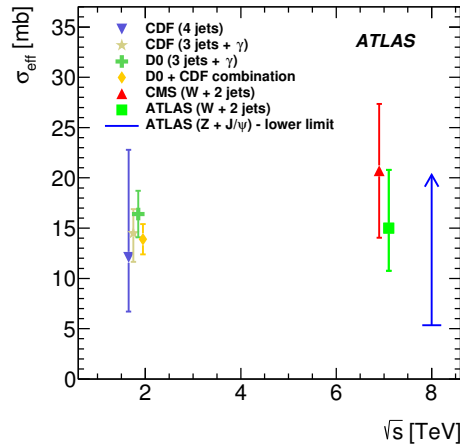
Figure 4.34: *Lower limit on estimated DPS effective cross-section extracted from the $\Delta\phi(Z, J/\psi)$ distribution, with a 68% confidence level, compared with previous measurements at the LHC and Tevatron as a function of $\sqrt{s}$.*

from DPS is expected.

4.14 $Z \to \ell^+\ell^- J/\psi$ **decay**

During the early LEP years, theorists suggested the possible decay of the *Z* boson to a *J/ψ* meson and two additional leptons [43, 44, 45]. This potential decay was examined for the analysis of the *Z* + *J/ψ* associated production, since they both have the same final state.
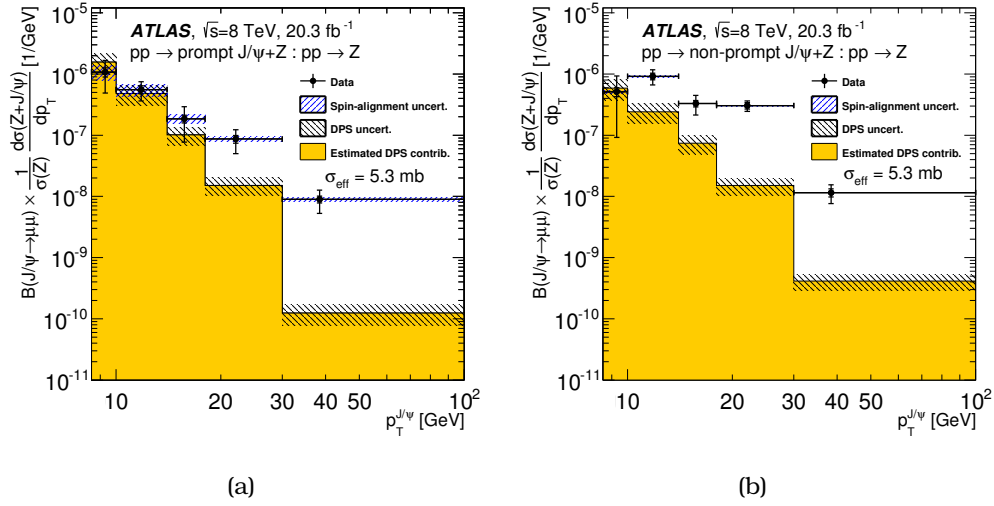
Figure 4.35: *(a) Prompt and (b) non-prompt production cross-section ratios as a function of the transverse momentum of the J/ψ meson. Overlaid is the contribution from DPS, using as σ_{eff} the lower limit extracted, $\sigma_{\mathrm{eff}} = 5.3$ mb*

The potential contamination of the signal events from this decay was examined by checking the $J/\psi \ell^+\ell^-$ invariant mass (figure 4.36(d)) for the J/ψ mesons with invariant mass $2.6 < m_{J/\psi} < 3.6$ GeV. Figures 4.36(b) and 4.36(c) show the invariant mass and pseudo-proper time of these J/ψ candidates. There is a clear evidence of the Z boson in figure 4.36(d) that has a significance of the order of $\sim 2.6\sigma$. Despite of the peak in the J/ψ invariant mass is promising, the low statistics and the interfering $Z \to 4\ell$ decay [110, 50] make it hard to reach any solid conclusions about the validity of the $Z \to \ell^+\ell^- J/\psi$ decay.

The events, where the $\ell^+\ell^-$ combination gives an invariant mass within the signal region of the analysis ($m_Z \pm 10$ GeV) are shown in figure 4.36(a). The effect in the analysis was examined by removing these 13 events and comparing the differences in the cross-section ratios. The impact was found to be insignificant.
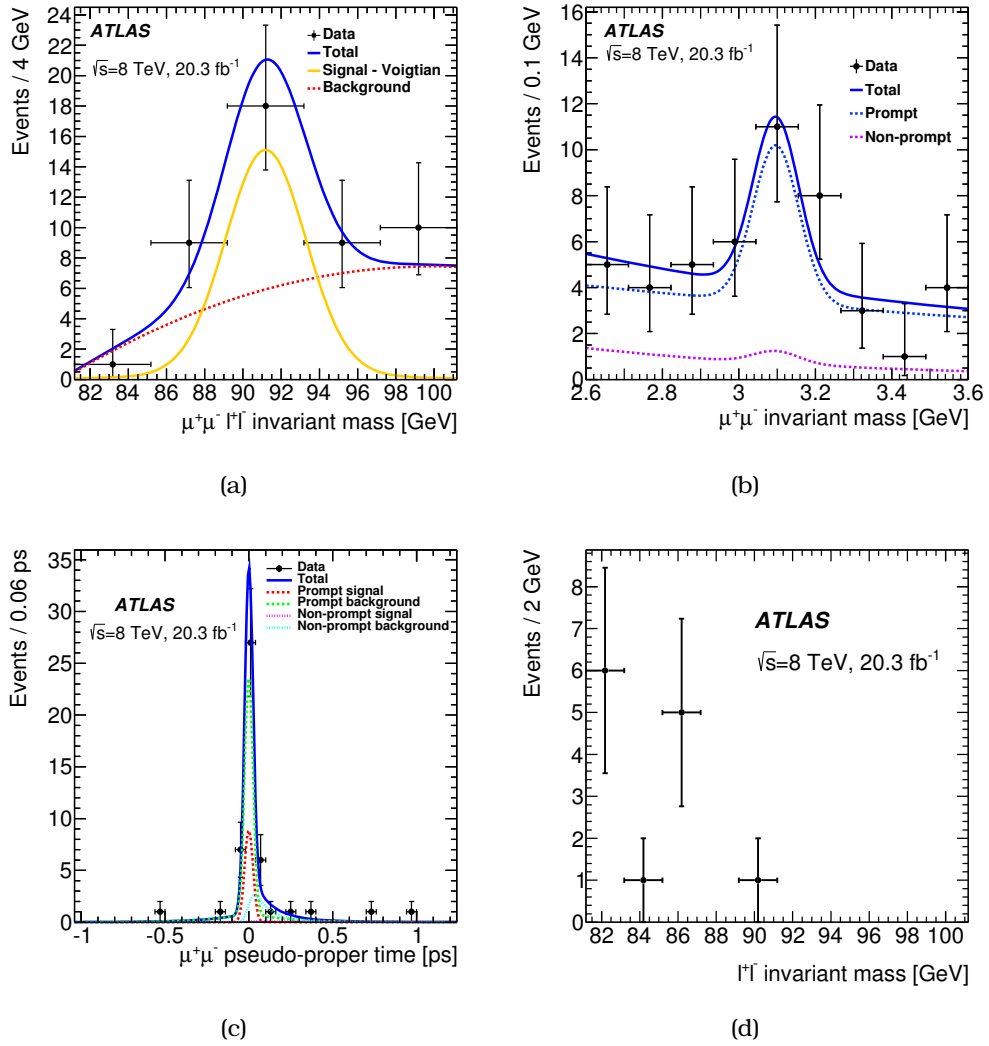
Figure 4.36: *(a) $\mu^+\mu^-\ell^+\ell^-$ invariant mass, (b) J/ψ invariant mass, (c) J/ψ pseudo-proper time and (d) $\ell^+\ell^-$ invariant mass inside the analysis Z signal region.*

Search for the $B_s^0 \to \mu^+\mu^-$ decay

5.1 Introduction

Flavour of quarks can change through the weak interactions, like in the decay of $\Lambda \to pe\bar{\nu}_e$, with $s \to uW$ transitions. The flavour changing current interactions are governed by the Cabibbo - Kobayashi - Maskawa (CKM) matrix [111, 112], which represent the probabilities of quarks to change flavour. The CKM matrix is formulated as:

$$
\begin{pmatrix} d' \\ s' \\ b' \end{pmatrix} = \begin{pmatrix} V_{ud} & V_{us} & V_{ub} \\ V_{cd} & V_{cs} & V_{cb} \\ V_{td} & V_{ts} & V_{tb} \end{pmatrix} \begin{pmatrix} d \\ s \\ b \end{pmatrix} = V_{\text{CKM}} \begin{pmatrix} d \\ s \\ b \end{pmatrix}
$$

with the V_{xy} being the coupling strengths of the x quark to y. The values of the CKM parameters are defined experimentally and are [29]:

$$
V_{\text{CKM}} = \begin{pmatrix} 0.97427 \pm 0.00014 & 0.22536 \pm 0.00061 & 0.00355 \pm 0.00015 \\ 0.22522 \pm 0.00061 & 0.97343 \pm 0.00015 & 0.0414 \pm 0.0012 \\ 0.00886 \pm 0.00033 & 0.0405 \pm 0.0012 & 0.99914 \pm 0.00005 \end{pmatrix}
$$

*F*lavour *C*hanging *N*eutral *C*urrents (FCNC) are the processes where fermions change their flavour, keeping their electric charge unchanged. In the Standard Model, such processes can occur only in loops (the so called box and penguin diagrams - see figure 5.1).

For example, the $b \to s + Z$ process is forbidden due to flavour violation and can happen only indirectly ($b \to q + W \to s + Z$, where $q = u, c, t$) and are governed by the CKM parameters. These transitions are highly suppressed by the *G*lashow-*I*liopoulos-*M*aiani (GIM) mechanism [113]. Examples of such process is the $K_s \to \mu^+\mu^-$ decay, that initiated the finding of the GIM mechanism and the B_s^0 meson decay to two muons.

Due to the very low branching fraction predicted by the SM ($(3.54 \pm 0.30) \times 10^{-9}$) [114], the decay mode of $B_s^0 \to \mu^+\mu^-$ is used for the search of physics beyond the standard model (BSM). Some of these BSM models propose the existence of leptoquarks, imposing the symmetry between quarks and leptons, and the *SU*per *SY*mmetry (SUSY), where the FCNC processes can occur in tree level. These models can interfere with the production modes and enhance (or suppress) the $B_s^0 \to \mu^+\mu^-$ branching ratio (see figure 5.2).
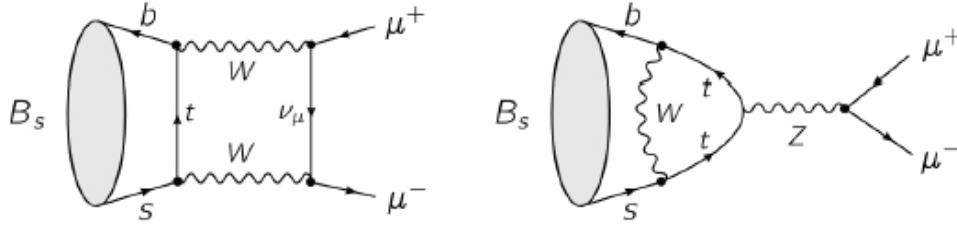
Figure 5.1: *Feynman diagram for the decay of $B_s^0 \to \mu^+\mu^-$ in the SM.*
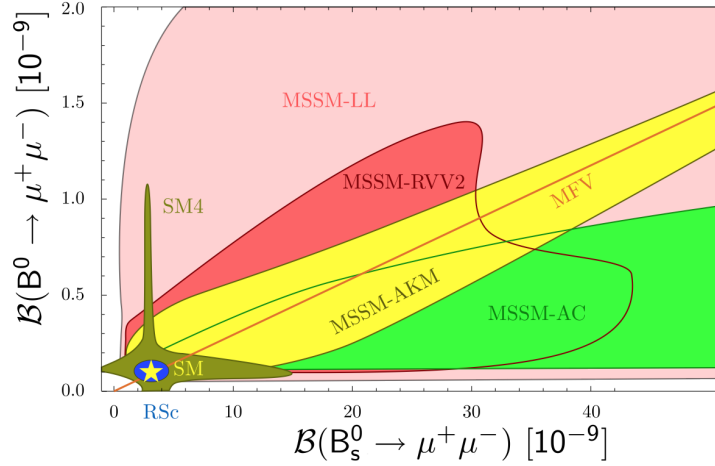
Figure 5.2: *Predictions for the branching fractions of the $B \to \mu^+\mu^-$ and $B_s^0 \to \mu^+\mu^-$ from many BSM theories and the SM.*

Both CMS [65] and LHCb [67] experiments performed search for this decay mode [115, 116]. Using the full dataset of RUN-1 both experiments managed to separately obtain a branching fraction for the $B_s^0 \to \mu^+\mu^-$ decay mode, with a significance of more than 4σ, and set limit on the $B^0 \to \mu^+\mu^-$. The combination of their measurements resulted in a measurement of
$\mathcal{B}(B_s^0 \to \mu^+\mu^-) = \left(2.8^{+0.7}_{-0.6}\right) \times 10^{-9}$ [117].

5.2   Search for the $B_s^0 \to \mu^+\mu^-$ decay with the first $2.4\,\mathrm{fb}^{-1}$

ATLAS performed a search for the decay of $B_s^0 \to \mu^+\mu^-$ with the first $2.4\,\mathrm{fb}^{-1}$ of pp collisions data at $\sqrt{s} = 7\,\mathrm{TeV}$, collected during 2011 [118]. The aim was the measurement of the $B_s^0 \to \mu^+\mu^-$ branching ratio with respect to the $B^\pm \to J/\psi K^\pm$ decay (see figure 5.13). The branching ratio is given by the formula:

$$\mathcal{B}(B_s^0 \to \mu^+\mu^-) = \mathcal{B}(B^\pm \to J/\psi K^\pm \to \mu^+\mu^- K^\pm) \times \frac{f_u}{f_s} \times \frac{N_{\mu^+\mu^-}}{N_{J/\psi K^\pm}} \times \frac{\mathcal{A}_{J/\psi K^\pm}}{\mathcal{A}_{\mu^+\mu^-}} \frac{\epsilon_{J/\psi K^\pm}}{\epsilon_{\mu^+\mu^-}} \tag{5.1}$$

where the $\mathcal{B}(B^\pm \to J/\psi K^\pm \to \mu^+\mu^- K^\pm)$ is taken from reference [29] and the f_u/f_s ratio from LHCb's measurement [119]. Although the f_u/f_s measurement is performed in a different kinematic region compared to ATLAS, it is used since the f_u/f_s ratio is

independent of p_T and η. The $\epsilon \times \mathcal{A}$ for the two channels is determined using MC. Grouping the components on the second half of the equation 5.1, it can be re-written as:

$$\mathcal{B}(B_s^0 \to \mu^+\mu^-) = N_{\mu^+\mu^-} \times \mathrm{SES} \tag{5.2}$$

where SES is the "Single Event Sensitivity".

The search for the $B_s^0 \to \mu^+\mu^-$ decay was the first blind analysis performed by the ATLAS collaboration. The reason for this, is to avoid any biases in the result. Due to this choice, the $5066 - 5666\,\mathrm{MeV}$ di-muon invariant mass region was blinded. The $5066 - 5666\,\mathrm{MeV}$ is now called signal region and the mass range out of this window is called data-sidebands.

After the blinding of the data, it was decided that only the odd-numbered events would be used for the cuts and optimisation and after the cuts were defined they would be used in the even events for the interpolation in the signal region and the extraction of the background events. This was decided in order to avoid any further biases by using the same sample for optimisation and measurement.

The analysis is performed in 3 mass resolution bins, in order to enhance the sensitivity of the analysis and exploit the improved background rejection. These categories are identified by the maximum $|\eta^\mu_\mathrm{MAX}|$, with the ranges defined as $[0 < \eta^\mu < 1.0]$, $[1.0 < \eta^\mu < 1.5]$ and $[1.5 < \eta^\mu < 2.5]$. These bins are driven by the di-muon invariant mass resolution, which is approximately 60, 80 and 110 MeV respectively.

After this procedure and all the components of the SES in equation 5.2 are determined, the data would be unblinded.

5.2.1 Multivariate analysis

The main strategy in all analyses is the discrimination of the signal from the background. This is typically done by observing variables that significantly differ between the data and the signal sample, and applying selections on these variables, where the biggest number of signal events is observed compared to background. This is usually done by applying rectangular cuts in each variable, after optimising them, using MC and background samples (either these being data-driven samples or MC). A more sophisticated way of defining these cuts, is the multivariate method (MVA) [120].

Decision trees

By taking a number i, of parameters x_i, that show significant difference between the background and signal, a function $f(x_i)$ is constructed that has useful properties for the decision making. A simple example of a two-dimensional collection of variables is illustrated in figure 5.3. From the distributions of signal and background in figure 5.3(a) is difficult to distinguish and apply a reliable cut to separate signal and MC, but by examining the dependence of the one variable to the other (figure 5.3(b)) it is evident that a linear function (in this example is called linear discriminant) can provide the most optimal signal to background discrimination.
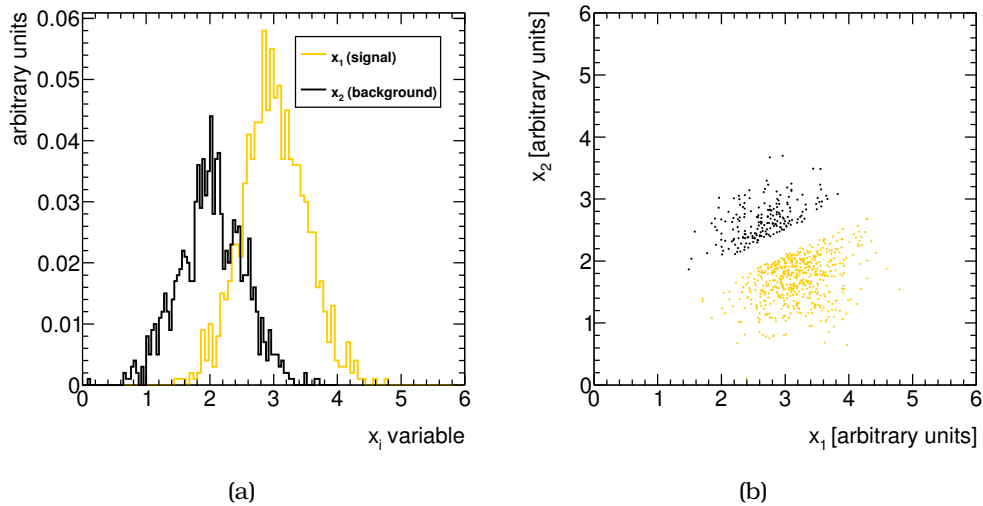
Figure 5.3: *(a) Distributions of observables x_i for signal and background. (b) Two dimensional correlation plot between x_i observables.*

A representation of a decision tree is shown in figure 5.4. The discriminating variables x_i are applied to the data, starting from the root node to sequentially split them in nodes. When the data are split, the variable that provides the best signal to background separation at this node, is used. This results in some variables to be used more often that others, based on their discriminating power. At the bottom of each tree, the leaf nodes are named as Signal (S) or Background (B), based on the number of events resulting on that node.
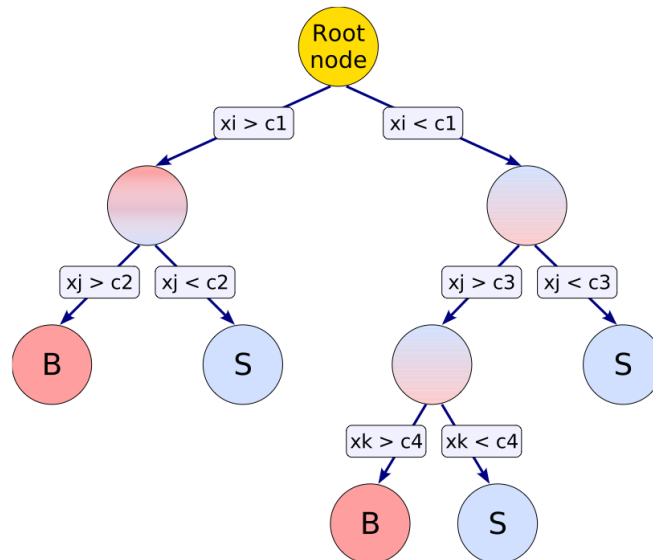
Figure 5.4: *Sketch of a decision tree.*

A type of discrimination is the Decision Trees (DT). DTs starts from a *root node* and applies sequential questions/cuts in the events. In each iteration the best derived

cut for each variable is found that gives the maximum separation between signal and background, combined into one overall best cut and then applied to the sample to further split it in two branch nodes. The search for the best criteria for each node is the training of the DT. The splitting of the samples stops when the number of events left in the nodes is too small to continue, or, in other words, there is no possible improvement in impurity. Impurity is measured with the index of $n_s n_b/(n_s + n_b)$, where the n_s and n_b is the number of signal and background events respectively in each step. When a node is split and the impurity of the new node is not better than the previous, then the splitting stops and this node is called a *leaf*.

All in all, DT is making an *i*-dimensional histogram with k bins with a response value assigned in each bin. Increasing the dataset, the bin sizes become smaller and the discrimination provided by the DT approaches the target function.

An alternative DT is the Boosted DT (BDT). The adaptive boosting assigns a larger weight in signal events that are classified as background-like compared to the events that end up in the correct node. The weights creates a new training sample, where the DT process can be repeated.

5.2.2 Multivariate analysis for signal/background separation

For the separation of signal and background in the $B_s^0 \to \mu^+\mu^-$ analysis, the MVA technique was adopted. For this, the TMVA analysis tool [120], embedded in the ROOT framework [71], was used.

As mentioned in section 5.2.1, the BDT needs a signal and background sample for the training phase. For $B_s^0 \to \mu^+\mu^-$ events a signal MC sample was generated with the full ATLAS GEANT Monte Carlo simulation [68]. The data sidebands were used as background sample. The data were collected during 2011 and include periods B2 up to K4, which corresponds to an integrated luminosity of $2.4\,\mathrm{fb}^{-1}$. The full data collected during 2011 were split in to two samples, due to trigger changes during that year.

After the BDT is trained and the BDT response is obtained (q variable), the next step that follows is the optimisation. This is done by using the estimator:

$$\mathcal{P} = \frac{\epsilon}{1 + \sqrt{n_B}},$$

where ϵ is the signal efficiency and n_B is the number of background events [121]. Since the data are blinded, the number of background events is calculated using the sideband data, after the application of the BDT cut, and interpolating in the signal region.

In the number of background events, contamination from $B \to hh$, with $h = K, \pi,$ etc, decays was estimated to be negligible. The optimisation is done in two dimensions, the BDT response (q) and the blinded window (Δm) in MeV.

5.2.3 Discriminating variables

The selection of the variables has as initial point preliminary studies performed with data collected during 2010. The variables examined were the pointing angle, calculated in 2D (α_{2D}), ΔR, defined as $\Delta R = \sqrt{(\Delta\phi)^2 + (\Delta\eta)^2}$ and the L_{xy}. Sensitivity studies were also performed with the same variables on the 2011 data and then compared with a

classifier trained only with these three variables. Since the sensitivity was proven to be better with the use of BDT, the use of the MVA tool was preferred, compared to a cut based approach.

The list of variables was expanded with the addition of more observables, in order to enhance the discriminating power of the classifier. The variables along with their description are listed in table 5.1 and shown in figure 5.5 for both signal MC and data sidebands.

Table 5.1: *Table with definitions of the variables used in the classifier.*

Variable	Definition
α_{2D}	Absolute value of the angle in the transverse plane between $\Delta\vec{x}$ and $\vec{p}^B$
ΔR	Angle $\sqrt{(\Delta\phi)^2 + (\Delta\eta)^2}$ between $\Delta\vec{x}$ and $\vec{p}^B$
L_{xy}	Scalar product in the transverse plane of $\left(\Delta\vec{x} \cdot \vec{p}^B\right)/|\vec{p}_T^B|$
ct significance	Proper decay length $ct = L_{xy} \times m_B/p_T^B$ divided by its uncertainty
χ^2_{xy}, χ^2_z	Vertex separation significance $\Delta\vec{x}^T \cdot \left(\sigma^2_{\Delta\vec{x}}\right)^{-1} \cdot \Delta\vec{x}$ in (x,y) and z respectively
$I_{0.7}$ isolation	Ratio of $|\vec{p}_T^B|$ to the sum of $|\vec{p}_T^B|$ and the transverse momenta of all tracks with $p_T > 0.5\,\text{GeV}$ within a cone $\Delta R < 0.7$ from the B direction, excluding B decay products
$|d_0^{\max}|, |d_0^{\min}|$	Absolute values of the maximum and minimum impact parameter in the transverse plane of the B decay products relative to the primary vertex
$D_{xy}^{\min}, D_z^{\min}$	Absolute values of the minimum distance of closest approach in the xy plane (or along z) of tracks in the event to the B vertex
p_T^B	B transverse momentum
$p_L^{\max}, p_L^{\min}$	Maximum and minimum momentum of the two muon candidates along the B direction

(a)   (b)   (c)

(d)   (e)   (f)

(g)   (h)   (i)

(j)   (k)   (l)

(m)   (n)
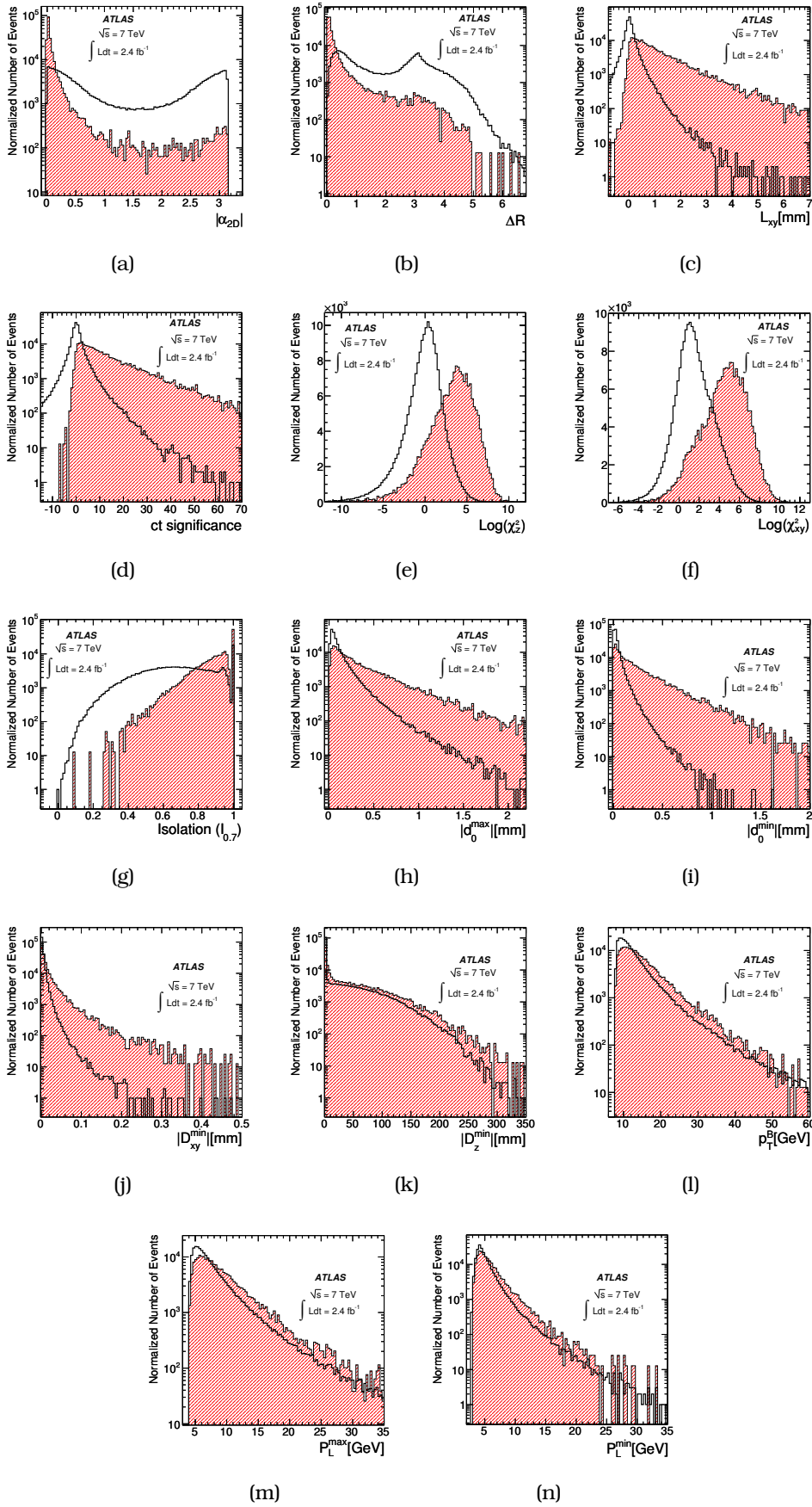
Figure 5.5: *Signal (filled histogram) and sideband (empty histogram) distributions for the selection variables described in Table 5.1. The $B_s^0 \to \mu^+\mu^-$ signal (normalized to the background histogram) is from simulation and the background is from data in the invariant-mass sidebands.*

A study was performed in order to validate that the classifier was gaining discrimination power with the addition of variables. The BDT was trained, keep the same configuration, with the three initial variables (a_{2D}, ΔR and L_{xy}) and then sequentially, the variables listed in table 5.1, were added. In each step, the efficiency of the BDT, trained with $3 + n$ variables ($n = 1, \ldots, 12$), was compared with respect to the previous trainings (trained with $3 + n - 1$ variables).

The result of this exercise is shown, for two of the 15 variables, in figure 5.6. The increase of the discriminating power of the classifier as more variables are introduced is clearly visible.

(a) (b)
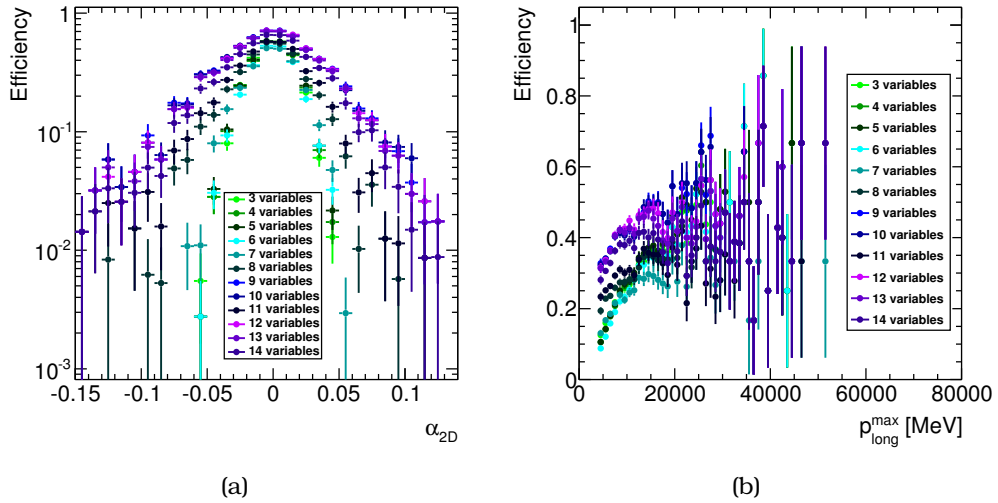
Figure 5.6: *Distributions of (a) α_{2D} and (b) $p_{\text{long}}^{\text{max}}$ as a function of the number of variables that are used in the training of the classifier. Starting with the 3 variable trained BDT (cyan) to nominal BDT training (dark purple).*

5.2.4 BDT configuration

The configuration of the BDT that showed the best performance and was chosen had the following settings:

- Number of trees in the forest: 1700;

- Maximum depth of the decision tree allowed: 2;

- Number of grid points in variable range used in finding optimal cut in node splitting: -1;

- Separation criterion for node splitting: Cross Entropy.

The response of the BDT configuration to the sideband and signal MC is shown in figure 5.7.
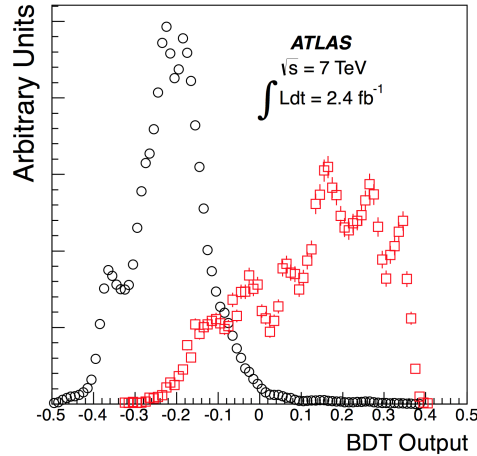
Figure 5.7: *Distributions of the response of the BDT classifier. $B_s^0 \to \mu^+\mu^-$ MC sample (squares) and data sidebands (circles).*

5.2.5 Bias checks

A classifier that use a finite data sample for training, is subject in selecting certain features of the data sample instead of the general signature of signal events. This phenomenon is called over-training and causes a bias in the event selection. For confirming that the classifier is free from such distortions, the classifier output for the training and testing events are compared (see figure 5.8). The comparison is quantified with a Kolmogorov-Smirnov (KS) test, where overtraining signatures would be indicated by values close to 0.
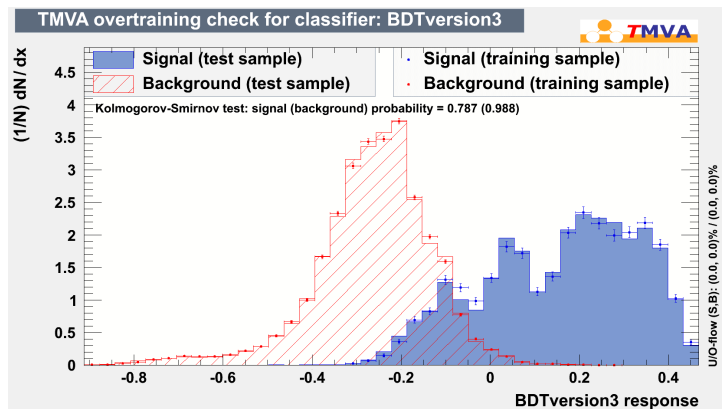
Figure 5.8: *Classifier output for signal MC (blue points and histogram) and data-sidebands (red points and dashed histogram). Points and histogram are overlaid, comparing the classifier output from the test and training sample. KS test for signal and data sidebands show results in ∼ 0.9 and ∼ 0.8 respectively.*

Another possible bias is an artificial peak formation in the signal region. This is a big headache, especially for this analysis, because it will provide a wrong estimation for the number of background events, confusing the potential artificial excess of events with signal $B_s^0 \to \mu^+\mu^-$ events. The dependence of the classifier output as a function of

the di-muon invariant mass is studied, for both data sidebands and signal MC samples. Figure 5.9 shows this dependence for data sidebands (left) and signal MC (right) and a first order polynomial that agrees with the no-dependence scenario.
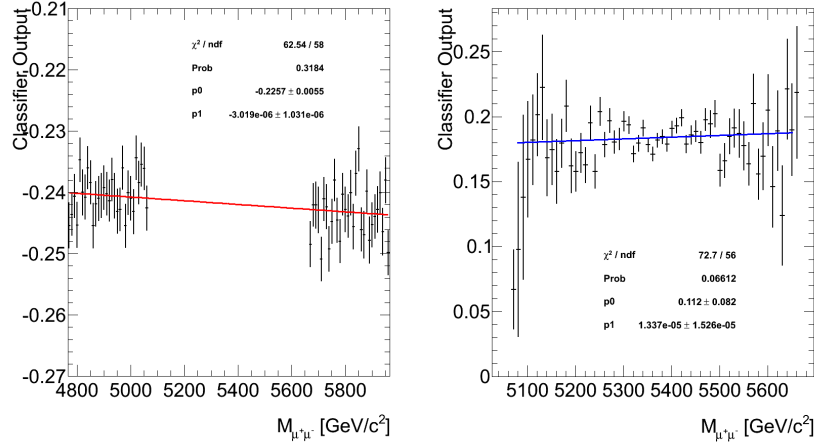
Figure 5.9: *The output of the classifier as a function of the di-muon invariant mass. Left: Data sidebands. Right: Signal MC sample.*

Bias check on a fictitious $6.5\,\mathrm{GeV}$ $\mu^+\mu^-$ **resonance**

Although it has been proven that there is no dependence between the classifier output and the di-muon invariant mass, the B_s^0 signal region is still blinded, so it is still not clear that any peaks are not created by the BDT in that region and it is not straightforward to check. For this reason, an artificial $X \to \mu^+\mu^-$ MC sample was generated, by shifting the B_s^0 mass to $6.5\,\mathrm{GeV}$. The $\pm 300\,\mathrm{MeV}$ region $[6.2 - 6.8\,\mathrm{GeV}]$ was defined as signal region and the $[5.9 - 6.2\,\mathrm{GeV}]$ and $[6.8 - 7.0\,\mathrm{GeV}]$ as the data sidebands.

The same regions were applied to the data, blinding the signal region. The shifted mass MC and the data sidebands are used in the training with the same BDT configuration as in the main analysis. The classifier output is then plotted as a function of the unblinded di-muon invariant mass window, to check if possible artificial peaks are created. Figure 5.10 shows no distortions in the signal region of the data, proving that the classifier can be used for signal to background discrimination.

5.2.6   Optimisation of the classifier output

The interpolation is done in a 6D space, due to the 3 mass resolution bins and the two variables; Δm and classifier output q. Functional forms are derived to describe signal di-muon invariant mass (third row in figure 5.11) and classifier output (first row in figure 5.11). Data sidebands q and invariant mass are shown in rows 2 and 4 respectively, of figure 5.11. The interpolations is done linearly in the di-muon data sidebands search region.

Using the interpolations, the $\mathcal{P}$ is calculated as a function of the $(q_1, q_2, q_3, \Delta m_1, \Delta m_2, \Delta m_3)$, as shown in figure 5.12.
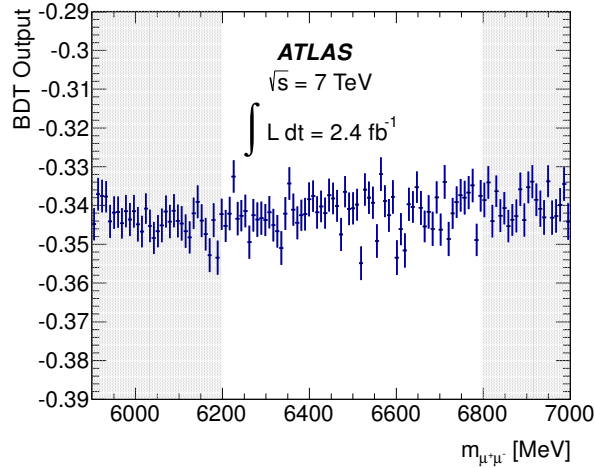
Figure 5.10: *Mean and RMS (error bars) of the BDT output in bins of di-muon invariant mass, for background events in the region 5900 to 7000 MeV, with the 6200 to 6800 MeV region not used in the training of the classifier. The BDT used is the one trained for the search of the fictitious 6500 MeV signal.*

The optimal selection is identified, and corresponds to $(q_1, q_2, q_3) = (0.2344, 0.2534, 0.2697)$ and $(\Delta m_1, \Delta m_2, \Delta m_3) = (116, 132, 171)$.

5.2.7 Extraction of reference channel yield

After the definition of the selections, the $B^\pm \rightarrow J/\psi K^\pm$ reference yield is needed for the measurement of the branching fraction $\mathcal{B}(B_s^0 \rightarrow \mu^+\mu^-)$. The extraction of the $B^\pm \rightarrow J/\psi K^\pm$ yield is done by performing a binned fit in the three mass resolution categories selected for the analysis. The fitted range is $4.93 - 5.63\,\text{GeV}$.

In the $J/\psi K^\pm$ invariant mass distribution (see figure 5.13) the signal is quite evident, but with visible contribution from at least three background sources. The first background component is coming from partially reconstructed B decays (e.g. $B^+ \rightarrow \chi_{c1} K^+$, $B^+ \rightarrow J/\psi K^*$, where one or more of the final state particles are missed in the reconstruction, see figure 5.14). This source of background dominates the region left of the signal peak. The second background component is the reflection of the $B^\pm \rightarrow J/\psi \pi^\pm$ decay with the mis-assignment of the kaon mass to the final state pion inducing a shift to higher masses of roughly the mass-difference between K and π (this component is less pronounced and appears on the right of the signal peak). Third is the combinatorial background (which MC studies suggest to be composed, after the selection cuts, mostly by $b\bar{b} \rightarrow J/\psi X$ that spans on the whole mass range, and consists of non-resonant muon pairs.

The parameterisation chosen is as follows:

- Signal: double or triple gaussian with common mean and variable relative fractions and resolutions

- Combinatorial background: first order polynomial or exponential
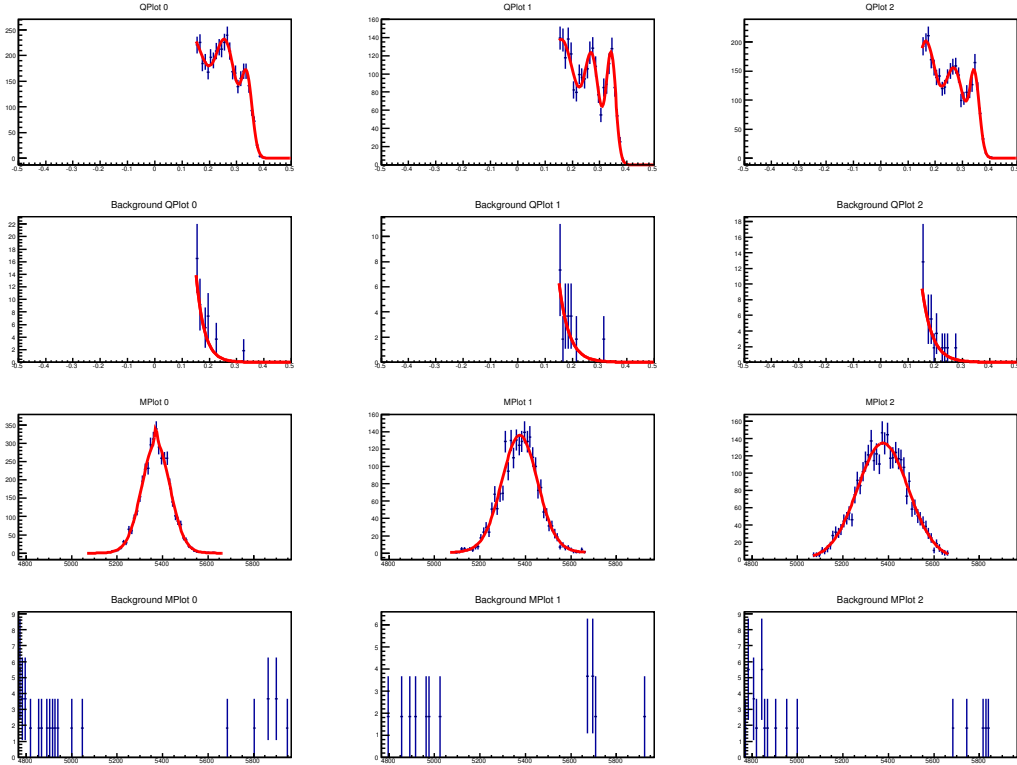
Figure 5.11: *Inputs to the optimization performed in the 6D space of multiple mass resolution categories for $(\Delta m, q)$. Each column of plots corresponds to one of the resolution categories. The first and third rows show the result of the fits to the signal MC in q (top) and invariant mass (third row). The second row shows the result of the fit to the q distribution for background events modeled with odd-numbered sideband candidates in data. The bottom row reports the invariant mass distribution for the same candidates, which is interpolated linearly in the sarch region.*

- Partially reconstructed B decays: exponential multiplied with a complementary error function

- $B^\pm \to J/\psi\pi^\pm$ mode: single gaussian with floating normalisation, mean $5360\,\mathrm{MeV}$ and $\sigma = 60\,\mathrm{MeV}$

The choice for modelling the partially reconstructed modes with not a single complementary function was based on MC studies. All the components contributing in that background were estimated and included in figure 5.14. It is clear that the additional exponential is needed for modelling the falling spectrum.

The initialisation of the shape-related parameters and the functional forms chosen were validated using MC samples.

Summarising, the results and the systematics, were calculated as the biggest difference among the initial model and all other possible variations. The results are shown in table 5.2.

For the analysis of the full 2011 data, a more sophisticated technique was used. A
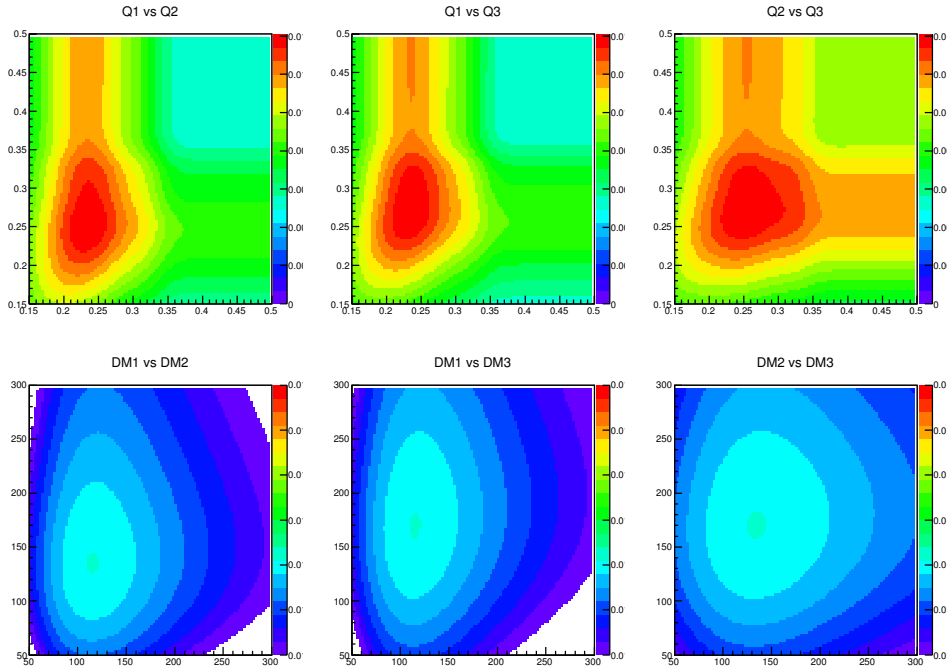
Figure 5.12: *2D projections of the 6D function $\mathcal{P}$ of the selection cuts on Δm and q on the three mass resolution categories. From top left to bottom right: q_1 vs q_2, q_1 vs q_3, q_2 vs q_3, Δm_1 vs Δm_2, Δm_1 vs Δm_3, Δm_2 vs Δm_3*
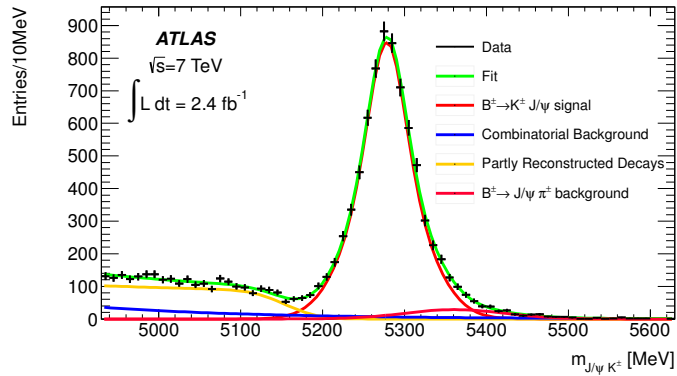
Figure 5.13: *Invariant mass of $J/\psi K^{\pm}$ pairs. Green curve corresponds to the total fit model fitted on data (black points). The components of the fit model are the $B^{\pm} \to J/\psi K^{\pm}$ signal (red line), the combinatorial background (blue line), the partially reconstructed B decays (yellow line) and the $B^{\pm} \to J/\psi \pi$ mis-reconstructed decays (magenta line).*

two-dimensional simultaneous unbinned maximum likelihood fit was adapted and is described in detail in appendix B.
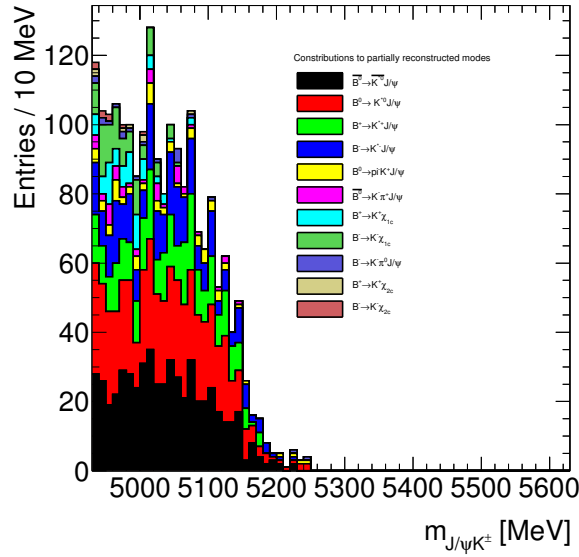
Figure 5.14: *Partially reconstructed B-meson decays contributing to the background distribution of figure 5.13, as described in MC.*

Table 5.2: *$B^\pm$ event yields for the three resolution bins and the single bin case.*

Category	yield ± stat. ± syst.	relative stat.	relative syst.	Fit probability
1	4298 ± 67 ± 120	1.6%	2.8%	41%
2	1407 ± 39 ± 22	2.8%	1.6%	93%
3	1126 ± 34 ± 33	3.0%	2.9%	21%
All	6968 ± 86 ± 91	1.2%	1.3%	82%

5.2.8 Overview of the analysis

In previous sections, the definition of the selections is described. Applying these selections to the data, all the components of equation 5.1 are derived. The extraction of the reference channel yield is described in section 5.2.7. After all the ingredients of equation 5.1 are defined, the data are unblinded. The result of the unblinding is shown in figures 5.15(a),5.15(b) and 5.15(c) for the three analysis bins. In these figures, the observed data are compared with the expected signal, multiplied with a factor of 10.

Since there is no signal observed, a lower limit was set. This was calculated to be smaller than $2.2(1.9) \times 10^{-8}$ at 95%(90%) CL.

5.3 Swap odd/even datasets technique

As it was described in section 5.2 for avoiding biases in the result, the data were split into two subsets, odd-numbered and even-numbered events. The training of the BDT was based on the odd-numbered events and the optimisation on the even-numbered events. By splitting the events in two though, the dataset used for the training shrunk,
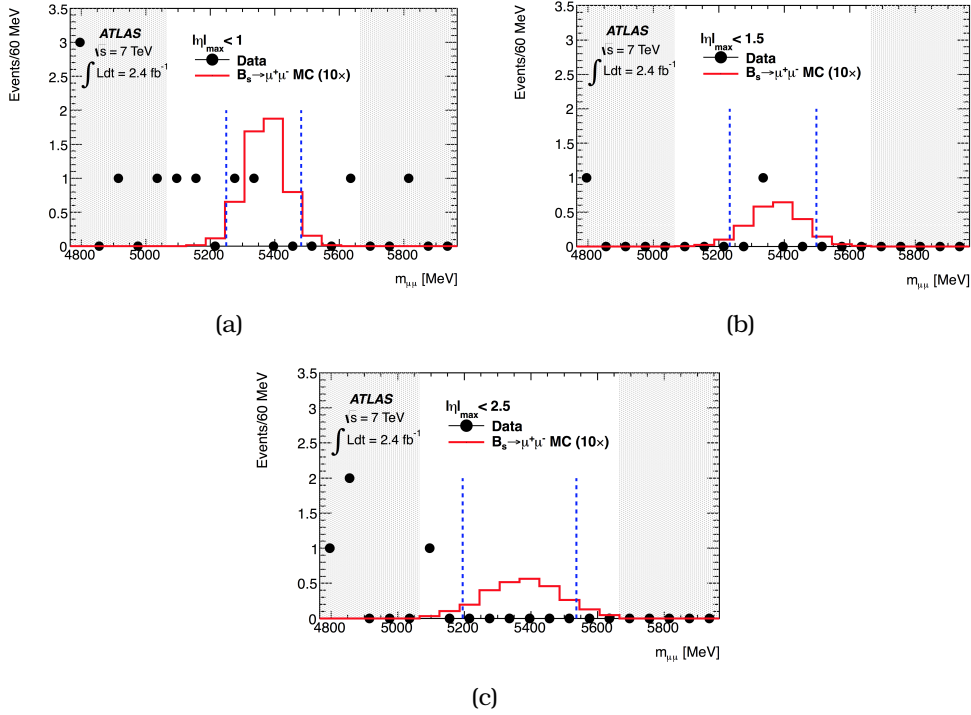
Figure 5.15: *Unblinding of the three rapidity bins.*

and with that resulted a loss in the discrimination power of the classifier.

In order to exploit the full dataset, the idea of switching the optimisation/measurement samples was proposed. In the first round of the analysis the odd events were used for train and optimisation and the even events for the measurement. The proposal suggests the even events to be used for training and optimisation and the odd events for the measurement. Then the combination of the two measurements, would improve the result.

Since the data are going to be used twice, if:

- Number of events in even-numbered events over-fluctuate

  ○ BDT will translate it and produce a more strict response

  ○ applied that to odd-numbered events will be underestimated

- Number of events in even-numbered events under-fluctuate

  ○ BDT will translate it and produce a more loose response

  ○ applied that to odd-numbered events will be overestimated

a bias will be introduced in the measurement.

In order to quantify such biases, potential correlations between the estimated background events in the odd and even sample needs to be taken into account and calculated. This correlation factor (k) is essential for the limit extraction procedure.

Correlation measurement strategy

In order to measure these correlations, without splitting in three resolution categories to simplify things, we use the following strategy:

- Perform training using odd events and extract the classifier output (q_{odd}) as shown in figure 5.16(a)

    - Optimize on odd events
    - Flucutate with a poisson and generate N_{odd} and N_{even} q_{odd} values
    - Obtain q_{odd}^{max} and ΔM_{odd}^{max} cuts optimising $\mathcal{P}$ using analytical interpolation of q distribution
    - measure $N_{background}^{odd}$

- Repeat the same procedure exchaning odd and even samples, as shown in figure 5.16(b)

    - Obtain q_{even}^{max} and $\Delta M_{even}^{max} \to N_{background}^{even}$

- Repeat this n times, where $n = 100000$

- Measure the correlation of $N_{background}^{odd}$ and $N_{background}^{even}$

(a)   (b)
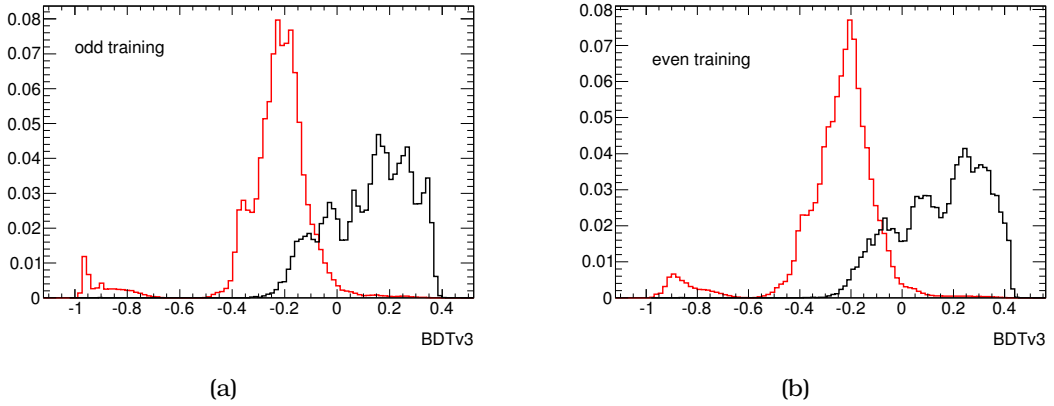
Figure 5.16: *(a) Odd-numbered and (b) even-numbered events with odd and even-numbered events used for training the classifier.*

After performing the toy MC studies we can examine the correlation between the two sets of data. This is shown in figure 5.17. The correlation factors were extracted for two different scenarios, varying the q range. The two ranges used were $q = [0, 0.5]$ and the full range. The correlation factor was calculated to be $k = 1.4 \pm 1.8\%$ for the first case and $k = 1 \pm 1\%$ for the latter.

Plugging this correlation factor to the likelihood of the limit extraction, resulted no significant enhancement in the limit.
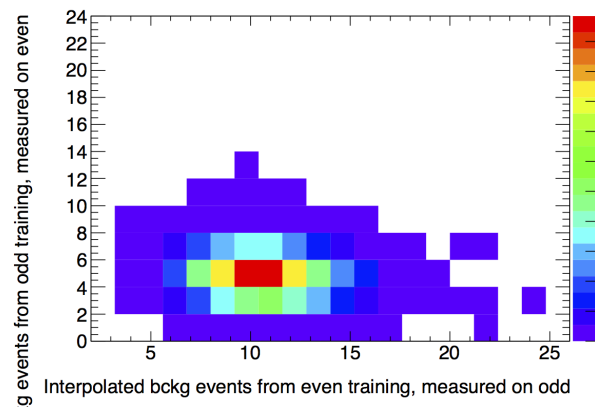
Figure 5.17: *Correlation plot of the number of number odd even etc*

6

Towards high luminosity LHC

At the end of 2012, LHC stopped its remarkable operation, after delivering the total of $28\,\text{fb}^{-1}$ of proton–proton collision data. The December of 2012 was marked as the end of Run-1 and the commence of the Long Shutdown 1 (LS1). During the shutdown of the LHC, both accelerator complex and experiments had the opportunity to upgrade and repair their apparatus and prepare for Run-2. Some of the upgrades include the vacuum system [122] for the LHC and the installation of the Insertable B-Layer [123] in the ATLAS experiment.

The LHC schedule, as illustrated in figure 6.1, includes two other long shutdowns in $2018 - 2019$ and $2022 - 2023$. LHC plan is to upgrade its complex in order to deliver $300\,\text{fb}^{-1}$ of data during Run-3 and more than $3\,\text{ab}^{-1}$ in the High-Luminosity LHC (HL-LHC) Run. ATLAS experiment has planned a series of upgrades of the detector subsystems in order to cope with the higher rates and the radiation damage on the detectors and guarantee the safe data-taking under the new conditions expected from the LHC. The foreseen upgrades include the new calorimeter [124], the Fast TracKer (FTK) [125], the TDAQ system [126] and the tracker [127].
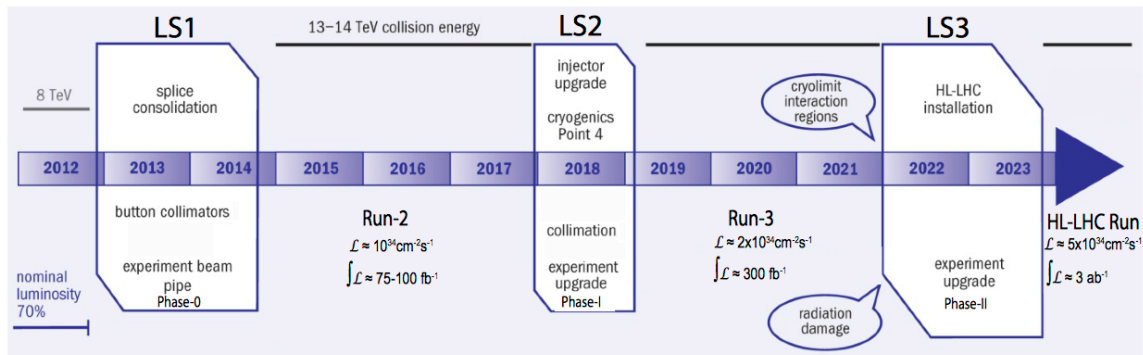
Figure 6.1: *Schedule for the LHC programme (figure taken from reference [124]).*

One of the upgrades planned for the LS2 and concerns the muon spectrometer of the ATLAS experiment, is the upgrade of the Small Wheel (SW). The SW region provides coverage in the $1.3 < |\eta| < 2.7$ range, as indicated with the orange area in figure 6.15(a).

The motivation of upgrading this part of the detector is twofold. First the improvement of the muon tracking system and second to cope with the high trigger rates expected in the HL-LHC (see figure 6.2(a)).

The efficiency and resolution of the tracking performance is expected to worsen as higher levels of cavern background is expected. The extra hits, from the SW detectors, in the track reconstruction, will improve the momentum resolution (see figure 6.2(b)).

(a)   (b)
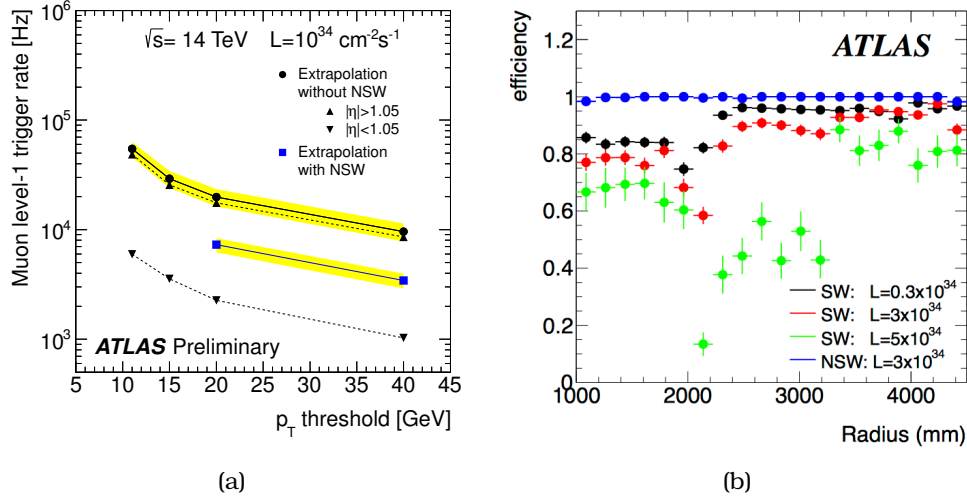
Figure 6.2: *(a) Estimated muon level-1 trigger rates at $\sqrt{s} = 14$ TeV collisions with and without the contribution of the NSW (figure taken from reference [128]) (b) Expected segment reconstruction efficiency using $Z \rightarrow \mu^+\mu^-$ decays with and without the NSW (figure taken from reference [129]).*

6.1   Requirements of the NSW

The list of requirements for the detectors that are going to replace the already existing SW starts by the fact that, the performance of the new technology at the expected environmental conditions at HL-LHC, must be as good as the current performance of the SW. That implies that the transverse momentum measurement must be accomplished with a precision of 10% for 1 TeV muons in both barrel and endcap. Other requirements include, the efficiency for segment finding to be greater than 97% for muons with $p_T > 10$ GeV, the segment position resolution to be better than 100 μm per plane and the efficiency and resolution not to degrade at high momenta or due to ageing effects.

Two detector technologies were endorsed by the ATLAS collaboration for the replacement of the Small Wheel: the Small strip Thin Gap Chambers (sTGC) [130] and the *MICRO-MEsh GA*seous Structure (micromegas) detectors [131]. The sTGC chambers were selected primarily for Level-1 triggering and the micromegas technology complements the sTGC performing high-precision tracking. The principle of work of these detectors is illustrated in figure 6.3 and explained in the next subsection.
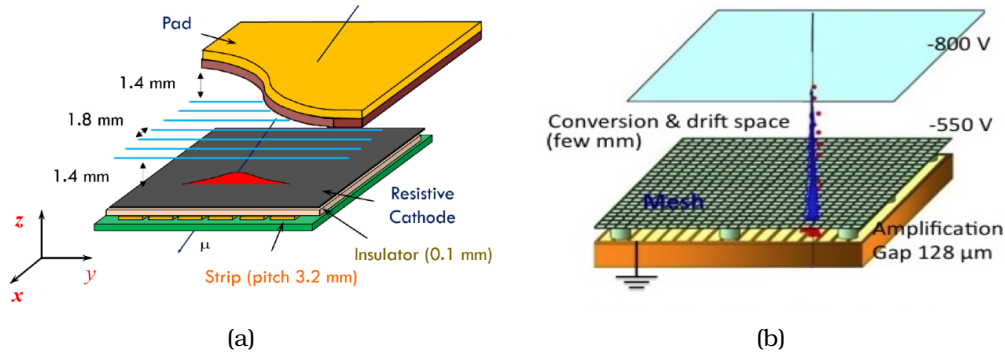
Figure 6.3: *Graphic representation of the operation principle of the two detectors chosen for the NSW. (a) sTCG (figure taken from reference [132]) and (b) micromegas detector (figure taken from reference [133])).*

6.1.1 NSW layout

The NSW will feature 16 detector planes in two multilayers, with each plane including four sTGC and four micromegas detectors. Although both technologies will perform tracking and triggering, the sTGC will be used primarily for triggering and the micromegas for tracking. This implies the configuration in the NSW to follow the sTGC-micromegas-micromegas-sTGC format. To ensure the reliable reconstruction of muon tracks, against background neutrons, photons and δ rays, eight planes per detector was necessary.

6.2 The sTGC detector

The sTGC operation principle is the same as the multi-wire proportional chambers. As the particle passes by the gas gap, it ionises the surrounding atoms and the resulting electrons are accelerated, due to the electric field, creating secondary avalanches. These electrons cause signals in the three different readouts of the sTGC detectors.

The sTGC is a gas ionisation chamber with a 2.8 mm gas gap, operated with $CO_2 + n - C_5H_{12}$ 55 : 45 as gas mixture and features multiple readouts. Pads (~ 10 cm × 80 cm), that provide a very fast signal for the bunch crossing identification, readout strips (3.2 mm pitch) for a more accurate position measurement and wires (1.8 mm pitch) to improve the offline reconstruction.

6.3 The micromegas detector

The micromegas detector was first proposed by Y. Giomataris et al. [134] in the late 90s. A schematic of the micromegas detector is illustrated in figure 6.3(b). Micromegas is a gaseous, two-stage parallel-plate avalanche chamber, with an amplification gap of the order of 100 μm and a drift gap, of the order of 5 mm. The structure of the micromegas technology includes anode copper strips, with a width of the order of 300 μm. The drift

and the amplification gap are separated with a mesh (micromesh). The micromesh sits on pillars, separated by about 2.5 mm. The gas used is for its operation is Ar : CO_2 93 : 7.

The operation principle of the micromegas detector is shown in figure 6.3(b). When a particle enters the drift gap, it interacts with the gas and ionises its molecules. The gas ionisation creates electrons, that under the electric field effect go towards the micromesh, and positive ions that are induced, head towards the cathode electrode. After the micromesh, the electrons are found in the amplification gap, where secondary ionisations occur and the charge induced is collected by the readout strips.

For the high-rate environments of the LHC, an improved version of the micromegas detectors was realised [135]. Its novelty is the use of a resistive (protective) layer with a set of strips that is placed on top of the copper strips. This novelty of the separated strips creates the advantage that the charge is not collected by a single strip, but spreads and collected by many, avoiding unwanted discharges, possibly created by large charge depositions.

The micromegas detector, that was endorsed by the ATLAS collaboration, was the product of a continuous effort of the *M*uon *A*TLAS *M*icro*M*egas *A*ctivity (MAMMA collaboration). For the continuous research and development of the detector, a series of test-beam activities were planned, realised in experimental facilities, including NCSR Demokritos, DESY, CERN Proton Sychotron (PS) and CERN Super Proton Sychotron (SPS) [136]. An example setup of the these test-beams can be seen in figure 6.4. These test-beams featured micromegas detectors with various characteristics. Although the aim of these tests was the study of the characteristics of the micromegas like the spatial resolution (described in section 6.3.2) and the efficiency (described in section 6.3.4), many other interesting results came up from these R&D efforts (see appendix C).
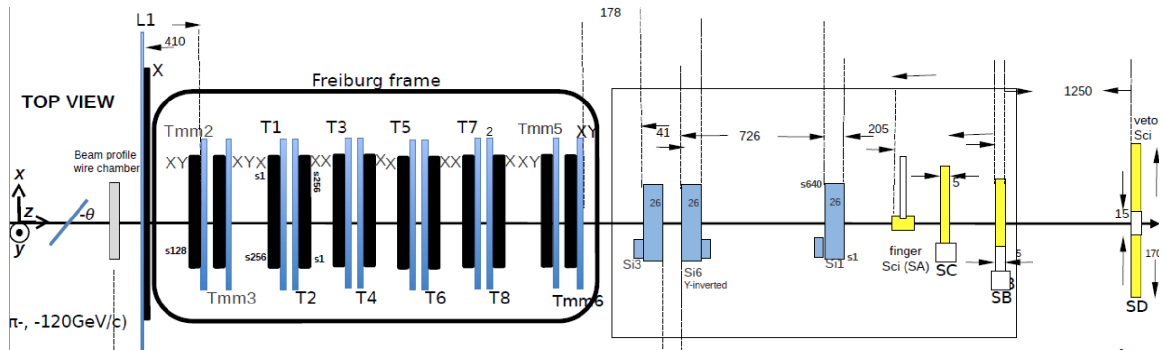
Figure 6.4: *Test beam setup at CERN H6 test-beam line. The micromegas detectors, mounted in a frame, are shown inside the oval shape. Scintillators (shown with yellow) are used for triggering and silicon modules were further employed for high-precion track reconstrucion (marked as blue boxes).*

6.3.1 Clustering algorithm

The strips are fired when charge is induced by a particle crossing and creating a charge avalanche. Consecutive strips that receive charge, allowing for empty strips in between,

are summed up to form a cluster. The centre of the cluster position is given by $x_{\text{cluster}} = \sum x_i q_i / \sum q_i$, with x_i being the number of the strip fired and q_i its corresponding charge.

6.3.2 Spatial resolution

The spatial resolution characteristic can be checked with two methods: the centroid and the µTPC. The centroid method is based in the difference of two clusters formed by two similar detectors. The difference of the two clusters gives the residual distribution, of which the width divided by $\sqrt{2}$ gives the intrinsic resolution of the detector. The centroid method, as the angle of incoming particle increases, becomes more and more unreliable, due to increasing multiplicity of the strips.

In higher incoming angles, the µTPC method is used. This method use the charge distribution of each strip and the drift velocity of the electrons, in order to reconstruct space points inside the detector. These space points form a tracklet.

The time for each hit is extracted from fitting the charge distributions with a Fermi-Dirac function

$$\text{FD} = \alpha \frac{1}{1 + e^{-\frac{x-t}{\sigma}}} + \beta$$

The choice of the space points are selected after a series of quality selections and further improved by other analysis techniques (like the Hough transform [137]). After the formation of the tracklets in two chambers, two points, one in each detector, are compared in order to form the residual distribution, from which the resolution is extracted.

The centroid method shows a resolution of about 100µm for incident particles of 10° increasing to ∼ 600µm for 40°. The µTPC method shows a resolution of about 100µm for incoming particles with angles 10° − 40°, decreasing with the larger angles.

The two methods described above can be combined, resulting in spatial resolutions bellow 90µm for incident angles between 10° and 40°. The combination of the two methods is performed using the formula

$$\sigma_{\text{comb}} = \frac{w_{\mu\text{TPC}} x_{\mu\text{TPC}} + w_{\text{centroid}} x_{\text{centroid}}}{w_{\mu\text{TPC}} +_{\text{centroid}}}$$

where $w_{\mu\text{TPC}} = (N_{\text{strip}}/N_{\text{cut}})^2$ and $w_{\text{centroid}} = (N_{\text{cut}}/N_{\text{strip}})^2$. The variable N_{strip} shows the size of the cluster of each track and the N_{cut} is a constant set for this analysis equal to 4. With this way if $N_{\text{strip}} > N_{\text{cut}}$, then $\sigma_{\mu\text{TPC}}$ dominates and if the $N_{\text{strip}} < N_{\text{cut}}$ the centroid method dominates. The results of all three methods are summarised in figure 6.5.

6.3.3 Examining the geometric mean method for the extraction of spatial resolution

There is a third method for the extraction of the spatial resolution, using hits collected by more than three chambers and perform tracking. The so called "geometric mean method" is a method that was applied for the extraction of the spatial resolution of a
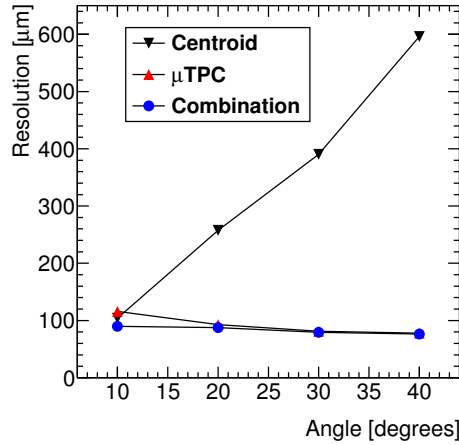
Figure 6.5: *Spatial resolution of the micromegas detector using the centroid (black triangles) and μTPC (red triangles) methods and their combination (blue circles).*

GEM[1] detector [139, 140] and in performance studies of the micromegas detector [141, 142].

The geometric mean method uses a track, formed by hits on the detectors included in the experimental setup (see figure 6.6). There are two ways in forming the track, either using, or excluding, the hit from the test chamber.
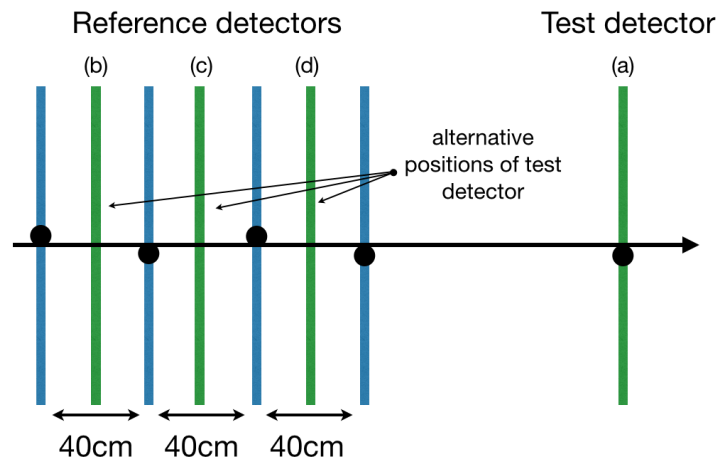
Figure 6.6: *An example of the track formation using hits reconstructed on all chambers. Configuration used for the modeling of the MC.*

When the hit from the test detector (x_i), is excluded from the track fit, and having an extrapolated position in this chamber from the track ($\hat{x}_i$), the residuals are given by

$$\Delta x_i = x_i - \hat{x}_i$$

---

[1]Gas Electron Multiplier (GEM) is a gaseous detector [138] widely used in nuclear and high energy experiments.

The variance of the residuals, and since the x_i and $\hat{x}_i$ are uncorrelated variables, is

$$\sigma_{\text{ex}}^2 = \left\langle (\Delta x_i)^2 \right\rangle = \sigma_{x_i}^2 + \sigma_{\hat{x}_i}^2, \tag{6.1}$$

σ_{x_i} reflects the true detector resolution and $\sigma_{\hat{x}_i}$ is the tracking uncertainty.

When the hit in the test chamber (x_i) is included in the track fitting, the position is given by the weighted mean

$$\hat{x}'_i = \frac{w_{\hat{x}_i} \hat{x}_i + w_{x_i} x_i}{w_{\hat{x}_i} + w_{x_i}}$$

where the weights w_{x_i} and $w_{\hat{x}_i}$ are the corresponding weights and given by $1/\sigma_{x_i}^2$ and $1/\sigma_{\hat{x}_i}^2$. The variance of the $x_i - \hat{x}'_i$ is

$$\Delta x'_i = x_i - \hat{x}'_i = \frac{\sigma_{x_i}^2}{\sigma_{x_i}^2 + \sigma_{\hat{x}_i}^2}(x_i - \hat{x}_i) = \frac{\sigma_{x_i}^2}{\sigma_{x_i}^2 + \sigma_{\hat{x}_i}^2} \Delta x_i$$

Its variance is

$$\sigma_{\text{in}}^2 = \left\langle \left(\Delta x'_i \right)^2 \right\rangle = \frac{\sigma_{x_i}^4}{\sigma_{\hat{x}_i}^2 + \sigma_{x_i}^2} \tag{6.2}$$

Calculating the standard deviation of the residuals, including the test detector in the fit, will bias the result in favour of smaller resolution values (σ_{in}). Excluding the test detector hit from the fit will result in a systematically larger resolution (σ_{ex}). The combination of the equations 6.1 and 6.2, gives the estimated true resolution:

$$\sigma^2 = \sigma_{\text{in}} \sigma_{\text{ex}} \tag{6.3}$$

For the validation of this method, a MC algorithm was used [143]. The algorithm is based on test-beam setups and its aim is either to validate the geometric mean method or to indicate and quantify possible biases.

Description of the simulation

Following the test-beam setup, the simulation algorithm features five detectors. Four of them are used as reference chambers with the fifth being the detector under study (test detector). As illustrated in figure 6.6, the reference chambers are placed perpendicularly to the incoming particle beam and separated by equal distances of 40 cm. The reference chambers are supposed to have the same characteristics (same spatial resolution) and follow the micromegas capabilities. Three possible configurations are used with $\sigma_{\text{intrinsic}} = 50\,\mu\text{m}$, $75\,\mu\text{m}$ and $100\,\mu\text{m}$).

In order to test the geometric mean method, the intrinsic resolution of the test chamber is varied from $35\,\mu\text{m}$ to $215\,\mu\text{m}$ in steps of $20\,\mu\text{m}$. In each step, the resolution of the test chamber is extracted, using equation 6.3, and compared to its true resolution.

Assuming 100% efficiency in all five detectors, single hits are generated for each chamber and then smeared with a gaussian, that follows each considered scenario for each event. According to reference [139] we use the hits on the chambers to form two tracks. First by fitting only the hits from the reference detectors (*excluded* track) and a

second track using all five hits coming from the reference and test chambers (*included* track).

Residual distributions calculated from the distance of the test detector's hit position from the *included* and *excluded* track are fitted with a single gaussian function to extract the σ_{in} and σ_{ex} resolutions. The two are then combined using equation 6.3, in order to extract the resolution of the test chamber.
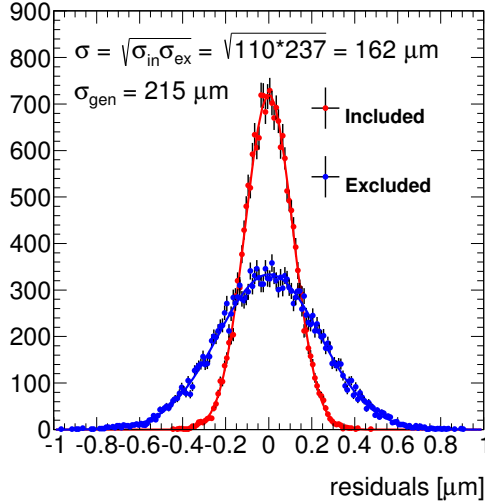
Figure 6.7: *Spatial resolution plots using the two tracks, including (red points) and excluding (blue points) the hit from the test detector in the track fit. Both distributions are fitted with a gaussian function.*

An example of this procedure is illustrated in figure 6.7, where a sample of $10\,000$ events is presented. In this example, the intrinsic resolution of the test chamber is chosen to be $215\,\mu$m and of the reference chamber $100\,\mu$m. The distribution of blue points reflects the residuals of the *excluded* track from the test chamber and the red points the *included* distribution. The σ_{in} and σ_{ex} resolutions extracted are found to be $110\,\mu$m and $237\,\mu$m respectively, leading to a combined resolution of $162\,\mu$m by using the geometric mean method (compared to the true $215\,\mu$m).

Results

The comparison of the extracted and the intrinsic resolution for all steps, is illustrated in figure 6.8(a). The three different scenarios - three different resolutions for the test chambers are displayed with three different colours. The true resolution of the test chamber is shown in the *x*-axis and the reconstructed using the geometrical mean method in the *y*-axis. Results show that the combination is unbiased only when all the chambers have the same spatial resolution (crossing point of blue/red/black points with the diagonal). In all other situations the results are biased, either reflecting better performance when the reference chambers are better than the chamber under test either showing worst characteristics when the reference chambers are worst than the test chamber.
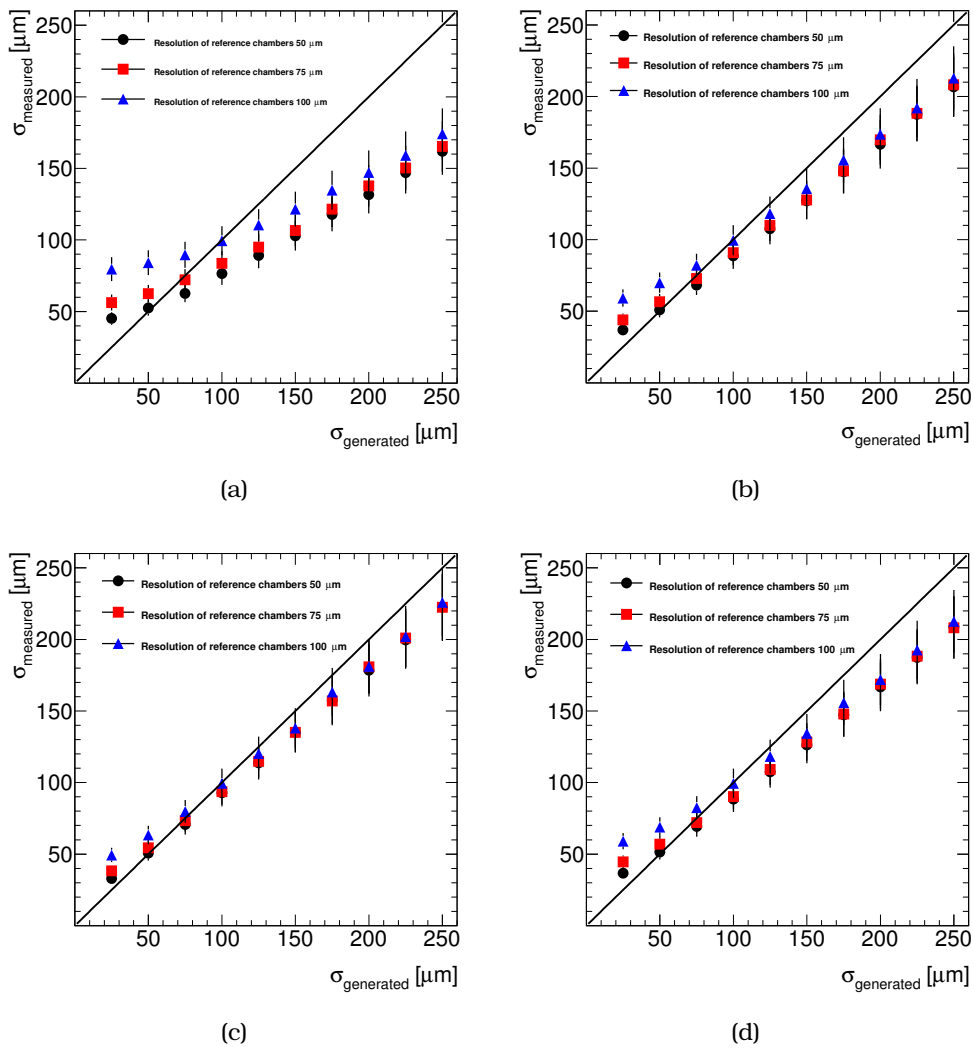
Figure 6.8: *(a) Comparison of measured and generated resolution, assuming three different scenarios. With the black circles the reference detectors are modelled to have 50 μm resolution, with red squares 75 μm resolution and with blue triangles 100 μm resolution. The black line assumes that the generated value is equal to the measured. (b), (c), (d) Same as Figure 6.8(a), but the test chamber positioned in the alternative positions (b), (c) and (d), respectively (see Figure 6.6). The errors on all figures are multiplied by 10 in order to be visible.*

The same idea was used in order to check if the positioning of the test chamber can affect the outcome of this exercise. For this, the position of the test chamber is altered using the (b), (c), (d) positions as illustrated in figure 6.6. Although the results show a smaller effect on the bias of the extracted resolution, still the effect is visible (see figures 6.8(b),6.8(c) and 6.8(d).

Figures 6.8(b) and 6.8(d) correspond to positions (b) and (d) and were used as a validation of the algorithm. The results are the same, as it was expected.

The last test was to check the dependence of the geometric mean method from the distance between the detector under test and the reference chamber. For this

test, the true resolution of all five detectors is fixed to $70\,\mu$m and the distance of the test detector is varied from the rest of the chambers in a fraction of the distance that separates the reference chambers. Starting from 25% it is moved up to 475% in steps of 25%. The results are shown in figure 6.9 and show that the geometric mean method is independent of the distance between the reference and test chambers.
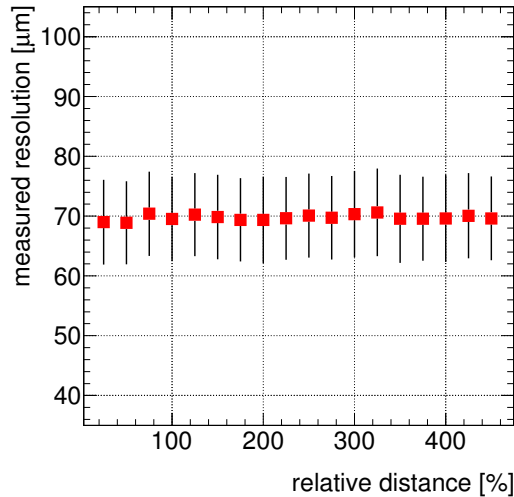
Figure 6.9: *Calculated resolution using the geometric mean method as a function of the distance of the test detector from the reference detectors. Errors on both figures are multiplied by 10 in order to be visible.*

6.3.4   Efficiency of the micromegas detector

The efficiency of the micromegas detector has been tested using data collected in test-beam activities of the MAMMA collaboration. For the efficiency measurements a test-beam setup of more than 5 detectors placed in a particle beam in a row was used. Three types of efficiencies are defined, in order to evaluate the performance of the micromegas detector. This is done in order to study the reconstruction of clusters (clusters required to have more than two strips fired) in all reference chambers. After selecting events where all reference chambers have a single reconstructed cluster (see figure 6.10(a)), the three different categories of inefficiencies are defined as:

- *Hardware*: not a single hit found in the test chamber

- *Cluster*: not a single cluster found in the test chamber

- *Software*: not a single cluster found in the test chamber, within 1 mm from the extrapolated position of the track reconstructed from hits in the reference chambers

The first type of inefficiency is caused primarily when the particle which crosses the chambers, hits the pillars. This is obvious in observing the extrapolated position of the

track formed by the reference chambers, to the test chamber, when not a single hit is found (figure 6.10(b)). The peaks correspond to the pillar structure, separated by 5 mm, equal to the pillar spacing of the micromegas detector.
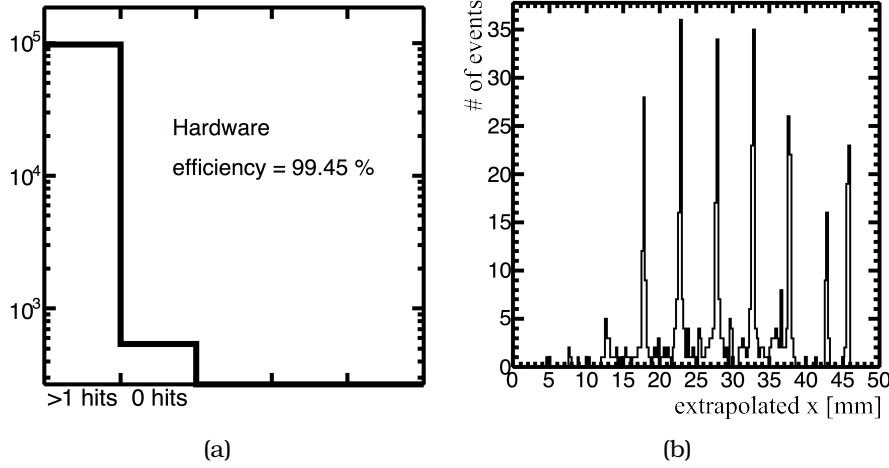
Figure 6.10: *(a) Efficiency (b) pillar structure*

Efficiency was found to be better than 99% for all three definitions. The $\sim 1\%$ geometrical inefficiency, for perpendicular tracks, is created from the pillars structure. In the case that the test chamber is tilted, with respect to the incoming particle, due to the charge spread in more strips, the efficiency increases. The results from all inefficiency definitions are summarised in table 6.1.

Table 6.1: *Table with micromegas efficiencies*

	Type of efficiency		
Placement towards the beam direction	Hardware	Cluster	Software
Perpendicular	99.45%	99.22%	98.63%
30°	99.90%	99.63%	99.28%

6.3.5   Study of misaligned resistive and readout strips

The possible deformations/misalignments of the resistive and the copper strips (as described in section 6.3) were studied with the use of a dedicated chamber (TQF). The TQF chamber features four different areas with custom resistive-readout strip alignment. One quadrant has the standard configuration, the second uses a half-pitch and the two others have the readout strips tilted by 1° and 2° degrees with respect to the resistive strips. This configuration makes the resistive strips to cross more than one readout strips and this can be seen by the correlation of the residuals on the precision coordinate and the extrapolated hit in the second coordinate (see figure 6.11). The period of the modulation ϕ' is expected to be pitch/$\tan\theta \approx 23(11)$ mm, with $\theta = 1°(2°)$.
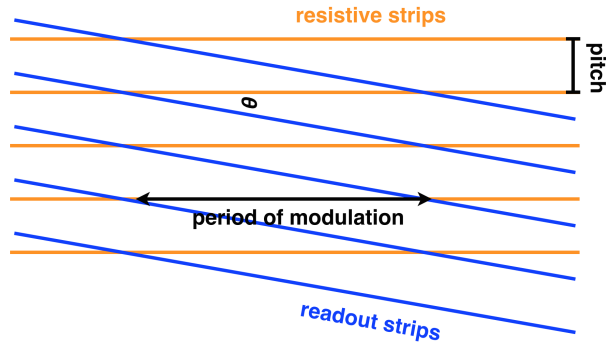
Figure 6.11: *Sketch of the strip configuration of the TQF chamber.*

In order to measure this, data collected on the summer of 2014 at the PS with the TQF chamber were used. During this test-beam, the experimental setup had four Tmm chambers. Requiring single cluster events in all four chambers, a track is formed and then the correlation between the residuals in the x-axis and the extrapolated position in the y is checked. This distribution is the fitted by $\delta x = p_0 + p_1 y + p_2 \sin\left(p_3 y + p_4\right)$, from which p_2 is the size of the modulation and the period of modulation is given by $2\pi/p_3$.

Sizeable effect on the hit reconstruction measured to be of the order of $15\,\mu$m. The period of the observed modulation is $2\pi/p_3 = 25\,(10)$ mm for the one and two degrees area, respectively, in agreement with what expected.
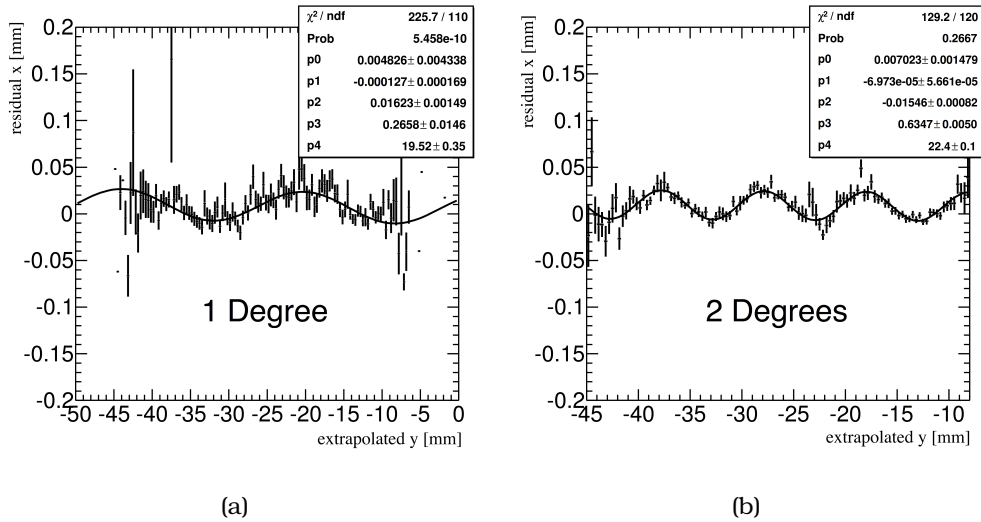
Figure 6.12: *Correlation between the residuals in the x-axis and the extrapolated position in the y for the (a) $1°$ (b) $2°$ regions of the TQF chamber.*

6.3.6 Test under magnetic field

Since the NSW will be inside a magnetic field, the understanding of the micromegas detector under the magnetic field is essential. The results of the Lorentz angle as a function of the electric field, obtained with Garfield simulations [144] are compared to data measurements. The beam profile due to the effect of the Lorentz angle is expected to be displaced by $\delta x = d \tan \theta_L / 2$, where d is the drift gap.

Using the displacement of the cluster position, defined by the centroid method, for the $0\,\text{T}$ and $1\,\text{T}$, $2\,\text{T}$ situations, the Lorentz angle is calculated. The results are compared with what is expected from Garfield simulations in figure 6.13 for electric fields of $0.6 - 2\,\text{kV/cm}$.
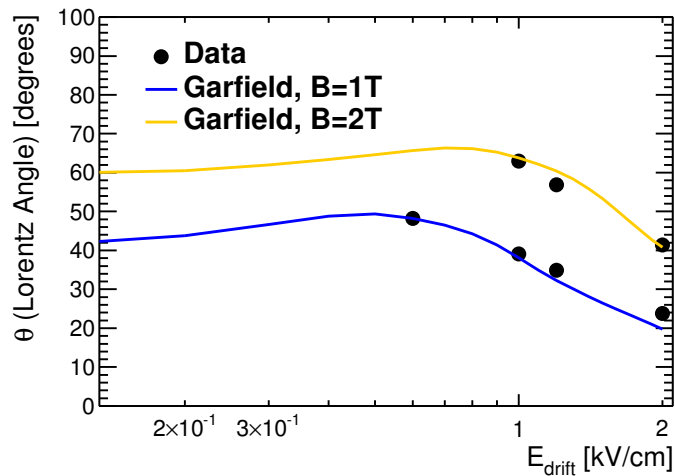
Figure 6.13: *Lorentz angle as a function of the electric field.*

6.4 Integration of the NSW in the ATHENA framework

The performance of the NSW, as an integrated unit, needed to be tested. For this purpose, the NSW was integrated in the ATHENA framework in order to create MC samples simulating its response in pp collisions. This process was done following three steps, same as described in section 2.4.1: the definition of the new geometry, the hit deposition and the detector response (digitisation). The first one refers to the creation of the NSW entity in the already existing infrastructure of the ATLAS experiment. The hit deposition is the modelling of the physics processes and the energy deposition in the sensitive area of the detectors, and the digitisation refers to the simulation of the detector response in order to reproduce the detector functionality.

In the digitisation process all the information from particles crossing the active area is saved. Particles refer not only to muons, but also muon related secondaries, like electrons.

For the needs of the NSW Technical Design Report (TDR) [129], the full digitisation option was rejected for the sake of a fast-digitisation process. The response of the

detector was based on a function of smearing the true position of the hits, based on the incoming angle on the active area. Detector resolution followed the test-beam results (see section 6.3). The true hits on the detector received a smearing, using a gaussian with a width defined from the formula:

$$\sigma = \left(-\frac{0.001}{3}\theta + \frac{0.28}{3} \right)\mu m \tag{6.4}$$

assuming a linear dependence of the resolution as a function of the incoming track angle with $\sigma = 90\mu m$ for $\theta = 10°$ and $\sigma = 80\mu m$ for $\theta = 40°$ (see figure 6.14(c)).

The algorithms were validated comparing the results with the results from test-beam studies. The strip multiplicity as a function of angle, as presented in figure 6.14(a) is in good agreement with what was found in test-beam data. Other validation studies included angular distributions and energy of the incoming muons, as both variables could hint biases in the MC reconstruction. This is illustrated in figure 6.14(b) where the incoming angle is indeed what is expected from the geometry of the NSW and the energy is what was expected from the MC truth sample. A last cross-check was to test the distribution of the smearing that the hits received. According to equation 6.4 the hits received a smearing of that is a function of the incoming angle. The average smearing of all hits is shown in figure 6.14(c) is of the order of 88 μm, in agreement with the expected resolution.

6.5   Micromegas in the ATLAS experiment

Except for the capabilities of the micromegas detector mentioned above, the ageing of micromegas was an important aspect that was studied in specialised facilities with X-ray, neutron and alpha exposure [145]. Another excellent opportunity to study the micromegas chamber, under realistic LHC conditions, was the ATLAS cavern during the LHC operation.

Five small micromegas chambers were installed in the ATLAS experiment on the February of 2012. One of them was an MBT type detector, featuring two-gaps and an active area of $9 \times 4.5\,cm^2$. The MBT was installed in the high-rate environment in front of the electromagnetic end-cap calorimeter, with a distance of 3.5 m from the interaction point in the z direction and $r \sim 1$ m in radius (see figures 6.15(a) and 6.15(b)). The other four detectors were attached in the SW, at about 1.8 m further from the beam pipe.

6.5.1   Data

The data were collected from March 2012 to February 2013 and read-out by APV25 hybrid cards [146] through the Scalable Readout System [147]. The high voltage settings used were independent of the LHC beam conditions and the current was monitored through the CAEN SY1527 HV system using the A1821 HV module with a monitor current resolution of 2 nA (see Figure 6.16). The data recorded correspond to 15 fb^{-1} of integrated luminosity.

Figure 6.17 shows the MBT current together with the ATLAS luminosity for one day of data taking. The structure of the spill is clearly visible as well as the correlation

(a)

(b)

(c)
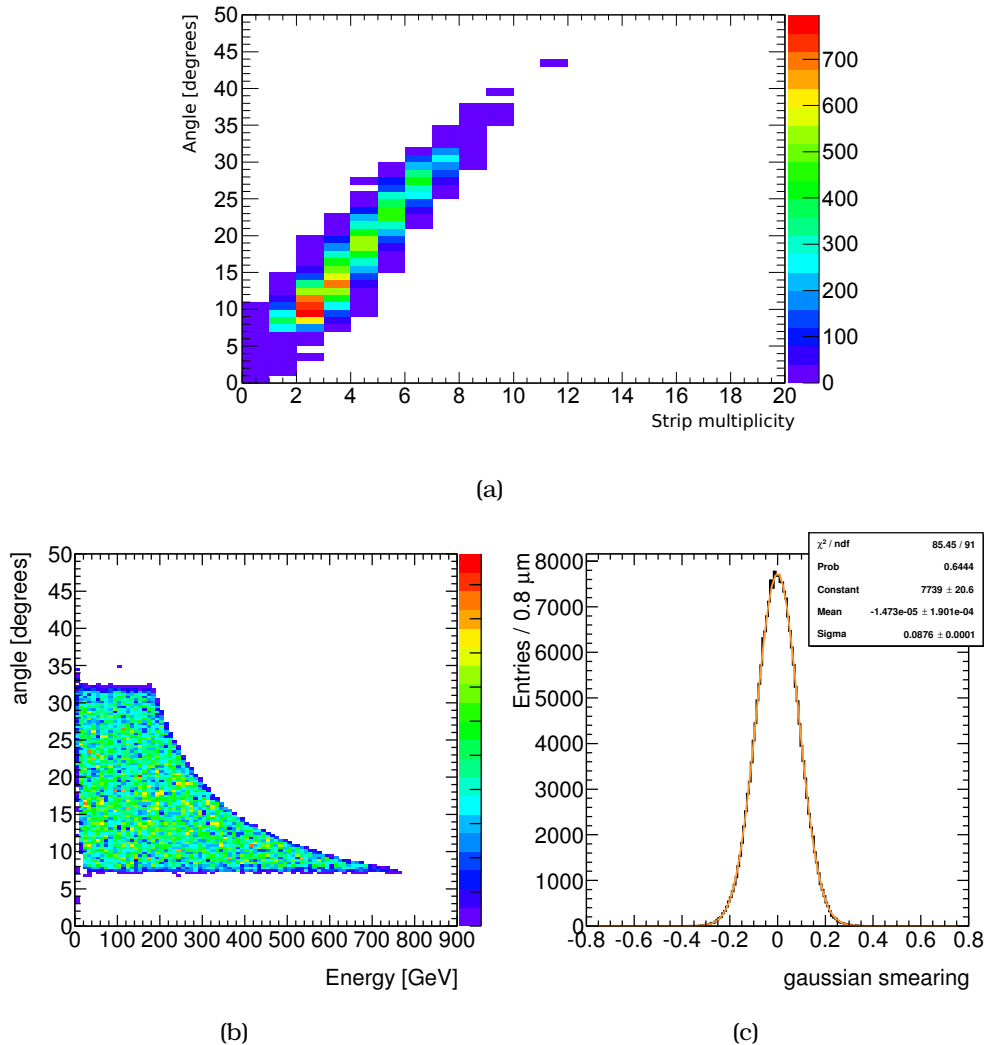
Figure 6.14: *(a) Angle as a function of strip multiplicity. (b) angle as a function of energy (c) gaussian smearing that the hits received*

between the current and luminosity. The lower plot shows for the same day the correlation plot between the current (black points) and the luminosity and a first order polynomial fit is overlaid.

In order to check possible ageing effects, the relation of luminosity and the MBT current is checked. Splitting the full data-set in three different ranges of luminosity $(0.20 - 0.21, 0.30 - 0.31$ and $0.40 - 0.41 \times 10^{34}\,\mathrm{cm}^{-2}\mathrm{s}^{-1})$, it is found to be constant between May and end of August 2012, as shown in figure 6.18.

Extrapolating the data from a single day as shown in figure 6.17 to the full dataset (see figure 6.19(a)) the correlation between the MBT current and the ATLAS luminosity is extracted. The linear fit applied to the full dataset reports an intercept of -6 nA and a slope of $0.56\,\mu\mathrm{A}/10^{34}\,\mathrm{cm}^{-2}\mathrm{s}^{-1}$.

An interesting phenomenon, observed in figure 6.19(a), is that the linear fit overshoots the data in the high luminosity - high current data. In order to examine this behaviour the micromegas current is spit in slices of 50 nA, starting from 50 nA and

(a)   (b)
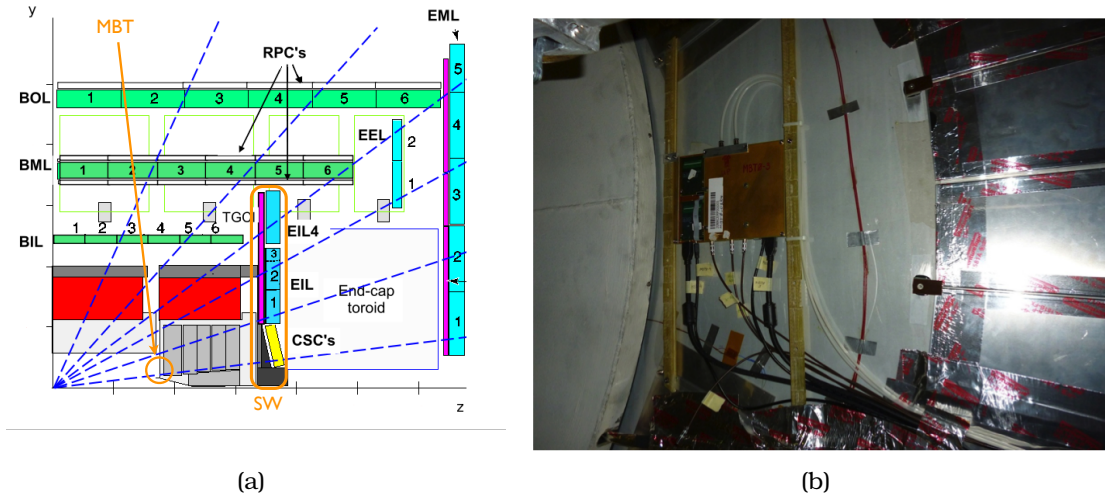
Figure 6.15: *(a) Sketch of the ATLAS detector. The place where the MBT chamber was installed is indicated with an orange arrow. (b) MBT chamber installed in front of the LAr calorimeter.*
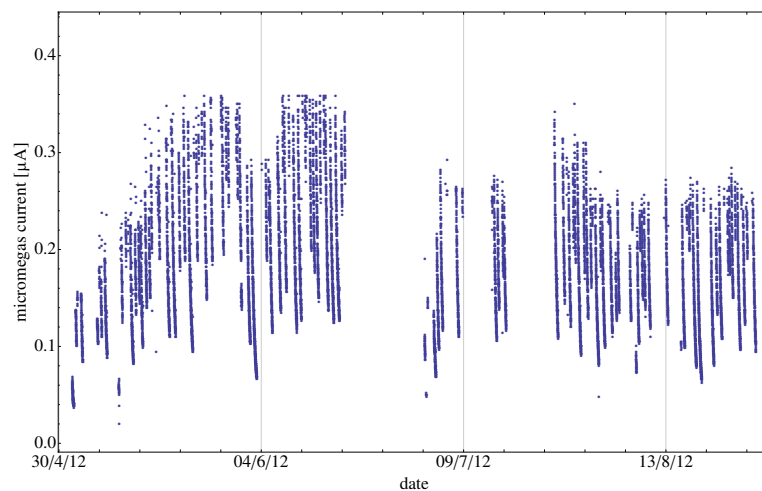
Figure 6.16: *An example of the MBT currents as a function of time starting from early May until September. The structure of the LHC fills is clearly visible.*

going up to 350 nA, and fit the correlation data of the micromegas current versus the ATLAS luminosity data. The slopes are extracted from the first order polynomial fits and examined as a function of the MBT currents (see 6.19(b)). The trend of the data-points clearly demonstrates the non-linearity in the high current area.

As the current of the MBT chamber increase the slope extracted decreases. This is due to the voltage drop along the resistive strips, because of the high strip resistivity (300 MΩ/cm) and the base resistance of 100 MΩ. At the higher rates, an average voltage drop (~ 1 V) is expected (gas gain drop of 4%).

By showing the clear correlation between the MBT current and luminosity, it is proven that the micromegas detector can be used for luminosity measurement along
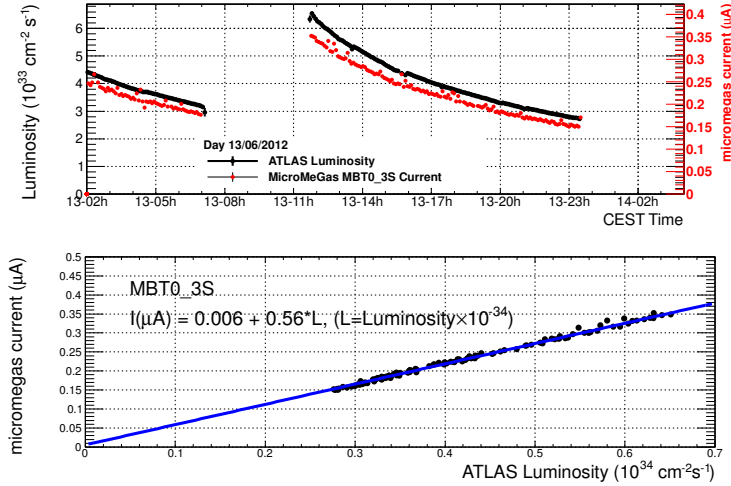
Figure 6.17: *The top plot shows the MBT current (red points) and the ATLAS luminosity (black line). The lower plot gives the MBT current versus the ATLAS luminosity. The blue line is a linear fit to the data.*
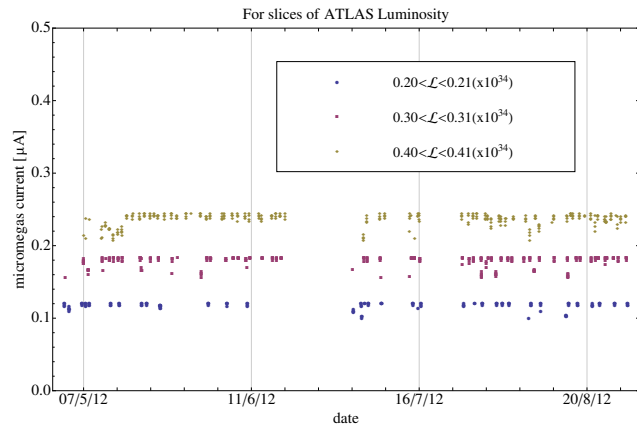
Figure 6.18: *Micromegas current as a function of time for three slices of ATLAS luminosity. With the red squares luminosity is required to be between $0.30 - 0.31 \times 10^{34} \, \mathrm{cm}^{-2}\mathrm{s}^{-1}$, with blue circles between $0.20 - 0.21 \times 10^{34} \, \mathrm{cm}^{-2}\mathrm{s}^{-1}$ and with the yellow triangles between $0.40 - 0.41 \times 10^{34} \, \mathrm{cm}^{-2}\mathrm{s}^{-1}$.*

with LUCID and BCM [148], after the correction for the gain drop.

The uncertainty on the luminosity measurement is calculated by taking the horizontal residual of every data-point from the fitted line of figure 6.19(a) (parameter is called $\delta\mathcal{L}$). The $\delta\mathcal{L}$ parameter is then divided by the measurements ($\mathcal{L}$) and is plotted versus $\mathcal{L}$ (see figure 6.20(a)). The projection of this distribution (see figure 6.20(b)) is fitted with a gaussian function and the mean value of 0.040 is extracted. Taking into account that the ATLAS luminosity error [149] is $(\delta\mathcal{L}/\mathcal{L})_{\mathrm{ATLAS}} = \pm 3.6\%$ the final uncertainty of the luminosity is estimated by the MBT current measurement to be $\delta\mathcal{L}/\mathcal{L} = \pm 1.7\%$.
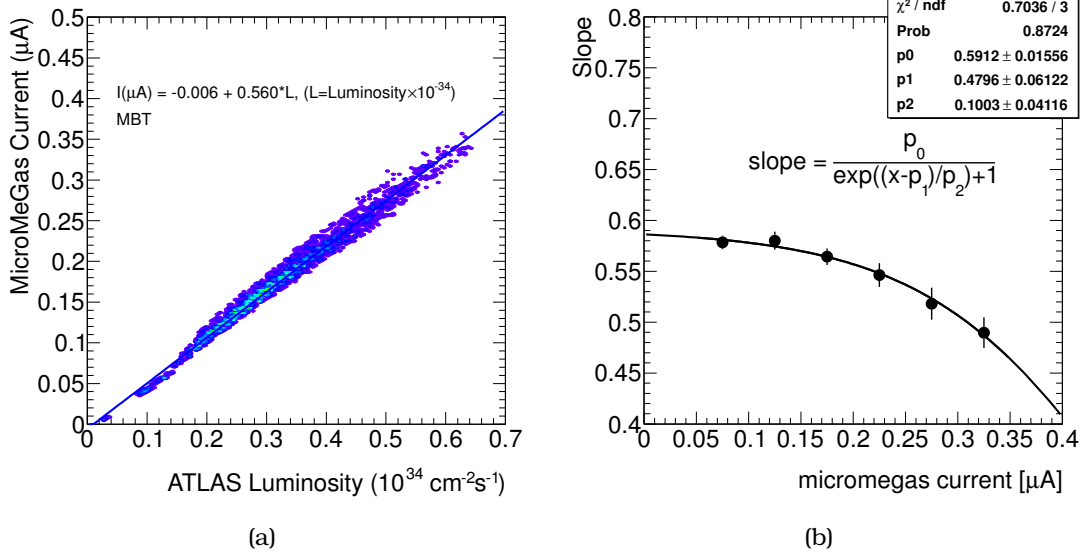
Figure 6.19: *(a) Correlation plot of the MBT current and the luminosity as measured in the ATLAS experiment. The data are fitted with a first order polynomial (blue line). (b) Variation of the slope of the MBT currents versus the ATLAS luminosity as a function of the MBT currents.*
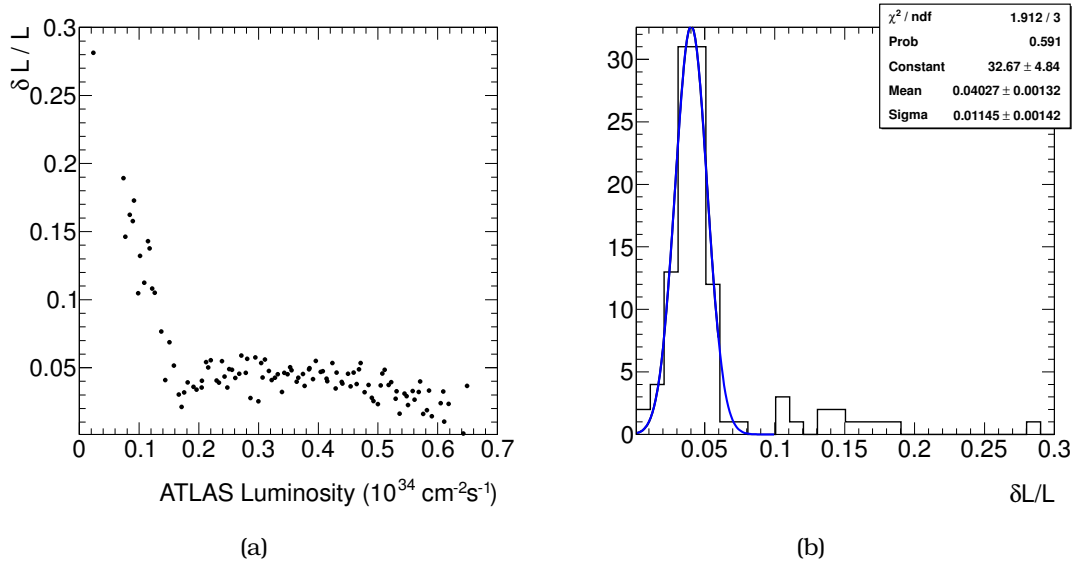
Figure 6.20: *(a) Correlation plot of the uncertainty of the luminosity calculation exctracted from the MBT current measurement versus the ATLAS luminosity. (b) Uncertainty of the ATLAS luminosity measurement based on the micromegas current.*

6.6 Charge sharing studies

Charge sharing in electronics (alternatively called cross-talk) has been a problem creating background in many analyses [150, 151]. Cross-talk is the potential distortion of the electric charge that occurs to two, not necessarily neighbouring, read-out channels. There are two ways that the cross-talk can created. Inductance, when high charge re-

ceived by strips is induced to an adjacent strip, and capacitance, where strong electric field of one strip interferes with the neighbouring.

For the readout of the micromegas detectors, the APV25 [152] hybrid cards are used. The APV chip was designed for the read-out of the CMS tracker and supports 128 channels. An example charge measurement with the APV chip as a function of the sampling time bins (25 ns) is shown in figure 6.21.
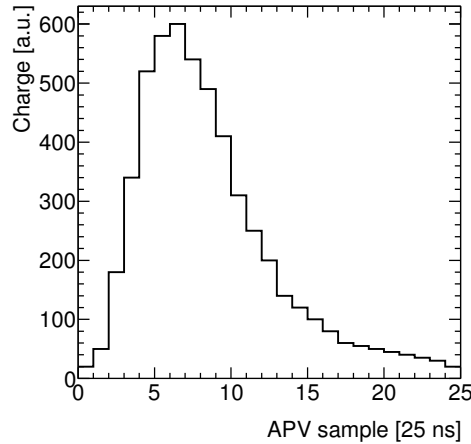
Figure 6.21: *Example of charge, sampled every* 25 ns *by an APV chip.*

6.6.1   Study of the cross-talk

In order to create the cross-talk map and define how the charge is shared between the strips, the following strategy is applied in data collected in the H4 test-beam line. For each event, after subtracting the pedestals, the channel (strip) with the maximum charge is plotted as a function of all the other channels fired in this event. This is shown in figure 6.22(a). In such a plot, the only expected correlation should be observed in the diagonal, which indicates that neighbouring channels are fired, with the width of the correlation band indicating the strip multiplicity.

Apart from this line, that is evident in figure 6.22(a), other lines are observed, in parallel of the diagonal line. These bands are repeated in a 32 strip pattern in the forward direction (e.g. channel 25 firing, might cause channel 57 to be fired). From the third band in the correlation plot, we also extract the information that secondary cross-talk effects can be observed, meaning that a channel fired from cross-talk can subsequently fire a third channel. Using this plot, we create a cross-talk map, where we list the interconnection of the channels that are fired from primary cross-talk effects (black points) and secondary effects (yellow points). This correlation of the channels is shown in figure 6.22(b).

Evaluation of the cross-talk effect

After the definition and observation of the cross-talk effect in the data, the evaluation of the cross-talk levels is the next natural step. For each event in a run, the map shown in

(a)

(b)
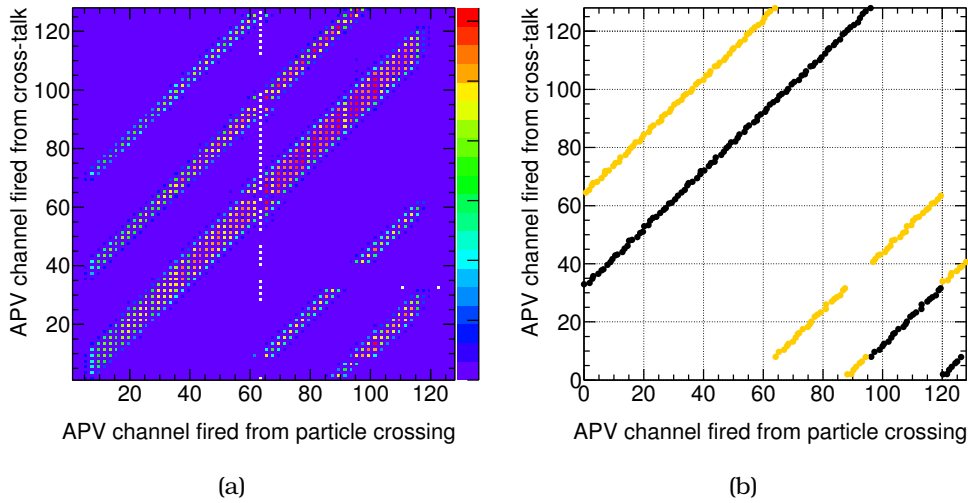
Figure 6.22: *(a) Correlation plot of channels fired within an APV chip. The channel with the maximum charge per event is compared with all the other channels fired within the same event. The non-diagonal lines are evidence of cross-talk effects. (b) Correlation plot, showing the cross-talking channels, fired due to first (black points) or second (yellow points) order effects.*

figure 6.22(b) is used, and if a channel was fired in association with its corresponding cross-talking channel, their maximum charge is extracted and plotted in figure 6.23(a). By taking the ratio of these two charges $f = q_{\mathrm{CH_b}}^{\mathrm{max}}/q_{\mathrm{CH_a}}^{\mathrm{max}}$, where $\mathrm{CH_b}$ is the cross-talk fired channel and $\mathrm{CH_a}$ is the channel fired by the beam the cross-talk effect can be evaluated (see figure 6.23(b)). Such a plot is created for every channel in a single APV chip and can be seen in figure 6.23(c). This plot shows the level of cross-talk per channel in a APV chip. The levels of cross talk varies between $9 - 11\%$.

The factor f in previous estimations and analyses was to taken to be $f = 10\%$. A data-driven technique was developed for the extraction of the f factor. For this, the correlation between the initial fired channel and the cross talk channel is used (see figure 6.23(a)). For each event, we calculate the ratio of the charge that was received by the triggered channel to the charge that was found to the cross-talking channel. This is repeated for each channel of the APV Chip, so for each channel the cumulative distribution of the ratio f (see figure 6.23(b)) is extracted. Then, this ratio is plotted as a function of the number of the channel, as shown in figure 6.23(c). The f values per channel in an APV are then used as a per-channel input of the cross-talk correction.

6.6.2 Cross-talk correction algorithm

After the level of cross-talk (f) is defined for each channel separately, an algorithm was developed in order to correct it. The cross-talk correction algorithm developed, is based on the cross-talk map (see figure 6.22(b)). The algorithm scans each channel fired and finds its corresponding maximum charge (q^{max}). In the case that two interconnected channels are fired simultaneously, assume $\mathrm{CH_a}$ shares charge with $\mathrm{CH_b}$ then their maximum charges, $q_{\mathrm{CH_a}}^{\mathrm{max}}$ and $q_{\mathrm{CH_b}}^{\mathrm{max}}$ respectively, are compared and the following actions

(a)

(b)

(c)
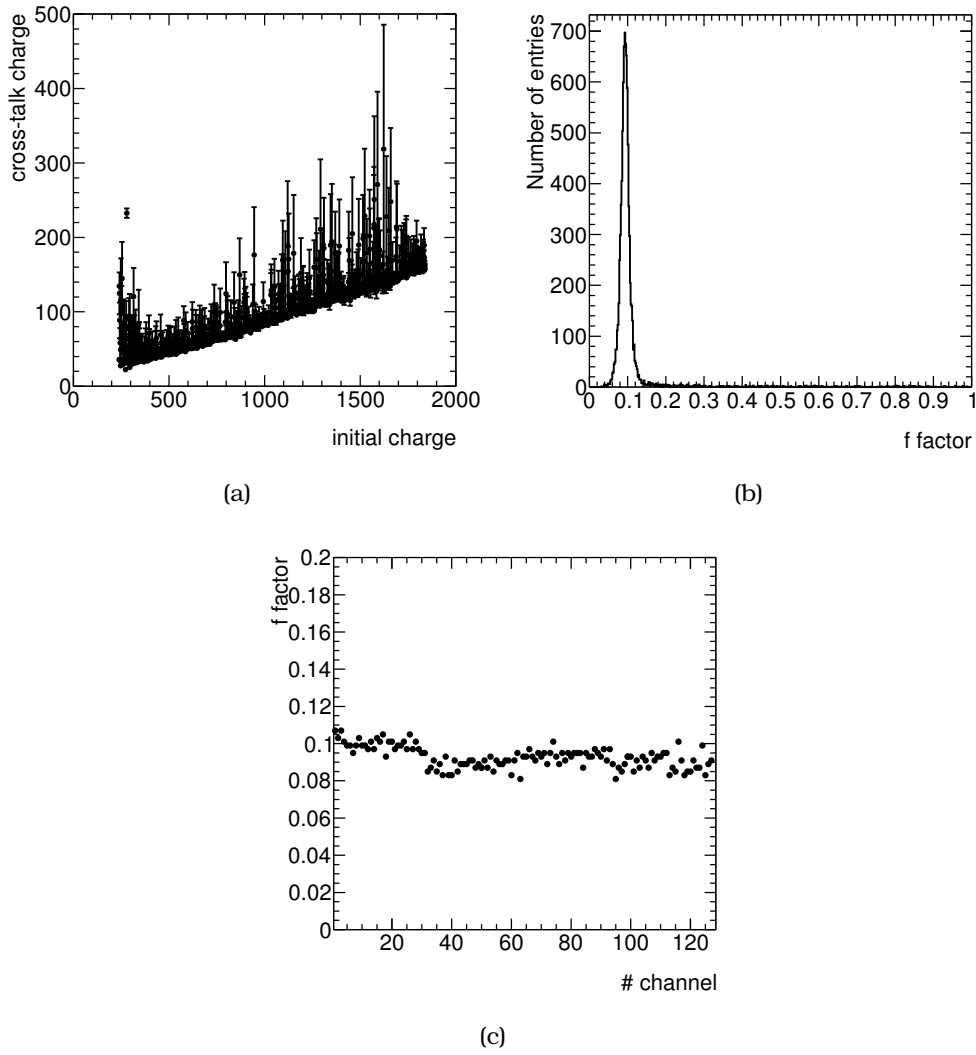
Figure 6.23: *(a) Correlation plot between the maximum charge of a channel and the maximum charge of the cross-talking channel. (b) f factor distribution for one channel, showing a cross-talk factor of the order of 9%. (c) f factor, extracted from distributions shown in (b) as a function of the 128 channels of an APV.*

are applied:

1. $q_{\mathrm{CH_a}}^{\max} < f q_{\mathrm{CH_b}}^{\max}$

   - $q_{\mathrm{CH_a}}^{i} = q_{\mathrm{CH_a}}^{i} + q_{\mathrm{CH_b}}^{i}$
   - $q_{\mathrm{CH_b}}^{i} = 0$

2. $q_{\mathrm{CH_a}}^{\max} \geq f q_{\mathrm{CH_b}}^{\max}$

   - $q_{\mathrm{CH_a}}^{i} = q_{\mathrm{CH_a}}^{i} + f q_{\mathrm{CH_a}}^{i}$
   - $q_{\mathrm{CH_b}}^{i} = q_{\mathrm{CH_b}}^{i} - f q_{\mathrm{CH_a}}^{i}$

6.6.3 Results

The cross-talk correction algorithm is applied, taking into account first and second order cross-talk effects in a data sample collected during the test-beam activities on H6 beam line. Re-evaluating the channel correlation plot in cross-talk corrected data it is clear that the secondary bands induced by cross-talk are now removed and only the main diagonal remains, due to neighbouring strips fired by the beam (see figure 6.24(a)).

A second check for the removal of the cross-talk is examined, by taking the strip number fired, weighted with the maximum charge, in oder to check the efficiency of the cross-talk removal (see figure 6.24(a)). The original distribution is plotted with the black line, and cross-talk effects is evident by the two bumps in the low and high numbered channels and by the irregularities in the beam profile (main bulk of distribution). After the correction of the algorithm (red line) the bumps are removed and a significant part of the main part is return to the centre of the distribution restoring the beam profile and enhancing the pillar-structure. The weighted events that are removed and returned are shown by the residual plot (subtracting cross-talk corrected data from the original data) in the bottom of figure 6.24(a).

(a)   (b)
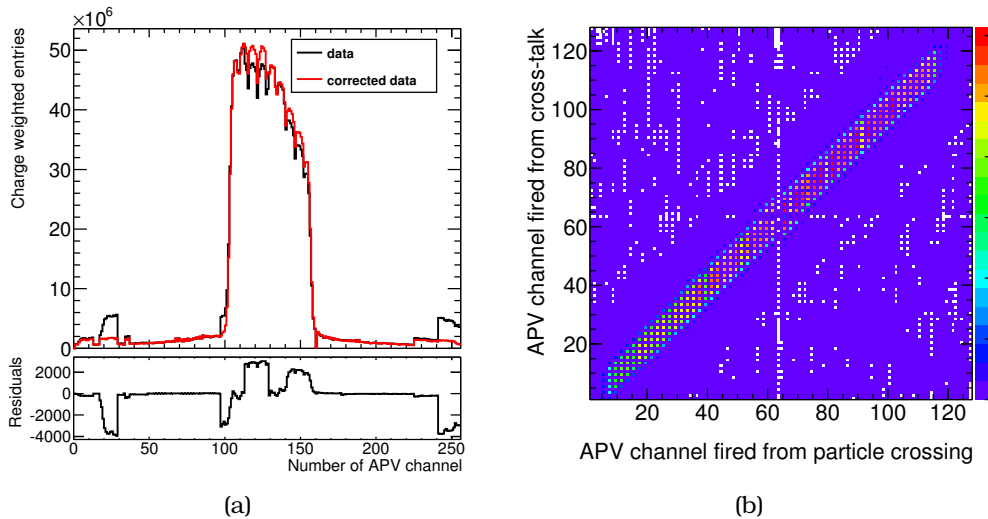
Figure 6.24: *(a) Comparison of data recorded before and after the application of the cross-talk correction algorithm. (b) Channel correlation plot after the application of the cross-talk correction algorithm.*

6.7 Physics prospects

With the data to be delivered from the HL-LHC and the realisation of the ATLAS upgrades, many physics studies will become feasible. One very interesting study will be the search for the higgs boson decay to the $Z + Q$ final state (where $Q = \Upsilon, J/\psi$).

Theoretical predictions [153] predict a branching ratio of $\sim 10^{-5}$ for the decay of higgs to either Υ or J/ψ mesons (see figure 6.25). The decay to $Z + J/\psi$ is particularly

interesting because with this final state the higgs coupling to the charm quark can be studied.
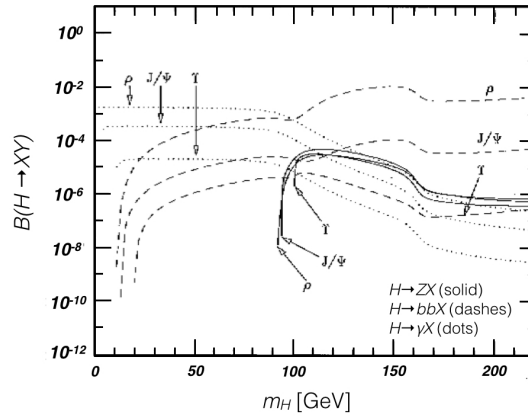
Figure 6.25: *Higgs boson branching ratio to Z* + quarkonia, $b\bar{b}$ + quarkonia *and γ* + quarkonia

This study is very relevant to the associated production of *Z* bosons with *J/ψ* mesons, because this is a background to the resonant higgs decay. The invariant mass of the four leptons, without separating *J/ψ* from background candidates is shown in figure 6.26(a).

After the separation of prompt and non-prompt *J/ψ*, sPlot weights are applied to the four lepton invariant mass distribution (figures 6.26(b) and 6.26(c) respectively). The range of 116 − 136 GeV is kept blind, because a search for such decay is in progress. The shape of the *Z*+ prompt *J/ψ* mesons is particularly interesting, because this would be the background of the resonant $H \rightarrow ZJ/\psi$ decay.
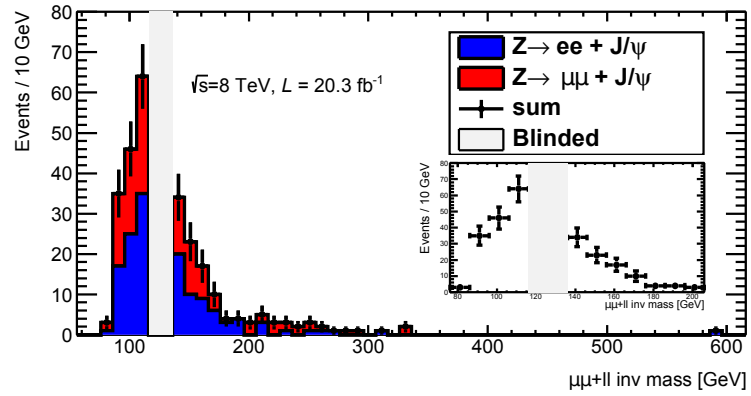
(a)
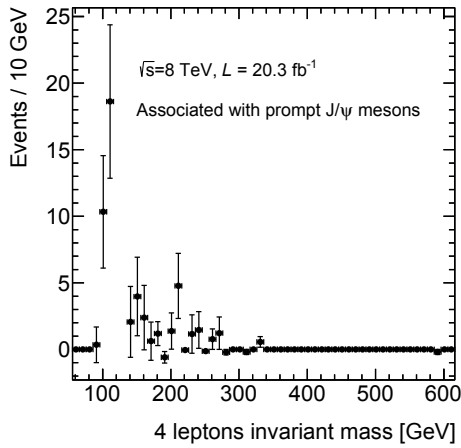
(b)
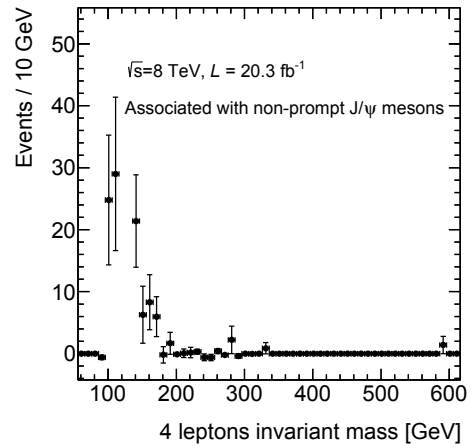
(c)

Figure 6.26: *$J/\psi(\to \mu^+\mu^-)Z(\to \ell^+\ell^-)$ invariant mass for (a) all candidate events, (b) prompt and (c) non prompt J/ψ mesons.*

Chapter 7

Conclusions

This thesis presents work related with B-physics analyses and R&D and performance studies for the muon spectrometer of the ATLAS experiment.

The first observation made of the associated production of Z bosons with prompt and non-prompt J/ψ mesons is described. The production cross-section, normalised to inclusive Z production, is measured and compared to COM and CSM theories. CSM initial predictions stated that, such processes would not be possible to be seen with the recorded luminosity by LHC, while COM underestimates the measurement by approximately 1σ.

This analysis provides valuable information, not only about the J/ψ formation, but for DPS processes as well. The σ_{eff}, that governs DPS, is considered to be process independent with only a handful of measurements available. The associated production of $Z + J/\psi$ offers the first insight for σ_{eff} at $\sqrt{s} = 8\,\text{TeV}$.

Contributions to the search of the rare decay of $B_s \rightarrow \mu^+\mu^-$ are also described. Namely, the multivariate analysis used in the signal to background separation as well as the method of measuring the $B^\pm \rightarrow J/\psi K^\pm$ yield, for the reference channel.

Studies for the present and future operation and performance of the muon spectrometer were also presented. Starting with the data collected during 2012, and measuring the muon reconstruction efficiency to be 99%, to the preparations for the NSW. Contributions were made in the understanding of the micromegas detector, as part of the NSW. Micromegas detector was studied thoroughly in testbeam setups and in the ATLAS detector, examining its performance, efficiency and ageing.

Looking towards the future, more proton–proton collisions await to be delivered, data to be recorded, and rare and exciting processes, like the $H \rightarrow ZJ/\psi$ and $Z \rightarrow \ell^+\ell^- J/\psi$ decays, to be searched therein.

J/ψ cross-section estimations at $\sqrt{s} = 8\,\mathrm{TeV}$

J/ψ cross-sections for pp collisions at $\sqrt{s} = 8\,\mathrm{TeV}$ are a key ingredient for the estimation of the DPS and pileup backgrounds. Unfortunately, up to the date of the analysis, there were no available experimental measurements for the centre-of-mass energy of interest. In order to overcome this, the FONLL package was used [17, 91]. FONLL provides calculations for total or single inclusive differential cross-sections for charm or bottom quark production at $p\bar{p}$ or pp colliders. Comparing ATLAS measurements (non-prompt J/ψ production cross-sections) and FONLL theory predictions, shows a very good agreement (see figure A.1).
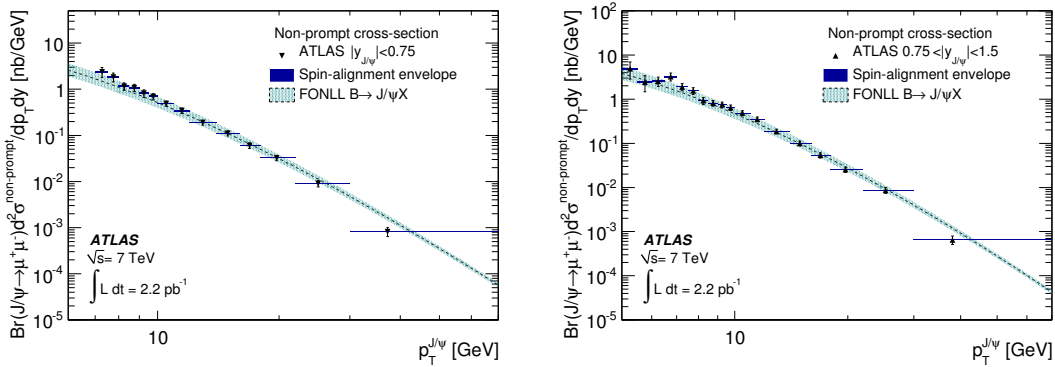
Figure A.1: *Non-prompt production cross-sections as a function of the J/ψ transverse momentum, compared to FONLL theory predictions.*

Making the assumption that the prompt to non-prompt production fractions is independent of the $\sqrt{s}$, as shown in figure A.2, the $\sqrt{s} = 7\,\mathrm{TeV}$ results from ATLAS [92] and non-prompt predictions from FONLL are used to derive the prompt cross sections at $8\,\mathrm{TeV}$.

The prompt to non-prompt production cross sections for the 5 transverse momentum bins and 2 rapidity bins defined in the $Z + J/\psi$ analysis are shown in table A.1.

The additional problem was that there are no data measurements for the last bin
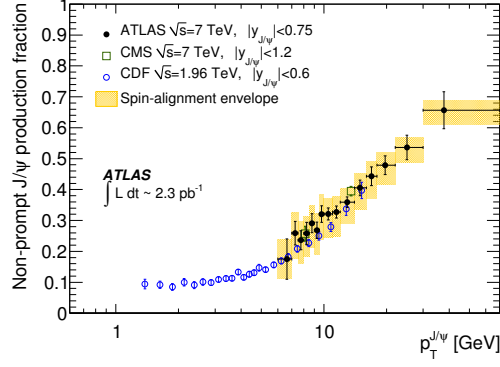
Figure A.2: *J/ψ non-prompt to inclusive fractions as a function of J/ψ transverse momentum. Results from CMS in the same and from CDF in lower, centre-of-mass energy are overlaid.*

Table A.1: *Table with cross section for* $\sqrt{s} = 7\,\text{TeV}$, *rebinned into the and rapidity bins used in this analysis.*

$\sigma(J/\psi \to \mu\mu)$ for $\sqrt{s} = 7\,\text{TeV}$ from ATLAS publication

Bin $|y| \times p_T$ GeV	$\langle p_T \rangle$	σ(Prompt $J/\psi \to \mu\mu$) (nb)	σ(NonPrompt $J/\psi \to \mu\mu$) (nb)	prompt / non-prompt
$(0,1) \times (8.5, 10)$	9.3	$6.34 \pm 0.23 \pm 0.42 \pm 1.06$	$2.50 \pm 0.12 \pm 0.13 \pm 0.03$	$2.54 \pm 0.16 \pm 0.21 \pm 0.43$
$(0,1) \times (10, 14)$	11.8	$4.85 \pm 0.10 \pm 0.25 \pm 0.65$	$2.43 \pm 0.07 \pm 0.12 \pm 0.023$	$2.00 \pm 0.07 \pm 0.14 \pm 0.27$
$(0,1) \times (14, 18)$	15.7	$0.93 \pm 0.04 \pm 0.06 \pm 0.14$	$0.67 \pm 0.03 \pm 0.04 \pm 0.01$	$1.40 \pm 0.08 \pm 0.12 \pm 0.21$
$(0,1) \times (18, 30)$	22.1	$0.39 \pm 0.02 \pm 0.03 \pm 0.05$	$0.39 \pm 0.02 \pm 0.02 \pm 0.01$	$1.01 \pm 0.08 \pm 0.09 \pm 0.14$
$(1, 2.1) \times (8.5, 10)$	9.3	$6.14 \pm 0.15 \pm 0.27 \pm 0.68$	$2.19 \pm 0.09 \pm 0.10 \pm 0.02$	$2.80 \pm 0.13 \pm 0.18 \pm 0.31$
$(1, 2.1) \times (10, 14)$	11.8	$4.59 \pm 0.07 \pm 0.21 \pm 0.42$	$2.30 \pm 0.06 \pm 0.10 \pm 0.03$	$1.99 \pm 0.06 \pm 0.12 \pm 0.18$
$(1, 2.1) \times (14, 18)$	15.7	$0.82 \pm 0.03 \pm 0.05 \pm 0.08$	$0.61 \pm 0.03 \pm 0.03 \pm 0.01$	$1.34 \pm 0.07 \pm 0.11 \pm 0.13$
$(1, 2.1) \times (18, 30)$	22.1	$0.33 \pm 0.02 \pm 0.02 \pm 0.03$	$0.33 \pm 0.02 \pm 0.02 \pm 0.00$	$1.00 \pm 0.07 \pm 0.07 \pm 0.09$

in the $Z + J/\psi$ analysis ($30 - 100\,\text{GeV}$). In order to derive an estimate for that bin, the prompt to non-prompt ratio for the p_T bins available in the $\sqrt{s} = 7\,\text{TeV}$ analysis are fit and the fit is extrapolated to the high p_T bin (see figure A.3). The prompt to non-prompt ratios are positioned in each bin, based on the mean value of the p_T within that bin, taken from the inclusive J/ψ sample (see figure A.4).

The calculated non-prompt J/ψ production cross-sections, along with the prompt to non-prompt ratio and the estimated prompt J/ψ production cross-sections are summarised in table A.2.

Two additional approaches are considered for the extrapolation procedure, in order to check potential differences in the estimated number of DPS and pileup events. The first check was done by including an extra point, the $30 - 70$ p_T bin, in the extrapolation fit. This value was taken from the same ATLAS inclusive J/ψ production cross-section measurement. The second check was to use directly the $30 - 70$ p_T ATLAS measurement, instead of the extrapolated estimation. Both variations gave comparable results for DPS and pileup number of events.
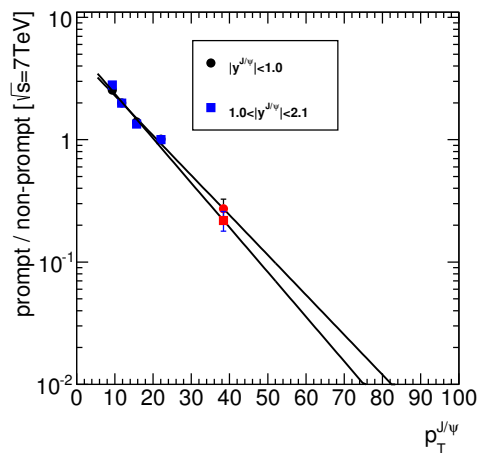
Figure A.3: *J/ψ prompt to non-prompt ratios extrapolated to the last p_T bin.*

Table A.2: *Table with summarized cross sections for $\sqrt{s} = 8$ TeV.*

	FONLL prediction and $\sqrt{s} = 8$ TeV extrapolation		
Bin $|y| \times p_T$ GeV	$\sigma(\text{Non} - \text{prompt } J/\psi \to \mu\mu)$ (nb) FONLL	prompt/non-prompt ratio at $\sqrt{s} = 7$ TeV	$\sigma(\text{Prompt } J/\psi \to \mu\mu)$ (nb) extrapolated
$(0,1) \times (8.5, 10)$	$2.42^{+0.86}_{-0.58}$	2.54 ± 0.26	$6.16^{+2.28}_{-1.61}$
$(0,1) \times (10, 14)$	$2.69^{+0.86}_{-0.60}$	2.00 ± 0.16	$5.37^{+1.76}_{-1.27}$
$(0,1) \times (14, 18)$	$0.83^{+0.22}_{-0.17}$	1.40 ± 0.14	$1.17^{+0.33}_{-0.26}$
$(0,1) \times (18, 30)$	$0.52^{+0.11}_{-0.09}$	1.01 ± 0.12	$0.53^{+0.13}_{-0.11}$
$(0,1) \times (30, 100)$	$0.09^{+0.01}_{-0.01}$	0.31 ± 0.09	$0.03^{+0.01}_{-0.01}$
$(1, 2.1) \times (8.5, 10)$	$2.24^{+0.80}_{-0.54}$	2.80 ± 0.22	$6.27^{+2.28}_{-1.58}$
$(1, 2.1) \times (10, 14)$	$2.43^{+0.77}_{-0.54}$	1.99 ± 0.14	$4.85^{+1.58}_{-1.12}$
$(1, 2.1) \times (14, 18)$	$0.73^{+0.20}_{-0.14}$	1.34 ± 0.13	$0.98^{+0.28}_{-0.21}$
$(1, 2.1) \times (18, 30)$	$0.44^{+0.10}_{-0.08}$	1.00 ± 0.10	$0.44^{+0.11}_{-0.09}$
$(1, 2.1) \times (30, 100)$	$0.07^{+0.01}_{-0.01}$	0.28 ± 0.06	$0.02^{+0.01}_{-0.01}$
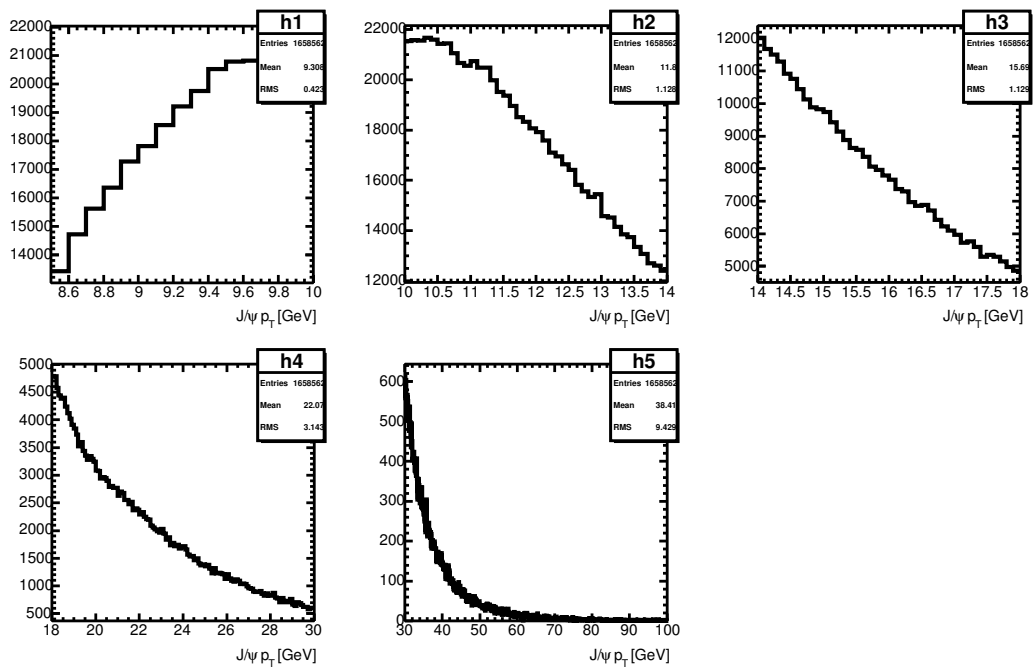
Figure A.4: *J/ψ* p_T *spectra in each* p_T *bin.*

$B^{\pm} \rightarrow J/\psi(\rightarrow \mu\mu)K$ yield extraction for the search of $B_s^0 \rightarrow\rightarrow \mu\mu$ decay using $4.9\,\mathrm{fb}^{-1}$ of $\sqrt{s} = 7\,\mathrm{TeV}$ data.

As described in chapter 5, the branching fraction of the $B_s^0 \rightarrow\rightarrow \mu\mu$ decay is measured using the $B^{\pm} \rightarrow J/\psi K^{\pm}$ decay as a reference channel (see equation 5.1). The first analysis of the ATLAS experiment used the first half of the pp collusion data collected during 2011. For this analysis, the extraction of the $B^{\pm}$ yield was performed using a binned fit in the $J/\psi K^{\pm}$ invariant mass spectrum (see section 5.2.7).

For the analysis of the full 2011 dataset ($4.9\,\mathrm{fb}^{-1}$ a more sophisticated method of extracting the yield was used. An unbinned extended maximum likelihood fit is performed simultaneously to the data and 3 MC samples. These samples are introduced to model accurately the shapes of the signal as well as the most critical background components: the partially reconstructed modes and the mis-reconstructed $J/\psi\pi^{\pm}$ decays. The probability density function chosen for the description of the signal component is a double gaussian, with the widths of the gaussians driven by the per-event resolution computed from the three-track vertex fit. The inclusion of per-event mass resolution, entails the expansion of the fit likelihood to two dimensions (m and δm). The projection of the fit in both dimensions is illustrated in figure B.1.

As a consequence, all fit models will have to be described in both the m and δm variables. While potentially improving the signal-background separation power, this procedure may give rise to additional systematic uncertainties, and certainly renders the visualisation of the fit results, more difficult. The results of the fits are presented in section B.3 by projecting the fit model separately in mass and mass resolution.

B.1 Fit likelihood

The yield extraction is based on an extended unbinned maximum likelihood fit. The extended maximum likelihood formalism allows the extraction of the signal event yield directly from the fit model.

By fitting the above mentioned MC samples simultaneously, the fit parameters are
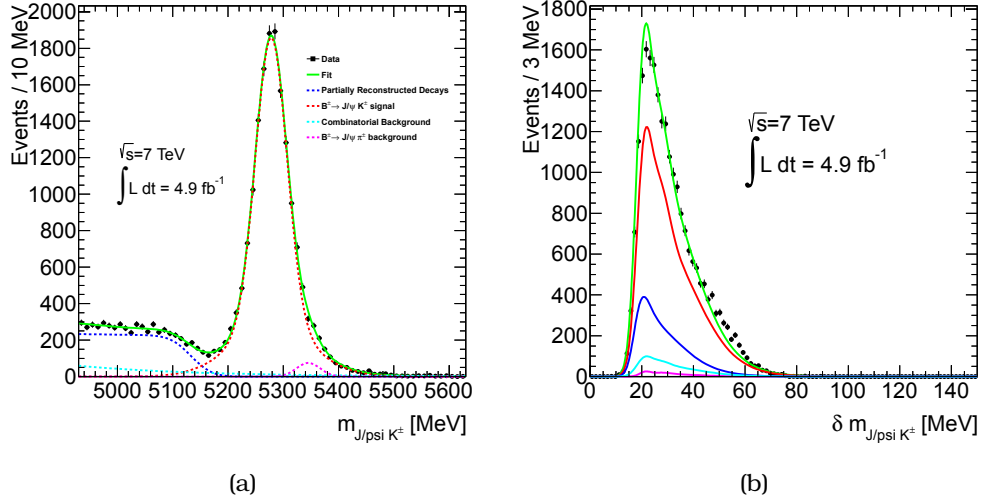
Figure B.1: *Projections of an unbinned maximum likelihood fit on (a) invariant mass spectrum and (b) mass resolution of $J/\psi K^{\pm}$ candidates. The solid green line is the total fit projection, the dotted red line is the $B \to J/\psi K^{\pm}$ signal component, the dotted magenta curve is the $B^{\pm} \to J/\psi\pi^{\pm}$ decay and the dotted blue line the partially reconstructed B modes. Finally, the dotted cyan line shows the combinatorial background.*

constrained from the corresponding fit components. This results in a "MC assisted" determination of the background and signal shape, without artificially fixing or constraining the shape related parameters, according to separate MC-based fits, while automatically accounting for the statistical uncertainties of the MC.

The advantage of an accurate description of the background shape parameters is exemplified when the partially reconstructed modes that are dominating the background are considered (described with a complementary error function times an exponential, see subsection B.2.3): the intrinsic degeneracy between the falling shape of this component and that of the exponential model for the combinatorial background is removed thanks to the constraints coming from the simultaneous fit to the partially reconstructed background MC.

The full fit[1] likelihood is parametrised as:

$$\mathcal{L} = \prod_{i=1}^{N_{\text{obs}}^{\text{data}}} M^{\text{data}}(m_i, \delta m_i) \text{Poisson}(N_{\text{obs}}^{\text{data}}, N_{\text{exp}}^{\text{data}}) \prod_{j=1}^{N_{\text{obs}}^{\text{Signal}}} M_{\text{ctl}}^{\text{Signal}}(m_j, \delta m_j | \mu, s_1, s_2, f) \text{Poisson}(N_{\text{obs}}^{\text{Signal}}, N_{\text{exp}}^{\text{Signal}})$$

$$\prod_{k=1}^{N_{\text{obs}}^{\text{PRD}}} M_{\text{ctl}}^{\text{PRD}}(m_k, \delta m_k | \alpha_{PRD}, m', \mu_{\text{PRD}}, \sigma_{PRD}) \text{Poisson}(N_{\text{obs}}^{\text{PRD}}, N_{\text{exp}}^{\text{PRD}})$$

---

[1]The data mass distribution is modeled with a double gaussian for the signal, a crystal ball function for the mis-reconstructed $J/\psi\pi$ decays, an exponential for the combinatorial background and a complementary error function multiplied with an exponential for the partially reconstructed modes. All the functions are described with detail in the chapter B.2.

$$\prod_{l=1}^{N_{\text{obs}}^{\text{JPSIPI}}} M_{\text{ctl}}^{\text{JPSIPI}}(m_l, \delta m_l | \mu_{J/\psi\pi}, k, s, \alpha_{J/\psi\pi}, n)\text{Poisson}(N_{\text{obs}}^{\text{JPSIPI}}, N_{\text{exp}}^{\text{JPSIPI}})$$

where: $N_{\text{obs}}^{\text{data}}$, $N_{\text{obs}}^{\text{Signal}}$, $N_{\text{obs}}^{\text{PRD}}$ and $N_{\text{obs}}^{\text{JPSIPI}}$ are the number of events in the data, signal MC, partially reconstructed modes MC and $J/\psi\pi$ MC dataset respectively. $N_{\text{exp}}^{\text{data}}$, $N_{\text{exp}}^{\text{Signal}}$, $N_{\text{exp}}^{\text{PRD}}$ and $N_{\text{exp}}^{\text{JPSIPI}}$ being the number of expected events.

The poisson terms account for the fluctuation in the number $N_{\text{obs}}^{\text{xxx}}$ of events observed in each of the samples, with N_{exp} representing the asymptotic mean of N_{obs}.

$M^{\text{data}}(m, \delta m)$ is in turn parameterized as:

$$M^{\text{data}}(m, \delta m) = \frac{N_{\text{Signal}}\text{Signal}(m, \delta m | \mu, s_1, s_2, f) + N_{\text{PRD}}\text{PRD}(m, \delta m | \alpha_{\text{PRD}}, m', \mu_{\text{PRD}}, \sigma_{\text{PRD}})}{N_{\text{Signal}} + N_{\text{PRD}} + N_{\text{JPSIPI}} + N_{\text{CBCKG}}}$$
$$+ \frac{N_{\text{JPSIPI}}\text{JPSIPI}(m, \delta m | \mu_{J/\psi\pi}, k, s, \alpha_{J/\psi\pi}, n) + N_{\text{CBCKG}}\text{CBCKG}(m|a)}{N_{\text{Signal}} + N_{\text{PRD}} + N_{\text{JPSIPI}} + N_{\text{CBCKG}}}$$

where m and δm are the fit variables while Signal, PRD, JPSIPI and CBKG are the functions used to describe the shape of the data and control samples (they will be defined, together with the parameters mentioned in the expressions above, in the following sub-sections).

$N_{\text{exp}}^{\text{data}}$ and $N_{\text{obs}}^{\text{data}}$ are finally defined as:

$$N_{\text{exp}}^{\text{data}} = N_{\text{Signal}} + N_{\text{PRD}} + N_{\text{JPSIPI}} + N_{\text{CBCKG}}$$

$$N_{\text{obs}}^{\text{data}} = N_{\text{Signal}}^{\text{obs}} + N_{\text{PRD}}^{\text{obs}} + N_{\text{JPSIPI}}^{\text{obs}} + N_{\text{CBCKG}}^{\text{obs}}$$

B.2 Fit models

In this chapter the functions used to describe the various components of the fit model are presented. Section B.2.1 analyses the PDF used to model the signal component and section B.2.2 the models for the 3 background components.

The parameters of each function are tied among the samples, so that effectively the parameters' values that are determined by the fit on the MC components are propagated to functions used to fit the data components.

B.2.1 Signal

The probability density function selected to describe the signal component is a double gaussian with equal mean value. The width of the two gaussians are defined as $s_1\delta m$ and $s_2\delta m$, where δm is the per-event mass resolution and s_1, s_2 are resolution scale factors allowing a modeling of the mass resolution with a narrower and a wider gaussian rather than the approximate single-gaussian, assumed in the vertex fit calculations.

$$\text{Signal}(m, \delta m) = M_{\text{signal}}(m|\delta m) \cdot \Delta_{\text{signal}}(\delta m)$$

where the mass is described with

$$M_{\text{signal}}(m, \delta m | \mu, s_1, s_2, f) = f \cdot e^{-\frac{1}{2}\left(\frac{m-\mu}{s_1 \delta m}\right)^2} + (1-f) \cdot e^{-\frac{1}{2}\left(\frac{m-\mu}{s_2 \delta m}\right)^2}$$

and the mass resolution is defined as

$$\Delta_{\text{signal}}(\delta m) = f(\delta m | a_{\text{signal}}, b_{\text{signal}}, c_{\text{signal}}, d_{\text{signal}}, r_{\text{signal}}, u_{\text{signal}}, w_{\text{signal}}) \otimes \frac{1}{\sigma_{\text{signal}} \sqrt{2\pi}} e^{-\frac{1}{2}\left(\frac{\delta m - \mu_{\text{signal}}}{\sigma_{\text{signal}}}\right)^2}$$

with

$$f(\delta m | a_{\text{signal}}, b_{\text{signal}}, c_{\text{signal}}, d_{\text{signal}}, r_{\text{signal}}, u_{\text{signal}}, w_{\text{signal}}) = \theta(\delta m - a_{\text{signal}})(b_{\text{signal}} \delta m - a_{\text{signal}})^2$$
$$\left(p_{\text{signal}} e^{-c_{\text{signal}}(\delta m - a_{\text{signal}})^2} + r_{\text{signal}} e^{-d_{\text{signal}}(\delta m - a_{\text{signal}})} + w_{\text{signal}} e^{-u_{\text{signal}}(\delta m - a_{\text{signal}})} \right)$$

and $\theta(\delta m)$ the unit step (Heaviside) function.

B.2.2 Background Models

In this section the probability density functions chosen to describe the 3 background components considered in our model are listed. The partially reconstructed decays are described in subsection B.2.3, the mis-reconstructed $J/\psi\pi^\pm$ modes in subsection B.2.4 and the combinatorial background in subsection B.2.5.

B.2.3 Partially reconstructed decays

Partially reconstructed modes are modelled with a complementary error function multiplied by an exponential in order to account for the lack of flatness of the partially reconstructed background plateau as a function of mass. The mass and mass resolution dependencies are assumed to be uncorrelated:

$$\text{PRD}(m, \delta m) = M_{\text{PRD}}(m) \cdot \Delta_{\text{PRD}}(\delta m)$$

where the mass dependency is described with

$$M_{\text{PRD}}(m, \delta m | \alpha_{PRD}, m', \mu_{\text{PRD}}, \sigma_{PRD}) = e^{(-|\alpha_{PRD}|(m-m'))} \cdot \text{erfc}\left(\frac{m - \mu_{PRD}}{\sigma_{\text{PRD}}}\right)$$

and the mass resolution PDF is defined as

$$\Delta_{\text{PRD}}(\delta m) = f(\delta m | a_{\text{PRD}}, b_{\text{PRD}}, c_{\text{PRD}}, d_{\text{PRD}}, r_{\text{PRD}}, u_{\text{PRD}}, w_{\text{PRD}}) \otimes \frac{1}{\sigma_{\text{PRD}} \sqrt{2\pi}} e^{-\frac{1}{2}\left(\frac{\delta m - \mu_{\text{PRD}}}{\sigma_{\text{PRD}}}\right)^2}$$

with

$$f(\delta m | a_{\text{PRD}}, b_{\text{PRD}}, c_{\text{PRD}}, d_{\text{PRD}}, r_{\text{PRD}}, u_{\text{PRD}}, w_{\text{PRD}}) = \theta(\delta m - a_{\text{PRD}})(b_{\text{PRD}} \delta m - a_{\text{PRD}})^2$$
$$\left(p_{\text{PRD}} e^{-c_{\text{PRD}}(\delta m - a_{\text{PRD}})^2} + r_{\text{PRD}} e^{-d_{\text{PRD}}(\delta m - a_{\text{PRD}})} + w_{\text{PRD}} e^{-u_{\text{PRD}}(\delta m - a_{\text{PRD}})} \right)$$

and $\theta(\delta m)$ the unit step (Heaviside) function.

B.2.4 $J/\psi\pi^{\pm}$ Peak

For this background component, uncorrelated PDFs for mass and mass resolution, are also considered:

$$\mathrm{JPSIPI}(m, \delta m) = \mathrm{M}_{\mathrm{JPSIPI}}(m) \cdot \Delta_{\mathrm{JPSIPI}}(\delta m)$$

The crystal ball function is empirically found to adequately model the $B^{\pm} \to J/\psi\pi^{\pm}$ MC mass dependency:

$$\mathrm{M}_{\mathrm{JPSIPI}}(m|\mu_{J/\psi\pi}, k, s, \alpha_{J/\psi\pi}, n) = \begin{cases} e^{-\frac{1}{2}\left(\frac{m-\mu_{J/\psi\pi}}{k \cdot s}\right)^2} & , \; m > -|\alpha_{J/\psi\pi}| \\[2em] \left(\frac{n}{|\alpha_{J/\psi\pi}|}\right)^n e^{-\frac{|\alpha_{J/\psi\pi}|^2}{2}} \left(\frac{n}{|\alpha_{J/\psi\pi}|} - |\alpha_{J/\psi\pi}| - \frac{m-\mu_{J/\psi\pi}}{k \cdot s}\right)^{-n} & , \; m \le -|\alpha_{J/\psi\pi}| \end{cases}$$

and the mass resolution is defined as

$$\Delta_{\mathrm{JPSIPI}}(\delta m) = f(\delta m|a_{\mathrm{JPSIPI}}, b_{\mathrm{JPSIPI}}, c_{\mathrm{JPSIPI}}, d_{\mathrm{JPSIPI}}, r_{\mathrm{JPSIPI}}, u_{\mathrm{JPSIPI}}, w_{\mathrm{JPSIPI}})$$
$$\otimes \frac{1}{\sigma_{\mathrm{JPSIPI}}\sqrt{2\pi}} e^{-\frac{1}{2}\left(\frac{\delta m - \mu_{\mathrm{JPSIPI}}}{\sigma_{\mathrm{JPSIPI}}}\right)^2}$$

with

$$f(\delta m|a_{\mathrm{JPSIPI}}, b_{\mathrm{JPSIPI}}, c_{\mathrm{JPSIPI}}, d_{\mathrm{JPSIPI}}, r_{\mathrm{JPSIPI}}, u_{\mathrm{JPSIPI}}, w_{\mathrm{JPSIPI}}) = \theta(\delta m - a_{\mathrm{JPSIPI}})(b_{\mathrm{JPSIPI}}\delta m - a_{\mathrm{JPSIPI}})^2$$
$$\left(p_{\mathrm{JPSIPI}}e^{-c_{\mathrm{JPSIPI}}(\delta m - a_{\mathrm{JPSIPI}})^2} + r_{\mathrm{JPSIPI}}e^{-d_{\mathrm{JPSIPI}}(\delta m - a_{\mathrm{JPSIPI}})} + w_{\mathrm{JPSIPI}}e^{-u_{\mathrm{JPSIPI}}(\delta m - a_{\mathrm{JPSIPI}})}\right)$$

and $\theta(\delta m)$ the unit step (Heaviside) function.

B.2.5 Combinatorial Background

The falling spectrum of the non-resonant combinatorial background is described using an exponential.

$$\mathrm{CBCKG}(m, \delta m) = \mathrm{M}_{\mathrm{CBCKG}}(m) \cdot \Delta_{\mathrm{CBCKG}}(\delta m)$$

where the mass is described with

$$\mathrm{M}_{\mathrm{CBCKG}}(m|a) = e^{\alpha m}$$

and the mass resolution is defined as

$$\Delta_{\mathrm{CBCKG}}(\delta m) = f(\delta m|a_{\mathrm{CBCKG}}, b_{\mathrm{CBCKG}}, c_{\mathrm{CBCKG}}, d_{\mathrm{CBCKG}}, r_{\mathrm{CBCKG}}, u_{\mathrm{CBCKG}}, w_{\mathrm{CBCKG}})$$
$$\otimes \frac{1}{\sigma_{\mathrm{CBCKG}}\sqrt{2\pi}} e^{-\frac{1}{2}\left(\frac{\delta m - \mu_{\mathrm{CBCKG}}}{\sigma_{\mathrm{CBCKG}}}\right)^2}$$

Table B.1: *Event yields for the $B^{\pm} \rightarrow J/\psi K^{\pm}$ channel.*

$|\eta|_{\max}$ Range	Exponential	Polynomial	Binned	Δ	Statistical [%]	Systematic [%]	χ^2/ndf
$0 - 1.0$	9036 ± 96	9153 ± 97	9098 ± 98	117	± 1.07	± 1.29	0.87
$1.0 - 1.5$	3485 ± 60	3475 ± 60	3524 ± 62	10	± 1.71	± 0.29	0.57
$1.5 - 2.5$	3051 ± 56	3141 ± 57	3347 ± 60	90	± 1.85	± 2.95	0.49
single bin	15222 ± 217	15187 ± 147	14498 ± 6	35	± 0.23	± 0.23	1.01

$$f(\delta m | a_{\text{CBCKG}}, b_{\text{CBCKG}}, c_{\text{CBCKG}}, d_{\text{CBCKG}}, r_{\text{CBCKG}}, u_{\text{CBCKG}}, w_{\text{CBCKG}}) = \theta(\delta m - a_{\text{CBCKG}})(b_{\text{CBCKG}}\delta m - a_{\text{CBCKG}})^2$$
$$\left(p_{\text{CBCKG}} e^{-c_{\text{CBCKG}}(\delta m - a_{\text{CBCKG}})^2} + r_{\text{CBCKG}} e^{-d_{\text{CBCKG}}(\delta m - a_{\text{CBCKG}})} + w_{\text{CBCKG}} e^{-u_{\text{CBCKG}}(\delta m - a_{\text{CBCKG}})} \right)$$

and $\theta(\delta m)$ the unit step (Heaviside) function.

B.3 Results

Fit projections in mass and mass resolutions for each component from the MC and the data are illustrated below in figures B.2, B.3, B.4 and B.5 respectively.

(a) Projection of mass.

(b) Projection of mass resolution.
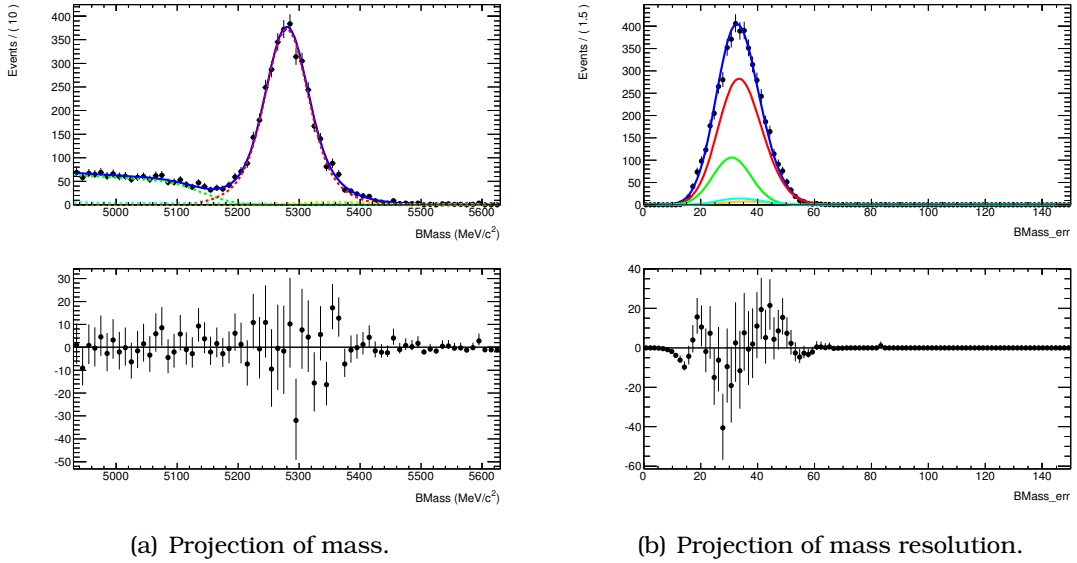
Figure B.2: *Fit on data. The cyan line represents the combinatorial background, the green line shows the partially reconstructed modes sample and the red line shows the signal. The total of all functions is presented with the blue line.*

The resulting $B^{\pm}$ event yields are given in table B.1. The systematic uncertainties shown in this table were calculated by varying the PDF (exponential and polynomial) for the combinatorial background.

(a) Projection of mass.

(b) Projection of mass resolution.
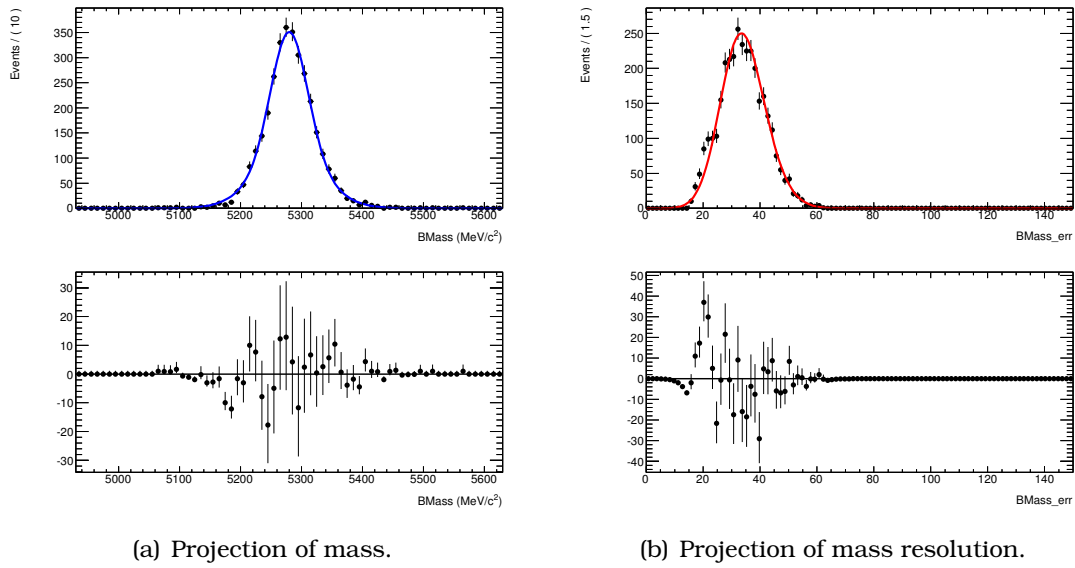
Figure B.3: *Fit on signal MC.*

(a) Projection of mass.

(b) Projection of mass resolution.
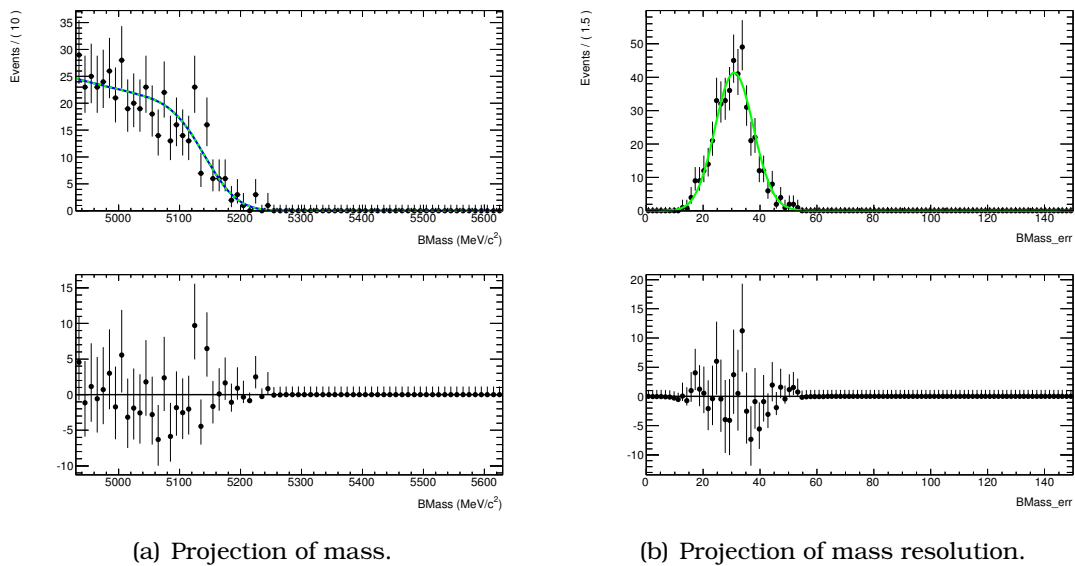
Figure B.4: *Fit on partially reconstructed modes MC.*
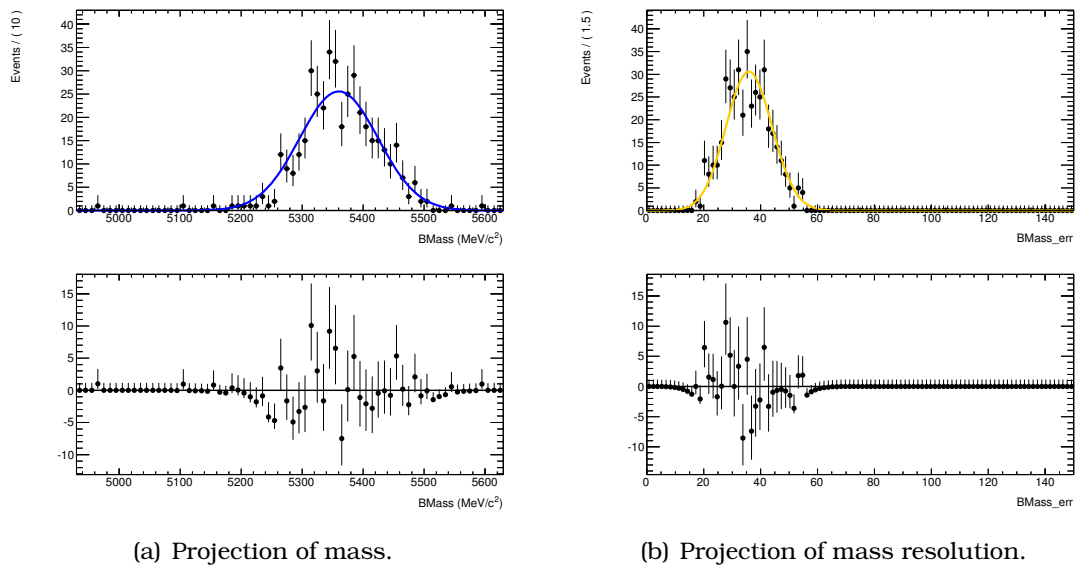
(a) Projection of mass.

(b) Projection of mass resolution.

Figure B.5: *Fit on $J/\psi\pi^\pm$ MC.*

C

Indentification of circles from datapoints

C.1 Introduction

The problem addressed is the identification of the centre (x_0, y_0) and the radius R of a circle from a given set of n datapoints (x_i, y_i). This idea originated from test-beam activities of the micromegas detectors. The goal was to fit hits on chambers, created by the bent beam, and reconstruct a circle with a radius and centre that verifies the hits on the detectors.

Two methods are proposed for the reconstruction of a circle. The first method use gaussian sums [154] and the second the geometrical Legendre transform [155].

C.2 Description of the methods

The starting point of both methods is a first estimation of the centre $(x_{\text{est}}, y_{\text{est}})$ and the radius, R_{est}, of the circle. Given three datapoints $\mathbf{r_1} = A(x_1, y_1)$, $\mathbf{r_2} = B(x_2, y_2)$ and $\mathbf{r_3} = C(x_3, y_3)$, as shown in figure C.1(a), the slopes of the lines connecting AB and BC are given by:

$$m_r = \frac{y_2 - y_1}{x_2 - x_1} \text{ and } m_t = \frac{y_3 - y_2}{x_3 - x_2}$$

The centre of the circle is the intersection of the lines perpendicular to the midpoints of $\overline{AB}$ and $\overline{CB}$ respectively. The equations for perpendicular lines passing through the midpoints are

$$y - \frac{y_1 + y_2}{2} = -\frac{1}{m_r}\left(x - \frac{x_1 + x_2}{2}\right) \text{ and } y - \frac{y_2 + y_3}{2} = -\frac{1}{m_t}\left(x - \frac{x_2 + x_3}{2}\right)$$

The intersection of the lines described above reflect the centre of the circle. The centre of the circle (x_0, y_0) is calculated by solving the system of equations:
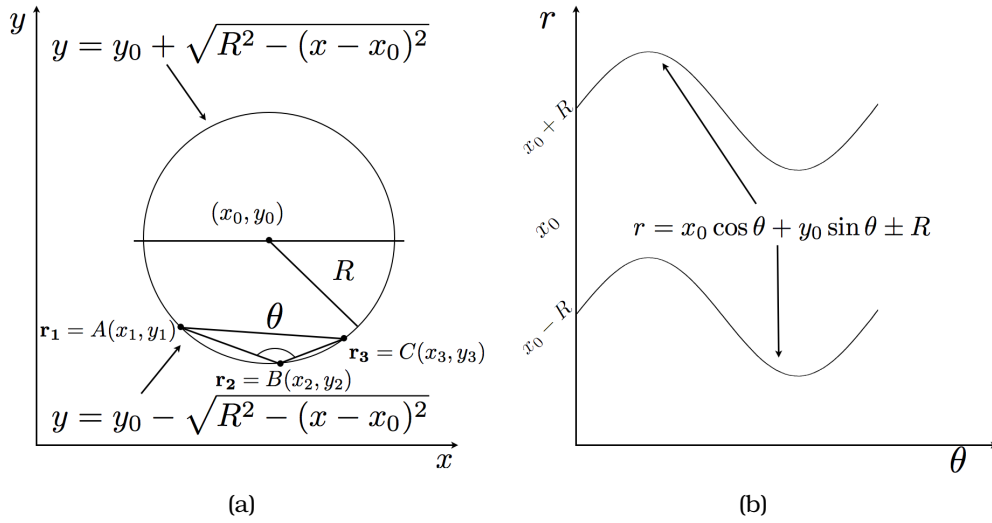
Figure C.1: *(a) Representation of a circle by a convex and a concave function. (b) Representation of the circle in Legendre transformation space. The circle corresponds to two sinograms in the Legendre transformation space.*

$$x_{\text{est}} = \frac{m_t m_r (y_3 - y_1) + m_r(x_2 + x_3) - m_t(x_1 + x_2)}{2(m_r - m_t)}$$

$$y_{\text{est}} = -\frac{1}{m_r}\left(x_{\text{est}} - \frac{x_1 + x_2}{2}\right) + \frac{y_1 + y_2}{2}$$

The radius R of the circle is given by:

$$R_{\text{est}} = \sqrt{(x_{\text{est}} - x_1)^2 + (y_{\text{est}} - y_1)^2}$$

The radius, R_{est}, of the circle can also be estimated from the equations:

$$R_{\text{est}} = \frac{|\mathbf{r_1} - \mathbf{r_3}|}{2\sin\theta}, \quad \sin\theta = \frac{|(\mathbf{r_1} - \mathbf{r_2}) \times (\mathbf{r_3} - \mathbf{r_2})|}{|\mathbf{r_1} - \mathbf{r_2}||\mathbf{r_3} - \mathbf{r_2}|}$$

Therefore, the radius may be estimated by the following formula

$$R_{\text{est}} = \frac{\sqrt{\alpha\beta\gamma}}{2|x_1y_2 + x_2y_3 + x_3y_1 - x_1y_3 - x_2y_1 - x_3y_2|}$$

with $\alpha = (x_1 - x_2)^2 + (y_1 - y_2)^2$, $\beta = (x_3 - x_2)^2 + (y_3 - y_2)^2$ and $\gamma = (x_3 - x_1)^2 + (y_3 - y_1)^2$.

C.2.1   First method - Gaussian sum

With a dataset including events with n given datapoints, $k = \binom{n}{3}$ different centres and radii can be estimated. Using the formulas described above the global sums are constructed:

$$G(x) = \sum_{i=1}^{k} \frac{1}{\sqrt{2\pi}\sigma_x} e^{-(x-x_{est}^i)^2/2\sigma_x^2}$$

$$G(y) = \sum_{i=1}^{k} \frac{1}{\sqrt{2\pi}\sigma_y} e^{-(y-y_{est}^i)^2/2\sigma_y^2}$$

$$G(R) = \sum_{i=1}^{k} \frac{1}{\sqrt{2\pi}\sigma_R} e^{-(R-R_{est}^i)^2/2\sigma_R^2}$$

where x_{est}^i, y_{est}^i and R_{est}^i are the circle's parameters for the ith triplet of datapoints that defines the circle. The σ_x, σ_y and σ_R are set of a fraction of the geometrical scale of the problem and for the MC events generated here the values $\sigma_x = \sigma_y = \sigma_R = 0.1$ are chosen. Gaussian functions are used in the global sums, because datapoints created by noise will result to a value that is further away from the correct one. Noise datapoints are estimated to have a small contribution to the global sum, while true datapoints will enhance the gaussian sum near the correct value.

For each event the functions described above (see figure C.2) are constructed and the value of the bin with the maximum number of entries is chosen. The value of these bins are the estimate of the (x_{est}, y_{est}) and R_{est} of the circle.

C.2.2 Second method - Transformation into Legendre space

In the second method, the Legendre transform is implemented [156, 157] for the determination of the characteristics of the circle. The general idea is that every set of estimations, as described above, is transformed into the Legendre space. Then, the maximum in the Legendre space indicates the true value of the circle's parameters.

A circle can be split and described by the combination of a convex and a concave function (see figure C.1(b)). The equation of a circle with centre (x_0, y_0) and radius R is given by

$$f(x) = \begin{cases} f_1(x) = y_0 + \sqrt{R^2 - (x - x_0)^2} \\ \\ f_2(x) = y_0 - \sqrt{R^2 - (x - x_0)^2} \end{cases}$$

where equation $f_1(x)$ refers to the concave part and $f_2(x)$ to the convex part of $f(x)$, respectively.

The Legendre transform take the following form

$$f(x) \leftrightarrow \mathcal{L} \begin{cases} r_1 = x_0 \cos\theta + y_0 \sin\theta + R_0, & \text{concave part} \\ r_2 = x_0 \cos\theta + y_0 \sin\theta - R_0, & \text{convex part} \end{cases}$$

by taking into account the canonical form of a straight line [158]. These two curves ($r_{1,2}$ versus θ) of the Legendre transform represent sinograms.

With n given datapoints, all the possible circles for each triplet of datapoints are constructed. The Legendre transform, of all reconstructed circles, will be given by the sinograms

(a)

(b)

(c)

(d)
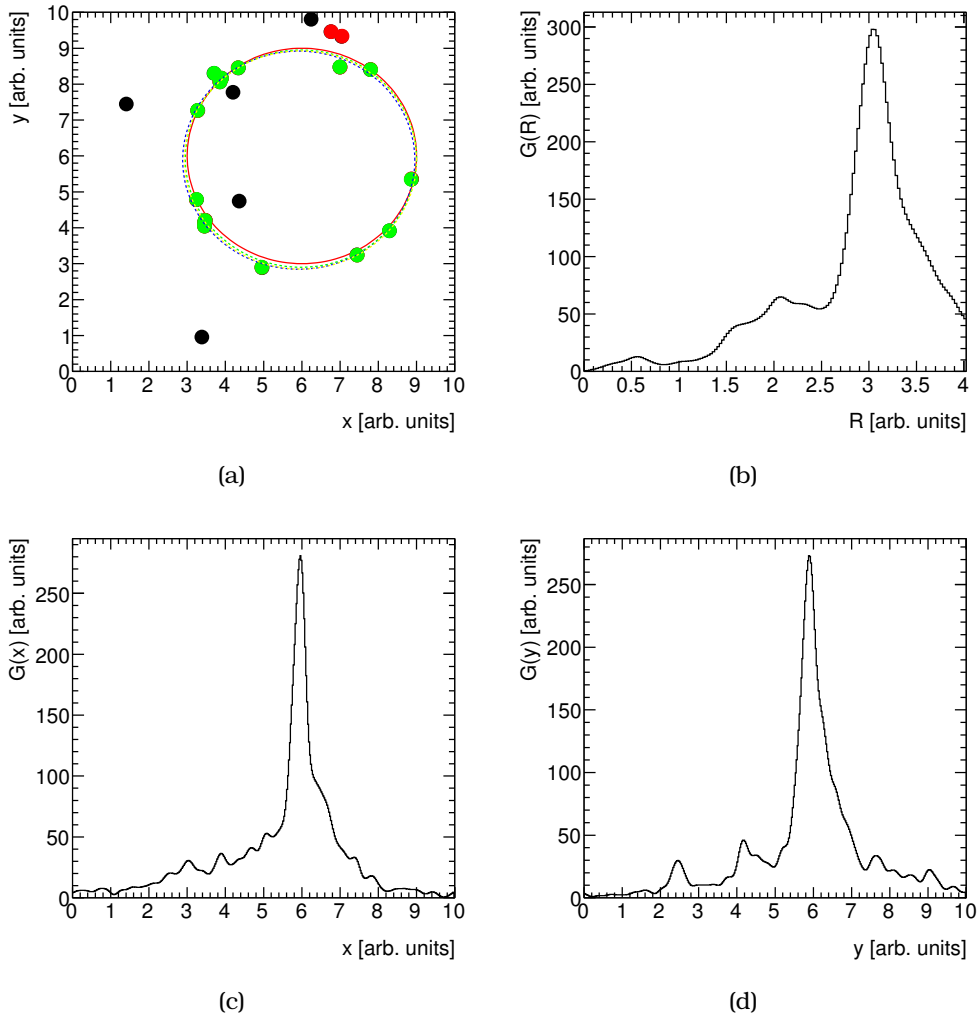
Figure C.2: *(a) The red datapoints originate from the circle (red line) having received a smearing of 10%. The datapoints that missed the radius R (noise hits - black datapoints) are on a 50% percentage of the circle's datapoints. Red circle is the original circle used to generate the datapoints, blue is reconstructed by using χ^2 minimization, green is reconstructed by using the Legendre technique and yellow using the gaussian sum. (b) Example of the G(R) function for the reconstruction of the radius R. (c) Example of the G(x) function for the reconstruction of the x_0. (d) Example of the G(y) function for the reconstruction of the y_0.*

$$r_{1,2} = \sum_{i=1}^{k} \left(x_{\text{est}}^i \cos\theta + y_{\text{est}}^i \sin\theta \pm R_{\text{est}}^i \right)$$

where x_{est}^i, y_{est}^i and R_{est}^i are the circle's parameters for the ith triplet of datapoints that defines a circle, as described in the beginning of this section.

Apart from the concave and convex part, the difference and sum of r_1 and r_2 are also

considered. Taking the difference

$$r_1 - r_2 = 2 \sum_{i=1}^{k} R_{est}^i \qquad (C.1)$$

the x_{est}^i and the y_{est}^i dependence is omitted, creating a new Legendre space where direct estimation of the radius of the circle by searching for a maximum is possible. Using the sum of r_1 and r_2

$$r_1 + r_2 = 2 \sum_{i=1}^{k} (x_{est}^i \cos\theta + y_{est}^i \sin\theta) \qquad (C.2)$$

the scan along the lines of $\theta = 0$ and $\theta = \pi/2$ for maxima, will provide estimations for (x_{est}, y_{est}), respectively.

An example of the procedure mentioned above is shown in figure C.3. Figure C.3(b) shows the Legendre transform for the r_1 and r_2, while their difference and sum is shown in figures C.3(a) and C.3(c) respectively.

C.2.3   Extraction of the circle parameters

After the presentation of the methods for the circle's characteristics extraction, the algorithms to derive the estimations on the coordinates and the radius of the circle are described.

Extraction of the circle parameters from the gaussian sum method

The circle parameters are extracted by scanning the x-axis of each $G(x)$, $G(y)$ and $G(R)$ and defining the bin with the maximum number of entries.

Figure C.2 illustrates an example of this algorithm. The circle shown in figure C.2(a) is used to generate datapoints in the $x - y$ plane. Using the combinations of the datapoints, the generated $G(R)$, $G(x)$ and $G(y)$ are shown in figures C.2(b), C.2(c) and C.2(d). The peaks of the three distributions are in very good agreement with the true value of the circle's centre and radius.

Extraction of the circle parameters by scanning the Legendre space

The Legendre space is more flexible and offers the application of more than one algorithm for the circle parameters extraction.

Scan the Legendre space   This algorithm scans the $\theta = 0, \pi/2$ bins in the $r_1 + r_2$ Legendre space and searches for maxima (black lines in figure C.3(c)). The maximum points correspond to the x_{est} (for $\theta = 0$) and y_{est} (for $\theta = \pi/2$) points. By projecting the Legendre space of $r_1 - r_2$ (see figure C.3(a)) on the y-axis the estimation of the radius R_{est} is extracted.

The advantage of this algorithm is that it can be used in cases where two circles co-exist (see figure C.4). Following the same strategy and scan the Legendre space in

(a)

(b)

(c)
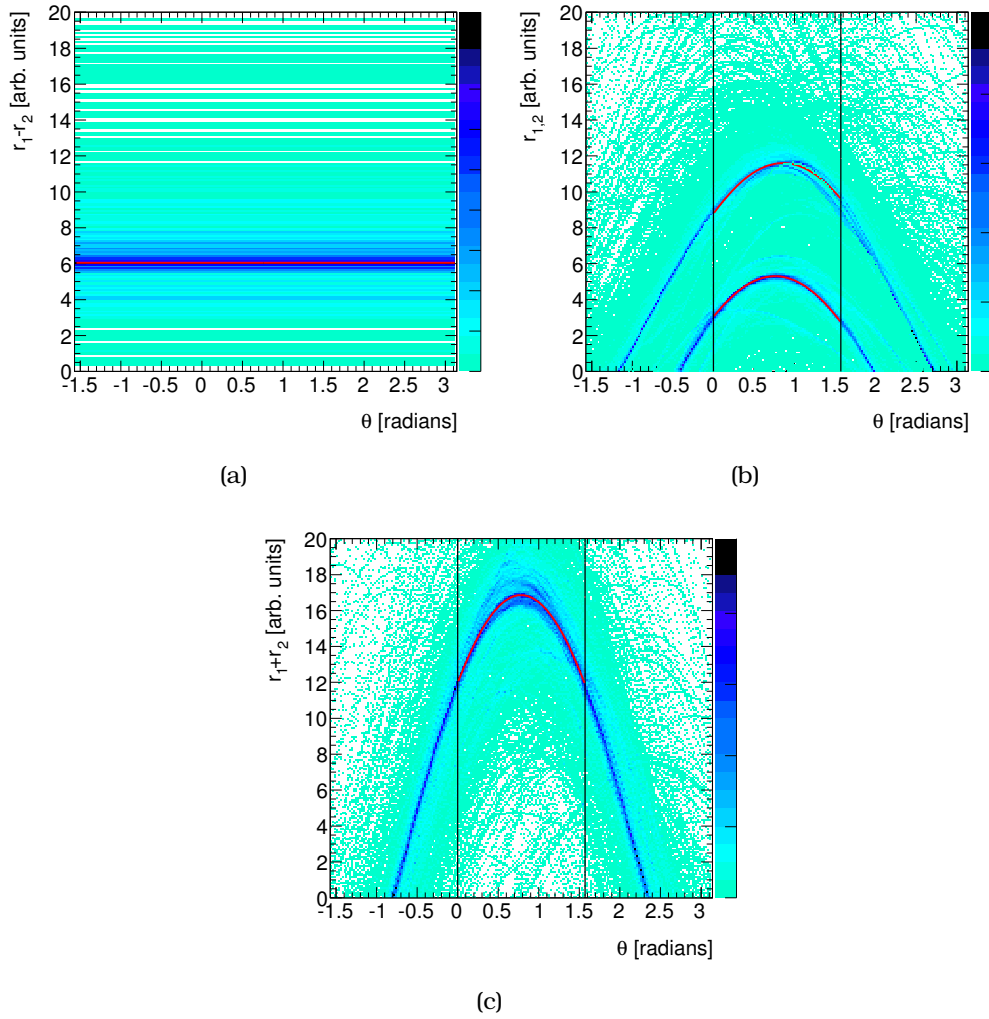
Figure C.3: *(a) The Legendre space of $r_1 - r_2$ from the datapoints of figure C.2(a). (b) Concave and convex representation of the circle's datapoints. (c) The Legendre space of $r_1 + r_2$ from the datapoints of figure C.2(a).*

the $\theta = 0, \pi/2$ bins and searching for two maxima in each bin, estimates for the centre coordinates and the radii of both reconstructed circles are calculated.

An example is given in figure C.4(b). In this figure, the two most populated bins are for $r_1 - r_2 = 6$ and $r_1 - r_2 = 2$. Using the equation C.1 the radii of both circles are extracted, $R_1 = 3$ and $R_2 = 1$, which are in excellent agreement with the values used for the creation of the circles (see figure C.4(a)). From the $r_1 + r_2$ Legendre space (see figure C.4(d)), for $\theta = 0$ we can estimate $x_1/2 = 6$ and $x_2/2 = 12$ and for $\theta = \pi/2$ we find $y_1/2 = 8$ and $y_2/2 = 12$, again in agreement with the true values.

Fit the Legendre space Instead of scanning along the axes, the second algorithm fits the Legendre space. This algorithm is relieved from the bin size constrain but has the disadvantage that is time consuming.

Figures C.3(a) and C.3(c) show examples of these fits. The fitted function is $f(\theta) =$

$p_0 \cos\theta + p_1 \sin\theta$, where the parameters p_0 and p_1 are the x_{est} and y_{est} estimates. The determination of the radius comes from a linear fit, $h(\theta) = p_2$, where p_2 is the estimation of R, in the $r_1 - r_2$ Legendre space (see figure C.3(a)).

(a)

(b)

(c)

(d)
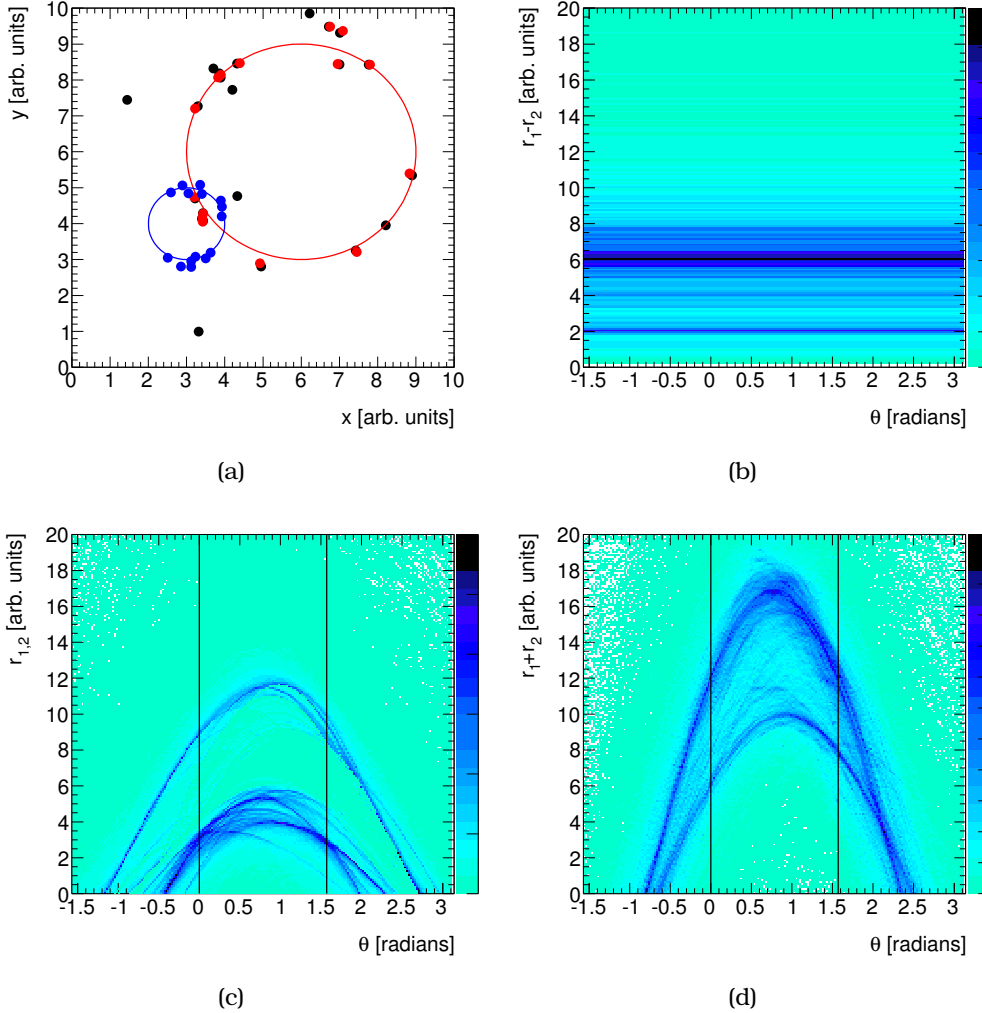
Figure C.4: *(a) The red datapoints originate from the circle (red line) having received a smearing of 10%. The outliers/noise hits (black datapoints) are on a 50% percentage of the circle's datapoints. (b) The Legendre space of $r_1 - r_2$ from the datapoints of figure C.2(a). (c) Concave and convex representation of the circle's datapoints. (d) The Legendre space of $r_1 + r_2$ from the datapoints of figure C.2(a).*

After the first fit is performed, the circle's parameters are obtained by using a χ^2 fit [159] on a new, reduced, set of datapoints, which are found to be closed to the circle's circumference. The new set is created by following the criterium:

$$\frac{|\sqrt{(x_i - x_{est})^2 + (y_i - y_{est})^2} - R_{est}|}{R_{est}} < \kappa$$

where κ is a fraction of the estimated radius, R_{est}, by the algorithm described earlier in the text. (here $\kappa = 10\%$ is used). It was also found that the χ^2 fit is robust, by trying

a wider range (10% to 30%) of the κ parameter. The χ^2 test is based on minimising the function

$$\chi^2 = \sum_{i=1}^{N} \left\{ (x_i - x_{\text{est}})^2 + (y_i - y_{\text{est}})^2 - R_{\text{est}}^2 \right\}^2$$

where the sum runs over the N selected datapoints that satisfy the criterium mentioned above. The final parameters x_{est}^f, y_{est}^f and R_{est}^f of the χ^2 minimisation are given by the following system of equations

$$\begin{pmatrix} A & B \\ B & C \end{pmatrix} \begin{pmatrix} x_{\text{est}}^f \\ y_{\text{est}}^f \end{pmatrix} = \begin{pmatrix} D \\ E \end{pmatrix}$$

$$(x_{\text{est}}^f)^2 + (y_{\text{est}}^f)^2 - (R_{\text{est}}^f)^2 = F$$

where

$$A = \sum_i x_i^2 - \frac{1}{N} \left(\sum_i x_i \right)^2$$

$$B = \sum_i x_i y_i - \frac{1}{N} \sum_i x_i \sum_i y_i$$

$$C = \sum_i y_i^2 - \frac{1}{N} \left(\sum_i y_i \right)^2$$

$$D = \sum_i x_i^3 + \sum_i x_i y_i^2 - \frac{1}{N} \sum_i x_i \sum_i (x_i^2 + y_i^2)$$

$$E = \sum_i y_i^3 + \sum_i x_i^2 y_i - \frac{1}{N} \sum_i y_i \sum_i (x_i^2 + y_i^2) \text{ and}$$

$$F = \frac{1}{N} \left\{ 2 x_{\text{est}}^f \sum_i x_i + 2 y_{\text{est}}^f \sum_i y_i - \sum_i x_i^2 - \sum_i y_i^2 \right\}$$

Applying this algorithm to a circle created with parameters $R_0 = 3$, $x_0 = 6$ and $y_0 = 6$, it returns $R_{\text{est}}^f = 3.04$, $x_{\text{est}}^f = 5.92$ and $y_{\text{est}}^f = 5.88$.

C.3   Algorithm validation using MC

Both algorithms are validated using simulated experiments. In these MC events, one or two circles are defined and a random number n of datapoints is generated using the circles ($n = 8 \ldots 20$). Gaussian smearing in both x and y coordinates, as well as noise hits, are used in order to check the robustness of the algorithms.

C.3.1   Test on one circle scenario

For the extraction of a single circle parameters both the gaussian sum method and the Legendre space are used.

The test scenario features a circle with centre $(4, 5)$ and a radius of 2 (arbitrary units). Using this circle, n datapoints (n = 8, 10, 15 and 20) are randomly created for 1000 events. Both the x_i and y_i positions of the datapoints are smeared, independently on x and y, by 5%, 10% or 15% of the circle's radius R. Apart from the uncertainty introduced in the position of the datapoints, noise hits in certain percentage of the datapoints that originate from the circle are included. The noise hits are randomly generated in the ranges $0 \leq x \leq 10$ and $0 \leq y \leq 10$.

An random example of this toy MC is presented in figure C.2(a). The red and green datapoints (n = 15) are generated from the circle and the black datapoints are the noise hits (50% noise level is used in this event). The positions of all the generated datapoints (x_i, y_i) are smeared by 10% of its radius R.

(a)   (b)   (c)
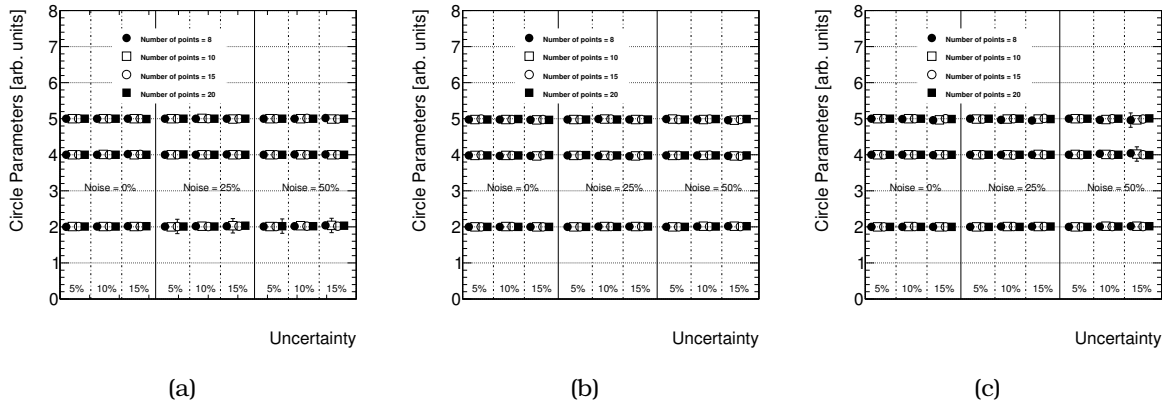
Figure C.5: *Results of the algorithms described in section C.3.1. We try four different sets of number of datapoints (n = 8, 10, 15, 20), three different percentages of position uncertainty (5%, 10% and 15% of the radius R) and three levels of noise hits (0%, 25% and 50% of the actual datapoints). Results on figure C.5(a) are extracted by the gaussian sum method, on figure C.5(b) are extracted by scanning the Legendre space and on figure C.5(c) by fitting it.*

The results of the methods described in section C.2 are summarized in figure C.5. It is evident that all three algorithms proposed for the extraction of the circle's parameters (section C.2.3) work equally well under all test scenarios.

A second scenario, that unfortunately happens often in experimental setups, was tested. This scenario implies the situation where part of the detector is malfunctioning. For this, n = 10 datapoints are generated, restricting the generation in three quadrants of the circle. Five noise hits are included in each event and all the points are smeared, independently in x and y, by 5%, 10% or 15% of the circle's radius R (an example event can be seen in figure C.6).

The results are summarised in the following table and show the robustness of all the algorithms.
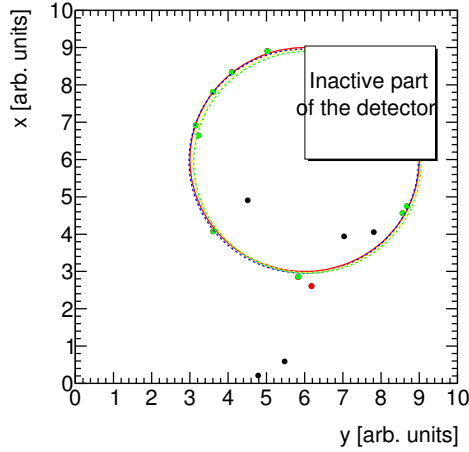
Figure C.6: *The red datapoints originate from the circle (red line) having received a smearing of 5%. The datapoints that missed the radius R (noise hits - black datapoints) are on a 50% percentage of the circle's datapoints. Red circle is the original circle used to generate the datapoints, blue is reconstructed by using χ^2 minimization, green is reconstructed by using the Legendre technique and yellow using the gaussian sum. The top right quadrant of the detector is supposed to be inactive.*

Table C.1: *Results of the algorithms described in section C.3.1. We use n = 10 datapoints, generated in three quadrants of the circle, three different percentages of position uncertainty (5%, 10% and 15% of the radius R) and five additional noise hits. The original values of the circle's parameters can be found in the first row.*

Original Values	$R = 3$	$x = 6$	$y = 6$
Uncertainty [%]	5	10	15
R gaussians	3.01 ± 0.00	3.03 ± 0.00	3.04 ± 0.01
x gaussians	6.00 ± 0.00	5.99 ± 0.01	6.00 ± 0.02
y gaussians	6.00 ± 0.00	5.99 ± 0.01	5.98 ± 0.01
R Legendre scan	3.00 ± 0.00	3.02 ± 0.00	2.88 ± 0.02
x Legendre scan	5.97 ± 0.00	5.97 ± 0.01	5.94 ± 0.01
y Legendre scan	5.97 ± 0.00	5.95 ± 0.01	5.92 ± 0.01
R Legendre fit	3.00 ± 0.01	3.02 ± 0.00	3.04 ± 0.01
x Legendre fit	5.97 ± 0.01	5.97 ± 0.02	5.96 ± 0.02
y Legendre fit	5.99 ± 0.00	5.98 ± 0.01	5.97 ± 0.01

C.3.2   Test on two circles scenario

For the two circles case, the Legendre mode is examined. In order to verify the algorithm, two circles with centres $(x_1, y_1) = (6, 6)$, $(x_2, y_2) = (3, 4)$ and radii $R_1 = 3$, $R_2 = 1$ are defined. For both circles $n = 8$, 10, 15 and 20 datapoints are generated and an example event is shown in figure C.4(a). As, with the one circle scenario, the datapoints receive an additional Gaussian smearing, independently on x and y, with the standard deviation being 5%, 10% and 15% of the circles' radius, R_1. Additionally, n_r random noise

hits are included in the ranges $0 \leq x \leq 10$ and $0 \leq y \leq 10$, with n_r being a percentage, 0%, 25% and 50%, of the circles' reconstructed datapoints n.

(a)   (b)   (c)
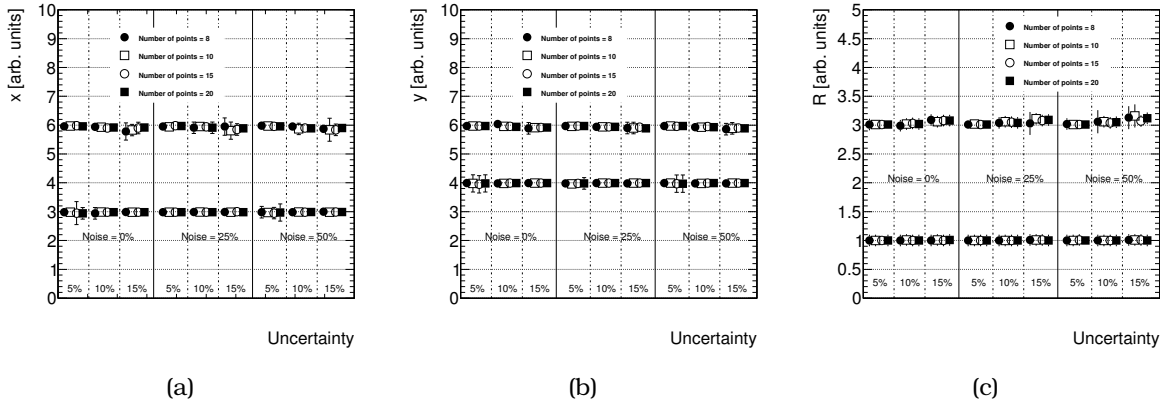
Figure C.7: *Results of the algorithm (described in section C.3.2) for the indentification of the two circles' parameters. The centre coordinates are shown in figures C.7(a) and C.7(b) and the radius in figure C.7(c). We try four different sets of number of datapoints (n = 8, 10, 15 and 20), three different percentages of position uncertainty (5%, 10% and 15% of the radius R) and three levels of noise hits (0%, 25% and 50% of the actual datapoints). The original values of the circle's parameters can be found in section C.3.2.*

The centre coordinates and the radii of the two circles, as a function of the number of datapoints generated by the circles, their gaussian smearing and the noise are shown in figures C.7(a), C.7(b) and C.7(c) respectively. All measurements are in good agreement with the initial values used in the MC ($R_1 = 3$ and $R_2 = 1$).

Timing performance

The performance of the algorithm described in section C.3.1 is examined as a function of the time that is needed to process a single event. For this event, the gaussian smearing is set to 10% of the radius R and $n = 20$ points are considered. Using a 2.5 GHz Intel Core i5 processor, 0.30 ms is needed to calculate the circle's parameter.

C.4   Conclusions

Both methods proposed are mathematical simple and fast to implement. The results of both methods show that they are robust under noise, malfunction of part of the detector or poor reconstruction of the hits. The geometrical Legendre transform method proved to work efficiently also for the identification and reconstruction of two overlapping circles.

Appendix D

Benford's law in astrophysics and astronomy

D.1 Introduction

S. Newcomb, an astronomer and mathematician, by examining the logarithmic books made an exceptional observation in 1881 [160]. The observation he made was related to the correlation of the wear of the pages and their position in the logarithmic book. He connected the use of the pages with the frequency that the significant numbers occur in various physical datasets. The conclusion was that these significant digits were not distributed with equal probability, but the smaller ones had a higher chance of occurrence. Following Newcomb's observation, F. Benford in 1938 derived the law of the anomalous numbers [161].

The general significant digit law [162] for all $k \in \mathbb{N}$, $d_1 \in \{1, 2, \ldots, 9\}$ and $d_k \in \{0, 1, \ldots, 9\}$, for $k \geq 2$ is

$$P(d_1, d_2, \ldots, d_k) = \log_{10}\left[1 + \left(\sum_{i=1}^{k} d_i \times 10^{k-i}\right)^{-1}\right] \tag{D.1}$$

where d_k is the kth leftmost digit. For example, the probability to find a number whose first leftmost digit is 2, second digit is 3 and third is 5 is $P(d_1 = 2, d_2 = 1, d_3 = 1) = \log_{10}(1 + 1/211) = 0.21\,\%$.

The formula for the first significant digit can be written as

$$P(k) = \log_{10}\left(1 + \frac{1}{k}\right), \quad k = 1, 2, \ldots, 9 \tag{D.2}$$

Benford's law has been validated using a variety of datasets from statistics [163] to geophysical sciences [164] and from financial data [165] to multiple choice exams [166]. Of course, studies were also performed on physical data like complex atomic spectra [167], full width of hadrons [168] and half life times for alpha and β decays [169, 170].

Although the significant digit law was studied thoroughly, is not yet fully understood. One of the greatest achievements towards the understanding of this law was its extension of scale to base invariance (the dependance of the base in which numbers are written) by Theodore Hill [171]. With the proof of these properties and by pointing out that all the datasets that follow Benford's law are a mixture from different distributions, he made a step closer to the full explanation of the law. A different way of interpreting the logarithmic law was proposed by Jeff Boyle [172] using the Fourier series method.

D.2   Benford's law in numerical series

Benford's law applies perfectly well on numerical sequences, like the Fibonacci and Lucas numbers [173] which are defined as:

- Fibonacci numbers (F_n), defined as

    - $F_0 = 0$
    - $F_1 = 1$
    - $F_n = F_{n-1} + F_{n-2}$, $\forall\, n > 1$

- Lucas numbers (JL_n), defined as

    - $L_0 = 2$
    - $L_1 = 1$
    - $L_n = L_{n-1} + L_{n-2}$, $\forall\, n > 1$

Expanding the list, three more series are examined, Jacobsthal, Jacobsthal-Lucas and Bernoulli [174] which are defined as follows:

- Jacobsthal numbers (J_n), defined as

    - $J_0 = 0$
    - $J_1 = 1$
    - $J_n = J_{n-1} + 2J_{n-2}$, $\forall\, n > 1$

- Jacobsthal-Lucas numbers (JL_n), defined as

    - $JL_0 = 2$
    - $JL_1 = 1$
    - $JL_n = JL_{n-1} + 2JL_{n-2}$, $\forall\, n > 1$

- and Bernoulli numbers (B_n), defined by the contour interval

    - $B_0 = 1$
    - $B_n = \frac{n!}{2\pi i} \oint \frac{z}{e^z - 1} \frac{dz}{z^{n+1}}$

In order to test if the numerical series mentioned above follow Benford's law, the first 1000 number are calculated from these sequences. From these numerical samples the probabilities of the first significant digits to be $1, 2, ..., 9$ and the second and third significant digits to be $0, 1, ..., 9$ are extracted. These probabilities are then compared with the probabilities derived from Benford's law (equation D.1) in figure D.1. It is evident that all three sequences follow Benford's law for the first (black), second (red) and third (blue) significant digit.

Full circles represent the result from the analysis of the Jacobsthal and Jacobsthal-Lucas numbers and the empty circles indicate the probabilities calculated from Benford's formula (equation D.1).
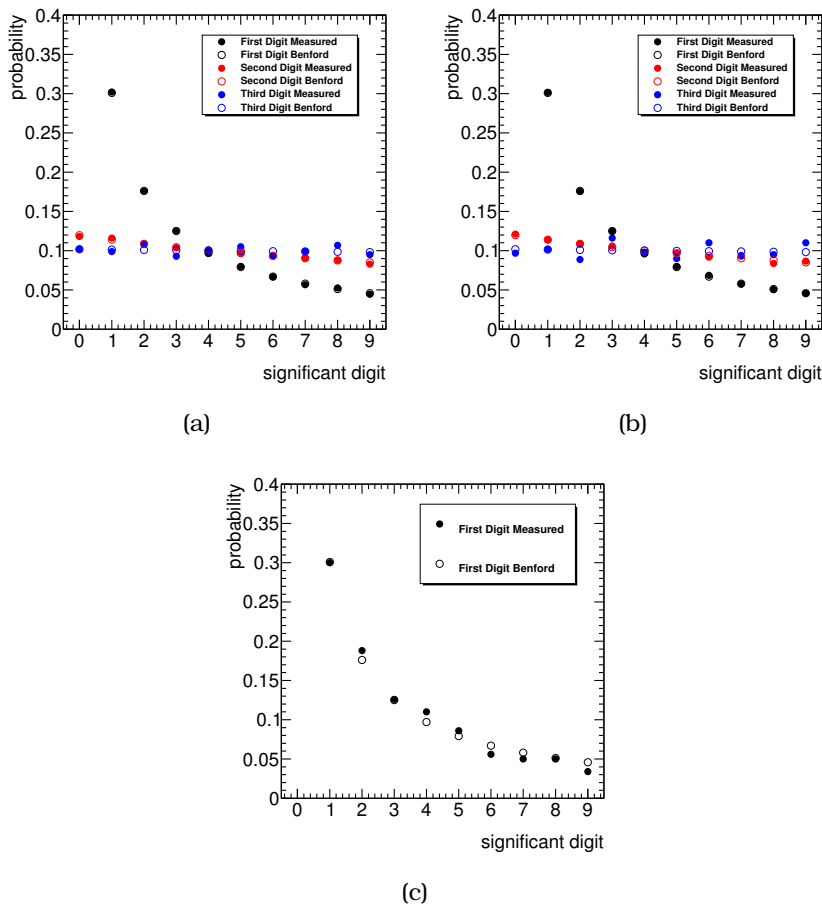
Figure D.1: *Comparison of Benford's law probability predictions (empty circles) and the probabilities for the first, second and third significant digit of the (a) Jacobsthal, (b) Jacobsthal-Lucas and (c) Bernoulli sequences (full circles). The probabilities for the first digit is plotted with black, the second with red and the third with blue circles.*

D.3   Applying Benford's law to astronomical data

An interesting application of this law is to the galaxy and star distances (all measured from the earth). A discrepancy between theses data and Benford probabilities might

occur if the location of the galaxies and stars in our universe are caused by uncorrelated random processes. For this, measurements of celestial objects are used [175, 176].

D.3.1 Comparison with galaxy distances

The dataset with the galaxy distances was compiled from measurements from type II Supernova and all units chosen to be Mpc[1] [175]. 702 galaxies were selected with the distances up to 1660 Mpc as illustrated in figure D.2(a).

The comparison between the probabilities from Benford observation (open circles) and the data-derived ones (full circles) are shown in figure D.2(b). An reasonably good agreement is observed for the first significant digit. Unfortunately due to insufficient measurements the comparison of the second and third digit was not possible.

(a)   (b)
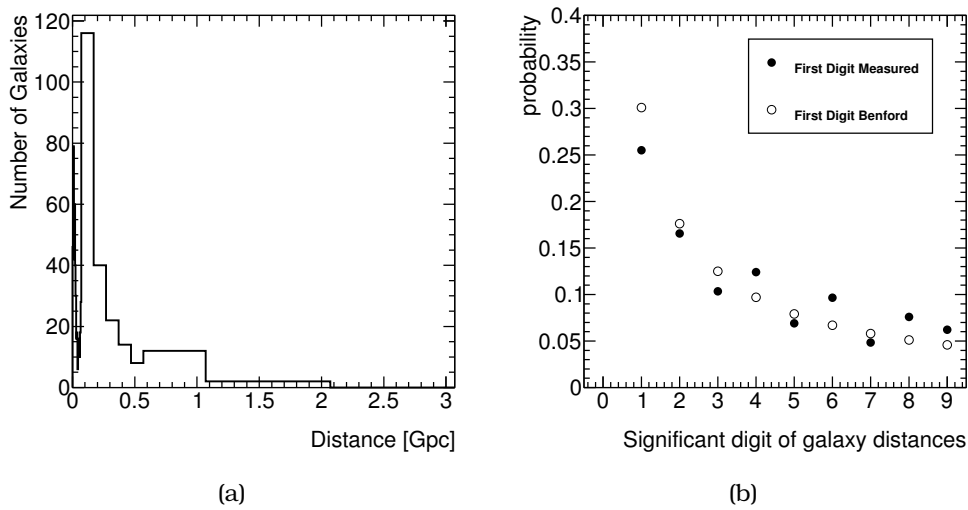
Figure D.2: *Complete dataset from where the measurements for the galaxies (a) and stars (b) is shown.*

D.3.2 Stars

The dataset for the comparison of the star distances the HYG database [176] was used. A total of 115 256 star distances was extracted going up to 14 kpc[1]) as illustrated in figure D.3(a)). Due to the large statistics of the sample a comparison of the first digits was possible, showing again a good agreement between data and Benford's expectations (see figure D.3(b)).

D.4 A possible explanation

Initiated from these studies, a possible explanation was given trying to link Hubble's and Benford's law [178].

---

[1] It is also worth mentioning the choice of units is not affecting the result, as one of the properties of Benford's law is its invariance under the choice of units of the dataset (scale invariance) [177].

(a)

(b)
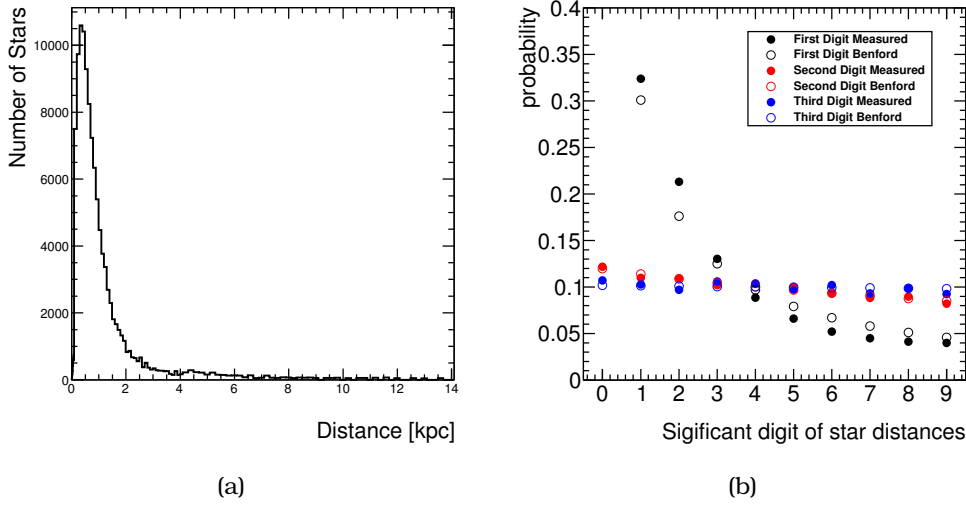
Figure D.3: *Comparisons of Benford's law (empty circles) and the distribution of the first (black), second (red) and third (blue) significant digit of the distances of the (a) galaxies and (b) stars (full circles).*

The distance of stars is measured by the light that the stars emits. Thus, the *observed distance* of the star ($\hat{x}$) is given by the formula

$$\hat{x}(t) = x\left(t_{\text{present}} - t_c(t)\right), \tag{D.3}$$

where $x(t)$ is the *actual distance*, t_{present} is the current time and $t_c(t)$ is the time that needed the light to reach the earth and is equal to $t_c(t) = \hat{x}(t)/c$, with c being the speed of light.

Hubble's law [179, 180] explains that the stars are receding from the earth at a rate proportional to their distance $dx/dt = Hx$ which formula's solution is

$$x(t) = x(t_{\text{base}}) \exp\left(H(t - t_{\text{base}})\right) \tag{D.4}$$

From D.3 and D.4

$$\hat{x}(t_{\text{present}}) = x(t_{\text{base}}) \exp\left(H\left(t_{\text{present}} - t_{\text{base}} - \frac{\hat{x}(t_{\text{present}})}{c}\right)\right)$$

and expressing this to the base time t_{base}

$$x(t_0) = \hat{x}(t_{\text{present}}) \exp\left(H\frac{\hat{x}(t_{\text{present}})}{c}\right) \exp\left(-H(t_{\text{present}} - t_{\text{base}})\right) \tag{D.5}$$

Starting from the *principle of indifference* it is assumed that the distance to a random galaxy ($\hat{x}(t_{\text{present}})$) can take any value among the $\{\alpha, \alpha + \delta, \alpha + 2\delta, \alpha + 3\delta, \ldots, \alpha + N\delta\}$. Using equation D.5 the following is derived

$$x(t_{\text{base}}) = (\alpha + \delta n) \exp\left(H\frac{\delta n}{c}\right) \exp\left(-H\left(t_{\text{present}} - t_{\text{base}} - \frac{\alpha}{c}\right)\right) = \mathcal{X}(\alpha + \delta n)b^n \tag{D.6}$$

with

$$X = \exp\left(-H\left(t_{\text{present}} - t_{\text{base}} - \frac{\alpha}{c}\right)\right) > 0 \text{ and } b = \exp\left(H\frac{\delta}{c}\right) > 1.$$

In order to complete the argument we use the following two hypotheses:

- If (x_n) is a Benford sequence then αx_n will follow Benford as well

- If b is not a rational power of 10 then the sequence (b^n) is Benford [181]

Combining the above and substituting $\alpha = p(n)$ the statement that if $b > 0$ and not an exact rational power of 10, the $(p(n)b^n)$ is a Benford sequence for all non-zero polynomials p is derived.

With $p(n) = \alpha + \delta n$, equation D.6 is derived.

Bibliography

[1] G. Altarelli, *Collider Physics within the Standard Model: a Primer*, arXiv:1303.2842.

[2] F. Bezrukov, G. K. Karananas, J. Rubio, and M. Shaposhnikov, *Higgs-Dilaton Cosmology: an effective field theory approach*, Phys.Rev. **D87** (2013), no. 9 096001, [arXiv:1212.4148].

[3] S. Leontsinis, *New Physics searches in heavy flavours in ATLAS*, EPJ Web Conf. **60** (2013) 15004, [arXiv:1311.2747].

[4] J. H. Kuhn and P. Zerwas, *The Toponium Scenario*, Phys.Rept. **167** (1988) 321.

[5] J. J. Aubert et al., *Experimental observation of a heavy particle j*, Phys. Rev. Lett. **33** (Dec, 1974) 1404–1406.

[6] J. E. Augustin et al., *Discovery of a narrow resonance in e^+e^- annihilation*, Phys. Rev. Lett. **33** (Dec, 1974) 1406–1408.

[7] S. Herb, D. Hom, L. Lederman, J. Sens, H. Snyder, et al., *Observation of a Dimuon Resonance at 9.5-GeV in 400-GeV Proton-Nucleus Collisions*, Phys.Rev.Lett. **39** (1977) 252–255.

[8] C.-H. Chang, *Hadronic Production of J/ψ Associated With a Gluon*, Nucl.Phys. **B172** (1980) 425–434.

[9] R. Baier and R. Ruckl, *Hadronic Production of J/ψ and Υ: Transverse Momentum Distributions*, Phys.Lett. **B102** (1981) 364.

[10] E. L. Berger and D. L. Jones, *Inelastic Photoproduction of J/ψ and Υ by Gluons*, Phys.Rev. **D23** (1981) 1521–1530.

[11] H. Fritzsch, *Producing Heavy Quark Flavors in Hadronic Collisions: A Test of Quantum Chromodynamics*, Phys.Lett. **B67** (1977) 217.

[12] F. Halzen, *Cvc for Gluons and Hadroproduction of Quark Flavors*, Phys.Lett. **B69** (1977) 105.

[13] M. Gluck, J. Owens, and E. Reya, *Gluon Contribution to Hadronic J/ψ Production*, *Phys.Rev.* **D17** (1978) 2324.

[14] V. D. Barger, W.-Y. Keung, and R. Phillips, *On ψ and Υ Production via Gluons*, *Phys.Lett.* **B91** (1980) 253.

[15] P. Hagler, R. Kirschner, A. Schafer, L. Szymanowski, and O. Teryaev, *Direct J/ψ hadroproduction in k^- perpendicular factorization and the color octet mechanism*, *Phys.Rev.* **D63** (2001) 077501, [hep-ph/0008316].

[16] F. Yuan and K.-T. Chao, *Color singlet direct J/ψ and ψ prime production at Tevatron in the k_t factorization approach*, *Phys.Rev.* **D63** (2001) 034006, [hep-ph/0008302].

[17] M. Cacciari, M. Greco, and P. Nason, *The p_T spectrum in heavy flavor hadroproduction*, *JHEP* **9805** (1998) 007, [hep-ph/9803400].

[18] M. Cacciari, S. Frixione, and P. Nason, *The p_T spectrum in heavy flavor photoproduction*, *JHEP* **0103** (2001) 006, [hep-ph/0102134].

[19] J. C. Collins and D. E. Soper, *Angular Distribution of Dileptons in High-Energy Hadron Collisions*, *Phys.Rev.* **D16** (1977) 2219.

[20] K. Gottfried and J. D. Jackson, *On the Connection between production mechanism and decay of resonances at high-energies*, *Nuovo Cim.* **33** (1964) 309–330.

[21] T. Alexopoulos and S. Leontsinis, *Estimates of the Cross Section of the Production of Z Boson and J/ψ at the LHC*, *J.Exp.Theor.Phys.* **147** (2015) 937–941, [arXiv:1309.4736].

[22] B. A. Kniehl, C. P. Palisoc, and L. Zwirner, *Associated production of heavy quarkonia and electroweak bosons at present and future colliders*, *Phys.Rev.* **D66** (2002) 114002, [hep-ph/0208104].

[23] B. Gong, J.-P. Lansberg, C. Lorce, and J. Wang, *Next-to-leading-order QCD corrections to the yields and polarisations of J/ψ and Υ directly produced in association with a Z boson at the LHC*, *JHEP* **1303** (2013) 115, [arXiv:1210.2430].

[24] S. Mao, M. Wen-Gan, L. Gang, Z. Ren-You, and G. Lei, *QCD corrections to J/ψ plus Z^0-boson production at the LHC*, *JHEP* **1102** (2011) 071, [arXiv:1102.0398].

[25] L. Gang, M. Wen-Gan, S. Mao, Z. Ren-You, and G. Jian-You, *Associated production of Υ(1S)W at LHC in next-to-leading order QCD*, *JHEP* **1301** (2013) 034, [arXiv:1212.2417].

[26] E. Braaten, J. Lee, and S. Fleming, *Associated production of υ and weak gauge bosons at the Tevatron*, *Phys.Rev.* **D60** (1999) 091501, [hep-ph/9812505].

[27] M. Song, G. Li, W.-G. Ma, R.-Y. Zhang, L. Guo, et al., *J/ψ Production Associated with a W-Boson at the 7 TeV Large Hadron Collider*, *Chin.Phys.Lett.* **30** (2013) 091201, [arXiv:1304.4670].

[28] G. Li, M. Song, R.-Y. Zhang, and W.-G. Ma, *QCD corrections to J/ψ production in association with a W-boson at the LHC*, *Phys.Rev.* **D83** (2011) 014001, [arXiv:1012.3798].

[29] Particle Data Group , K. Olive et al., *Review of Particle Physics*, *Chin.Phys.* **C38** (2014) 090001.

[30] G.-Z. Xu, Y.-J. Li, K.-Y. Liu, and Y.-J. Zhang, *Relativistic Correction to Color Octet J/psi Production at Hadron Colliders*, *Phys.Rev.* **D86** (2012) 094017, [arXiv:1203.0207].

[31] ATLAS Collaboration, G. Aad et al., *Observation and measurements of the production of prompt and non-prompt J/ψ mesons in association with a Z boson in pp collisions at $\sqrt{s} = 8$, TeV with the ATLAS detector*, arXiv:1412.6428.

[32] ATLAS Collaboration, G. Aad et al., *Observation of a new particle in the search for the Standard Model Higgs boson with the ATLAS detector at the LHC*, *Phys.Lett.* **B716** (2012) 1–29, [arXiv:1207.7214].

[33] CMS Collaboration, S. Chatrchyan et al., *Combined results of searches for the standard model Higgs boson in pp collisions at $\sqrt{s} = 7$ TeV*, *Phys.Lett.* **B710** (2012) 26–48, [arXiv:1202.1488].

[34] ATLAS Collaboration, G. Aad et al., *Search for Higgs and Z Boson Decays to J/ψγ and Υ(nS)γ with the ATLAS Detector*, arXiv:1501.0327.

[35] ATLAS Collaboration, G. Aad et al., *Evidence for the Higgs-boson Yukawa coupling to tau leptons with the ATLAS detector*, arXiv:1501.0494.

[36] ATLAS Collaboration, G. Aad et al., *Search for the Standard Model Higgs boson decay to $\mu^+\mu^-$ with the ATLAS detector*, *Phys.Lett.* **B738** (2014) 68–86, [arXiv:1406.7663].

[37] B. Bhattacharya, A. Datta, and D. London, *Probing New Physics in Higgs Couplings to Fermions using an Angular Analysis*, *Phys.Lett.* **B736** (2014) 421–427, [arXiv:1407.0695].

[38] D.-N. Gao, *A note on Higgs decays into Z boson and J/ψ(Υ)*, arXiv:1406.7102.

[39] G. Isidori, A. V. Manohar, and M. Trott, *Probing the nature of the Higgs-like Boson via h → VF decays*, *Phys.Lett.* **B728** (2014) 131–135, [arXiv:1305.0663].

[40] H. Davoudiasl, H.-S. Lee, and W. J. Marciano, *'Dark' Z implications for Parity Violation, Rare Meson Decays, and Higgs Physics*, Phys.Rev. **D85** (2012) 115019, [arXiv:1203.2947].

[41] M. Gonzalez-Alonso and G. Isidori, *The $h \to 4l$ spectrum at low m_{34}: Standard Model vs. light New Physics*, Phys.Lett. **B733** (2014) 359–365, [arXiv:1403.2648].

[42] J. D. Clarke, R. Foot, and R. R. Volkas, *Phenomenology of a very light scalar ($100\,\mathrm{MeV} < m_h < 10\,\mathrm{GeV}$) mixing with the SM Higgs*, JHEP **1402** (2014) 123, [arXiv:1310.8042].

[43] E. Braaten, K.-m. Cheung, and T. C. Yuan, *Z^0 decay into charmonium via charm quark fragmentation*, Phys.Rev. **D48** (1993) 4230–4235, [hep-ph/9302307].

[44] S. Fleming, *Electromagnetic production of quarkonium in Z^0 decay*, Phys.Rev. **D48** (1993) 1914–1916, [hep-ph/9304270].

[45] S. Fleming, *J/ψ production from electromagnetic fragmentation in Z^0 decay*, Phys.Rev. **D50** (1994) 5808–5815, [hep-ph/9403396].

[46] LEP Collaboration, *LEP Design Report. Vol. 1. The LEP Injector Chain*, Tech. Rep. CERN-LEP/TH/83-29, CERN/PS/DL/83-31, CERN/SPS/83-26, LAL/RT/83-09, CERN, 1983.

[47] B. Guberina, J. H. Kuhn, R. Peccei, and R. Ruckl, *Rare Decays of the Z^0*, Nucl.Phys. **B174** (1980) 317.

[48] V. D. Barger, K.-m. Cheung, and W.-Y. Keung, *Z boson decays to heavy quarkonium*, Phys.Rev. **D41** (1990) 1541.

[49] ATLAS Collaboration, G. Aad et al., *Measurements of Four-Lepton Production at the Z Resonance in pp Collisions at $\sqrt{s}$ =7 and 8 TeV with ATLAS*, Phys.Rev.Lett. **112** (2014), no. 23 231806, [arXiv:1403.5657].

[50] CMS Collaboration, S. Chatrchyan et al., *Observation of Z decays to four leptons with the CMS detector at the LHC*, JHEP **1212** (2012) 034, [arXiv:1210.3844].

[51] CDF Collaboration, F. Abe et al., *Search for associated production of Υ and vector boson in $p\bar{p}$ collisions at $\sqrt{s}$ = 1.8 TeV*, Phys. Rev. Lett. **90** (2003) 221803.

[52] CDF Collaboration, T. Aaltonen et al., *Search for production of an $\Upsilon(1S)$ meson in association with a W or Z boson using the full 1.96 TeV proton anti-proton collision data set at CDF*, arXiv:1412.4827.

[53] ATLAS Collaboration, G. Aad et al., *Measurement of the production cross section of prompt J/ψ mesons in association with a $W^{\pm}$ boson in pp collisions at $\sqrt{s}$ = 7 TeV with the ATLAS detector*, JHEP **1404** (2014) 172, [arXiv:1401.2831].

[54] LHCb Collaboration, R. Aaij et al., *Observation of associated production of a Z boson with a D meson in the forward region*, *JHEP* **1404** (2014) 091, [arXiv:1401.3245].

[55] Axial Field Spectrometer Collaboration , T. Akesson et al., *Double Parton Scattering in pp Collisions at $\sqrt{s}$ = 63 GeV*, *Z.Phys.* **C34** (1987) 163.

[56] CMS Collaboration, S. Chatrchyan et al., *Study of double parton scattering using W + 2-jet events in proton-proton collisions at $\sqrt{s}$ = 7 TeV*, *JHEP* **1403** (2014) 032, [arXiv:1312.5729].

[57] M. H. Seymour and A. Siodmok, *Constraining MPI models using σ_{eff} and recent Tevatron and LHC Underlying Event data*, *JHEP* **1310** (2013) 113, [arXiv:1307.5015].

[58] CDF Collaboration, F. Abe et al., *Study of four jet events and evidence for double parton interactions in $p\bar{p}$ collisions at $\sqrt{s}$ = 1.8 TeV*, *Phys.Rev.* **D47** (1993) 4857–4871.

[59] CDF Collaboration, F. Abe et al., *Double parton scattering in $\bar{p}p$ collisions at $\sqrt{s}$ = 1.8TeV*, *Phys.Rev.* **D56** (1997) 3811–3832.

[60] D0 Collaboration, V.M. Abazov et al. , *Double parton interactions in γ+3 jet events in pp^- bar collisions $\sqrt{s}$ = 1.96 TeV.*, *Phys.Rev.* **D81** (2010) 052012, [arXiv:0912.5104].

[61] ATLAS Collaboration, G. Aad et al., *Measurement of hard double-parton interactions in $W(\rightarrow l\nu)$+ 2 jet events at $\sqrt{s}$=7 TeV with the ATLAS detector*, *New J.Phys.* **15** (2013) 033038, [arXiv:1301.6872].

[62] L. Evans and P. Bryant, *LHC Machine*, *JINST* **3** (2008) S08001.

[63] ATLAS Collaboration, G. Aad et al., *Improved luminosity determination in pp collisions at $\sqrt{s}$ = 7 TeV using the ATLAS detector at the LHC*, *Eur.Phys.J.* **C73** (2013), no. 8 2518, [arXiv:1302.4393].

[64] ATLAS Collaboration, G. Aad et al., *The ATLAS Experiment at the CERN Large Hadron Collider*, *JINST* **3** (2008) S08003.

[65] CMS Collaboration, S. Chatrchyan et al., *The CMS experiment at the CERN LHC*, *JINST* **3** (2008) S08004.

[66] ALICE Collaboration, F. Carminati et al., *ALICE: Physics performance report, volume I*, *J.Phys.* **G30** (2004) 1517–1763.

[67] LHCb Collaboration, A.A. Alves, *The LHCb Detector at the LHC*, *JINST* **3** (2008) S08005.

[68] ATLAS Collaboration, G. Aad et al., *The ATLAS Simulation Infrastructure*, *Eur.Phys.J.* **C70** (2010) 823–874, [arXiv:1005.4568].

[69] G. Barrand, I. Belyaev, P. Binko, M. Cattaneo, R. Chytracek, et al., *GAUDI - A software architecture and framework for building HEP data processing applications*, *Comput.Phys.Commun.* **140** (2001) 45–55.

[70] L. Lonnblad, *CLHEP: A project for designing a C++ class library for high-energy physics*, *Comput.Phys.Commun.* **84** (1994) 307–316.

[71] R. Brun and F. Rademakers, *ROOT: An object oriented data analysis framework*, *Nucl.Instrum.Meth.* **A389** (1997) 81–86.

[72] M. Dobbs and J. B. Hansen, *The HepMC C++ Monte Carlo event record for High Energy Physics*, *Comput.Phys.Commun.* **134** (2001) 41–46.

[73] GEANT4 Collaboration, S. Agostinelliet al. et al., *GEANT4: A Simulation toolkit*, *Nucl.Instrum.Meth.* **A506** (2003) 250–303.

[74] M. Capeans, G. Darbo, K. Einsweiller, M. Elsing, T. Flick, M. Garcia-Sciveres, C. Gemme, H. Pernegger, O. Rohne, and R. Vuillermet, *ATLAS Insertable B-Layer Technical Design Report*, Tech. Rep. CERN-LHCC-2010-013. ATLAS-TDR-19, CERN, Geneva, Sep, 2010.

[75] K. Lantzsch, S. Arfaoui, S. Franz, O. Gutzwiller, S. Schlenker, et al., *The ATLAS detector control system*, *J.Phys.Conf.Ser.* **396** (2012) 012028.

[76] O. Holme, M. Gonzalez Berges, P. Golonka, and S. Schmeling, *The JCOP framework*, tech. rep., 2005.

[77] T. Alexopoulos, E. Gazis, G. Iakovidis, S. Leontsinis, E. Mountricha, G. Tsipolitis, and S. Vlachos, *MDT Power Supply Developers Documentation*, Tech. Rep. ATL-MUON-INT-2011-004, CERN, Geneva, Sep, 2011.

[78] ATLAS Collaboration, G. Aad et al., *Muon reconstruction efficiency using J/ψ*, *ATL-COM-MUON-2012-013* (2012).

[79] A. Valassi, R. Basset, M. Clemencic, G. Pucciani, S. A. Schmidt, and M. Wache, *COOL, LCG Conditions Database for the LHC Experiments: Development and Deployment Status. LHC: Large Hadron Collider*, Tech. Rep. CERN-IT-Note-2008-019, CERN, Geneva, Nov, 2008.

[80] T. Alexopoulos et al., *MDT DCS conditions data and DCS COOL folder configuration*, *ATL-MUON-INT-2014-006* (2012).

[81] ATLAS Collaboration, G. Aad et al., *Luminosity Determination in pp Collisions at $\sqrt{s} = 7$ TeV Using the ATLAS Detector at the LHC*, *Eur.Phys.J.* **C71** (2011) 1630, [arXiv:1101.2185].

[82] ATLAS Collaboration, G. Aad et al., *Measurement of the muon reconstruction performance of the ATLAS detector using 2011 and 2012 LHC proton-proton collision data*, *Eur.Phys.J.* **C74** (2014), no. 11 3130, [arXiv:1407.3935].

[83] ATLAS Collaboration, G. Aad et al., *Muon reconstruction efficiency and momentum resolution of the ATLAS experiment in proton-proton collisions at* $\sqrt{s}$ = 7 TeV *in 2010, Eur.Phys.J.* **C74** (2014), no. 9 3034, [arXiv:1404.4562].

[84] T. Sjostrand, S. Ask, J. R. Christiansen, R. Corke, N. Desai, et al., *An Introduction to PYTHIA 8.2,* arXiv:1410.3012.

[85] ATLAS Collaboration, G. Aad et al., *Improved electron reconstruction in ATLAS using the Gaussian Sum Filter-based model for bremsstrahlung,* tech. rep., 2012.

[86] J. Kretzschmar and L. Iconomidou-Fayard, *Electron performances measurements using the 2011 LHC proton-proton collisions,* Tech. Rep. ATL-COM-PHYS-2012-1024, CERN, Geneva, Jul, 2012.

[87] M. C. Stockton, *Isolated direct photon production and the Atlantis event display for the ATLAS experiment.* PhD thesis, University of Birmingham, 2009.

[88] ATLAS Collaboration, G. Aad et al., *Measurement of the production cross section of prompt J/ψ mesons in association with a Z boson in pp collisions at* $\sqrt{s}$ = 8 TeV *with the ATLAS detector,* Tech. Rep. ATL-COM-PHYS-2014-412, CERN, Geneva, May, 2014.

[89] R. A. Fisher, *Combining independent tests of significance, American Statistician* **2, issue 5** (1948).

[90] M. Pivk and F. R. Le Diberder, *SPlot: A Statistical tool to unfold data distributions, Nucl.Instrum.Meth.* **A555** (2005) 356–369, [physics/0402083].

[91] M. Cacciari, S. Frixione, N. Houdeau, M. L. Mangano, P. Nason, et al., *Theoretical predictions for charm and bottom production at the LHC, JHEP* **1210** (2012) 137, [arXiv:1205.6344].

[92] ATLAS Collaboration, G. Aad et al., *Measurement of the differential cross-sections of inclusive, prompt and non-prompt J/ψ production in proton-proton collisions at* $\sqrt{s}$ = 7 TeV, *Nucl.Phys.* **B850** (2011) 387–444, [arXiv:1104.3038].

[93] P. Nason, *A New method for combining NLO QCD with shower Monte Carlo algorithms, JHEP* **0411** (2004) 040, [hep-ph/0409146].

[94] S. Frixione, P. Nason, and G. Ridolfi, *A Positive-weight next-to-leading-order Monte Carlo for heavy flavour hadroproduction, JHEP* **0709** (2007) 126, [arXiv:0707.3088].

[95] S. Frixione, P. Nason, and C. Oleari, *Matching NLO QCD computations with Parton Shower simulations: the POWHEG method, JHEP* **0711** (2007) 070, [arXiv:0709.2092].

[96] T. Sjostrand, S. Mrenna, and P. Z. Skands, *A brief introduction to PYTHIA 8.1, Comput. Phys. Commun.* **178** (2008) 852–867, [arXiv:0710.3820].

[97] H.-L. Lai et al., *New parton distributions for collider physics, Phys.Rev.* **D82** (2010) 074024, [arXiv:1007.2241].

[98] ATLAS Collaboration, G. Aad et al., *Atlas tunes of pythia 6 and pythia 8 for mc11, ATL-PHYS-PUB-2011-009 (2011)* [https://cds.cern.ch/record/1363300] (2011).

[99] S. Frixione and B. R. Webber, *Matching NLO QCD computations and parton shower simulations, JHEP* **0206** (2002) 029, [hep-ph/0204244].

[100] S. Frixione, P. Nason, and B. R. Webber, *Matching NLO QCD and parton showers in heavy flavor production, JHEP* **0308** (2003) 007, [hep-ph/0305252].

[101] G. Corcella et al., *HERWIG 6: an event generator for hadron emission reactions with interfering gluons (including supersymmetric processes), JHEP* **0101** (2001) 010, [hep-ph/0011363].

[102] J. Butterworth, J. R. Forshaw, and M. Seymour, *Multiparton interactions in photoproduction at HERA, Z.Phys.* **C72** (1996) 637–646, [hep-ph/9601371].

[103] ATLAS Collaboration, G. Aad et al., *New atlas event generator tunes to 2010 data, ATL-PHYS-PUB-2011-008 (2011)* [https://cds.cern.ch/record/1345343] (2011).

[104] B. P. Kersevan and E. Richter-Was, *The Monte Carlo event generator AcerMC versions 2.0 to 3.8 with interfaces to PYTHIA 6.4, HERWIG 6.5 and ARIADNE 4.1, Comput. Phys. Commun.* **184** (2013) 919, [hep-ph/0405247].

[105] J. Pumplin et al., *New generation of parton distributions with uncertainties from global QCD analysis, JHEP* **0207** (2002) 012, [hep-ph/0201195].

[106] T. Sjostrand, S. Mrenna, and P. Z. Skands, *PYTHIA 6.4 Physics and Manual, JHEP* **0605** (2006) 026, [hep-ph/0603175].

[107] CDF Collaboration, A. Abulencia et al., *Polarization of J/ψ and ψ_{2S} mesons produced in $p\bar{p}$ collisions at $\sqrt{s}$ = 1.96-TeV, Phys.Rev.Lett.* **99** (2007) 132001, [arXiv:0704.0638].

[108] M. Butenschoen and B. A. Kniehl, *World data of J/psi production consolidate NRQCD factorization at NLO, Phys.Rev.* **D84** (2011) 051501, [arXiv:1105.0820].

[109] ATLAS Collaboration, G. Aad et al., *Measurement of the differential cross-section of B^+ meson production in pp collisions at $\sqrt{s}$ = 7 TeV at ATLAS, JHEP* **1310** (2013) 042, [arXiv:1307.0126].

[110] ATLAS Collaboration, G. Aad et al., *ATLAS measurements of the 7 and 8 TeV cross sections for $Z \rightarrow 4\ell$ in pp collisions, ATLAS-CONF-2013-055, ATLAS-COM-CONF-2013-063* (2013).

[111] N. Cabibbo, *Unitary Symmetry and Leptonic Decays*, *Phys.Rev.Lett.* **10** (1963) 531–533.

[112] M. Kobayashi and T. Maskawa, *CP Violation in the Renormalizable Theory of Weak Interaction*, *Prog.Theor.Phys.* **49** (1973) 652–657.

[113] S. Glashow, J. Iliopoulos, and L. Maiani, *Weak Interactions with Lepton-Hadron Symmetry*, *Phys.Rev.* **D2** (1970) 1285–1292.

[114] K. De Bruyn, R. Fleischer, R. Knegjens, P. Koppenburg, M. Merk, et al., *Probing New Physics via the $B_s^0 \to \mu^+\mu^-$ Effective Lifetime*, *Phys.Rev.Lett.* **109** (2012) 041801, [arXiv:1204.1737].

[115] CMS Collaboration, S. Chatrchyan et al., *Measurement of the $B_s^0 \to \mu^+\mu^-$ branching fraction and search for $B^0 \to \mu^+\mu^-$ with the CMS Experiment*, *Phys.Rev.Lett.* **111** (2013) 101804, [arXiv:1307.5025].

[116] LHCb Collaboration, R. Aaij et al., *Measurement of the $B_s^0 \to \mu^+\mu^-$ branching fraction and search for $B^0 \to \mu^+\mu^-$ decays at the LHCb experiment*, *Phys.Rev.Lett.* **111** (2013) 101805, [arXiv:1307.5024].

[117] CMS, LHCb Collaborations , V. Khachatryan et al., *Observation of the rare $B_s^0 \to \mu^+\mu^-$ decay from the combined analysis of CMS and LHCb data*, arXiv:1411.4413.

[118] ATLAS Collaboration, G. Aad et al., *Search for the decay $B_s^0 \to \mu\mu$ with the ATLAS detector*, *Phys.Lett.* **B713** (2012) 387–407, [arXiv:1204.0735].

[119] R. Aaij et al., *Measurement of b-hadron production fractions in 7 TeVpp collisions*, *Phys.Rev.* **D85** (2012) 032008, [arXiv:1111.2357].

[120] A. Hocker, J. Stelzer, F. Tegenfeldt, H. Voss, K. Voss, et al., *TMVA - Toolkit for Multivariate Data Analysis*, *PoS* **ACAT** (2007) 040, [physics/0703039].

[121] G. Punzi, *Sensitivity of searches for new signals and its optimization*, *eConf* **C030908** (2003) MODT002, [physics/0308063].

[122] V. Baglin, G. Bregliozzi, P. Chiggiato, J. Jimenez, and G. Lanza, *CERN Vacuum System Activities during the Long Shutdown 1: The LHC Beam Vacuum*, tech. rep., 2014.

[123] ATLAS Collaboration, G. Aad et al., *ATLAS Insertable B-Layer Technical Design Report Addendum*, Tech. Rep. CERN-LHCC-2012-009. ATLAS-TDR-19-ADD-1, CERN, Geneva, May, 2012. Addendum to CERN-LHCC-2010-013, ATLAS-TDR-019.

[124] M. C. Aleksa, W. P. Cleland, Y. T. Enari, M. V. Fincke-Keeler, L. C. Hervas, F. B. Lanni, S. O. Majewski, C. V. Marino, and I. L. Wingerter-Seez, *ATLAS Liquid Argon Calorimeter Phase-I Upgrade Technical Design Report*, Tech. Rep. CERN-LHCC-2013-017. ATLAS-TDR-022, CERN, Geneva, Sep, 2013. Final version presented to December 2013 LHCC.

[125] M. Shochet, L. Tompkins, V. Cavaliere, P. Giannetti, A. Annovi, and G. Volpi,
      Fast TracKer (FTK) Technical Design Report, Tech. Rep. CERN-LHCC-2013-007.
      ATLAS-TDR-021, CERN, Geneva, Jun, 2013. ATLAS Fast Tracker Technical
      Design Report.

[126] R. S. Bartoldus, C. M. C. Bee, D. C. Francis, N. R. Gee, S. L. R. George, R. M. S.
      Hauser, R. R. Middleton, T. C. Pauly, O. K. Sasaki, D. O. Strom, R. R. I. Vari,
      and S. R. I. Veneziano, *Technical Design Report for the Phase-I Upgrade of the
      ATLAS TDAQ System*, Tech. Rep. CERN-LHCC-2013-018. ATLAS-TDR-023,
      CERN, Geneva, Sep, 2013. Final version presented to December 2013 LHCC.

[127] L. Wiik, *ATLAS tracker upgrade: Silicon strip detectors for the sLHC*,
      Nucl.Phys.Proc.Suppl. **215** (2011) 154–156.

[128] "Atlas experiment, muon trigger public results." https://twiki.cern.ch/
      twiki/bin/view/AtlasPublic/MuonTriggerPublicResults.
      Accessed: 11-02-2015.

[129] ATLAS Collaboration, G. Aad et al., *New Small Wheel Technical Design Report*,
      Tech. Rep. CERN-LHCC-2013-006. ATLAS-TDR-020, CERN, Geneva, Jun, 2013.
      ATLAS New Small Wheel Technical Design Report.

[130] K. Nagai, *Thin gap chambers in ATLAS*, *Nucl.Instrum.Meth.* **A384** (1996)
      219–221.

[131] T. Alexopoulos, J. Burnens, R. de Oliveira, G. Glonti, O. Pizzirusso, et al., *A
      spark-resistant bulk-micromegas chamber for high-rate applications*,
      Nucl.Instrum.Meth. **A640** (2011) 110–118.

[132] J. Chapman, T. Dai, E. Diehl, H. Feng, L. Guan, et al., *Understand ATLAS NSW
      Thin Gap Chamber from Garfield Simulation*, *PoS* **EPS-HEP2013** (2013) 093.

[133] MAMMA Collaboration, T. Alexopoulos et al., *The micromegas project for the
      ATLAS upgrade*, tech. rep., 2013. proceedings for 2013 IEEE Nuclear Science
      Symposium and Medical Imaging.

[134] Y. Giomataris, P. Rebourgeard, J. Robert, and G. Charpak, *MICROMEGAS: A
      High granularity position sensitive gaseous detector for high particle flux
      environments*, *Nucl.Instrum.Meth.* **A376** (1996) 29–35.

[135] T. Alexopoulos, A. Altintas, M. Alviggi, M. Arik, S. Cetin, et al., *Development of
      large size Micromegas detector for the upgrade of the ATLAS muon system*,
      Nucl.Instrum.Meth. **A617** (2010) 161–165.

[136] K. Ntekas, *Micromegas chambers for the ATLAS muon spectrometer upgrade*,
      Tech. Rep. ATL-MUON-PROC-2014-011, CERN, Geneva, Nov, 2014.

[137] R. Duda and P. Hard, *Use of the Hough Transformation to Detect Lines and
      Curves in Pictures*, *Comm. ACM* **15** (1972) 11–15.

[138] F. Sauli, *Progress with the gas electron multiplier*, *Nucl.Instrum.Meth.* **A522** (2004) 93–98.

[139] R. Carnegie, M. Dixit, J. Dubeau, D. Karlen, J. Martin, et al., *Resolution studies of cosmic ray tracks in a TPC with GEM readout*, *Nucl.Instrum.Meth.* **A538** (2005) 372–383, [physics/0402054].

[140] K. Gnanvo, N. Liyanage, V. Nelyubin, K. Saenboonruang, S. Sacher, et al., *Large Size GEM for Super Bigbite Spectrometer (SBS) Polarimeter for Hall A 12 GeV program at JLab*, [arXiv:1409.5393].

[141] D. Arogancia, A. Bacala, K. Boudjemline, D. Burke, P. Colas, et al., *Study in a beam test of the resolution of a Micromegas TPC with standard readout pads*, *Nucl.Instrum.Meth.* **A602** (2009) 403–414, [arXiv:0705.2210].

[142] J.-E. Ducret, P. Legou, J. Lukasik, A. Boudard, M. Combet, et al., *Heavy-ion test of detectors with conventional and resistive Micromegas used in TPC configuration*, *Nucl.Instrum.Meth.* **A628** (2011) 166–171.

[143] T. Alexopoulos, G. Iakovidis, S. Leontsinis, K. Ntekas, and V. Polychronakos, *Examining the geometric mean method for the extraction of spatial resolution*, *Journal of Instrumentation* **9** (2014), no. 01 P01003, [arXiv:1311.2556].

[144] R. Veenhof, *Garfield, a drift chamber simulation program*, *Conf.Proc.* **C9306149** (1993) 66–71.

[145] J. Galan, D. Attie, E. Ferrer-Ribas, A. Giganon, I. Giomataris, et al., *An ageing study of resistive micromegas for the HL-LHC environment*, *JINST* **8** (2013) P04028, [arXiv:1301.7648].

[146] L. Jones, M. French, Q. Morrissey, A. Neviani, M. Raymond, et al., *The APV25 deep submicron readout chip for CMS detectors*, *Conf.Proc.* **C9909201** (1999) 162–166.

[147] S. Martoiu, H. Muller, A. Tarazona, and J. Toledo, *Development of the scalable readout system for micro-pattern gas detectors and other applications*, *Journal of Instrumentation* **8** (2013), no. 03 C03015.

[148] ATLAS Collaboration, G. Aad et al., *Improved luminosity determination in pp collisions at $\sqrt{s} = 7\,\mathrm{TeV}$ using the atlas detector at the lhc*, *The European Physical Journal C* **73** (2013), no. 8.

[149] E. Torrence, *Luminosity Determination in pp Collisions using the ATLAS Detector at the LHC*, 2012. Presentation at the International Conference on High Energy Physics 2012, Melbourne, Australia.

[150] M. Blatnik, K. Dehmelt, A. Deshpande, D. Dixit, N. Feege, et al., *Performance of a Quintuple-GEM Based RICH Detector Prototype*, [arXiv:1501.0353].

[151] MOLLER Collaboration , J. Benesch et al., *The MOLLER Experiment: An Ultra-Precise Measurement of the Weak Mixing Angle Using Møller Scattering*, arXiv:1411.4088.

[152] L. Jones, *APV25-S1: User guide version 2.2.* RAL Microelectronics Design Group, Chilton, 2001.

[153] M. A. Diaz and T. J. Weiler, *Decays of a fermiophobic Higgs*, hep-ph/9401259.

[154] T. Alexopoulos, G. Iakovidis, S. Leontsinis, K. Ntekas, and V. Polychronakis, *Identification of circles from datapoints using Gaussian sums*, arXiv:1403.4413.

[155] T. Alexopoulos, G. Iakovidis, S. Leontsinis, K. Ntekas, and V. Polychronakos, *Identification of circles from datapoints using the Legendre transform*, *Nucl.Instrum.Meth.* **A745** (2014) 16–23.

[156] V. Arnold, *Mathematical Methods of Classical Mechanics.* Springer.

[157] T. Alexopoulos, *Introduction to Signal Analysis.* NTUA Press, 2010.

[158] T. Alexopoulos, M. Bachtis, E. Gazis, and G. Tsipolitis, *Implementation of the legendre transform for track segment reconstruction in drift tube chambers*, *Nuclear Instruments and Methods in Physics Research Section A: Accelerators, Spectrometers, Detectors and Associated Equipment* **592** (2008), no. 3 456 – 462.

[159] J. Crawford, *A non-iterative method for fitting circular arcs to measured points*, *Nuclear Instruments and Methods in Physics Research* **211** (1983), no. 1 223 – 225.

[160] S. Newcomb, *Note on the Frequency of Use of the Different Digits in Natural Numbers*, *American Journal of Mathematics* **4** (1881) 39–40.

[161] F. Benford, *The Law of Anomalous Numbers*, *Proceedings of the American Philosophical Society* **78** (1938), no. 4 551–572.

[162] T. P. Hill, *A Statistical Derivation of the Significant-Digit Law*, *Statistical Science* **10** (1995), no. 4 354–363.

[163] L. Shao and B.-Q. Ma, *First-digit law in nonextensive statistics*, *Phys. Rev. E* **82** (Oct, 2010) 041110.

[164] A. Sen(De) and U. Sen, *Benford's law detects quantum phase transitions similarly as earthquakes*, *EPL (Europhysics Letters)* **95** (2011), no. 5 50008.

[165] P. Clippe and M. Ausloos, *Benford's law and Theil transform of financial data*, arXiv:1208.5896.

[166] F. M. Hoppe, *Benford's Law and Distractors in Multiple Choice Exams*, arXiv:1311.7606.

[167] J.-C. Pain, *Benford's law and complex atomic spectra*, `arXiv:0801.0946`.

[168] L. Shao and B.-Q. Ma, *First Digit Distribution of Hadron Full Width*, `arXiv:1004.3077`.

[169] B. Buck, A. C. Merchant, and S. M. Perez, *An illustration of benford's first digit law using alpha decay half lives*, *European Journal of Physics* **14** (1993), no. 2 59.

[170] N. Dong-Dong, W. Lai, and R. Zhong-Zhou, *Benford's law and β-decay half-lives*, *Communications in Theoretical Physics* **51** (2009), no. 4 713.

[171] T. P. Hill, *Base-invariance implies benford's law*, *Proc. Amer. Math. Soc.* **123** (1995) 887–895.

[172] J. Boyle, *An application of fourier series to the most significant digit problem*, *The American Mathematical Monthly* **101** (1994), no. 9 pp. 879–886.

[173] J. Wlodarski, *Fibonacci and lucas numbers tend to obey benford's law*, *The Fibonacci Quarterly* **9** (1971), no. 1 87–88.

[174] T. Alexopoulos and S. Leontsinis, *Benford's Law and the Universe*, *J.Astrophys.Astron.* **35** (2014) 639–648, [`arXiv:1401.5794`].

[175] NASA and IPAC, "Ned - nasa/ipac extragalactic database." `http://ned.ipac.caltech.edu`, 2014.

[176] T. A. Nexus, "The hyg database." `http://www.astronexus.com`, 2014.

[177] M. R. Wojcik, *Notes on scale-invariance and base-invariance for benford's law*, *Communications in Theoretical Physics* (2013) 25, [`arXiv:1307.3620`].

[178] R. F. Fox and T. P. Hill, *Hubble's Law Implies Benford's Law for Distances to Galaxies*, `arXiv:1412.1536`.

[179] Supernova Search Team , A. G. Riess et al., *Observational evidence from supernovae for an accelerating universe and a cosmological constant*, *Astron.J.* **116** (1998) 1009–1038, [`astro-ph/9805201`].

[180] Supernova Cosmology Project , S. Perlmutter et al., *Measurements of Omega and Lambda from 42 high redshift supernovae*, *Astrophys.J.* **517** (1999) 565–586, [`astro-ph/9812133`].

[181] A. Berger and T. Hill, *A basic theory of Benford's Law*, *Probability Surveys* **8** (2011) 1–126.

List of Tables

List of Figures

Glossary

A | **B** | **C** | **D** | **F** | **G** | **K** | **L** | **M** | **N** | **S**

A

ATLAS A Toroidal LHC Apparatus.

B

BDT Boosted Decision Tree.

C

CEM Colour Evaporation Model.

CKM Cabibbo - Kobayashi - Maskawa matrix.

CL Confidence Level.

CMS Compact Muon Solenoid.

COM Colour Octet Model.

CSM Colour Singlet Model.

D

DCS Detector Control System.

F

FCNC Flavour Changing Neutral Currents.

G

GRL Good Run List.

K

KS Kolmogorov-Smirnov test.

L

LDME Long Distance Matrix Elements.

LHC Large Hadron Collider.

LS Long Shutdown.

M

MAMMA Muon ATLAS MicroMegas Activity.

MVA Multivariate Data Analysis.

N

NSW New Small Wheel.

S

SES Single Event Sensitivity.

SM Standard Model.

Index